

The effect of changing temperature and mass flow rate on the charging and discharging time in a horizontal packed bed passive space heating system

RJ Homann

 **orcid.org 0000-0001-9099-2581**

Dissertation submitted in fulfilment of the requirements for the degree *Master of Science in Mechanical Engineering* at the North-West University

Supervisor: Prof LJ Grobler
Co-supervisor: Mr LF Lagrange

Graduation May 2018
Student number: 23079223

ABSTRACT

Research into rock-beds for residential use has declined over the past three decades. Although rock-beds were constructed for agricultural and solar home applications in the 1970's and 1980's, very little research has been undertaken to establish their viability as a Thermal Energy Storage (TES) option in the residential sector. Therefore, there is insufficient up-to-date research that provides overall information on the utilisation of horizontal uni-directional rock-beds for domestic space heating. The intention of this study was to investigate the use of a horizontal packed bed with a uni-directional flow, as a method of storing thermal energy for residential use.

The quantitative research method was selected for this study. Both an empirical and a numerical research design were included. The empirical research design was comprised of the proposed horizontal, uni-directional packed bed, followed by the construction phase. The most important performance metrics of the packed bed were identified, as well as how they were measured and what instruments were used. Tests were conducted for inlet temperatures of 40°C, 45°C, 50°C and 55°C and mass flow rates of 150 kg.h⁻¹, 200 kg.h⁻¹, 250 kg.h⁻¹ and 300 kg.h⁻¹. The numerical design was developed by using the STAR-CCM+[®] Computational Fluid Dynamics (CFD) package to model the empirical design.

The horizontal, uni-directional packed bed provided a good platform for space heating in the residential sector. The results indicated that an increase of 50 kg.h⁻¹ in the mass flow rate and 5°C of the inlet temperature resulted in an average reduction in the charging time of 750 and 500 seconds, respectively. It was established that the packed bed could be charged to more than 90% of its charging capacity in two-and-a-half hours of the total eight-hour charging time. After a 16-hour discharge cycle, the packed bed retained, on average, 70.211% of its maximum stored thermal energy.

The results showed that the heating table that was developed as the input to the numerical model, correlated well with the empirical inlet temperature data, with an average percentage error of 0.138%. It was concluded that the heating table of the numerical model was a suitable method for mimicking the empirical inlet curve. The final temperature states of the space region, for all the tests that were conducted, had a maximum error of 2.973% and a minimum error of -0.051%. The numerical model proved to be an efficient and accurate method for predicting the final temperature state of the space region, although the trends were not accurately followed during the charging and discharging phases throughout the packed bed.

The energy flow balance of the horizontal, uni-directional packed bed displayed very low efficiencies; however, if the system were completely passive and continuously made use of the retained energy in the packed bed for each charging cycle, it could become a viable option to be implemented in the residential sector.

Keywords: Randomly packed beds; rock-bed; thermal energy storage; TES; CFD, STAR-CCM+[®]; horizontal packed bed; uni-directional flow; mass flow rate; charge time; discharge time; passive; space heating.

DECLARATION

I, Roelof Jacobus Homann (Identity Number: 910605 5108 084), hereby declare that the work contained in this dissertation is my own. All information, which has been gained from various journal articles, text books or other sources, has been referenced accordingly.

.....

Mr. RJ Homann

.....

Date

ACKNOWLEDGEMENTS

I would like to thank the following people for their influence, guidance and support during the thesis.

To my Father God, for providing me with the strength to carry on when times were tough, for giving me the ability to complete the thesis and for showering me with unconditional love and an excellent support structure of family, friends and colleagues.

To my wife, Marése, who has stood with me since the start of the thesis. Thanks for your love, endless support, late night working sessions, encouragement and positive spirit.

To my family: my Dad, André, whose wise words cannot be captured on paper; my Mom, Riana, who has a heart of gold and who will do anything to keep her children happy; my aunt, Lorraine, who has been such an inspiration, role-model and caring god-mother; and my brother, Hugo and sister Helize, thanks for being such supportive siblings.

To my supervisors, Professor LJ Grobler and Mr LF Lagrange. Without you, this Masters degree would not have seen the light of day. A special thanks to Mr Lagrange, who has not just been a supervisor, but also an exceptional mentor. Your passion for Engineering and life is admirable.

To the Engineering Sciences team, Ms du Toit, Professor HJ Marx and Mr Lubbe. Ms du Toit, thanks for the moral support and encouragement throughout the project. Thank you to Prof Marx, for reminding me to continuously ask myself “So what?” during the research, and Mr Lubbe, for assisting during the construction phases.

To Piet Botes and Barry Crous, from the Instrumentation Department at the University of the Free State, for their assistance with the construction of materials for the research project.

To the Aerotherm team, for their assistance with the simulation setup. A special thanks to Christiaan de Wet, for his help and support, as well as his fine attention to detail.

To Mrs Rees, thanks a million for your hours and hours of hard work - I appreciate it deeply.

Finally, my social support structure, my friends, who managed to get my mind off the Masters studies when the dissertation blues crept near, and who always kept a smile on my face. A special thanks to Nathan Bernstein, for being a sounding board during the research process.

TABLE OF CONTENTS

	Page
1. INTRODUCTION.....	1
1.1 Background.....	1
1.2 Need Statement.....	2
1.3 Research Statement.....	3
1.4 Research Objectives.....	3
1.5 Dissertation Layout.....	3
2. LITERATURE SURVEY	5
2.1 Solar Energy Utilisation Types.....	5
2.2 Solar Energy Conversion Technologies	7
2.2.1 Photovoltaics.....	7
2.2.2 Concentrated solar power	8
2.2.3 Solar thermal energy.....	8
2.3 Thermal Energy Storage	14
2.3.1 Thermochemical energy storage.....	15
2.3.2 Latent heat storage	17
2.3.3 Sensible heat storage.....	18
2.4 Packed beds	21
2.4.1 Packed bed classification	21
2.4.2 Background.....	23
2.4.3 Performance effects	26
2.4.4 Porosity	28
2.4.5 Permeability	32
2.4.6 Heat transfer.....	34
2.4.7 Rocks properties.....	37
2.4.8 Fluid flow.....	38
2.4.9 Bed structure	38
2.4.10 Metrics for packed beds	46
2.5 Conclusions of the Literature Survey	54
2.5.1 Contextualisation of the need.....	54
2.5.2 Solar energy utilisation	55
2.5.3 Packed beds.....	55
2.5.4 Performance effects of packed beds	56
2.5.5 Performance metrics	58
3. METHODOLOGY.....	59
3.1 Research Methods.....	59
3.2 Research Designs.....	59
3.3 Empirical Design	60
3.3.1 Proposed design	60
3.3.2 Construction.....	65
3.3.3 Performance metrics	69

3.3.4	Test procedure.....	75
3.4	Numerical Design	77
3.4.1	Geometry.....	78
3.4.2	Boundary conditions	78
3.4.3	Mesh continua.....	80
3.4.4	Physics continua.....	80
3.4.5	Field functions	82
3.4.6	Tables.....	84
3.4.7	Solvers and stopping criteria.....	85
3.4.8	Derived parts, scenes and reports.....	85
3.4.9	Monitors and plots	85
3.4.10	Running the simulation.....	86
3.5	Data Analysis Methods.....	87
3.5.1	Empirical performance effects data	87
3.5.2	Empirical test data.....	88
3.5.3	Numerical test data	88
3.6	Quality Assurance.....	89
3.6.1	Verification	89
3.6.2	Validation.....	89
3.7	Conclusions of the Methodology.....	89
4.	RESULTS AND DISCUSSION	91
4.1	Verification	91
4.1.1	Empirical method.....	91
4.1.2	Numerical method.....	91
4.2	Empirical Test Data	92
4.2.1	Inlet and outlet	92
4.2.2	Packed bed	97
4.2.3	Concrete slab.....	103
4.2.4	Space.....	108
4.2.5	Energy Balance	112
4.3	Validation	114
4.3.1	Empirical vs. literature.....	114
4.3.2	Empirical vs. thermography.....	115
4.3.3	Empirical vs. numerical	116
4.4	Conclusions of the Results.....	129
4.4.1	Verification	129
4.4.2	Empirical test data.....	130
4.4.3	Validation.....	132
5.	CONCLUSIONS AND RECOMMENDATIONS	135
5.1	Conclusions.....	135
5.2	Recommendations.....	138
6.	REFERENCES.....	140
7.	APPENDIX A: RESIDENTIAL SECTOR ELECTRICITY CONSUMPTION	148
8.	APPENDIX B: PACKED BED DESIGN DRAWINGS	149

9.	APPENDIX C: PRESSURE DROP CALCULATIONS	159
10.	APPENDIX D: PRESSURE-PRODUCING DEVICE DETAILS	161
11.	APPENDIX E: MESH INDEPENDENCE STUDY.....	165
12.	APPENDIX F: MESH DEVELOPMENT FOR REGIONS, BOUNDARIES AND INTERFACES.....	167
13.	APPENDIX G: PHYSICS DEVELOPMENT FOR REGIONS, BOUNDARIES AND INTERFACES	169
14.	APPENDIX H: GENERATING THE HEATING TABLE.....	175
15.	APPENDIX I: HEAT TRANSFER AND THERMAL RESISTANCE CALCULATIONS	179
16.	APPENDIX J: POROUS INERTIAL RESISTANCE CALCULATIONS	181
17.	APPENDIX K: SENSITIVITY ANALYSIS OF SELECTED VARIABLES	184
18.	APPENDIX L: AVERAGE CHARGING TIME WITH A CHANGE IN TEMPERATURE AND MASS FLOW RATE	192
19.	APPENDIX M: ENERGY BALANCE DATA	193

LIST OF FIGURES

	Page
Figure 2.1 Active-direct system (adapted from Florida Solar Energy Center Cocoa, 2006)	6
Figure 2.2 Passive-direct system (after Florida Solar Energy Center Cocoa, 2006)	6
Figure 2.3 Passive-direct system	6
Figure 2.4 Active-indirect system (adapted from Florida Solar Energy Center Cocoa, 2006)	6
Figure 2.5 Active-indirect system (after Central, 2010)	6
Figure 2.6 Passive-indirect system (after Florida Solar Energy Center Cocoa, 2006)	6
Figure 2.7 Passive-indirect system (after Beken, 1984)	6
Figure 2.8 Classification of chemical storage and sorption storage (after N'Tsoukpoe <i>et al.</i> , 2009)	16
Figure 2.9 Schematic representation of the difference between a horizontal and vertical packed bed (adapted from Choudhury <i>et al.</i> , 1995)	21
Figure 2.10 Summary of the effect of material shape on a packed bed	30
Figure 2.11 Summary of the effect of packing on a packed bed	31
Figure 2.12 Summary of the effect of material sorting on a packed bed	32
Figure 2.13 Summary of the effect of material size on a packed bed	34
Figure 2.14 Vertical rock-bed (after Choudhury <i>et al.</i> , 1995)	39
Figure 2.15 Vertical packed bed (after Singh <i>et al.</i> , 2006)	39
Figure 2.16 Horizontal packed bed for greenhouse (after Kürklü <i>et al.</i> , 2003)	40
Figure 2.17 Horizontal packed bed for a greenhouse (after Bouhdjar <i>et al.</i> , 1996)	40
Figure 2.18 Storage pit (after Phueakphum and Fuenkajorn, 2010)	40
Figure 2.19 Schematic representation of test facility (after Srinivasan and Raghunandan, 2013)	41
Figure 2.20 Vertical thermal energy storage system (after Zavattoni <i>et al.</i> , 2011)	41
Figure 2.21 Schematic and operating principle of the packed bed (after Zanganeh <i>et al.</i> , 2015)	42
Figure 2.22 Wind tunnel layout (after Allen, 2010)	42
Figure 2.23 Schematic of a low energy consumption home (after Woolridge, 1980)	42
Figure 2.24 Rotating vane anemometers	48
Figure 2.25 Bridled vane anemometer	48
Figure 2.26 Thermocouples placement at different cross-sections in bed (after Singh <i>et al.</i> , 2006)	51
Figure 3.1 Roadmap of the methodology process	59
Figure 3.2 Proposed experimental design of a horizontal, uni-directional packed bed	60
Figure 3.3 Section view of the proposed experimental design	61
Figure 3.4 Inlet duct design View 1	62
Figure 3.5 Inlet duct design View 2	62
Figure 3.6 Stage 2 duct Section 1 front	63
Figure 3.7 Stage 2 duct Section 1 rear	63

Figure 3.8	Stage 2 rock-bed section with a 75 mm thick concrete slab	63
Figure 3.9	Stage 3 outlet duct front view	64
Figure 3.10	Stage 3 outlet duct rear view	64
Figure 3.11	Stage 4 room	64
Figure 3.12	Stage 4 room section view	64
Figure 3.13	Temperature probes proposed placement	65
Figure 3.14	Construction of Section 1 and 3	66
Figure 3.15	Construction of Section 2	66
Figure 3.16	The placement of toggle locks and temperature probes	66
Figure 3.17	Rock levelling and probe placement	67
Figure 3.18	Probe placement onto concrete surface	67
Figure 3.19	Weather strips at connecting sections	68
Figure 3.20	Heating element between Stages 1 and 2	68
Figure 3.21	Blower attached to the inlet	68
Figure 3.22	Horizontal uni-directional packed bed experimental setup	69
Figure 3.23	Implementing the liquid saturation method to calculate porosity	70
Figure 3.24	Measuring the mass of rocks in the container	71
Figure 3.25	Measuring the total mass of rocks and water	71
Figure 3.26	Measuring the mass of the rocks	72
Figure 3.27	Measuring specific heat capacity of the rocks	72
Figure 3.28	Photograph of hot water and rocks	72
Figure 3.29	Thermograph of hot water and rocks	72
Figure 3.30	Photograph of polystyrene container	73
Figure 3.31	Thermograph of container	73
Figure 3.32	General sequence of operation in a STAR-CCM+ analysis (adapted from CD-Adapco, 2016)	77
Figure 3.33	Geometry of a horizontal, uni-directional packed bed for CFD analysis	78
Figure 3.34	Data analysis process and categorisation	87
Figure 4.1	Graph of an inlet temperature of 40°C and 50°C at different mass flow rates	92
Figure 4.2	Graph of an inlet temperature of 45°C and 55°C at different mass flow rates	93
Figure 4.3	Graph of a mass flow rate of 150 kg.h ⁻¹ at different temperature ranges	94
Figure 4.4	Graph of a mass flow rate of 200 kg.h ⁻¹ at different temperature ranges	94
Figure 4.5	Graph of a mass flow rate of 250 kg.h ⁻¹ at different temperature ranges	94
Figure 4.6	Graph of a mass flow rate of 300 kg.h ⁻¹ at different temperature ranges	95
Figure 4.7	The difference between the inlet temperature and maximum outlet temperature for a range of mass flow rates	96
Figure 4.8	Graph of the amount of energy produced and lost for each charging test	97
Figure 4.9	Graph of the temperature wave-front through the packed bed	98
Figure 4.10	Graph of the packed bed temperature data	98
Figure 4.11	Graph of the different inlet temperatures and mass flow rates for Level_1	99
Figure 4.12	Graph of the different inlet temperatures and mass flow rates for Level_2	99
Figure 4.13	Graph of the different inlet temperatures and mass flow rates for Level_3	100

Figure 4.14	Graph of the difference between the inlet temperature and the maximum packed bed temperature, for a range of mass flow rates for Level_1	101
Figure 4.15	Graph of the difference between the inlet temperature and the maximum packed bed temperature, for a range of mass flow rates for Level_2	101
Figure 4.16	Graph of the difference between the inlet temperature and the maximum packed bed temperature, for a range of mass flow rates for Level_3	102
Figure 4.17	Photograph of probes	102
Figure 4.18	Thermograph of probes	102
Figure 4.19	Graph of the amount of energy stored, lost and retained for each test for packed bed heating.....	103
Figure 4.20	Temperature wave-front through the concrete slab	104
Figure 4.21	Graph of the concrete temperature of the packed bed	105
Figure 4.22	Graph of the difference between the inlet temperature and the maximum outlet temperature for a range of mass flow rates and concrete temperature ..	106
Figure 4.23	Photograph of concrete slab.....	106
Figure 4.24	Thermograph of concrete slab.....	106
Figure 4.25	Photograph of concrete slab, side view.....	107
Figure 4.26	Thermograph of concrete slab, side view	107
Figure 4.27	Thermograph of the concrete slab after the discharge phase	107
Figure 4.28	Graph of the amount of energy produced and lost for each test of the concrete surface.....	108
Figure 4.29	Space temperature data of the packed bed.....	109
Figure 4.30	Graph of the difference between the inlet temperature and the maximum space temperature for a range for mass flow rates.....	110
Figure 4.31	Graph of the space temperature vs the ambient temperature	111
Figure 4.32	Photograph of thermal losses	111
Figure 4.33	Thermograph of thermal losses.....	111
Figure 4.34	Graph of the amount of energy produced and lost for each test for space heating.....	112
Figure 4.35	The energy balance of the horizontal, uni-directional packed bed, with an inlet temperature of 40°C and mass flow rate of 150 kg.h ⁻¹	113
Figure 4.36	A thermograph of the concrete slab, at an inlet temperature of 55°C and a mass flow rate of 300 kg.h ⁻¹	116
Figure 4.37	Graph of surface probe data vs thermal image data.....	116
Figure 4.38	Empirical vs numerical inlet temperatures.....	117
Figure 4.39	Difference between the empirical and numerical temperatures as a percentage of the empirical inlet temperatures	117
Figure 4.40	Empirical vs numerical data of the outlet temperatures.....	118
Figure 4.41	Difference between the empirical and numerical temperatures as a percentage of the empirical outlet temperatures	119
Figure 4.42	Empirical vs numerical average temperature for Level_1	120
Figure 4.43	Difference between the empirical and numerical temperatures as a percentage of the empirical temperature for Level_1	120
Figure 4.44	Empirical vs numerical average temperature for Level_2.....	121

Figure 4.45	Difference between the empirical and numerical temperatures as a percentage of the empirical temperature for Level_2	121
Figure 4.46	Empirical vs numerical average temperature for Level_3	122
Figure 4.47	Empirical vs numerical percentage error for Level_3 average temperatures ..	122
Figure 4.48	Comparison of the numerical data for the different levels in the packed bed .	123
Figure 4.49	Air stream velocity profile at an inlet temperature of 45°C and a mass flow rate of 200 kg.h ⁻¹	124
Figure 4.50	Temperature profile through packed bed at an inlet temperature of 45°C and a mass flow rate of 200 kg.h ⁻¹	124
Figure 4.51	Empirical vs numerical average concrete surface temperature.....	126
Figure 4.52	Empirical vs numerical percentage error of the concrete surface temperature	126
Figure 4.53	Empirical vs numerical results of the space temperatures	127
Figure 4.54	Empirical vs numerical percentage error for space temperature.....	128
Figure 11.1	Mesh independence study placement.....	165
Figure 11.2	Mesh independence study for different cell amounts	166
Figure 14.1	Empirical results of the inlet temperature before the packed bed.....	175
Figure 14.2	Finding the numerical inlet temperature	176
Figure 14.3	Empirical and numerical extrapolation data	178
Figure 14.4	Extrapolation method results compared with the empirical results	178
Figure 16.1	Pressure drop characterisation of pressure vs velocity	182
Figure 16.2	Expanded metal pressure drop characterisation.....	183
Figure 17.1	Graph of empirical vs numerical data of the baseline for Level 0.....	184
Figure 17.2	Graph of empirical vs numerical data of the baseline for Level 1	185
Figure 17.3	Graph of empirical vs numerical data of the baseline for Level 2.....	185
Figure 17.4	Graph of empirical vs numerical data of the baseline for Level 3.....	186
Figure 17.5	Graph of empirical vs numerical data of the baseline for Level 4.....	186
Figure 17.6	Graph of empirical vs numerical data of the changed porosity to 0.3 for Level 0	187
Figure 17.7	Graph of empirical vs numerical data of the changed porosity to 0.3 for Level 1	188
Figure 17.8	Graph of empirical vs numerical data of the changed specific heat capacity to 0.8 J.kg ⁻¹ .K ⁻¹ for Level 0.....	189
Figure 17.9	Graph of empirical vs numerical data of the changed specific heat capacity to 0.8 J.kg ⁻¹ .K ⁻¹ for Level 1	189
Figure 17.10	Graph of empirical vs numerical data of the changed thermal conductivity to 1.4 W.m ⁻¹ .K ⁻¹ for Level 0.....	190
Figure 17.11	Graph of empirical vs numerical data of the changed thermal conductivity to 1.4 W.m ⁻¹ .K ⁻¹ for Level 4.....	191

LIST OF TABLES

		Page
Table 2.1	A comparison of active, passive, direct and indirect systems, with schematics as examples.....	6
Table 2.2	Summary of photovoltaic developers, technologies and module efficiencies (adapted from Wessof, 2016)	7
Table 2.3	Final energy consumption in the commercial and residential sector in 2004 (after Pérez-Lombard <i>et al.</i> , 2008)	9
Table 2.4	Energy consumption in homes by end use (adapted from EIA, 2009).....	9
Table 2.5	Average energy use in an Australian home (adapted from GSA, 2008)	10
Table 2.6	Potential annual thermal energy storage results for Germany, Spain and the European Union-25 (after Arce Maldonado <i>et al.</i> , 2011).....	15
Table 2.7	Packed beds identification criteria, based on temperature, duration and classification	22
Table 2.8	Rock-bed thermal storage systems used in residential applications (after Fuller, 2003).....	24
Table 2.9	Summary of different heat transfer coefficients for liquids and gases (adapted from Cengel <i>et al.</i> , 2002; Borgnakke and Sonntag, 2009).....	35
Table 2.10	Solid media properties of sensible heat storage materials (after Singh <i>et al.</i> , 2010)	36
Table 2.11	Summary of several packed bed designs used by researchers	39
Table 2.12	Rock-bed thermal storage systems used in commercial applications (after Fuller, 2003).....	45
Table 2.13	Summary of airflow measuring devices	47
Table 3.1	Physical properties of polystyrene, that was used as insulation for the packed bed design (after ISOVER, 2015).....	62
Table 3.2	Summary of the flow rates used, with a duct size of 300 mm x 300 mm.....	73
Table 3.3	Summary of the flow rates used, with a vane probe diameter of 100 mm.....	74
Table 3.4	Testing procedure for the empirical design	76
Table 3.5	Summary of region and boundary types used in the CFD setup.....	79
Table 3.6	Summary of interface types used in CFD setup.....	79
Table 3.7	Field functions that were used in the numerical setup	83
Table 3.8	Probe descriptions for numerical investigation.....	85
Table 3.9	Summary of plots created for the specific point probes.....	86
Table 4.1	Inlet and outlet mass flow rate values of the empirical tests	91
Table 4.2	Summary of the results obtained for the porosity of the packed bed.....	114
Table 4.3	Summary of the results obtained for the density of the rocks.....	114
Table 4.4	Summary of the results obtained for the specific heat capacity of the rocks...	115
Table 4.5	Summary of the percentage error of the numerical model for the inlet and outlet temperature data.....	119
Table 4.6	Summary of the percentage error of the numerical model for the packed bed	125

Table 4.7	Summary of the percentage error of the numerical model for the concrete slab	127
Table 4.8	Summary of the percentage error of the numerical model for space data	129
Table 7.1	Estimated U.S. residential sector electricity consumption by end use in 2014 (after EIA, 2009).....	148
Table 9.1	Summary of the values used to calculate the pressure drop and particle Reynolds number	159
Table 11.1	Mesh independence base size and cell count	165
Table 12.1	Mesh for regions and boundaries	167
Table 12.2	Mesh for interfaces	168
Table 13.1	Physics for regions and boundaries.....	169
Table 13.2	Physics for interfaces	174
Table 14.1	Method of extrapolation based on empirical results	176
Table 15.1	Summary of thermal resistance values of selected materials.....	179
Table 15.2	Summary of the thermal resistance values for a combination of materials	179
Table 15.3	Summary of the thermal resistance and conductance values for a combination of materials.....	180
Table 16.1	Porous inertial resistance calculations	181
Table 16.2	Porous inertial resistance calculations for porous baffle	182
Table 18.1	Summary of the average reduction in charging time for a set temperature, with an increase in the mass flow rate	192
Table 18.2	Summary of the average reduction in the charging time for a set mass flow rate, with an increase in the inlet temperature	192
Table 19.1	Summary of the energy balance data of the charging phase for inlet temperatures of 40°C and 45°C at different mass flow rates.....	193
Table 19.2	Summary of the energy balance data of the charging phase for inlet temperatures of 50°C and 55°C at different mass flow rates.....	194
Table 19.3	Summary of the energy balance data of the discharge phase for inlet temperatures of 40°C and 45°C at different mass flow rates.....	195
Table 19.4	Summary of the energy balance data of the discharge phase for inlet temperatures of 50°C and 55°C at different mass flow rates.....	196

NOMENCLATURE

Abbreviations

ASHRAE	American Society of Heating, Refrigeration and Air Conditioning Engineers
BIPV	Building Integrated Photovoltaics
BS	Backup Systems
BVA	Bridled Vane Anemometer
CFD	Computational Fluid Dynamics
COP	Coefficient of Performance
CPV	Concentrated Photovoltaic
CSIRO	Commonwealth Scientific and Industrial Research Organisation
CSP	Concentrated Solar Power
CSV	Comma-Separated Values
DC	Direct Current
DEM	Discrete Element Method
EEB	Earth's Energy Balance
EU	European Union
GSA	Government of South Australia
HPCU	High Performance Computing Unit
HTF	Heat Transfer Fluid
HVAC	Heating Ventilation and Air Conditioning
IRT	Infrared Thermography
ITES	Ice Thermal Energy Storage
LCZ	Lower Convective Zone
LFR	Linear Fresnel Reflector
LFE	Laminar Flow Element
LTES	Latent Thermal Energy Storage
MS	Mild Steel
NCZ	Non-convective Zone
PCM	Phase Change Materials
PDS	Parabolic Dish Systems
PF	Packing Factor
PPD	Pressure-Producing Device
PSH	Passive Solar House
PTC	Parabolic Trough Collector
PV	Photovoltaics
PVT	Photovoltaic Thermal
PV-TW	Photovoltaic Trombe Wall
RISHS	Roof Integrate Solar Heating System
RVA	Rotating Vane Anemometer
SAH	Solar Air Heater
SANAS	South African National Accreditation System
SPT	Solar Power Tower

STES	Sensible Thermal Energy Storage
SWH	Solar Water Heater
TCES	Thermochemical Energy Storage
TES	Thermal Energy Storage
UCZ	Upper Convective Zone
USA	United States of America
WIHP	Wall Implanted with Heat Pipes
WTSW	Water Thermal Storage Wall

General

A	Surface area through which heat transfer takes place, [m ²]
B_r	Thermal expansion coefficient, [K ⁻¹]
c	Specific heat capacity, [kJ.kg ⁻¹ .K ⁻¹]
c_p	Specific heat capacity at constant pressure, [kJ.kg ⁻¹ .K ⁻¹]
c_r	Specific heat capacity of rock, [kJ.kg ⁻¹ .K ⁻¹]
c_w	Specific heat capacity of water, [kJ.kg ⁻¹ .K ⁻¹]
C_v	Flow coefficient, [unitless]
d	Particle size, [mm]
E	Replaced thermal power, [GW _{th}]
E_e	Replaced electrical power, [GW _e]
g	Gravitation, [m.s ⁻²]
G	Air mass flux, [kg.h ⁻¹ .m ⁻²]
h	Convection heat transfer coefficient, [W.m ⁻² .K ⁻¹]
k	Intrinsic permeability, [mm ⁻²]
L	Bed length, [m]
L_s	Specific latent heat for a particular substance, [kJ.kg ⁻¹]
LR	Load reduction, [MW _{th}]
m	Mass of the heat storage material, [kg]
m_r	Mass of the rock, [kg]
m_w	Mass of the water, [kg]
m_{r+w}	Mass of the rocks and water, [kg]
\dot{m}	Mass flow rate, [kg.h ⁻¹]
\dot{m}_{air}	Mass flow rate of air, [kg.s ⁻¹]
N_a	Number of atoms per cell, [m ⁻³]
P	Pressure, [Pa]
P_i	Porous inertial resistance, [kg.m ⁻⁴]
P_{im}	Porous inertial resistance mesh, [unitless]
P_v	Porous viscous resistance, [kg.m ⁻³ .s ⁻¹]
P_{vm}	Porous viscous resistance mesh, [m.s ⁻¹]
PF	Packing factor, [unitless]
Q	Heat storage capacity, [kJ]
\dot{Q}	Rate of heat transfer, [W]
\dot{Q}_{cond}	Rate of heat transfer by conduction, [W]
\dot{Q}_{emit}	Rate of heat transfer by radiation, [W]

R	Thermal resistance, [$\text{m}^2 \cdot \text{K} \cdot \text{W}^{-1}$]
R_{CO_2}	CO ₂ emissions reduction, [Tons]
Re^*	Particle Reynolds number, [unitless]
s	Dimensionless constant, [unitless]
T_i	Initial temperature, [K]
T_m	Maximum temperature, [K]
T_r	Initial rock temperature, [K]
T_s	Surface temperature, [K]
T_w	Initial water temperature, [K]
T_{r+w}	Rock and water temperature, [K]
U	Superficial velocity, [$\text{m} \cdot \text{s}^{-1}$]
\dot{V}_f	Volumetric flow rate, [$\text{m}^3 \cdot \text{s}^{-1}$]
\dot{V}_{fl}	Volumetric flow rate, [$\text{m}^3 \cdot \text{h}^{-1}$]
V_a	Volume of each atom, [m^3]
V_c	Volume of unit cell, [m^3]
V_r	Volume of rocks, [m^3]
V_s	Volume of solids, [m^3]
V_t	Total volume, [m^3]
V_v	Volume of voids, [m^3]
V_w	Volume of water, [m^3]
x	Spherical equivalent particle diameter, [m]
ΔP	Change in pressure, [Pa]
ΔT_r	Temperature difference of rock, [K]
ΔT_w	Temperature difference of water, [K]
ΔT	Temperature gradient, [K]
Δx	Thickness, [m]

Greek letters

α	Thermal diffusivity, [$\text{m}^2 \cdot \text{s}^{-1}$]
β	Absorption coefficient, [unitless]
ρ	Density, [$\text{kg} \cdot \text{m}^{-3}$]
ρ_a	Density of air, [$\text{kg} \cdot \text{m}^{-3}$]
ρ_f	Density of fluid, [$\text{kg} \cdot \text{m}^{-3}$]
ρ_r	Density of rock, [$\text{kg} \cdot \text{m}^{-3}$]
ρ_w	Density of water, [$\text{kg} \cdot \text{m}^{-3}$]
ψ	Sphericity, [unitless]
e	Emissivity, [unitless]
ε	Porosity, [%]
λ	Thermal conductivity, [$\text{W} \cdot \text{m}^{-1} \cdot \text{K}^{-1}$]
σ	Stefan-Boltzmann constant, [$\text{W} \cdot \text{m}^{-2} \cdot \text{K}^{-4}$]
κ	Dynamic viscosity, [Pa.s]

1. INTRODUCTION

The industrial revolution changed the way humans utilised resource-harnessing techniques to develop life-enhancing solutions in a sustainable, effective and efficient way. During these innovative times of “progress”, the balance of planet earth is slowly but surely being affected, resulting in the emission of greenhouse gases and a current imminent imbalance. The earth has been, and still is, reacting to this imbalance caused by “climate change” and is struggling to retain its equilibrium.

Currently, the use of non-renewable energy resources, as well as the generation of electricity as primary transporter between forms of energy, is prevalent. Opportunities exist to re-investigate how energy is transformed, by using alternative and renewable methods, and harnessing solar energy is one of them. Several technologies exist for the conversion of solar energy to a more usable form of energy (thermal or electrical) and the intention of this study is to investigate the use of a horizontal packed bed, with uni-directional flow, for residential use, as a method of storing thermal energy.

This chapter provides a brief background to this study, followed by a concise problem statement. The research objectives are illustrated and the methodology is explained, followed by the document layout.

1.1 Background

The earth consists of the atmosphere, ocean and land. Incoming shortwave radiation received from the sun is transmitted, reflected and radiated as energy in various ways, forms and quantities. The surrounding atmosphere consists of layers of gases, differing in density and composition, which react with the incoming shortwave solar radiation through: (i) reflection, (ii) absorption, (iii) re-radiation, and (iv) transmittance. The quantity of incoming solar radiation that is reflected, absorbed, transmitted or radiated, depends on: (i) the geographical position of the earth, (ii) the time of day, (iii) the time of year, (iv) the local landscape, and (v) the local climatic conditions. Tracking the distribution and quantities of the incoming shortwave radiation energy from the sun, by means of the different influencing factors, is known as the Earth’s Energy Balance (EEB).

Sunlight, as the largest available (renewable) energy source, dwarfs all the other carbon-neutral and fossil-based energy resources combined. The quantity of solar radiation that strikes the earth in one hour is more than all the energy consumed by humans in an entire year (Barlev *et al.*, 2011; Zhang *et al.*, 2013). From a cost, energy availability and sustainability point of view, it is necessary to utilise this energy in the most effective and efficient manner; however, it must be borne in mind that a less efficient, lower cost method can make more economic sense. Identifying the areas where “solar harvesting” can occur and selecting the correct technology to convert solar radiation into a usable form, is imperative.

Solar energy utilisation can be used either actively or passively, with each type being classified into direct or indirect systems. The three main technologies that are currently available for converting solar radiation to more usable energy, are: (i) solar-electric conversion, using Photovoltaic (PV) solar cells, which involves the use of solar cells to generate electricity directly via the photoelectric effect, (ii) solar-thermal conversion, using Concentrated Solar Power (CSP), which employs efficiency enhancing methods to capture solar energy to provide high temperature heat for use in power generation, and (iii) solar thermal energy for both heating and cooling.

The attainment and indefinite maintenance of the equilibrium of the environment, the economy and social systems in a healthy state is known as sustainability. The mind-set of humans has altered and heightened their consciousness regarding the management of energy resources (efficiency) and the implementation of the most appropriate technologies (effectiveness) in the utilisation of energy sources. The challenge is to maintain thermal comfort within buildings by not only reducing unit energy consumption, but by also using the appropriate technology as well. Current temperature swings in very hot and cold climates are presently met by space heating and air conditioning systems. These systems results in a high demand for energy and can have a great financial impact. The consumption of electrical energy, as well as the pricing system for off-peak and peak periods, differ considerably during the day and the night. Shifting the peak loads to off-peak loads with storage, reduces the energy cost, which can offer significant economic benefits. This load shift can be accomplished by making use of Thermal Energy Storage (TES). TES is an effective technology that provides end-use demand through energy redistribution, by placing energy (heat or cold) in a storage medium for a certain period and retrieving it from the same place, for use at a later stage (Kalaiselvam and Parameshwaran, 2014). TES can be classified into three categories, namely: (i) Thermochemical Energy Storage (TCES), (ii) Latent Thermal Energy Storage (LTES), and (iii) Sensible Thermal Energy Storage (STES).

Packed beds are STES systems and are defined as a contained volume of porous media, where an energy transfer fluid, with a high/low energy content, is passed through a porous medium of lower/higher energy content. Energy is transferred between the energy transfer fluid and the storage media in the form of thermal energy and it is stored for utilisation at a later stage. Packed beds are designed according to the storage temperature and duration requirements and are classified into vertical and horizontal systems.

Research on packed beds for residential use has not received much attention in recent years. Fuller (2003) comments that there are opportunities for the implementation of a horizontal uni-directional flow packed bed in low energy homes.

1.2 Need Statement

Research into rock-beds for residential use has declined over the past three decades (Fuller, 2003), based on the number of available publications. Although rock-beds were constructed for agricultural and solar home applications in the 1970's and 1980's, there has been a reduction

in the amount of research seeking to establish the viability of rock-beds as a TES option in the residential sector. A horizontal uni-directional flow packed bed was constructed and tested in 1978 by the Australian Commonwealth Scientific and Industrial Research Organisation, which showed great promise in low energy homes (Fuller, 2003). Hence, there is currently insufficient up-to-date research that provides overall information on the utilisation of horizontal uni-directional rock-beds for domestic space heating.

1.3 Research Statement

A comparison of the actual, versus the predicted, effects of the variation of the inlet temperature and mass flow rate variations of a horizontal, uni-directional Thermal Energy Storage system for residential use, on the: (i) thermal energy transfer, (ii) temperature wave front, and (iii) charging/discharging time.

1.4 Research Objectives

The need to increase the thermal comfort conditions of domestic housing during winter, while reducing national peak load, stresses the importance of implementing an underground uni-directional horizontal thermal energy storage system for space heating. The objectives of the study will be:

- (i) to conduct a thorough literature study on the theory of thermal energy storage in packed beds,
- (ii) to design and construct an experimental research unit for a horizontal, uni-directional packed bed,
- (iii) to investigate the effect of changing the inlet temperature and mass flow rate on the thermal energy transfer, temperature wave-front, and charging and discharging time of the system,
- (iv) to model the effects using Computational Fluid Dynamics (CFD), and
- (v) to assess and compare the empirical (experimental) results to the numerical (simulated) results through validation and verification.

1.5 Dissertation Layout

Chapter 2 provides a detailed literature survey of the solar energy utilisation types and conversion technologies, followed by thermal energy storage, with the emphasis on packed beds.

Chapter 3 consists of the research methods and designs used in this study. The empirical and numerical research designs are discussed, followed by the data analysis strategies, quality assurance and their contributions and limitations.

Chapter 4 entails the results that were obtained from the study. The verification of the empirical and numerical method were discussed, followed by the evaluation of the empirical test data for

the different sections of the horizontal, un-directional packed bed. Validation focused on the empirical results, compared to the data from literature, thermography and the numerical results.

Chapter 5 provides a summary of the investigation, the concluding remarks on the results that were obtained, followed by the recommendations that were made for future work on the current topic.

2. LITERATURE SURVEY

Planet earth consists of the atmosphere, the oceans and the land. The incoming shortwave radiation received from the sun is transmitted, reflected and radiated as energy in various ways, forms, and quantities. The atmosphere that surrounds the earth consists of layers of gases of different density and composition, which react with the incoming shortwave solar radiation through: (i) reflection, (ii) absorption, (iii) reradiation, and (iv) transmittance. The amount of incoming solar radiation reflected, absorbed, transmitted or radiated, depends on: (i) the geographical position of the earth, (ii) the time of day, (iii) the time of year, (iv) the local landscape, and (v) the local climatic conditions (InnovateUs, 2006). Tracking the distribution of the incoming sun energy, in the form of shortwave radiation, through the different changes and factors influencing this energy distribution, is known as the Earth's Energy Balance (EEB).

Geographically, South Africa has an excellent solar resource, which provides the opportunity to utilise the solar radiation. The solar irradiance that is absorbed on the earth can be stored in some medium and then released at a later stage, in the form of latent or sensible heat. The sun provides a vast amount of free energy to the earth. Understanding solar energy conversion types and the conversion technologies allows us to harness solar energy effectively and convert it efficiently into useful forms of energy.

2.1 Solar Energy Utilisation Types

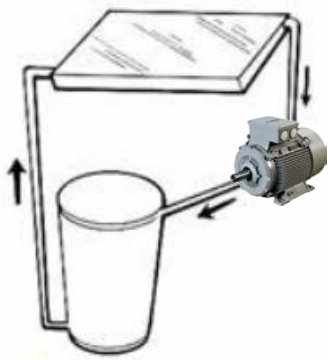
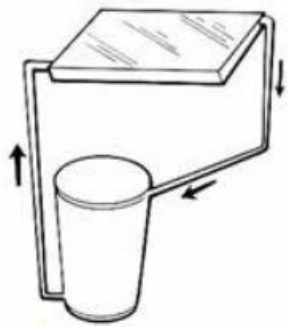
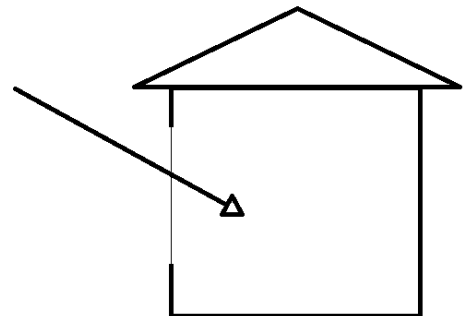
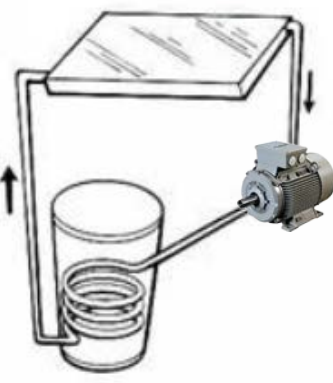
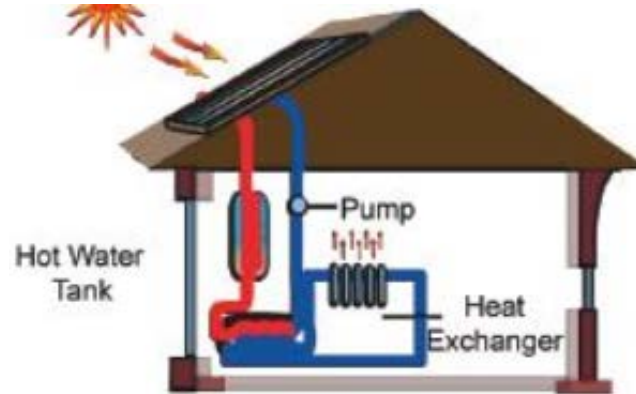
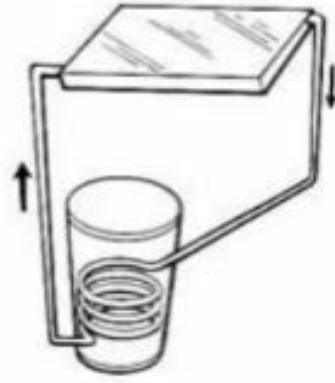
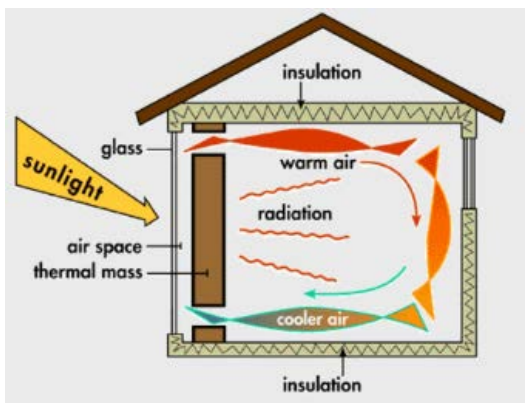
The utilisation types of solar energy are either active or passive, where each of the utilisation types can further be classified into direct or indirect systems. A short description of each is provided, with examples tabulated in Table 2.1.

An active solar system collects solar energy and uses mechanical equipment, such as a pump or a fan, which is powered by energy that is not derived from solar radiation, to circulate the heat transport fluid (Pinel *et al.*, 2011).

A passive solar collector does not have any supplementary devices (mechanical equipment) to collect and convert sunlight into different energy forms. The whole system works as a solar collector (Radosavljević *et al.*, 2004).

In passive systems, solar energy is predominantly collected and stored by natural means, making use of natural convection, conduction, radiation and density gradients (gravitational forces) to circulate the heat transfer fluid. Passive techniques involve making use of building materials with favourable thermal properties, as well as designing spaces, taking the position of the sun into consideration.

Table 2.1 A comparison of active, passive, direct and indirect systems, with schematics as examples

	Active (mechanical equipment)	Passive (natural means)
Direct (Heat transfer medium and heat sink in contact)	<p>Potable water circulates from the storage tank, to the collector, and back to the storage tank. Thus, the heat collecting fluid is the same potable water that is in the water heater (Florida Solar Energy Center Cocoa, 2006).</p>  <p>Figure 2.1 Active-direct system (adapted from Florida Solar Energy Center Cocoa, 2006)</p>	<p>In an open space, direct solar heating is when the sunlight directly enters the room through a clear screen, such as a window (Radosavljević <i>et al.</i>, 2004). The same process can also be followed, as described by Florida Solar Energy Center Cocoa (2006) in the active-direct system, but a mechanical device is not present, and the natural thermosyphon effect is used.</p>   <p>Figure 2.2 Passive-direct system (after Florida Solar Energy Center Cocoa, 2006)</p> <p>Figure 2.3 Passive-direct system</p>
Indirect (Heat transfer medium and heat sink not in contact)	<p>The heat transfer fluid (HTF) circulates from the storage tank, to the collector, and back to the storage tank. The HTF never comes into contact with the potable water in the storage tank. Instead, it transfers heat to the potable water through a heat exchanger (Florida Solar Energy Center Cocoa, 2006).</p>   <p>Figure 2.4 Active-indirect system (adapted from Florida Solar Energy Center Cocoa, 2006)</p> <p>Figure 2.5 Active-indirect system (after Central, 2010)</p>	<p>Radosavljević <i>et al.</i> (2004) describes an indirect solar heating system as exterior features of a body, such as Trombe walls, water walls, active massive wall, etc. These features receive and absorb incident rays and transmit thermal energy to the rooms which require heating. The same process can also be followed, as described by Florida Solar Energy Center Cocoa (2006) in the active-indirect system, but a mechanical device is not present, and the natural thermosyphon effect is used.</p>   <p>Figure 2.6 Passive-indirect system (after Florida Solar Energy Center Cocoa, 2006)</p> <p>Figure 2.7 Passive-indirect system (after Beken, 1984)</p>

In order to transform solar energy to a more usable form (thermal or electrical), solar energy conversion technologies are required.

2.2 Solar Energy Conversion Technologies

Suman *et al.* (2015) state that there are two broad methods for converting solar energy to a more useful form, including: (i) solar-electric conversion, using PV solar cells to generate electricity directly via the photoelectric effect, and (ii) solar-thermal conversion, which converts solar energy into thermal energy, using solar collectors. Barlev *et al.* (2011) mention that there are two main devices that are utilised as conversion technologies, namely, PV and CSP, with CSP employing efficiency enhancing methods for capturing solar thermal energy that is used in power-producing heat processes. Combining the conversion methods of Suman *et al.* (2015) and Barlev *et al.* (2011), the conversion technologies for solar energy can primarily be classified into PV, CSP and solar thermal energy (heating and cooling), which will briefly be discussed in the following subsections.

2.2.1 Photovoltaics

Photovoltaics convert incoming solar radiation into direct current (DC) electricity. Semi-conductors are used in PV systems and have properties intermediate to those of metals and insulators. Silicon, the material of microelectronics and the information age, is the most common semi-conductor (Green, 2000). Racks are applied onto rooftops to form a sturdy structure onto which the panels are fitted and this is known as a rack-mounted PV system. PV can also be integrated into buildings as Building Integrated Photovoltaics (BIPV), by covering the northern wall of a building, which is situated in the southern hemisphere, with PV panels. Rack-mounted PV and Building Integrated Photovoltaics (BIPV) are the most common PV systems used to convert incident solar radiation to electricity on a facade or surrounding area (Saber *et al.*, 2014).

Green (2000) states that solar electricity produced by PV solar cells is one of the most promising options yet to be identified for providing the world's future energy requirements in a sustainable manner. Most recently, Wessof (2016) commented that SunPower produced a panel that achieved 24.1% efficiency, which is a new record for silicon module efficiency. The module measured 272.5 watts on an 11310.1 cm² aperture area. Some of the previous efficiency values are summarised in Table 2.2.

Table 2.2 Summary of photovoltaic developers, technologies and module efficiencies (adapted from Wessof, 2016)

PV Module Builder	Technology	Record Efficiency
SunPower	N-type Si, back contact	24.10%
SunPower	N-type Si, back contact	22.80%
Panasonic	N-type Si, Cu-electrode	22.50%
SolarCity	N-type Si, heterojunction	22.04%
First Solar	CdTe	18.60%

Dr Mark Keevers and Professor Martin Green of the University of New South Wales (UNSW) in Australia established a new world record (of 34.5%) for sunlight-to-electricity conversion on

a 28 cm² module, surpassing the previous record made by Alta Devices of the United States of America (USA) of 24% on a surface area of 800 cm² (da Silva, 2016). The result by UNSW is nearly a 44% improvement on the record of Alta Devices.

An Australian company called RayGen Resources, utilises mirrors to concentrate sunlight onto photovoltaic modules, which converts the sunlight directly to electricity. This phenomenon is known as Concentrated Photovoltaic (CPV). The UNSW set yet another world record in 2014, utilising the CPV technology and reaching an electricity conversion rate of over 40% (da Silva, 2016).

2.2.2 Concentrated solar power

CSP has been under investigation for several decades, and is based on the general idea of using mirrors to redirect sunlight and then to focus and collect it as heat by means of a thermal energy carrier, which can be used to power a turbine or a heat engine, in order to generate electricity (Barlev *et al.*, 2011).

At present, there are four available CSP technologies, namely: (i) Parabolic Trough Collector (PTC), (ii) Solar Power Tower (SPT), (iii) Linear Fresnel Reflector (LFR), and (iv) Parabolic Dish Systems (PDS) (Zhang *et al.*, 2013).

CSP power plants are gaining interest, mainly by using the PTC, although SPT technology is highly favourable in the market, due to its advantages, in terms of higher efficiency, lower operating costs and good scale-up potential (Zhang *et al.*, 2013).

The variation of solar radiation flux throughout the day remains a problem for all CSP and PV technologies, notwithstanding the close match between the hours of the day when energy demand peaks and when solar irradiation is available. Conventional CSP technologies also experience short-term variations on cloudy days and are not able to provide energy during night hours. In order to improve the overall yield, in comparison with conventional systems, the CSP process can be enhanced by incorporating two technologies i.e. thermal energy storage (TES) and backup systems (BS) (Zhang *et al.*, 2013).

2.2.3 Solar thermal energy

Globally, the energy consumption of commercial and residential buildings has increased to between 20% and 40% in developed countries, which exceeds the main sectors, namely, industry and transportation (Pérez-Lombard *et al.*, 2008). Solar thermal energy can be utilised for both heating and/or cooling purposes in large-scale and small-scale applications.

Pérez-Lombard *et al.* (2008) stated that Heating Ventilation and Air Conditioning (HVAC) contribute to 50% of the consumption of buildings and 20% of the total energy consumption in the United States of America. Table 2.3 provides a summary of the energy consumption in the commercial and residential sector.

Table 2.3 Final energy consumption in the commercial and residential sector in 2004 (after Pérez-Lombard *et al.*, 2008)

	Final Energy Consumption (%)		
	Commercial	Residential	Total
USA	18	22	40
UK	11	28	39
EU	11	26	37
Spain	8	15	23
World	7	16	24

Pérez-Lombard *et al.* (2008) commented that the forecast for energy consumption in the built environment will increase by approximately 34% over the next two decades, at an average rate of 1.5%. This will result in the energy consumption of commercial and residential areas increasing to approximately 33% and 67%, respectively. Data from the U.S. Energy Information Administration (EIA, 2009) shows that 48% of energy consumption in U.S homes in 2009 was for heating and cooling. In South Africa, the energy demand by the major economic sectors for 2006 was 41% for industry, 28% for transport and 20% for residential (DOE, 2012).

A significant quantity of energy is consumed in buildings, largely because of indoor HVAC and lighting, with the major energy consumer being the heating systems, equating to approximately 40% of the energy consumed (Ozbalta and Kartal, 2010). Table 2.4 shows the energy consumption values that were obtained for residential home in the U.S.

Table 2.4 Energy consumption in homes by end use (adapted from EIA, 2009)

Source	Consumption (%)
Space Heating	41.5
Air Conditioning	6.2
Water Heating	17.7
Appliances, Electronics, and Lighting	34.6

Detailed data of the estimated electricity consumption in the U.S. residential sector by the end use of 2014, can be found in Table 7.1 in Appendix A. These can be compared with data from the Government of South Australia (GSA, 2008). The main usage of the residential buildings are summarised in Table 2.5.

Table 2.5 Average energy use in an Australian home (adapted from GSA, 2008)

Source	Consumption (%)
Heating and Cooling	38
Water Heating	25
Other Appliances	16
Fridges and Freezers	7
Lighting	7
Cooking	4
Stand by Power	3

Table 2.5 indicates that the heating and cooling are the major energy consumers in an Australian home. The following section will focus on solar heating and cooling for residential purposes.

2.2.3.1 Solar heating

The principle behind converting solar thermal energy is that the thermal energy from the sun replaces energy from combustion. The use of fossil fuels, as well as the threat to the climate and environment, are thus reduced. Crabtree and Lewis (2007) state that unconcentrated sunlight can elevate the temperature of a HTF to approximately 200°C, which is sufficient for water - and space-heating for commercial and residential applications.

Solar heating is the transfer of solar energy to a fluid, such as water, air or any other Heat Transfer Fluid (HTF), which acts as a medium for the transfer of thermal energy from the collector to the point of use, where the energy is normally thermally radiated. In the United States of America, solar thermal systems are predominantly used in the residential market, which has a large impact on local and national energy usage and conversion. Traditionally, the primary use of solar in this sector has been for swimming pool and domestic water heating, as well as space heating (Florida Solar Energy Center Cocoa, 2006).

A solar collector that uses water as the working fluid is classified as a solar water heater (SWH), whereas the collector that makes use of air as the working fluid, is known as a solar air heater (SAH) (Suman *et al.*, 2015). The SWH systems consist of a solar collector and a storage tank. The SWH system can further be classified as either an active or a passive system. SWHs have been in use for many years. One such case was documented during the Civil War. Pioneers utilised the available solar energy by leaving a black pot in the sun for the whole day, in order to have warm water upon their return (Florida Solar Energy Center Cocoa, 2006). SAHs are extensively used for space heating, making use of the walls, roofs and floors of a building. Implementing solar space heating methods to minimise the use of conventional energy systems has proven to be an effective method; however, generating a commercially viable product at a low cost has been challenging (Belusko *et al.*, 2004). The SAH are either single or double pass. The air flows over the absorber plate in the forward pass, and below the absorber plate in the return pass. The SWHs are much more efficient than the SAHs, due to the higher heat transfer coefficient between the fluid and the absorber plate (Suman *et al.*, 2015).

2.2.3.1.1 Roof

Lin *et al.* (2014) developed a ceiling ventilation system. The system included a combination of phase change materials (PCMs) and photovoltaic thermal (PVT) collectors. The PCM formed part of the ceiling insulation, whilst temporarily storing low grade energy, which was collected by the PVT collectors. The low grade energy (heating and cooling) of the PVT made use of the summer night-time sky radiative cooling and the winter daytime solar radiation, whilst generating electricity by using the PV integration (Lin *et al.*, 2014).

The roof integrated solar heating system (RISHS), with a glazed collector, was investigated by (Belusko *et al.*, 2004). The product had a fusion temperature of 40°C, a storage capacity of 100 kJ.kg⁻¹, and a cost of around R10.6 per kg (at R14.72 per U.S dollar), which amount to a mass of 700 kg and a volume of 2 m³. Glazing enhanced the performance of the RISHS by 20% more than that of a heat pump, but the added cost of R191.42 per m² was not economically feasible.

2.2.3.1.2 Wall heating

The heat transfer performance of a building wall has a great influence on energy conservation and the indoor thermal comfort of a passive house structure. If the thermal properties of the wall heating system can be adjusted according to the what is required, the wall can effectively regulate the indoor temperature and directly reduce the energy consumption of the building.

Zhang *et al.* (2014) investigated a new type of passive solar energy technology, consisting of a wall implanted with heat pipes (WIHP). The heat transfer performance and energy saving characteristics were investigated theoretically and experimentally, with a great correlation between the theoretical and experimental values. It was found that the heat loss of the southern external wall during the winter in a typical year of the Jinan area, was reduced by 14.47%, which showed that the WIHP effectively reduced the building heating load.

A passive solar house (PSH) could fully receive and store the incident radiation, by arranging the building structure rationally, and using massive construction materials.

The influence of a water thermal storage wall (WTSW) on the indoor thermal environment was investigated by Wang *et al.* (2013). The results of simulation and analysis indicate that, compared to a traditional wall in a PSH, the wall equipped with WTSW can reduce the annual energy consumption by 8.6% and improve the indoor thermal comfort evaluation index by 12.9%.

2.2.3.1.3 Trombe wall

A Trombe wall is a passive solar heating system used for space heating. It consists of a dark-coloured wall that is covered with glass, with an air gap in between. Air vents are placed at the top and the bottom of the wall. Solar energy heats the air mass between the glass and the darkened wall surface. Due to the stack-effect, the hot air mass rises and exits through the top

vents. This creates a force at the bottom of the vents, which draws cool air from the room to be heated by the wall surface. The thermo-circulation provides a direct heat path to the room, while the conduction through the wall has a time delay. These two paths are interactive (Chen *et al.*, 2006).

Ozbalta and Kartal (2010) investigated the heat gain from solar energy through a Trombe wall in Turkey, using different materials and surface colours. The level of performance of the material depends on the thermophysical properties, namely, thermal conductivity, density and specific heat capacity. The thermophysical properties used by Ozbalta and Kartal (2010) for concrete is the highest, compared to brick and aerated concrete. The different colours that were used in the study were dark, natural and light colours, each having different absorption coefficients (β) for the three types of materials that were used during the experiments. The absorption coefficients were used to calculate the annual heat gain from solar energy through the Trombe wall. The final results obtained for the heat gain from solar energy through the Trombe wall, using different materials and their respective surface colours, showed that the heat gain were between 9.7% - 26.9% for concrete, 7.1% - 20.5% for brick and 4.3% - 13.0% for aerated concrete.

Liping and Angui (2006) conducted a parametric study to predict the mass flow rate, temperature field and air velocity for a Trombe wall system under steady conditions. It was found that there must be an ideal ratio between the chimney gap and the height of the Trombe wall, in order to obtain a maximum ventilation rate that is directly related to the opening design, but independent of solar radiation. In most cases, the optimum width of the air gap is approximately equal to 1/10 of the chimney height. The optimum air gap width that is used to achieve the maximum ventilation ratio is about 0.2 m to 0.3 m. Meanwhile, reverse flow can be observed at the outlet, when the size of the chimney opening is increased to a certain value (Liping and Angui, 2006).

Stazi *et al.* (2008) conducted a numerical and experimental analysis of a case study in Ancona, Italy, which consisted of nine different solar passive systems. It was concluded that the Trombe wall is the most suitable for Italy's climate. The system is an ideal energy saving method and provides great thermal comfort. The Trombe wall can also be used as a passive cooling system. The optimal behaviour of the Trombe wall occurred during spring and the fall and the indoor comfort was related to the type of storage wall.

Irshad *et al.* (2015) conducted a detailed simulation model of a single room building integrated with a PV Trombe wall (PV-TW) that was initially designed by Ji *et al.* (2007). The performance was evaluated in terms of room temperature, cooling load and PV efficiency, by varying the air flow velocity for three different PV-TW glazing types i.e. single glazing, double glazing and double glazing filled with argon gas. The double glazing filled with argon gas displayed significant results in the cooling load reduction of the buildings and in the mean air duct temperature. The effect of air flow velocity became stagnant after attaining a value of $1.75 \text{ m}\cdot\text{s}^{-1}$. It was concluded that the double glazing filled with argon gas, with an air velocity

of $1.5 \text{ m}\cdot\text{s}^{-1}$, is preferable to the single glass PV-TW and can provide feasible solutions for high energy consumption (Irshad *et al.*, 2015).

An experimental study was conducted by Rabani *et al.* (2015) on a newly designed Trombe wall receiving solar irradiance from three directions (the East, South and West), compared to the traditional Trombe wall, which receives solar irradiance only from one side, namely the South, in northern hemisphere cases. The results indicated that the temperature range during the coldest winter days and week in Yazd, were kept between 15°C and 30°C . The absorber temperature reached approximately 47°C on the coldest winter days. The new design received approximately 16% more solar irradiance than the standard Trombe wall design. This increased the maximum temperature of the room between 3°C to 6°C and increased the maximum absorber temperature by approximately 15°C .

2.2.3.1.4 Floor heating

Gao *et al.* (2011) performed a computational fluid dynamics (CFD) simulation and variance analysis to predict the most appropriate spacing of the under-floor heating pipes. The heating pipes were centre-spaced at 300 mm, 400 mm, and 500 mm. The simulations were used to identify the changes of vertical air temperature gradients and thermal homogeneity over the floor. A supply temperature of 50°C was used and a return water temperature of 40°C . At 0.1 m above the floor, the air temperature field can be considered homogeneous, with a difference of no more than 1°C . It was recommended that the best layout method for the under-floor heating pipes are uniformly-laid at 400 mm spacing, which meets standard requirements, such as NEN-EN-ISO 7730, ASHRAE 55-2004 and GB 50019-2003 (Gao *et al.*, 2011).

An experimental verification of the Faxen-Rydberg-Huber expression was conducted by Todorović *et al.* (2014), to determine the thermal characteristics of three types of heating panels, differing in structure and geometric characteristics. This confirmed that the Faxen-Rydberg-Huber expression can be used to predict the temperature field in the wall heating panels. At the same time, this expression has proved itself to be extremely sensitive, primarily to thermophysical characteristics of the panel layers, as well as to the geometric parameters of the panels.

Todorović *et al.* (2015) further investigated the impact of basic geometric parameters and technological parameters on a temperature field on the wall heating panel surfaces that are formed during the steady conditions, using the Mikheev's criterion equation and the Faxen-Rydberg-Huber expression. The geometric parameters included pipe diameter and the spacing between the pipes, whereas the technological parameters included the volumetric flow and heating water inlet temperature. The theoretical results were compared with the experimental measurements, using a thermal imaging camera. The biggest impact on the growth of the temperature field was caused by an increase in the heating water inlet temperature, a reduction in the spacing between the pipes and an increase in the water volumetric flow value.

2.2.3.2 Solar cooling

Solar energy can also be used as a cooling mechanism. Solar cooling is very similar to solar heating, but instead of utilising the heat produced for a heating application, the heat is used to drive a heat-driven cooling machine, to produce a cooling effect (Huang *et al.*, 1998). The solar cooling systems can be used, either as stand-alone systems, or with conventional air-conditioning systems, to improve the indoor air quality of all types of buildings (Zhai *et al.*, 2011). With the financial implications of PV panels, solar thermal energy looks promising for the future. The higher source temperature, obtained with solar concentrators that occupy a smaller area, leads to an increased coefficient of performance (COP) and a reduction in the total cost of the system (Chidambaram *et al.*, 2011).

2.3 Thermal Energy Storage

Maintaining thermal comfort in buildings, while reducing energy consumption, has been a continuous battle. Extreme temperature swings in very hot and cold climates have forced humans to make use of space heating and air conditioning systems. These systems require a high energy demand and can have a great financial impact. The consumption of electrical energy during the day and at night, as well as the pricing system for off-peak and peak periods, differ considerably. Shifting the peak loads to off-peak loads reduces the energy cost, which offers significant economic benefits. This load shift can be accomplished by making use of TES. TES is an efficient technology that provides end-use demand through energy redistribution, by placing energy (heat or cold) in a storage medium for a certain period and retrieving it from the same place, to be used at a later stage (Kalaiselvam and Parameshwaran, 2014).

The benefits of implementing TES in an energy system are as follows: (i) better efficiency, due to more efficient use of energy achieved, (ii) better economics, by reducing capital and operational costs, (iii) a smaller amount of environmental pollution and less CO₂ emissions, and (iv) better system performance and reliability.

There are three steps in a TES process, namely, charge, storage and discharge (Cabeza, 2014). The charging process of a TES system usually occurs at part load conditions, where the quantity of thermal energy that is required to offset the critical load demand during on-peak periods is stored in the TES. The thermal energy is retrieved from the TES system during the discharge phase, from which the thermal energy is supplied to the end-use facility to be utilised for the desired purpose (Kalaiselvam and Parameshwaran, 2014). Implementing TES provides the opportunity to shift the load from on-peak to off-peak periods (load shifting), enables the utility to operate at the base capacity and accomplishes enhanced energy efficiency and operational performance.

Kalaiselvam and Parameshwaran (2014) state that the quantity of thermal energy that can be stored and discharged depends on the characteristics of the storage media, along with the temperature effects between the media and the energy source. The most important two

characteristics of TES are the amount of energy stored per unit volume (volumetric energy capacity) and the storage duration. Bindra *et al.* (2013) state that the ideal storage system stores and recovers energy at the same temperature i.e. at 100% exergy recovery.

According to Cabeza (2014), there are some main requirements for the design of a TES system, including: (i) storage material with a high energy density (storage capacity), (ii) good heat transfer between the storage material and the HTF, (iii) the chemical and mechanical stability of the storage material, (iv) the reversibility of a number of cycles, (v) low thermal losses during the storage period, and (vi) easy control. Cabeza (2014) confirms that the most important design criteria are the operation strategy, the maximum load needed, the nominal temperature and enthalpy drop and the incorporation into the entire system.

The potential savings, when implementing TES, could be very advantageous. The potential of saved energy in Europe, using TES, was determined by Arce Maldonado *et al.* (2011). The potential annual results for Germany, Spain and the European Union (EU-25) are summarised in Table 2.6.

Table 2.6 Potential annual thermal energy storage results for Germany, Spain and the European Union-25 (after Arce Maldonado *et al.*, 2011)

Parameter	Units	Germany	Spain	EU-25
Load Reduction (LR)	MW _{th}	480 844	541 266	5 854 139
Replaced Thermal Power (E)	GW _{th}	662 291	826 263	9 527 227
Replaced Electrical Power (E _e)	GW _e	not available	3 431	17 526
CO ₂ Emissions Reduction (R _{CO2})	Tons	165 572 663	207 670 938	2 579 088 559

The load reduction is the amount of energy that would have been used under normal conditions, without the use of TES. The replaced thermal and electrical energy is the energy stored (heat or cold) that will be re-utilised and that does not require any regeneration of energy. The reduction in CO₂ emissions is due to the use of the stored energy, rather than consuming fossil fuels, to generate the required energy.

Thermal energy (cold or heat) can be stored by virtue of an alteration in the internal energy of a material through thermochemical means, latent heat and sensible heat (Kalaiselvam and Parameshwaran, 2014). Energy can either be stored separately in each of the above-mentioned methods, or it can be combined into a hybrid system.

2.3.1 Thermochemical energy storage

Thermochemical energy storage (TCES) is a new and attractive energy storage concept that has recently become an attractive option for TES. It is an indirect method of storing energy by physico-chemical processes, such as adsorption or absorption, unlike the direct methods, such as sensible and latent (Bales *et al.*, 2005). The chemical potential of materials is used as the basis for storing and releasing thermal energy with minor thermal loss (Kalaiselvam and

Parameshwaran, 2014). TCES depends on the absorbed and released energy (heat), by breaking and reforming bonds in a totally reversible chemical reaction (Pintaldi *et al.*, 2015).

Bales *et al.* (2005) state that the main advantages of TCES are the high energy density, resulting in a small volume of material and several systems that act as heat pumps, making heating and cooling possible. The disadvantages include more complexity in the system (closed systems), several compounds are fairly expensive, relatively high temperatures are required and limited experience with long-term operation (after many thousand cycles).

There are two broad storage methods to effectively charge and discharge available energy, namely, sorption storage and chemical storage. Figure 2.8 was developed by N'Tsoukpoe *et al.* (2009) to indicate where TCES fits in as a TES method, taking into account the broader methods of sorption storage and chemical storage.

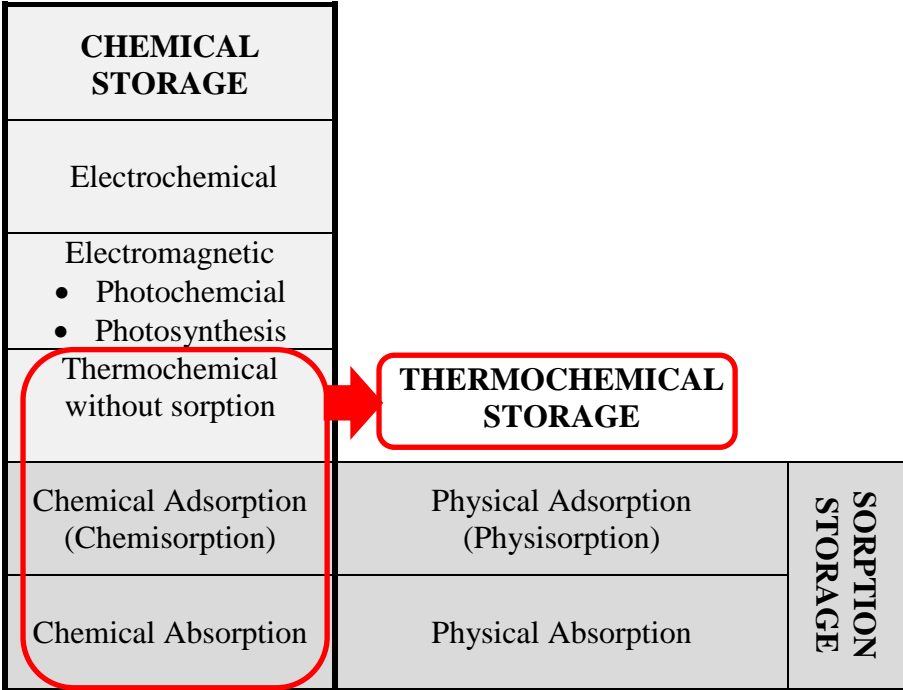


Figure 2.8 Classification of chemical storage and sorption storage (after N'Tsoukpoe *et al.*, 2009)

Sorption is a process, by which a substance, in the condensed state (sorbent), captures a gas or a vapour (sorbate), where the sorbent can either be in a solid or liquid form (Kalaiselvam and Parameshwaran, 2014). With reference to energy storage, absorption is the process of capturing a sorbate by a liquid (absorbent), whereas adsorption refers to the binding of a sorbate to the surface of a solid or porous medium (Kalaiselvam and Parameshwaran, 2014).

TCES systems can be divided into open and closed systems. The main difference between them is that in an open system the working fluid (in gaseous form) and entropy are released into the atmosphere; hence, water is the only candidate as a working fluid, whereas with a closed system only the entropy is released to the atmosphere via a heat exchanger (Bales *et al.*, 2005).

2.3.2 Latent heat storage

Latent thermal energy storage (LTES) is a process by which a material undergoes a phase change to store and release thermal energy. This transformation usually occurs from a solid to a liquid, or vice versa, and normally occurs at isothermal, or near isothermal, conditions (Kalaiselvam and Parameshwaran, 2014). The phenomenon of latent energy in materials is to store thermal energy in a material during melting (solid to liquid by absorbing heat energy) and to discharge it during freezing (solid to liquid by releasing heat energy). Generally, these materials are known as phase change materials (PCMs). PCMs were considered as TES materials in buildings before 1980 (Khudhair and Farid, 2004).

The heat storage capacity of PCMs can be calculated, using Equation (2.1), where the heat storage capacity is equal to the sum of the sensible heat being stored over the temperature swing of the energy storage process and the enthalpy of latent heat at the phase transition temperature (Kalaiselvam and Parameshwaran, 2014).

$$Q = m \left[(c_p \Delta T)_{sensible} + L_s \right] \quad (2.1)$$

where,

$Q = \text{heat storage capacity [kJ]}$,

$m = \text{mass of the heat storage material [kg]}$,

$c_p = \text{specific heat capacity at constant pressure [kJ.kg}^{-1}.\text{K}^{-1}]$,

$\Delta T = \text{temperature gradient [K]}$, and

$L_s = \text{specific latent heat for a particular substance [kJ.kg}^{-1}]$.

The potential utilisation of the phase transition of liquid to vapour is generally not considered, as the practical problem of storing the material in the gaseous phase, as well as the need for it to be pressurised, must be considered (Abhat, 1983).

LTES can be categorised into two types, namely, ice-thermal energy storage (ITES) and PCM-TES. ITES can be used in a solid, liquid or slurry form at 0°C. The latent heat of fusion of water is 333 kJ.kg⁻¹ or 0.093 kWh.kg⁻¹, which means that 0.093 kWh of heat is required to melt 1 kg of 0°C ice into 0°C of water. If the melt water is used for cooling up to 6°C, then 1000 kg of ice contains 100 kWh of cold (Cabeza, 2014). An alternative to ice-thermal energy storage is to use snow. There are three types of snow storage system, namely, those in thermally insulated buildings, those in a thermally insulated pit and those underground (without thermal insulation). For each of these systems, either air, water, or snow could be used as a cold carrier, to transport the required cold to the cold load.

Although the energy storage capacity of ITES (333 kJ.kg⁻¹) is generally higher than PCM-TES materials, PCMs are preferred, due to their high volumetric storage density (Cárdenas and León, 2013). The second method of LTES is PCM-TES.

PCM's can be categorised into inorganic compounds, organic compounds and eutectics. Inorganic compounds include salt hydrates, salt, metals and alloys. Organic compounds consist

of paraffins, non-paraffins, polyalcohols and fatty acids. Eutectics are a mixture of inorganic and/or organic compounds.

Energy storage systems that incorporate PCMs will have significantly smaller volumes, compared to materials only storing sensible heat. The heat storage and delivery of latent heat storage systems take place over a narrow temperature range, also known as the transition zone.

To achieve the maximum possible energy storage and release capabilities of the PCMs, encapsulation techniques were developed (Kalaiselvam and Parameshwaran, 2014). The encapsulation of PCM contains the specific material inside a capsule of various forms, sizes and materials. Micro- and macro-encapsulation are two methods used for encapsulating PCMs. PCM impregnation is a thermal energy storage method used to reduce the temperature swing within a structure.

There are many advantages of PCMs, as described above; however shortcomings still remain in the development of reliable and practical storage. Some practical difficulties that may arise when using latent heat storage include, low thermal conductivity, a density change, the stability of properties under extended cycling and occasionally, phase segregation and subcooling of the phase change materials (Farid *et al.*, 2004; Cabeza, 2014).

Pinel *et al.* (2011) state that latent and chemical storage methods still pose problems and require more research. The identification of appropriate materials that offer low cost and good thermal stability, are among these difficulties. The phase change and reversible thermochemical methods only operate over the limited temperature range at which the reactions occur (Bindra *et al.*, 2014). Due to the cost implications of phase change materials and thermochemical storage, most of the earlier and current systems have stored thermal energy in another form, such as sensible heat (Pinel *et al.*, 2011).

2.3.3 Sensible heat storage

Sensible TES (STES) entails storing thermal energy (heat) as internal energy in a medium, generally a solid or a liquid, and harnessing the energy, without changing the phase of the medium. The sensible systems are typically more cost-effective and simpler, when compared to TCES and LTES. STES are well-established, reliable, clearly understood and widely used concepts (Pinel *et al.*, 2011). In STES systems, the thermal energy stored in the material can be directly related to the mass, specific heat capacity and temperature difference of the material (referred to as the temperature swing) (Kalaiselvam and Parameshwaran, 2014). This is expressed in Equation (2.2):

$$Q = mc_p\Delta T \quad (2.2)$$

According to Kalaiselvam and Parameshwaran (2014), the most essential part of STES technology depends mainly on the selection of suitable materials and their properties to achieve the desired purpose of storing and discharging thermal energy efficiently. To achieve a high

heat storage density per volume (high heat content per volume), the heat storage material must have a high specific heat and a high density (Cabeza, 2014).

The materials used in STES can be classified into two main types, namely, solid storage materials and liquid storage materials. Solid storage materials include rocks, stones, bricks, concrete, dry and wet earth/soil, iron, wood, plasterboard, corkboard, etc., whereas liquid storage materials include water and oils, as well as pure alcohols and their derivatives (Kalaiselvam and Parameshwaran, 2014).

The above-mentioned STES types can be used in several applications. Some STES technologies comprise of the following: (i) storage tanks using water, (ii) rock-bed thermal storage, (iii) solar pond/lake thermal storage, (iv) building structure thermal storage, and (v) passive and active solar heating storage (Kalaiselvam and Parameshwaran, 2014). Both Cabeza (2014) and Kalaiselvam and Parameshwaran (2014) elaborated on the usage of seasonal STES, such as aquifers and boreholes, while Kalaiselvam and Parameshwaran (2014) also used caverns, earth to air, earth piles, sea water, rocks and roof ponds.

Storing thermal energy in water is highly favorable when working with temperatures below 100°C. The operating temperature to meet most of the heating and energy redistribution needs in residential applications is between 20°C and 80°C (Pinel *et al.*, 2011). Water can be used both as a storage medium, as well as an HTF due to its high specific heat capacity and convective heat transfer properties (Kalaiselvam and Parameshwaran, 2014).

Rock-beds as TES systems have been considered a highly favourable storage technology in the residential sector, when combined with solar thermal energy as a heat source. Rocks are usually loosely-packed in a bed-like structure, with inlet and outlet ducts to transfer heat to and from the storage system (Kalaiselvam and Parameshwaran, 2014). The charging cycle will consist of a heat transfer fluid (usually air), that will carry thermal energy from a solar collector through the rock-bed during the daytime. The discharge will occur at night, when cold air flows through the rock-bed to meet the space heating demand (Kalaiselvam and Parameshwaran, 2014). The performance of a rock-bed system for the same thermal load will be lower, compared to the water storage, due to the specific heat capacity of water being greater than that of air and rock. The rock-bed system could be approximately three times larger than the water storage system. However, the construction and operational cost of the rock-bed system is less than that of the water system and the rock-bed can be used at an elevated temperature (>100°C) (Kalaiselvam and Parameshwaran, 2014).

Solar ponds are used to store thermal energy from the sun and to extract the heat, using heat exchanger technologies. The salinity gradient is the driving force of storing and extracting heat energy from a solar pond. The solar ponds are generally classified into three levels: (i) the upper convective zone (UCZ), (ii) the middle non-convective zone (NCZ), and (iii) the lower convective zone (LCZ) (Kalaiselvam and Parameshwaran, 2014). The UCZ can contain little or no salt concentration and the salinity decreases from the UCZ to the LCZ. The UCZ acts as

an insulator for the NCZ and LCZ zones, where the heat energy is stored in the LCZ (Kalaiselvam and Parameshwaran, 2014).

Building structure thermal storage makes use of building fabric materials that are integral to their structure. The storage of thermal energy in fabric materials of buildings can be classified into either active or passive storage (see Section 2.1 for solar energy utilisation types). Thermal energy can be stored within the ceiling, the floor, slab components, etc. TermoDeck is a TES hollow core slab configuration that works as a heat storage facility, to reduce peak cooling and heating load demand, and that improves building energy efficiency (Kalaiselvam and Parameshwaran, 2014).

Solid storage materials are generally used as TES systems in buildings, to provide space heating (sparingly for cooling) and high temperature (solar) heating, as solid storage materials can operate in temperatures ranging from 40°C to 75°C for rock-beds/concrete and over 150°C for metals (Kalaiselvam and Parameshwaran, 2014).

The potential use of STES technologies is found in residential buildings, as the implementation of active or passive system may result in the enhancement of energy efficiency by 30-35% and thermal efficiency by 40-60%. With storage tanks that are properly designed and that have good stratification, the enhancement of useful heat energy utilisation can be expected to achieve 20 to 60% (Kalaiselvam and Parameshwaran, 2014)

According to Alam *et al.* (2014), water is reported to be the best sensible heat storage liquid, because of its high specific heat and low cost; however, it becomes problematic when using it above 100°C and to enclose it in its vapour state. The problems caused by water in its vapour pressure state and the restrictions caused by other liquids, can be avoided, by storing thermal energy in solids as sensible heat.

Rock-beds have been tested for many decades as a heat storage medium, but major technological challenges still remain, including the difficulty of producing sharp thermal gradients, as well as the presence of high pressure drops (Bindra *et al.*, 2014). Solid materials are generally preferred, for providing TES requirements, space heating (sparingly for cooling) and high temperature (solar) heating applications in buildings (Kalaiselvam and Parameshwaran, 2014).

Although there are advantages in using PCM and thermochemical storage techniques, the economical and technological facets make STES ideal. According to Alam *et al.* (2014), packed beds are the most appropriate technology for air-based solar systems.

STE are used for both heating and cooling conditions. With the increase in energy consumption of commercial and residential buildings (20-40%), and HVAC contributing approximately 50% of the residential usage, the need for alternative heating and cooling sources are prevalent. Storing the energy can be done by TES systems, such as TCES, LTES and STES. The volumetric heat capacity of TCSE and LTES is higher than for STES, but more expensive to incorporate in residential buildings.

2.4 Packed beds

Packed beds use a range of materials to store thermal energy and this energy can be utilised for various applications. A packed bed can be described as a contained volume of porous media, where an energy transfer fluid, with a high energy content is passed through a porous medium of lower energy content. Energy is transferred, in the form of heat, between the energy transfer fluid and the storage media, where thermal energy is stored, until it is utilised at a later stage (Zavattoni *et al.*, 2011; Andreozzi *et al.*, 2012). Packed beds are designed according to the storage temperature and duration requirements. The classification of a packed bed is an important factor to consider before designing a system.

2.4.1 Packed bed classification

The main features to consider, when selecting a TES system, are the storage temperature(s) and the storage duration (Fath, 1998). The storage temperature depends on the specific application and can be categorised as either: (i) low, which is less than 100°C, (ii) intermediate, which is between 100°C – 500°C, or (iii) high, which is higher than 500°C. The storage duration can either be short, namely, a few hours or days, or long, namely, a few months to several seasons.

A packed bed can be classified as a horizontal packed bed, or a vertical packed bed, and is based on the direction of flow of the HTF through the system, as indicated in Figure 2.9.

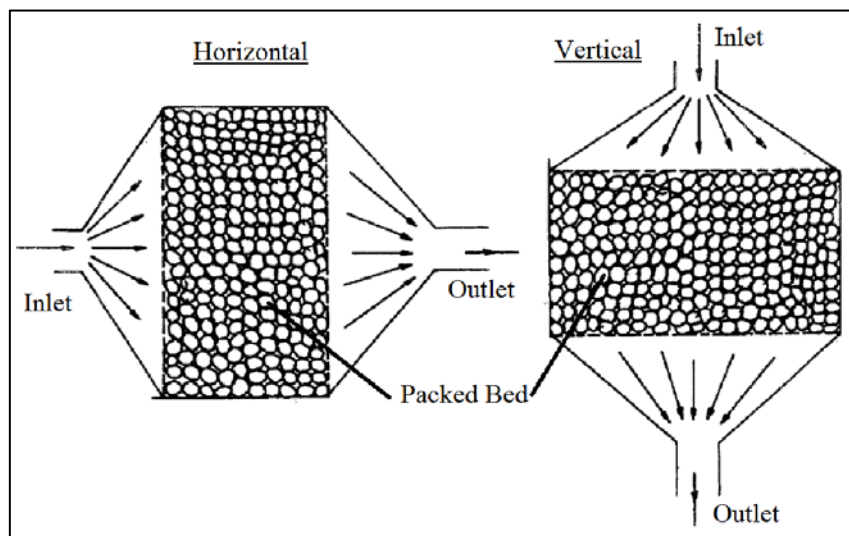


Figure 2.9 Schematic representation of the difference between a horizontal and vertical packed bed (adapted from Choudhury *et al.*, 1995)

The flow type can either be bi-directional or uni-directional, depending on the design requirements (Fuller, 2003). Figure 2.9 shows that, for a vertical system, in a bi-directional packed bed, heated air is forced through the top of the packed bed against natural buoyancy, and during the discharge phase, the airflow will be reversed. The storage medium absorbs the available energy in the air, until thermal equilibrium is reached. The air exit temperature will be similar to that of the bottom layer of the storage media. The ideal system will have a

sufficient charging time, in order to obtain a similar temperature for the top and bottom layers of storage media. The storage media at the upper part of the bed retains the most heat, due to natural stratification. During discharge, the air direction is reversed, forcing the air from the bottom to the top. The exit temperature will be similar to that of the storage media in the top layer. The packed bed can be controlled and operated as a normal heating system (Fuller, 2003).

The packed bed can also be operated with uni-directional airflow, as indicated in Figure 2.9 for the vertical system. The only difference is that the airflow will be in the same direction, for charging and discharging (top to bottom). During discharge, the cooler air at the bottom is warmed by the top layer of the storage media. If the packed bed is not fully charged, the air front can encounter a cooler layer of the storage media, as it flows through the system. This implies that the temperature at the outlet is lower than the temperature of the hottest storage media, reducing the efficiency of the system and making it less predictable. To achieve a more predictable system, the airflow direction can be changed; however, the complexity and cost of the system will increase (Fuller, 2003).

In order to overcome a few disadvantages of vertical packed beds, such as the height of the bed, the running costs and the complexity of reversing the flow, the thermal characteristics of horizontal flow packed beds were investigated. For residential use, horizontal packed beds use uni-directional flow, as the system only needs to be charged, using forced and/or natural convection. The underfloor horizontal packed bed system, as constructed by the CSIRO, does not release air into the living quarters, as the discharge phase occurs through the concrete slab (conduction), heating the inner space of the house. The thermal energy is dissipated throughout the house by radiation and natural convection, instead of utilising forced convection, as with vertical packed beds. This reduces the fan-operating time substantially and presents little danger to occupants, due to possibly contaminated air (Fuller, 2003).

According to Fuller (2003), a heating system, such as the rock-bed thermal storage system, was in high demand in Australia, where general, instead of localised, heating was needed. A summary of the identification criteria of a packed bed system is depicted in Table 2.7.

Table 2.7 Packed beds identification criteria, based on temperature, duration and classification

Storage Temperature (Fath, 1998)	Low	< 100°C
	Intermediate	100°C - 500°C
	High	> 500°C
Storage Duration (Fath, 1998)	Short	Hours - days
	Long	Months - seasons
Classification (Fuller, 2003)	Flow Direction	Horizontal
		Vertical
	Flow Type	Bi-directional
		Uni-directional

Some important factors to take into consideration, before deciding upon a storage method, include the initial operating and maintenance cost, as well as the size, efficiency and reliability (Fath, 1998).

Several research articles have been published in order to make packed beds more efficient, cost-effective and socially acceptable, as an alternative for conventional heating requirements. The application thereof will be discussed in the following section.

2.4.2 Background

The study of a liquid flowing through a porous medium dates back to the start of the 20th century (Schumann, 1929). Bed porosity is essential in a packed bed design, as it influences the flow characteristics, pressure drop and energy requirements.

Fath (1998) reviewed the basic concepts, the systems design and developments in TES. The parameters that influence the storage system selection, the advantages and disadvantages of each, as well as the problems encountered during the system operation, were discussed. Several energy storage materials and methods used for thermal energy storage were also studied. Fath (1998) concluded that the designer should aim to develop a storage system of long duration, small volume per unit energy and low cost.

Allen *et al.* (2014a) commented that the use of rocks as a TES medium in packed beds has shown great promise at temperatures of up to 600°C. Implementing rock-beds as a TES medium for use in steam power cycles was investigated. A cost-efficient method was developed, in order to determine the optimum bed length and particle size of packed beds, using rocks as the storage medium, by fixing the Biot number.

Hoffmann and Finkers (1995) proposed a semi-empirical relationship, which relates the void fractions of loosely-packed and tapped beds of particles with different diameters. Four parameters are used in the relationship that describe the properties of the particles, and these include: (i) the average particle diameter, μ , (ii) the size distribution of the particles, τ , (iii) particle density, ρ , and (iv) particle shape, ψ . Experimental void fractions, as well as several properties of different powders that, were obtained from literature were used to optimise the adjustable constant in the proposed semi-empirical relationship. Hoffmann and Finkers (1995) concluded that parameters describing the size, density, width of size distribution and shape, correlate well with an extensive range of industrial powders of packed beds with loosely-packed and tapped voidages.

A critical review was conducted by Delgado (2006) on dispersion in packed beds and the effect that the porous media and fluid properties have on the values of axial and radial dispersion coefficients. Previous work with experimental data on the axial and transverse dispersion of liquids, gases and non-Newtonian fluids were summarised and tabulated, taking into account the following: (i) the experimental method, (ii) the packed bed material used, (iii) the bed voidage (ϵ), (iv) the average diameter of inert particle (d), (v) the length (L), (vi) the diameter

of packed bed (D), (vii) the Reynolds number (Re), and (viii) the Schmidt number (Sc). The work that was conducted, specifically for gases, included:

- (i) several gas compositions were used,
- (ii) packed beds consisted mostly of glass spheres,
- (iii) the bed voidage varied from 0.330 to 0.556, with lower bed voidage being apparent,
- (iv) particle diameters of 0.097 mm (sand) – 25.4 mm (glass),
- (v) bed length of 50 mm – 36 576 mm,
- (vi) Reynolds number of 0.00237 – 1800, and
- (vii) Schmidt number of 0.3 – 2.2.

Delgado (2006) concluded that the improved technique developed, to determine the coefficient of transverse dispersion in fluid flow through packed beds, as well as the proposed correlations, are more accurate than the previous techniques used.

Singh *et al.* (2010) conducted an extensive review of the current research on rock-beds. The design, storage material used, heat transfer enhancement, flow phenomenon and pressure drop through rock-beds were analysed and also conducted for a vertical system. Singh *et al.* (2010) concluded from the literature review study that the packing materials most often used in packed beds were rocks and pebbles. They also found that not much emphasis has been placed on investigating large-sized packing materials, or medium-sized storage materials, in packed beds.

An evaluation of horizontal and vertical rock-bed storage technologies in Australia was conducted by Fuller (2003) for the period between 1980 and 2000. During the investigation, 31 systems were inspected and only seven in the residential application were found to be in proper working condition. This can be seen in Table 2.8.

Table 2.8 Rock-bed thermal storage systems used in residential applications (after Fuller, 2003)

No	Location	Date	Size (m ³)	Type	Status
R1	Myrtleford, Vic	1981	10.5	VB	working
R2	Violet Town, Vic	1983	14.0	HU	working
R3	Templestowe, Vic	1979	4.3	VB	unknown
R4	Highett, Vic	1978	49.4	HU	house dismantled
R5	Healesville, Vic	1979	60.0	VB	never worked
R6	Mooruduc, Vic	1984	5.6	VB	working
R7	Kensigton, Vic	1991	10.8	HU	working
R8	Hobart, Tas	1986	6.3	HU	working
R9	Hobart, Tas	1980	50.0	VU	working
R10	Mt Nelson, Tas	1979	8.0	VB	charging mode working discharge mode incomplete
R11	West Pennant Hills, NSW	1981	6.0	VB	not working
R12	Perth, WA	1979	17.0	VB	not working
R13	Perth, WA	1979	8.0	VB	not working
R14	Tammin, WA	1981	6.0	VB	not working

V = vertical, H = horizontal; B = bi-directional; U = uni-directional

The enthusiasm for rock-bed thermal storage for residential use has diminished, because of the large investment required, for a relatively small gain. However, it was found that horizontal, uni-directional flow systems, constructed and tested by the Commonwealth Scientific and Industrial Research Organisation (CSIRO), showed great promise in low energy homes. To achieve accurate control of a rock-bed as a heating system, the use of the vertical bi-directional rock-bed seems to be the best option. Although the vertical uni-directional flow rock-bed remains the simplest and the most economically viable option, the development of strategies to control the output of a vertical uni-directional flow system has not received much attention (Fuller, 2003).

A detailed theoretical analysis of a rock-bed, coupled to a vertical double pass, single cover air heater, was conducted by Choudhury *et al.* (1995). Operational and design parameters, such as, charging time, rock-bed size, cross-sectional area, rock size, air mass velocity and void fraction were studied and the selected design was based on the most energy gained at the lowest cost. The design selected had an air mass flux of $100 \text{ kg}\cdot\text{h}^{-1}\cdot\text{m}^{-2}$, a bed length of 1 m and cross-sectional area of 16 m^2 .

Bouhdjar *et al.* (1996) conducted an experimental study of a rock-bed storage system consisting of cylindrical ducts, which were buried horizontally beneath the soil in a tunnel greenhouse. Inlet temperature, outlet temperature and solar radiation were recorded, in order to present the efficiency of the system. The performance of the greenhouse system, which represents the ratio of the heat available in the greenhouse to the heat transferred by the air to the rock-bed, was found to be 8%, for the considered period.

Kürklü *et al.* (2003) also presented a study on an underground rock-bed for greenhouse heating and achieved an energy collection efficiency of 34%, which was higher than in the existing literature. An energy release, or recovery efficiency, of more than 80% was achieved. The mathematical model that was developed, correlated well with the measured data, although several assumptions were made.

Singh *et al.* (2006) conducted an experimental study to examine the pressure drop characteristics and heat transfer of a rock-bed TES system, with large diameter storage media of diverse shape. A relationship was developed for the friction factor and the Nusselt number, as a function of void fraction, sphericity and the Reynolds number. The correlation was used to predict the rock-bed performance, by varying the material shape and bed porosity. The Nusselt number is the ratio of convective to conductive heat transfer. The Reynolds number is the ratio of momentum forces to viscous forces and is used to classify different flow regimes and patterns. A descriptive definition of Reynolds number is provided by Allen (2010).

Phueakphum and Fuenkajorn (2010) assessed the efficiency of a scaled-down TES system, using basaltic rock. The change in temperature of several system components of the housing and storage system were monitored and compared with a mathematical model. The results showed that the night temperature of the housing can be increased by $4^{\circ}\text{C} - 6^{\circ}\text{C}$ more than the surrounding temperature. The efficiency of the system was approximately 35% and the thermal

energy gained in the house was equal to 203 kJ of electrical energy (Phueakphum and Fuenkajorn, 2010). The mathematical model that was used, correlated well with the experimental values.

Allen *et al.* (2013) investigated how pressure drop is dependent on: (i) the particle shape, (ii) the size distribution, (iii) the packing arrangement, and (iv) the roughness. It was concluded that the Ergun equation should not be used for pressure drop prediction in packed beds of smooth spheres, where $Re_{Erg} > 700$, as it over-predicts the pressure drop. The equation can also not be used for non-spherical particles (cylinders and cubes), as under-prediction of up to 100% can occur. The apparent friction factor of a packed bed changed significantly (10% - 100%) from that of a randomly packed smooth sphere, depending on the particle shape, packing arrangement and surface roughness (Allen *et al.*, 2013).

A numerical finite difference approximation method was used by Kürklü *et al.* (2003) to model a rock-bed in a greenhouse. The rock-bed was split into segments of equivalent thickness in the opposite direction of the air flow. In the study, the energy transfer in a rock in the radial direction, as well as the thermal energy lost to the surroundings by the rock-bed, were neglected. It was concluded that the numerical mathematical model correlated well with the experimental data.

A detailed mathematical model for analysing the solid and liquid phase of a packed bed TES system, for supplying air-cooling to a building, was developed by Marewo and Henwood (2006). A two-phase mathematical model was described for the packed bed, including heat dispersion in the fluid and heat loss to the environment, which is in contrast to other studies, where at least one of the terms are neglected, to simplify the mathematical model (Marewo and Henwood, 2006). The mathematical model used, was coded into a programme that uses the inlet air temperature (measured or analytically formed). The model correlated well with alternative numerical methods.

Barton (2013) used a computer simulation of air-blown TES in a loosely-packed rock-bed. The method developed was for one-dimensional airflow through the rock-bed, which includes a change in density with temperature. A major assumption made by Barton (2013) was that the pressure drop in the bed was negligible. The mathematical model of the simulations differs substantially from previous simulations in literature, especially in the case where the air flowing through the packed bed exhibits density variations.

2.4.3 Performance effects

A rock-bed solar heating system does not normally function at a constant temperature. During the daytime, dependent conditions such as solar radiation, ambient temperature, collector inlet temperature and load requirements, result in a variation of the collector outlet temperature (Singh *et al.*, 2010; Alam *et al.*, 2014). The solar heated air from the collector is transferred to the TES system.

Choudhury *et al.* (1995) list the design and operational parameters that affect the performance of a rock-bed as follows: (i) the rock size, (ii) the bed size, (iii) the air mass flow rate, (iv) the void fraction within the rock-bed, (v) the thermal and physical properties of rock, (vi) and the inlet temperature of the air. For a given inlet temperature, the rate of heating and cooling of the rock depends on: (i) the rock properties, (ii) the rock diameter, (iii) the air mass flux, and (iv) the bed length (Allen *et al.*, 2014b).

The Reynolds number, bed void fraction and material sphericity of a packed bed, affect the Nusselt number and friction factor, to a large extent. Singh *et al.* (2013) noted that an increase in the Reynolds number results in an increase in the Nusselt number. The maximum Nusselt number corresponds to a sphericity of one (sphere), for a minimum void fraction value of 0.275.

The parameters governing the performance of a TES are the temperature difference of the HTF and solid, the mass flow rate of the HTF, the geometry of the packed bed and bed porosity, which are dependent upon the orientation and shape of the storage media (Singh *et al.*, 2013).

The following factors influence the performance of a rock-bed, as described by Alam *et al.* (2014): (i) the physical properties of the solid phase used as storage material, (ii) the size and shape of the materials, and (iii) the void fraction that has an effect on the heat transfer and pressure drop characteristics of the rock-bed.

Singh *et al.* (2006) emphasised that the porosity and shape are the main features that affect the performance of the packed bed. The arrangement, shape and size of storage material are accountable for the variation in the contact area of air flowing through the system (Singh *et al.*, 2013). Allen *et al.* (2013) suggest that the particle shape and arrangement, as well as the packing method and surface roughness, have an effect on the pressure drop within a system.

The following is a summarised list of the design and operational parameters that affect the performance of a packed bed. These include:

- (i) the inlet temperature of the air (Choudhury *et al.*, 1995),
- (ii) the size of the materials (Choudhury *et al.*, 1995; Alam *et al.*, 2014),
- (iii) the shape of the materials (Singh *et al.*, 2006; Alam *et al.*, 2014),
- (iv) the geometric characteristics of the packed bed (Choudhury *et al.*, 1995; Singh *et al.*, 2013),
- (v) the mass flow rate of the energy transfer fluid (Choudhury *et al.*, 1995; Singh *et al.*, 2013),
- (vi) the thermal and physical properties of the storage material (Choudhury *et al.*, 1995; Alam *et al.*, 2014),
- (vii) the temperature difference of the energy transfer fluid and solid (Singh *et al.*, 2013), and
- (viii) the porosity within the rock-bed, (Choudhury *et al.*, 1995), which depends on the shape and orientation of the packing material (Singh *et al.*, 2013) and has an effect

on the pressure drop characteristics and the heat transfer of the rock-bed (Alam *et al.*, 2014).

Sanderson and Cunningham (1995b) commented that, to achieve a high operating efficiency for a given packed bed volume, rock-beds should make use of the smallest practical spheres, the longest practical packing lengths and the smallest practical packing dimensions normal to the direction of flow.

Implementing the smallest practical spheres and smallest packing dimensions in the system will lead to an increase in surface area, due to a change in the area of contact of the flowing energy transfer fluid (Singh *et al.*, 2006). This results in better heat transfer between fluid and solid, but with a rise in pressure drop over the specific bed length. Allen *et al.* (2013) state that the shape of the particles, as well as their arrangement, the packing methods and the surface roughness influence the pressure drop of the system.

The terms “porosity” and “permeability” are frequently confused and abused in geological literature (Graton and Fraser, 1935). Porosity and permeability have an adverse effect on the pressure drop, mass flow rate and energy input requirements of a packed bed. Porosity and permeability will be discussed in Sections 2.4.4 and 2.4.5 respectively.

2.4.4 Porosity

According to Graton and Fraser (1935), “porosity is the property of possessing pores or voids in the midst of ‘solid’ or non-porous material”. Porosity, or the void fraction, is defined as the ratio of the volume of voids to the total volume in a porous medium consisting of both voids and solids. This is represented in Equation (2.3).

$$\varepsilon = \frac{V_v}{V_t} = \frac{V_t - V_s}{V_t} = 1 - \frac{V_s}{V_t} \quad (2.3)$$

where,

$$\begin{aligned} \varepsilon &= \text{porosity } [\%], \\ V_v &= \text{volume of voids } [m^3], \\ V_t &= \text{total volume } [m^3], \text{ and} \\ V_s &= \text{volume of solids } [m^3]. \end{aligned}$$

The ε of a medium provides an indication of the volume available for fluid flow, and the permeability of the bed (Mueller, 2010). A value of unity implies an empty space, whereas a value of zero is a solid material (Allen, 2010).

With an increase in the bed ε , flow channelling occurs. Flow channelling is a reduction in the tortuousness (sharp corners or bends) of the airflow through the bed. This results in a lower heat transfer coefficient between the material and the air (Singh *et al.*, 2013).

Decreasing the ε of a rock-bed, results in an increase in the system's thermal capacity, which prolongs the charging and discharging time. With a higher ε value, steady state conditions are achieved in less time, both during the charging and discharging phase (Andreozzi *et al.*, 2012).

An improvement in stratification of a vertical bed occurs due to a decrease in the rock-beds void fraction. A reduction in the void fraction results in an increase in particle mass, thermal storage capacity and heat transfer (Singh *et al.*, 2013).

In a packed bed of uniformly-sized spheres, porosity is primarily and solely a function of the pure geometry of angles (Graton and Fraser, 1935). Magnifying, or demagnifying, the spheres to any degree, keeps the angular relationships and the porosity constant, regardless of the scale or absolute size.

The ε in the rock-beds is of great importance for predicting pressure drop in packed bed reactors and packed columns (Hoffmann and Finkers, 1995). The ε depends on the shape of the material, packing arrangement and sorting (same size vs different size). This will mostly affect the pressure drop in the system.

2.4.4.1 Shape

The shape of the packing material can be categorised according the degree of sphericity (ψ). The shape of a rock has an important effect on the flow regime in a system, which, in turn, affects the pressure drop, mass flow rate and energy requirements. Irregularly-shaped particles have higher tortuosity, which leads to higher pressure drops, compared to materials with a higher degree of sphericity.

Singh *et al.* (2006) studied several shapes and sizes of typical storage materials, and determined the correlations between the Nusselt number and friction factor as a function of the Reynolds number, material sphericity and bed void fraction. For cubical elements, a lower heat transfer coefficient value is expected, compared to spherical elements (Singh *et al.*, 2006), where a larger surface area between the energy transfer fluid and solid exists, due to smaller contact areas.

Pressure drops are highly unpredictable and vary substantially when using irregular asymmetric rocks. Empirical relationships are required that depend on the rock type and packing method, to calculate the pressure drop of a range of Reynold numbers (Allen *et al.*, 2014a).

Singh *et al.* (2013) found that the contact area between particles changes, from surface contacts (irregular shaped particles) to point contacts, for spherical-shaped particles. The larger surface area results in a larger resistance to flow, with a resulting increase in the friction factor. Singh *et al.* (2013) concluded that the thermo-hydraulic parameter is the largest for spherical-shaped particles at the lowest possible void fraction.

According to Allen *et al.* (2013), the pressure drop for cylinders and cubes, respectively, increases to almost 100% and 200% higher than those for smooth spheres.

The effect that the roundness of a particle has on the porosity, mass flow rate and energy input, is shown in Figure 2.10.

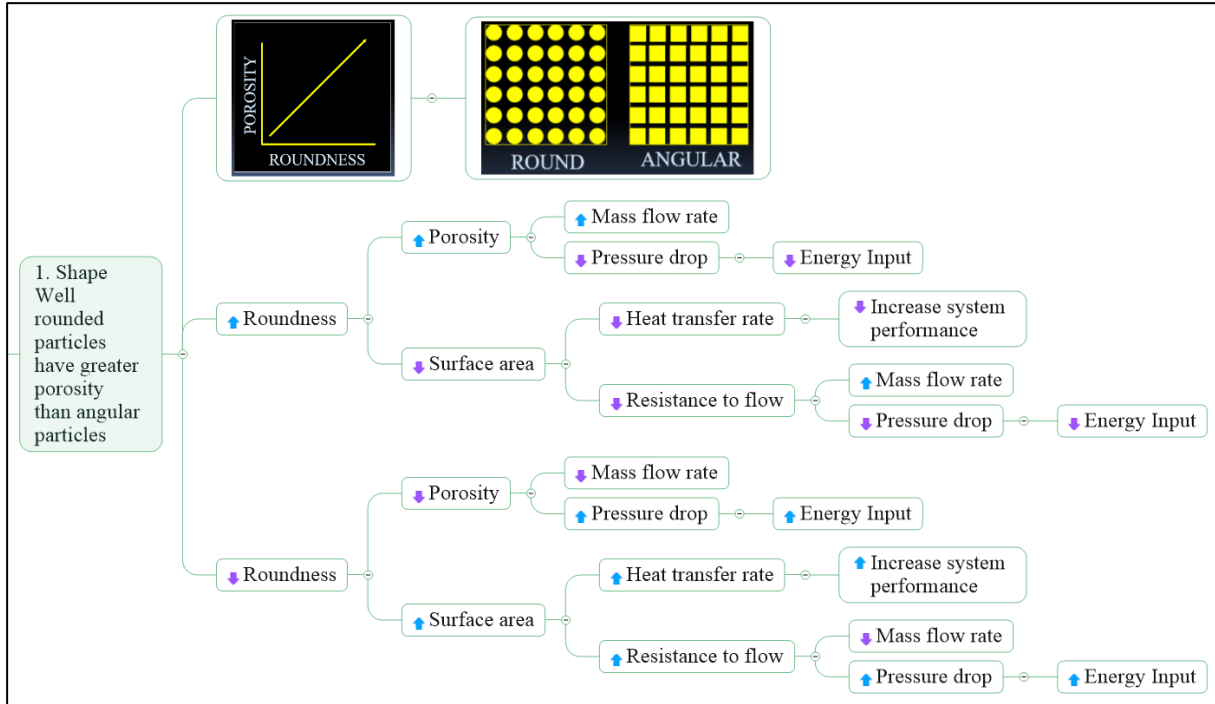


Figure 2.10 Summary of the effect of material shape on a packed bed

The second variable that affects the porosity of a packed bed is the packing arrangement. This is dependent on method of packing, as well as the type of packing structure selected. Alam *et al.* (2014) commented that the packing method in a bed has a significant effect on the flow resistance.

2.4.4.2 Packing

There are two methods of packing a rock-bed, namely, random and structured. With random packing, materials of similar shape and size are packed in an unsystematic manner into a vessel. Allen *et al.* (2013) found that the packing direction in random packing has a substantial influence on the apparent friction factor for irregularly-shaped particles, such as crushed rock. Apparent friction factors of up to 60% more were obtained when crushed rock was packed in a co-current direction, relative to the air flow, compared to a cross-flow packing direction. The crushed rock sizes used in the study were 13.5 mm and 26.5 mm. Allen *et al.* (2013) emphasised the importance of stating the packing direction, relative to the air flow. In order to obtain a desired bed ϵ , materials can be organised in a structured form (Singh *et al.*, 2013).

The packing factor is the fraction of space occupied by atoms, assuming that the atoms are hard spheres. The general expression for the Packing Factor (PF) is given by Equation (2.4):

$$PF = \frac{N_a * V_a}{V_c} = \frac{V_s}{V_t} \quad (2.4)$$

where,

$PF = \text{packing factor [unitless]}$,
 $N_a = \text{number of atoms per cell [m}^{-3}\text{]}$,
 $V_a = \text{volume of each atom [m}^{-3}\text{]}$, and
 $V_c = \text{volume of unit cell [m}^{-3}\text{]}$.

When comparing Equations (2.3) and (2.4), it should be noted that the ϵ and PF are directly related, as indicated by Equation (2.5).

$$\epsilon = 1 - \frac{V_s}{V_t} = 1 - PF \quad (2.5)$$

When calculating the PF, using Equation (2.4), values of 0.52, 0.68 and 0.74 were obtained for SC, BCC and FCC, respectively (Askeland *et al.*, 2011). For a spherical rock-bed storage system, the packing arrangement can have a maximum or minimum ϵ value. The maximum ϵ value of 0.476 is based on a SC arrangement, whereas the minimum ϵ value of 0.2595 is achieved with a FCC packing arrangement (Zavattoni *et al.*, 2011). A void fraction of 0.275 was used by (Singh *et al.*, 2013). When applying Equation (2.5) to the PF values calculated by Askeland *et al.* (2011), it is in excellent agreement with the ϵ values of Singh *et al.* (2013).

The effect that the roundness of a particle has on the porosity, mass flow rate and energy input, is shown in Figure 2.11.

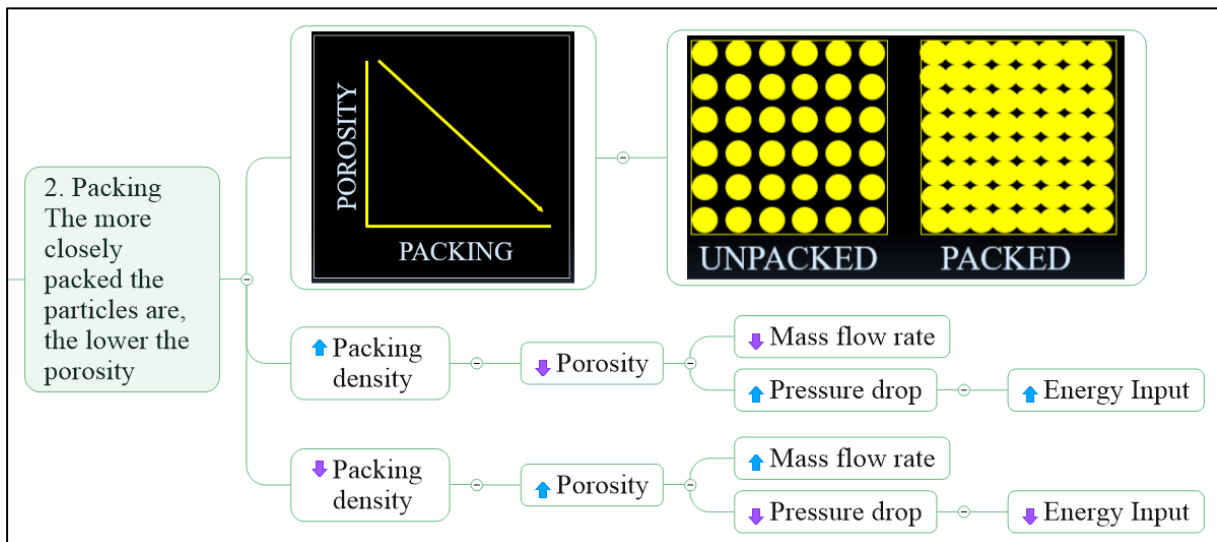


Figure 2.11 Summary of the effect of packing on a packed bed

The final variable that affects the porosity of a packed bed is sorting, which also affects the performance of the packed bed.

2.4.4.3 Sorting

The uniformity or non-uniformity of the particle size is of great importance, with respect to porosity. The highest porosity is obtained with particles of the same size and, by adding particles of either larger or smaller size, the porosity tends to decrease (Fraser, 1935). Figure 2.12 indicates the effect that sorting has on the porosity of a material and how it influences the mass flow rate and energy input of the packed bed.

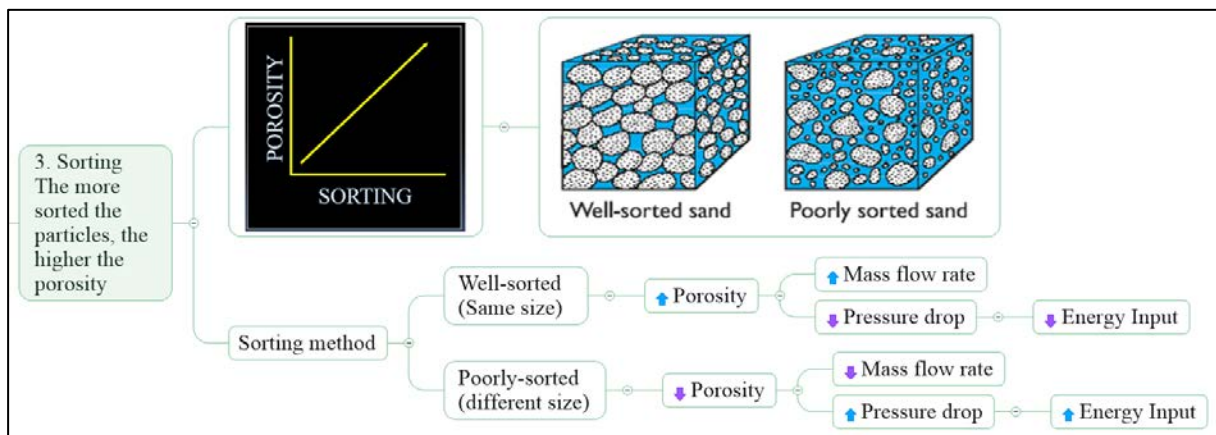


Figure 2.12 Summary of the effect of material sorting on a packed bed

The shape, packing and sorting of materials in a packed bed has a significant influence on the porosity, which, in turn, influences the performance of the packed bed. The diameter/size of the materials in a packed bed has no effect on the porosity of a structure, but influences its permeability.

2.4.5 Permeability

According to Graton and Fraser (1935). “permeability is the property of permitting a fluid to pass through the body which possesses this property”. Since permeability is only possible where there is a presence of voids, there is an obvious relationship between the porosity and permeability of a body. Notwithstanding the dependence of permeability on porosity and the relationship between the properties, it must be borne in mind that porosity and permeability do not vary proportionally (Graton and Fraser, 1935).

Permeability is a function of: (i) the particle size, (ii) sorting, (iii), the shape, and (iv) packing (Berg, 1970). The effect of (ii) – (iv) have been discussed in Section 2.4.4 and the emphasis will be placed on particle size in the text below. The relationship between permeability and particle size can be presented by Equation (2.6) (Shepherd, 1989), which forms part of Darcy’s Law.

$$k = s * d^2 \tag{2.6}$$

where,

$$k = \text{intrinsic permeability [mm}^2\text{]},$$

$s = \text{dimensionless constant [unitless]}, \text{ and}$
 $d = \text{particle size [mm]}.$

Hänchen *et al.* (2011) considered a variety of particle sizes and found that the maximum overall efficiency (outflow energy to input energy and pumping energy for charging and discharging) was for the smallest particle size. Decreasing the rock diameter results in a strong increase in the energy requirements for the pressure-producing device, due to a greater pressure drop over the system, as well as a reduction in the temperature difference between the inflow and the outflow (Zanganeh *et al.*, 2015).

The pressure drop in the system can be reduced by implementing larger storage materials; however, a reduction in the system's thermal performance may occur, by implementing a smaller surface area per unit bed volume, to achieve effective heat transfer (Singh *et al.*, 2013). Singh *et al.* (2006) state that, in order to achieve uniform flow through a packed bed of small particles, high pumping requirements are necessary, to overcome the pressure drop and to force the air through the bed. The large amount of energy consumed, due to the pumping requirements, reduces the overall system performance. Sanderson and Cunningham (1995a) suggest that the particle size used in packed beds should be larger than 13 mm, in order to prevent large pressure losses and energy requirements.

According to Hänchen *et al.* (2011), at a particle size of 2 mm, the energy requirement of the pressure-producing device reached nearly 2% of the energy delivered to the tank. The use of small particles in the packed bed allowed for a sharper temperature front through the system and the better extraction of the energy stored in the system; hence, the highest overall efficiency was achieved, using the smallest particles. The temperature difference between the solid and the HTF also decreases as the particle size reduces. A better convective heat transfer is achieved between the HTF and the solid.

Choudhury *et al.* (1995) found that varying the rock size within the range of 0.01 m – 0.05 m has an insignificant effect on the cost per unit energy storage and they concluded that the bed ϵ and rock size also had an insignificant influence on cost and performance, which contradicts existing literature on porosity, rock size and performance. The minimum daily cost to daily energy storage was observed for an air mass flux of $100 \text{ kg}\cdot\text{h}^{-1}\cdot\text{m}^{-2}$, a bed length of 1 m and a cross-sectional area of 16 m^2 . A higher bed temperature was achieved, when reducing the bed length and cross-sectional area.

Changing the scale of an assemblage (size of spheres) the permeability changes in the same direction, although the porosity remains constant (Graton and Fraser, 1935). This is depicted in Figure 2.13, which displays the effect of material size on the system performance.

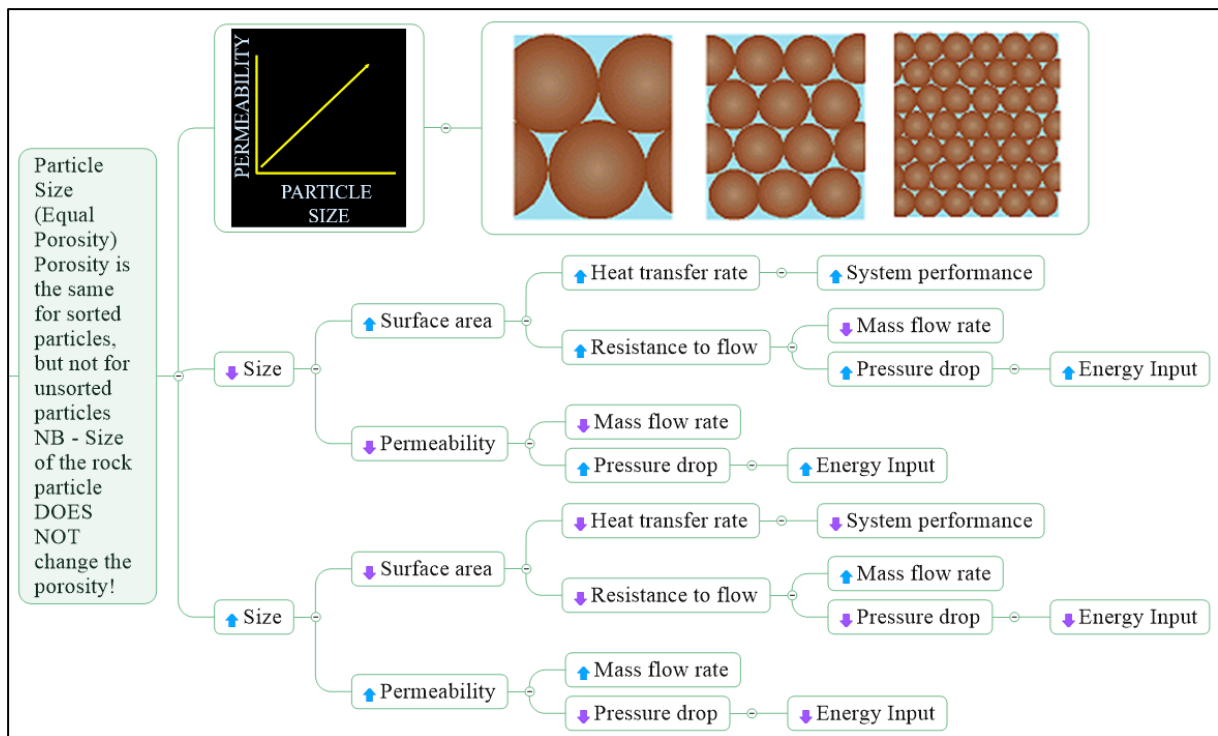


Figure 2.13 Summary of the effect of material size on a packed bed

Figure 2.13 indicates, when decreasing the size, the permeability and mass flow rate also decrease, but the pressure drop and energy input increase. On the contrary, the heat transfer rate increases with a decrease in size (increase in surface area), which results in an overall increase in system performance. Alam *et al.* (2014) reported that the heat transfer coefficient value decreases, with an increased particle diameter. The properties that influence the energy transfer between the storage material and the HTF will be discussed in the following section.

2.4.6 Heat transfer

Selecting the ideal storage material for a specific application requires that the storage material has certain desired properties, which will enhance the performance of the system. In a packed bed, storage material properties, such as, specific heat capacity (c - $\text{J.kg}^{-1}.\text{k}^{-1}$), thermal conductivity (k - $\text{W.m}^{-1}.\text{k}^{-1}$), density (ρ - kg.m^{-3}) and heat transfer coefficient (h - $\text{W.m}^{-2}.\text{k}^{-1}$) influence the energy storage and transfer of a system.

2.4.6.1 Density

In material that has a high density, molecules are closer to each other, which will lead to more collisions and larger heat transfer, compared to a gas, where molecules are further away from each other. Hence, the higher the density of a material, the better its heat transfer abilities.

2.4.6.2 Specific heat capacity

The specific heat is a property that is used to compare the ability of a material to store energy (Cengel *et al.*, 2002). Specific heat capacity values are commonly found in thermodynamic textbooks; for example, Cengel *et al.* (2002), Borgnakke and Sonntag (2009) and Moran *et al.* (2010), etc., where specific heat values of various common gases, liquids and solids at several temperature values are provided. A high specific heat capacity is required to store large amounts of energy.

2.4.6.3 Thermal conductivity

Thermal conductivity (λ) is a key component in calculating the heat transfer by conduction, as expressed by Fourier's Law in Equation (2.7). Values of conductivity, λ , are in the order of: (i) 100 W.m⁻¹.K⁻¹ for metals, (ii) 1 - 10 W.m⁻¹.K⁻¹ for non-metallic solids such as glass, ice and rock, (iii) 0.1 - 10 W.m⁻¹.K⁻¹ for liquids, (iv) 0.1 W.m⁻¹.K⁻¹ for insulation materials, and (v) 0.1 W.m⁻¹.K⁻¹, down to less than 0.01 W.m⁻¹.K⁻¹, for gases (Borgnakke and Sonntag, 2009).

$$\dot{Q}_{cond} = -\lambda * A * \frac{\Delta T}{\Delta x} \quad (2.7)$$

where,

\dot{Q}_{cond} = rate of heat transfer by conduction [W],

λ = thermal conductivity [W.m⁻¹.K⁻¹],

A = surface area through which heat transfer takes place [m²], and

Δx = thickness [m].

2.4.6.4 Heat transfer coefficient

The heat transfer coefficient forms part of Newton's Law of Cooling and is used to calculate heat transfer by convection. The transfer properties are lumped into the heat transfer coefficient, which becomes a function of the media properties, the flow and the geometry (Borgnakke and Sonntag, 2009). Typical values of h in W.m⁻².K⁻¹, are summarised in Table 2.9.

Table 2.9 Summary of different heat transfer coefficients for liquids and gases (adapted from Cengel *et al.*, 2002; Borgnakke and Sonntag, 2009)

Natural convection	$h = 5 - 25$, gas	$h = 50 - 1\ 000$, liquid
Forced convection	$h = 25 - 250$, gas	$h = 50 - 20\ 000$, liquid
Boiling phase change	$h = 2500 - 100\ 000$	

Singh *et al.* (2010) summarised properties of several solid materials, that are used for STES, in Table 2.10, including: (i) the medium, (ii) the density, (iii) the specific heat, (iv) the heat capacity, (v) the thermal conductivity, and (vi) the thermal diffusivity.

Table 2.10 Solid media properties of sensible heat storage materials (after Singh *et al.*, 2010)

Medium	Density (kg.m ⁻³)	Specific heat (J.kg ⁻¹ .K ⁻¹)	Heat capacity $\rho c \times 10^{-6}$ (J.m ⁻³ .K ⁻¹)	Thermal conductivity (W.m ⁻¹ .K ⁻¹)	Thermal diffusivity $\alpha=k/\rho c \times 10^6$ (m ² .s ⁻¹)
Aluminum	2707	896	2.4255	204 at 20°C	84.100
Aluminum oxide	2900	840	3.2760	-	-
Aluminum sulfate	2710	750	2.0325	-	-
Brick	1698	840	1.4263	0.69 at 29°C	0.484
Brick magnesia	3000	1130	3.3900	5.07	1.496
Concrete	2240	1130	2.5310	0.9-1.3	0.356-0.514
Cast iron	7900	837	6.6123	29.3	4.431
Pure iron	7897	452	3.5694	73.0 at 20°C	20.450
Calcium chloride	2510	670	1.6817	-	-
Copper	8954	383	3.4294	385 at 20°C	112.300
Earth (wet)	1700	2093	3.5581	2.51	0.705
Earth (dry)	1260	795	1.0017	0.25	0.250
Potassium chloride	1980	670	1.3266	-	-
Potassium sulfate	2660	920	2.4472	-	-
Sodium carbonate	2510	1090	2.7359	-	-
Stone, granite	2640	820	2.1648	1.73-3.98	0.799-1.840
Stone, limestone	2500	900	2.2500	1.26-1.33	0.560-0.591
Stone, marble	2600	800	2.0800	2.07-2.94	0.995-1.413
Stone, sandstone	2200	710	1.5620	1.83	1.172

For TES applications, the product of specific heat capacity and density should ideally be greater than 1 MJ.m⁻³.K⁻¹ (Özkahraman *et al.*, 2004). More thermal properties of materials can be obtained from reliable textbooks and databases.

Pinel *et al.* (2011) remarked that a storage material with a high specific heat capacity, as well as the capacity to release thermal energy at an adequate rate for the specific application, is essential for a packed bed design. The thermal energy transfer rate is reliant on two factors, namely, the thermal diffusivity of the solid medium and the high convective heat transfer rate for liquids. Liquids exchange thermal energy much easier than solids, although it is easier to contain and stratify solids.

Using everyday construction materials, fabrication costs will be less, compared to current storage systems, based on steam and molten salt. However, due to the lower volumetric heat capacity and thermal conductivity of using air as a HTF, compared to thermo-oils, molten salts, sodium, etc., the disadvantages, such as larger air mass flow rates and larger surface area requirements, need to be considered (Hänchen *et al.*, 2011).

Singh *et al.* (2010) stated that the heat transfer between rocks and air in a packed bed STES system is good, because of a big heat transfer area, low effective heat conductance of the rock

pile and small contact area between the rocks. This also contributes to low thermal energy losses from the packed bed.

2.4.7 Rocks properties

The use of rocks as a TES medium offers the following benefits: (i) they are not expensive, (ii) they are not toxic, nor flammable, and (iii) they act both as a storage medium and a heat transfer surface (Singh *et al.*, 2010). Other advantages highlighted by Zanganeh *et al.* (2015), include: (i) the storage media are plentiful and economical, (ii) there is direct heat transfer between the HTF and storage media, (iii) it is applied in a wide temperature range, with the temperature limited by the melting point of the rocks, (iv) there are no safety concerns, (v) there is no degradation or chemical instability, and (vi) it eradicates harmful and/or corrosive materials.

The rocks used in an experiment by Kürklü *et al.* (2003) had the following properties: (i) an equivalent diameter of 32 mm, (ii) a density of 1430 kg.m⁻³, (iii) a porosity of 49%, (iv) a specific heat of 0.8 kJ.kg⁻¹.K⁻¹, and (v) a thermal conductivity of 2.9 W.m⁻¹.K⁻¹.

During the investigation conducted by Fuller (2003) in Australia, the rock type that was mostly incorporated into the TES systems was washed basalt, which varied in size from 20 mm – 50 mm.

Allen *et al.* (2014b) conducted an extensive review on the rock characteristics in South Africa. The three types of rock, namely, igneous, metamorphic and sedimentary, were described, and their necessary characteristics were addressed. A selection of measured data for South African rock found in the Witwatersrand Supergroup was also discussed. Allen *et al.* (2014b) commented that the specific heat capacity of rock increases with increasing temperature.

The thermal conductivity of the rock needs to be sufficiently high, to allow the heat to conduct from the outer surface of the rock, to the inner core, with a small temperature gradient through the particle. The ratio of the thermal resistance to the convection resistance must be less than 0.1. This ratio is described by the Biot number (Allen *et al.*, 2014b).

Phueakphum and Fuenkajorn (2010) used Buriram basalt during an experimental evaluation, as it has the highest specific heat capacity and thermal conductivity in the north and northeast of Thailand. Buriram basalt has an average density of 2810 kg.m⁻³, a specific heat of 1174 kJ.kg⁻¹.K⁻¹, a thermal conductivity of 1.70 W.m⁻¹.K⁻¹, a thermal diffusivity of 5.15 x 10⁻⁷ m².s⁻¹, a thermal expansion coefficient (B_r) of 5.4 x 10⁻⁶ K⁻¹ and it has great potential for use as an STES material.

Hänchen *et al.* (2011) developed a one-dimensional, two-phase energy conservation equation, to study the heat transfer and charging/discharging cycles of a CSP plant, utilising rocks as a TES media. Under ideal circumstances and continuous operation, the overall efficiency exceeded 90%. Hänchen *et al.* (2011) concluded that the thermal conductivity of the storage material only has a small influence, but the volumetric heat capacity is the most important. The highest system efficiency was achieved when utilising the smallest particles. A reduction in

efficiency was achieved with a high mass flow rate, low storage heights and a low volumetric heat capacity (Hänchen *et al.*, 2011).

2.4.8 Fluid flow

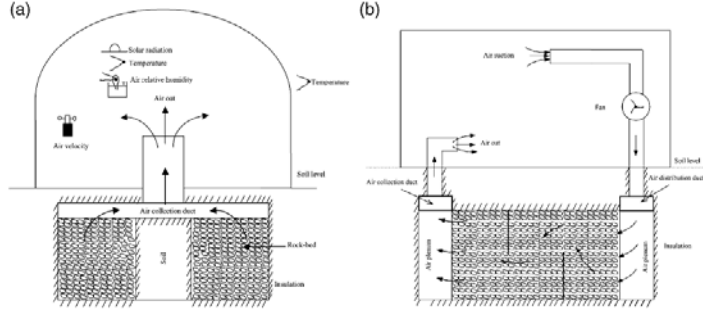
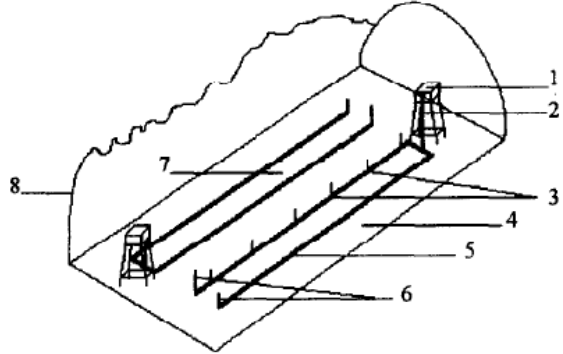
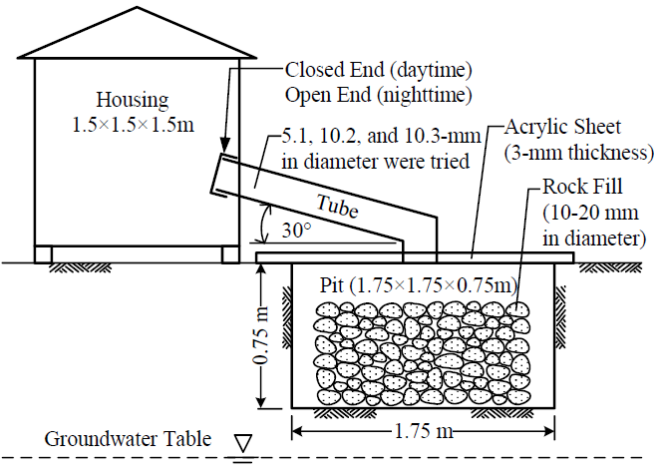
Convection can be either natural convection or forced convection. Natural convection is driven by the temperature difference between the packing and the working fluid, which is time- and position-dependent, and it is the strongest inside the wave-front (Sanderson and Cunningham, 1995b). Forced convection makes use of a pressure-producing device, normally a fan, to push the air through the rock-bed. Singh *et al.* (2013) mention that the overall advantage of a rock-bed is reduced, because of the fan's energy consumption, which propels the air through the bed. It is advantageous when natural convection aids forced convection, reducing the overall energy consumption. Choudhury *et al.* (1995) concluded that the most cost-effective mass flux of air obtained was less than $500 \text{ kg}\cdot\text{h}^{-1}\cdot\text{m}^{-2}$ or $1500 \text{ kg}\cdot\text{h}^{-1}$.

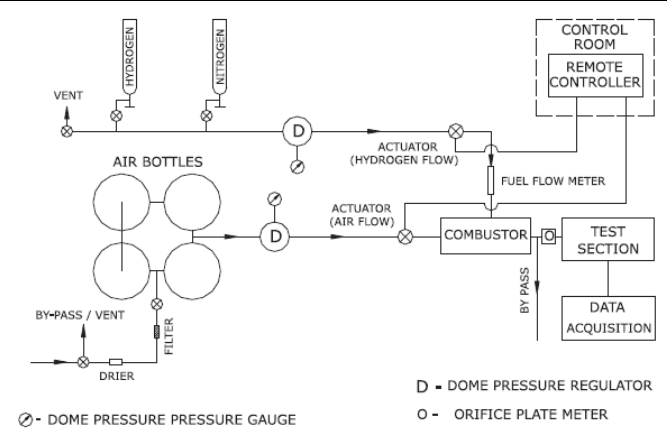

2.4.9 Bed structure

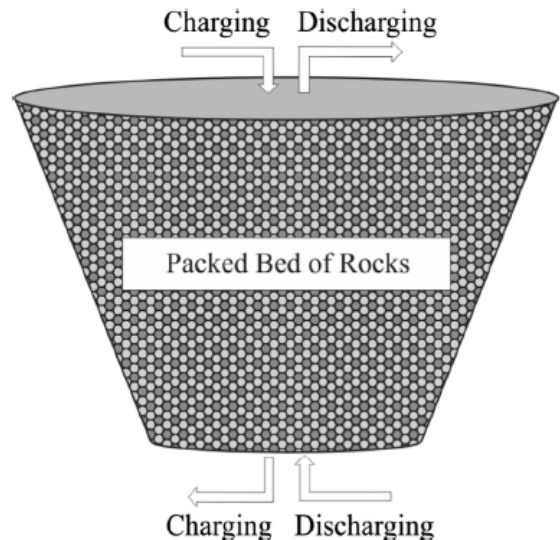
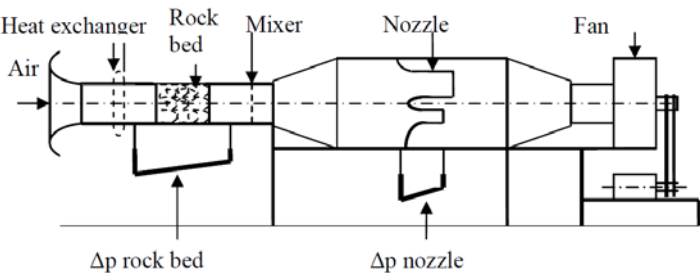
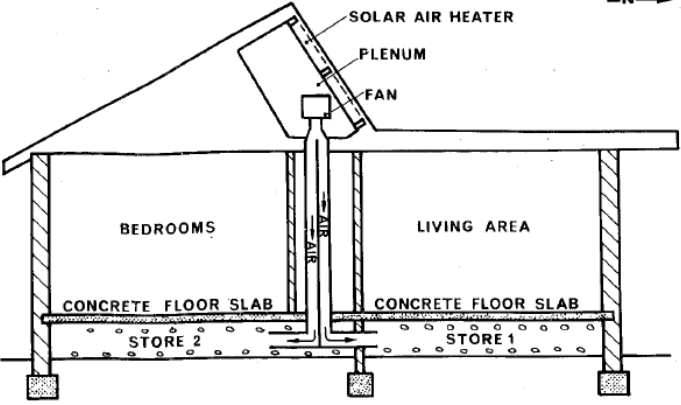
The optimum size of a TES system is related to many system parameters, including the following: (i) the storage temperature, (ii) the material, (iii) the storage heat losses, (iv) the storage medium container cost, (v) the heat exchanger, (vi) the cost of auxiliary energy, and (vii) the operating conditions. Operating conditions include insulation, ambient temperature, wind speed and solar fraction of the total heat load (Singh *et al.*, 2010). A summary of a few TES designs are provided in Table 2.11.

Table 2.11 Summary of several packed bed designs used by researchers

Author	Design and operational parameters	Design	Dimensions and material	Insulation																												
Choudhury <i>et al.</i> (1995)	<table border="1"> <tr> <td>Breadth of bed (B)</td> <td>1.0 – 4.0 m</td> </tr> <tr> <td>Width of bed (Z)</td> <td>1.0 – 4.0 m</td> </tr> <tr> <td>Height of bed (H)</td> <td>1.0 – 5.0 m</td> </tr> <tr> <td>Rock diameter (Dr)</td> <td>0.01 – 0.05 m</td> </tr> <tr> <td>Void fraction (ϵ)</td> <td>0.35 – 0.50</td> </tr> <tr> <td>Air mass flux (G)</td> <td>25 – 100 kg.h⁻¹.m⁻²</td> </tr> </table>	Breadth of bed (B)	1.0 – 4.0 m	Width of bed (Z)	1.0 – 4.0 m	Height of bed (H)	1.0 – 5.0 m	Rock diameter (Dr)	0.01 – 0.05 m	Void fraction (ϵ)	0.35 – 0.50	Air mass flux (G)	25 – 100 kg.h ⁻¹ .m ⁻²	<p>Figure 2.14 Vertical rock-bed (after Choudhury <i>et al.</i>, 1995)</p>	<p>The optimum charging time obtained for the design was 8 hours (8 a.m. to 4 p.m.). The minimum daily cost to energy stored per day was obtained for:</p> <table border="1"> <tr> <td>B</td> <td>4 m</td> <td>ϵ</td> <td>0.35</td> </tr> <tr> <td>Z</td> <td>4 m</td> <td>G</td> <td>100 kg.h⁻¹.m⁻²</td> </tr> <tr> <td>H</td> <td>1 m</td> <td>Ar</td> <td>16 m²</td> </tr> <tr> <td>Dr</td> <td>0.04 m</td> <td></td> <td></td> </tr> </table> <p>Higher bed temperatures were achieved for air mass flux of less than 100 kg.h⁻¹.m⁻² and cross-sectional area of less than 16 m².</p>	B	4 m	ϵ	0.35	Z	4 m	G	100 kg.h ⁻¹ .m ⁻²	H	1 m	Ar	16 m ²	Dr	0.04 m			No information on insulation of the packed bed was provided.
Breadth of bed (B)	1.0 – 4.0 m																															
Width of bed (Z)	1.0 – 4.0 m																															
Height of bed (H)	1.0 – 5.0 m																															
Rock diameter (Dr)	0.01 – 0.05 m																															
Void fraction (ϵ)	0.35 – 0.50																															
Air mass flux (G)	25 – 100 kg.h ⁻¹ .m ⁻²																															
B	4 m	ϵ	0.35																													
Z	4 m	G	100 kg.h ⁻¹ .m ⁻²																													
H	1 m	Ar	16 m ²																													
Dr	0.04 m																															
Singh <i>et al.</i> (2006)	<table border="1"> <tr> <td>Sphericity (ψ)</td> <td>0.55 – 1.00</td> </tr> <tr> <td>Void fraction (ϵ)</td> <td>0.306 – 0.63</td> </tr> <tr> <td>Air mass flux (G)</td> <td>0.155 – 0.266 kg.h⁻¹.m⁻²</td> </tr> <tr> <td>Reynolds number (Re)</td> <td></td> </tr> <tr> <td></td> <td>1257 – 2157 (T-joint masonry tile bricks)</td> </tr> <tr> <td></td> <td>1047 – 1797 (standard masonry tile bricks)</td> </tr> <tr> <td></td> <td>1558 – 2674 (concrete cubes)</td> </tr> <tr> <td></td> <td>1139 – 1955 (concrete spheres)</td> </tr> </table> <p>An air duct with an electric heater was implemented. A fan was inserted to force the air through the duct to the storage tank.</p>	Sphericity (ψ)	0.55 – 1.00	Void fraction (ϵ)	0.306 – 0.63	Air mass flux (G)	0.155 – 0.266 kg.h ⁻¹ .m ⁻²	Reynolds number (Re)			1257 – 2157 (T-joint masonry tile bricks)		1047 – 1797 (standard masonry tile bricks)		1558 – 2674 (concrete cubes)		1139 – 1955 (concrete spheres)	<p>Figure 2.15 Vertical packed bed (after Singh <i>et al.</i>, 2006)</p> <p>Description: 1-air duct with electric heater 2-storage tank 3-fan 4-micromanometer 5-orifice meter 6-U tube manometer 7-pipe line 8-flow control valve 9-taps for thermocouples 10-hot air inlet to packed bed 11-air out let 12-screen for supporting storage material</p>	<p>The duct size was 3 m x 0.5 m x 0.0254 m, Inlet and outlet length of 0.65 m and 0.96 m respectively, which included the plenum length of 0.61 m at the outlet. The heating section was 2 m x 0.5 m x 0.0254 m</p> <p>Electric heater 2 m x 0.5 m, constructed by combining series and parallel loops of heating wire wound around an asbestos sheet. The storage tank, with a diameter of 0.60 m constructed of mild steel (MS) sheet metal, 3 mm thick.</p> <p>The tank had a height of 1.25 m, including lower and upper plenums of 0.25 m each, which resulted in a in a packed bed height of 0.75 m.</p> <p>A 3 mm thick MS sheet with a circular shape and a number of holes was placed in the tank to support the storage material above the lower plenum.</p>	<p>In order to reduce heat losses within of the system, the back end of the heating device was insulated with glass wool on the outer layer.</p> <p>The tank was also insulated with polyethylene foam in order to reduce heat loss. Polyethylene foam was also used to cover a pipeline of 0.082 m.</p>												
Sphericity (ψ)	0.55 – 1.00																															
Void fraction (ϵ)	0.306 – 0.63																															
Air mass flux (G)	0.155 – 0.266 kg.h ⁻¹ .m ⁻²																															
Reynolds number (Re)																																
	1257 – 2157 (T-joint masonry tile bricks)																															
	1047 – 1797 (standard masonry tile bricks)																															
	1558 – 2674 (concrete cubes)																															
	1139 – 1955 (concrete spheres)																															

Kürklü <i>et al.</i> (2003)	Equivalent diameter	32 mm		<p>Two tunnel greenhouses were covered with 0.2 mm polyethylene. The ground area was 15 m². Two canals were excavated in the subsoil of the greenhouse to serve as the rock-bed storage space. The canal dimensions were 3 m x 1.25 m x 0.75 m. Each rock-bed canal was fitted with two 075 m x 0.6 m galvanised sheet baffles to generate air turbulence within the rock-bed.</p>	<p>Soil was used as insulation. The canals surfaces were insulated with 0.05 m glass wool.</p>										
	Density	1430 kg.m ⁻³													
	Porosity	49%													
	Specific heat	0.8 kJ.kg ⁻¹ .K ⁻¹													
	Thermal conductivity	2.9 W.m ⁻¹ .K ⁻¹													
	Air mass flow rate	0.366 kg.s ⁻¹													
	Air specific heat	1000.5 J.kg ⁻¹ .K ⁻¹													
	Volumetric heat transfer coefficient	2304.8 W.m ⁻³ .K ⁻¹													
Canal dimensions	3 m x 1.25 m x 0.75 m														
Bouhdjar <i>et al.</i> (1996)	<p>Gravel volume was projected to be 4.9 m³. Gravel size varying between 50 mm and 100 m. Air mass flow rate = 0.17 kg.s⁻¹ Inlet air temperature = 500°C</p>			<p>A tunnel greenhouse with a size of 240 m² (30 m x 8 m) Metallic arches and low density polyethylene cover (180 μm thickness). Storage system: 250 mm diameter pipes, filled with close to spherical gravel. Pipes were joined to form two U-shapes of 25 m length each. The pipes were buried 600 mm below the ground.</p>	<p>No information on insulation of the packed bed was provided.</p>										
	<p>Storage disposal scheme: 1- Blowers, 2 – Pipe inlet, 3 – Temperature measurements in pipe, 4 – Temperature measurements in soil, 5 – Pipes filled with gravels, 6 – Pipe outlet, 7 – Ambient temperature measurement, 8 – Greenhouse</p>														
Phueakphum and Fuenkajorn (2010)	<p>The Buriram basalt was used in the TES, with the following properties:</p> <table border="1" data-bbox="311 1262 884 1476"> <tbody> <tr> <td>average density</td> <td>2810 kg.m⁻³</td> </tr> <tr> <td>specific heat</td> <td>1174 kJ.kg⁻¹.K⁻¹</td> </tr> <tr> <td>thermal conductivity</td> <td>1.70 W.m⁻¹.K⁻¹,</td> </tr> <tr> <td>thermal diffusivity</td> <td>5.15 x 10⁻⁷ m².s⁻¹</td> </tr> <tr> <td>thermal expansion coefficient (Br)</td> <td>5.4 x 10⁻⁶ K⁻¹</td> </tr> </tbody> </table>		average density	2810 kg.m ⁻³	specific heat	1174 kJ.kg ⁻¹ .K ⁻¹	thermal conductivity	1.70 W.m ⁻¹ .K ⁻¹ ,	thermal diffusivity	5.15 x 10 ⁻⁷ m ² .s ⁻¹	thermal expansion coefficient (Br)	5.4 x 10 ⁻⁶ K ⁻¹		<p>Phueakphum and Fuenkajorn (2010) constructed a TES system of 1.75 m x 1.75 m x 0.75 m covered with 3 mm transparent acrylic sheet The acrylic sheet had: (i) a specific heat of 1470 J.kg⁻¹.K⁻¹, (ii) a thermal conductivity of 0.20 W.m⁻¹.K⁻¹, and (iii) a density of 1150 kg.m⁻¹. The pit was filled with four chain-link baskets of 0.5 m x 0.5 m x 0.5 m each, packed with predefined fragment-sized basalt of 0.1 m – 0.2 m. The pit was connected to a scale-down housing model (1.5 m x 1.5 m x 1.5 m) via a hot air tube, at an angle of 30°.</p>	<p>The soil surrounding the system and an acrylic sheet cover was used as insulation.</p>
	average density	2810 kg.m ⁻³													
	specific heat	1174 kJ.kg ⁻¹ .K ⁻¹													
	thermal conductivity	1.70 W.m ⁻¹ .K ⁻¹ ,													
	thermal diffusivity	5.15 x 10 ⁻⁷ m ² .s ⁻¹													
	thermal expansion coefficient (Br)	5.4 x 10 ⁻⁶ K ⁻¹													
<p>Figure 2.18 Storage pit (after Phueakphum and Fuenkajorn, 2010)</p>															

Srinivasan and Raghunandan (2013)	Exp.	Sphere diameter (mm)	Packed bed length L (mm)	Void fraction (ϵ)	Max inlet flow temperature, T_1 ($^{\circ}\text{C}$)	Inlet flow velocity, u_1 (m.s^{-1})	Re_d (10^4)	ΔP (MPa)	 <p>Fig. 1. Schematic representation of test facility.</p> <p>D - DOME PRESSURE REGULATOR O - ORIFICE PLATE METER</p>	<p>The packed bed test section was constructed with structural steel according to industrial standards for high-pressure operation.</p> <p>Internal diameter of 90 mm</p> <p>Maximum packed bed length of 500 mm in steps of 100 mm</p> <p>Carbon steel ball bearings (5 mm and 9.5 mm)</p> <p>Compression moulded Silica Phenolic (Silica cloth with phenolic resin) of 5 mm thick was used in the walls of the test section to prevent longitudinal conduction and radial heat transfer along the section walls.</p>	
	E1	9.5	215.1	0.440	73.4	3.6	0.9	0.02			
	E2	9.5	215.1	0.440	73.6	4.9	2.6	0.03			
	E3	9.5	215.1	0.440	83.5	9.0	4.4	0.12			
	E4	9.5	215.1	0.440	163.1	12.7	6.2	0.24			
	E5	9.5	312.9	0.423	121	2.5	0.98	0.04			
	E6	9.5	312.9	0.423	82	4.8	2.7	0.11			
	E7	9.5	312.9	0.423	165	10.2	4.4	0.24			
	E8	9.5	312.9	0.423	92.2	12.1	8.5	0.38			
	E9	5.0	216.0	0.385	90	3.3	0.5	-			
	E10	5.0	216.0	0.385	120	4.5	1.25	0.06			
	E11	5.0	216.0	0.385	90	6.2	2.4	0.4			
	E12	5.0	216.0	0.385	160	12	3.15	0.5			
	E13	5.0	310.0	0.398	105	4	0.6	0.07			
	E14	5.0	310.0	0.398	75	3.8	1.3	0.12			
	E15	5.0	310.0	0.398	132	9.6	2.7	0.51			
	E16	5.0	310.0	0.398	212	12	3.5	0.65			
Zavattoni <i>et al.</i> (2011)	<p>Three cases were analysed: Constant porosity value, Linear porosity variation, and Quadratic porosity variation. 25 m³ of homogeneous steatite rocks of average diameter 0.03 m.</p>									<p>Upper diameter of 4 m</p> <p>Lower diameter of 2.5 m</p> <p>Height of packed bed 3.16 m</p> <p>Total vessel height of 4.05 m</p>	<p>Insulated concrete vessel</p>
<p>Figure 2.19 Schematic representation of test facility (after Srinivasan and Raghunandan, 2013)</p>									<p>Figure 2.20 Vertical thermal energy storage system (after Zavattoni <i>et al.</i>, 2011)</p>		

Zanganeh <i>et al.</i> (2015)	<table border="1"> <thead> <tr> <th colspan="2">Operating conditions</th> </tr> </thead> <tbody> <tr> <td>t_{charging} (h)</td> <td>8</td> </tr> <tr> <td>t_{discharging} (h)</td> <td>16</td> </tr> <tr> <td>T_{charging} (°C)</td> <td>650</td> </tr> <tr> <td>T_{discharging} (°C)</td> <td>150</td> </tr> <tr> <td>T_{surrounding} (°C)</td> <td>20</td> </tr> <tr> <td>ṁ_{charging} (kg.s⁻¹)</td> <td>132</td> </tr> <tr> <td>ṁ_{discharging} (kg.s⁻¹)</td> <td>66</td> </tr> </tbody> </table>	Operating conditions		t _{charging} (h)	8	t _{discharging} (h)	16	T _{charging} (°C)	650	T _{discharging} (°C)	150	T _{surrounding} (°C)	20	ṁ _{charging} (kg.s ⁻¹)	132	ṁ _{discharging} (kg.s ⁻¹)	66		Ultra high performance concrete (UHPC) Low density concrete (LD)	Microtherm (insulation) <ul style="list-style-type: none"> Lid (0.6 m) Lateral walls (0.3 m) Bottom (0.0 m) Foamglas (insulation) <ul style="list-style-type: none"> Lid (0.5 m) Lateral walls (0.5 m) Bottom (0.4 m) UHPC (concrete thickness) <ul style="list-style-type: none"> Lid (0.02 m) Lateral walls (0.02 m) Bottom (0.02 m) LD (concrete thickness) <ul style="list-style-type: none"> Lid (0.7 m) Lateral walls (1.0 m) Bottom (0.48 m) 																						
	Operating conditions																																									
t _{charging} (h)	8																																									
t _{discharging} (h)	16																																									
T _{charging} (°C)	650																																									
T _{discharging} (°C)	150																																									
T _{surrounding} (°C)	20																																									
ṁ _{charging} (kg.s ⁻¹)	132																																									
ṁ _{discharging} (kg.s ⁻¹)	66																																									
<table border="1"> <thead> <tr> <th colspan="2">Rock properties</th> </tr> </thead> <tbody> <tr> <td>ρ (kg.m⁻³)</td> <td>2735</td> </tr> <tr> <td>C_s (J.kg⁻¹.K⁻¹)</td> <td>650 - 1100</td> </tr> <tr> <td>K_s (W.m⁻¹.K⁻¹)</td> <td>1 - 5</td> </tr> </tbody> </table>	Rock properties		ρ (kg.m ⁻³)	2735	C _s (J.kg ⁻¹ .K ⁻¹)	650 - 1100	K _s (W.m ⁻¹ .K ⁻¹)	1 - 5	<table border="1"> <thead> <tr> <th colspan="2">Dimensions</th> </tr> </thead> <tbody> <tr> <td>r_{top} (m)</td> <td>20</td> </tr> <tr> <td>R_{bottom} (m)</td> <td>16</td> </tr> <tr> <td>H (m)</td> <td>25</td> </tr> <tr> <td>d (m)</td> <td>0.03</td> </tr> <tr> <td>ε</td> <td>0.342</td> </tr> <tr> <td>ψ</td> <td>0.7</td> </tr> </tbody> </table> <table border="1"> <thead> <tr> <th colspan="2">Additional data</th> </tr> </thead> <tbody> <tr> <td>η_{fan}</td> <td>0.95</td> </tr> <tr> <td>η_{Rankine}</td> <td>0.35</td> </tr> </tbody> </table>	Dimensions		r _{top} (m)	20	R _{bottom} (m)	16	H (m)	25	d (m)	0.03	ε	0.342	ψ	0.7	Additional data		η _{fan}	0.95	η _{Rankine}	0.35	Figure 2.21 Schematic and operating principle of the packed bed (after Zanganeh <i>et al.</i> , 2015)												
Rock properties																																										
ρ (kg.m ⁻³)	2735																																									
C _s (J.kg ⁻¹ .K ⁻¹)	650 - 1100																																									
K _s (W.m ⁻¹ .K ⁻¹)	1 - 5																																									
Dimensions																																										
r _{top} (m)	20																																									
R _{bottom} (m)	16																																									
H (m)	25																																									
d (m)	0.03																																									
ε	0.342																																									
ψ	0.7																																									
Additional data																																										
η _{fan}	0.95																																									
η _{Rankine}	0.35																																									
Allen (2010)	<table border="1"> <thead> <tr> <th colspan="2">Operating conditions</th> </tr> </thead> <tbody> <tr> <td>Mass flow rate</td> <td>< 4 kg.m⁻².s⁻¹</td> </tr> <tr> <td>Operating Temperature</td> <td>< 70 °C</td> </tr> </tbody> </table> <table border="1"> <thead> <tr> <th>Material</th> <th>Shale</th> <th>Granite</th> <th>Dolerite</th> </tr> </thead> <tbody> <tr> <td>ρ_s, kg.m⁻³</td> <td>2750</td> <td>2893</td> <td>2657</td> </tr> <tr> <td>c_s, J.kg⁻¹.K⁻¹ 45°C</td> <td>820 (64)</td> <td>845 (40)</td> <td>839 (41)</td> </tr> <tr> <td>ε (± 0.008)</td> <td>0.381</td> <td>0.395</td> <td>0.385</td> </tr> <tr> <td>D, m</td> <td>0.0426</td> <td>0.0655</td> <td>0.0422</td> </tr> <tr> <td>ρ_s, c_s, MJ.m⁻³.K⁻¹</td> <td>2.3</td> <td>2.5</td> <td>2.2</td> </tr> </tbody> </table>	Operating conditions		Mass flow rate	< 4 kg.m ⁻² .s ⁻¹	Operating Temperature	< 70 °C	Material	Shale	Granite	Dolerite	ρ _s , kg.m ⁻³	2750	2893	2657	c _s , J.kg ⁻¹ .K ⁻¹ 45°C	820 (64)	845 (40)	839 (41)	ε (± 0.008)	0.381	0.395	0.385	D, m	0.0426	0.0655	0.0422	ρ _s , c _s , MJ.m ⁻³ .K ⁻¹	2.3	2.5	2.2		<table border="1"> <thead> <tr> <th colspan="2">Dimensions (without insulation)</th> </tr> </thead> <tbody> <tr> <td>Height (m)</td> <td>0.50</td> </tr> <tr> <td>Width (m)</td> <td>0.47</td> </tr> <tr> <td>Length (m)</td> <td>0.50</td> </tr> </tbody> </table>	Dimensions (without insulation)		Height (m)	0.50	Width (m)	0.47	Length (m)	0.50	Polystyrene insulation Foam lining for wall effect, Neoprene (7 mm) Side walls and top covered with sponge (15-20 mm) Sponge foam (20-25 mm)
	Operating conditions																																									
Mass flow rate	< 4 kg.m ⁻² .s ⁻¹																																									
Operating Temperature	< 70 °C																																									
Material	Shale	Granite	Dolerite																																							
ρ _s , kg.m ⁻³	2750	2893	2657																																							
c _s , J.kg ⁻¹ .K ⁻¹ 45°C	820 (64)	845 (40)	839 (41)																																							
ε (± 0.008)	0.381	0.395	0.385																																							
D, m	0.0426	0.0655	0.0422																																							
ρ _s , c _s , MJ.m ⁻³ .K ⁻¹	2.3	2.5	2.2																																							
Dimensions (without insulation)																																										
Height (m)	0.50																																									
Width (m)	0.47																																									
Length (m)	0.50																																									
Figure 2.22 Wind tunnel layout (after Allen, 2010)																																										
Woolridge (1980)	Crushed rock – 7 mm (type - unknown) Fan circulating heated air from solar collector through rock-bed and back to collector in a closed loop (mass flow rate unknown)		Packed bed 500 mm thick Width and length of packed bed not given Concrete floor slab	No information on insulation of the packed bed was provided.																																						
Figure 2.23 Schematic of a low energy consumption home (after Woolridge, 1980)																																										

The optimisation of a vertical rock-bed TES system, connected to a two pass single cover solar air heater, was investigated by Choudhury *et al.* (1995). Operational and design parameters, such as, charging time, rock-bed size, cross-sectional area, rock size, air mass velocity and void fraction were investigated. The design of the vertical system is depicted in Table 2.11, as well as the design and operational variables that were changed, in order to obtain the best economical design of a rock-bed TES system for storing solar thermal energy. Choudhury *et al.* (1995) concluded that the optimum charging time for the design was 8 hours (8 a.m. to 4 p.m.). The minimum daily cost of energy stored per day was obtained for the values that are summarised in Table 2.11. However, higher bed temperatures were achieved for an air mass flux of less than $100 \text{ kg}\cdot\text{h}^{-1}\cdot\text{m}^{-2}$ and a cross-sectional area of less than 16 m^2 .

Singh *et al.* (2006) studied the pressure drop and heat transfer characteristics of a solar energy storage packed bed with large storage media of varying sizes. The experimental setup thereof is summarised in Table 2.11, where a vertical packed bed was used (Figure 2.15), whilst changing several operating parameters. A relationship was developed for the friction factor and the Nusselt number as a function of the void fraction, the sphericity and the Reynolds number, which agreed well with the experimental data obtained.

A study was conducted by Kürklü *et al.* (2003), where solar energy was stored in a horizontal underground rock-bed for greenhouse heating. Two identical polyethylene greenhouses were used for the experiments, one as a control and the other for the rock-bed experiment. In the rock-bed experiment greenhouse, two canals were excavated, filled with rocks and covered with soil, as shown in Figure 2.16. Kürklü *et al.* (2003) summarised the results of the rock-bed study as follows:

- (i) A temperature difference of $6^{\circ}\text{C} - 9^{\circ}\text{C}$ was observed for the inside and outside air,
- (ii) The system performed more effectively during the day, due to higher solar radiation and air temperatures,
- (iii) The energy collection efficiency of the system was 34%,
- (iv) On an overcast day, with no TES, the system maintained the inner air temperature at around 10°C the next night,
- (v) The rock-bed system showed that it could be used effectively to prevent frost in greenhouses,
- (vi) In frost prevention applications, the rock-bed system was more economical than normal heating systems used under the Turkish economic conditions,
- (vii) The head fan used (140 mm) was too large. Using a lower head fan with the same air flow capacity will make the system more economically attractive, and
- (viii) The measured data correlated well with the mathematical model and could be used as a reference case in comparable studies.

Another TES for a greenhouse was experimentally analysed by Bouhdjar *et al.* (1996). The selection of gravel was advantageous, due to its low cost, good heat capacity, inertness and availability. The storage system consisted of pipes, placed in a U-form (Figure 2.17) and buried below the surface, where an almost constant soil temperature was obtained in prior experiments.

The pipes were filled with gravel and air was forced through the system with a pressure-producing device at a specified mass flow rate. Bouhdjar *et al.* (1996) concluded that the heat provided by the storage system, resulted in a temperature difference of 7°C between the inside and the outside, which might be enough to protect the plants from the damaging cold temperature. The implementation of a uni-directional flow system had a negative influence on the system's performance, due to the rocks being heated at the outlet during the heat recovery process.

Phueakphum and Fuenkajorn (2010) constructed a TES system covered with a transparent acrylic sheet, as indicated in Figure 2.18. The pit was filled with four chain-link baskets, packed with predefined fragment-sized basalt of 0.1 m – 0.2 m. The nearby soil and an acrylic sheet cover served as insulation for the TES system. The pit was connected to a scaled-down model (1.5 m x 1.5 m x 1.5 m) via a hot air tube, at an angle of 30°. The angle and diameter of the hot-air tube was varied within a mathematical model. The results indicated that the efficiency of the TES system depended on the degree of energy input, the inclination and size of the hot-air tube and heat losses from the housing and the pit. The most appropriate system was a 10.2 cm hot air tube that was inclined at about 30° (Phueakphum and Fuenkajorn, 2010).

In an experimental study conducted by Srinivasan and Raghunandan (2013), an air stream, with a changing inlet temperature, was used to investigate the transient temperature response of a packed beds with a low aspect ratio at high Reynolds numbers. During the experiment, packed bed lengths of 0.2 m – 0.3 m, a void fraction of 0.385 – 0.440, inlet temperatures of 73.4°C – 212°C, an inlet velocity of 3.6 m.s⁻² – 12.7 m.s⁻² and steel spheres of 5 mm and 9.5 mm were used, as summarised in Table 2.11. It was concluded by Srinivasan and Raghunandan (2013) that the axial heat transfer rate along the packed bed was highly affected by the Reynolds number of the inlet flow and the packing size.

Zavattoni *et al.* (2011) conducted a CFD simulation of a pebble bed TES system, taking the effect of porosity variation into account. As a benchmark for the simulation, an experimental design was used, consisting of a concrete vessel in the shape of a truncated cone, which can be seen in Figure 2.20. The cone was buried beneath the soil and filled with homogeneous steatite rocks, with an average diameter of 0.03 m. The simulation results indicated that the effect of porosity variation allowed the CFD model to better represent the actual behaviour of the charging phase of the experimental TES system.

Zanganeh *et al.* (2015) studied the effect of design and operation parameters (Table 2.11) on the performance of thermocline in a TES system, by making use of a quasi-one-dimensional transient two-phase heat transfer model that had previously been confirmed. The TES system was based on a rock-bed, with the HTF being high-temperature air from process heat. Zanganeh *et al.* (2015) concluded that, by decreasing the rock diameter and the tank diameter-to-height ratios, the efficiency of the system decreased, while a larger pressure drop and pumping requirements were prominent. Zanganeh *et al.* (2015) found that an insulation thickness of 20 cm for the lid, and 16 cm for the lateral walls, was shown to be sufficient to ensure low thermal losses.

Allen (2010) conducted experimental tests in a packed bed section, using three different rock types, and these are depicted in Figure 2.22. Current models and equations were used to predict fluid temperature and pressure drops in the system during the charging and discharging phases. It was concluded the Ergun equation under-predicts the pressure drop at particle Reynolds numbers below 3500.

Woolridge (1980) presented the approach to design a low energy consumption house at CSIRO, Highett, and Victoria in Australia. One of the approaches that was used for the space heating requirements, was to use a storage bed of 0.5 m deep, which was filled with 7 mm crushed rock. A solar collector was placed onto the roof and a fan was used to circulate the heated air from the collector, to the packed bed and back to the collector, in a closed loop. Several perforated ducts of 100 mm in diameter were used to obtain an even heat distribution through the system. The thermal energy stored in the packed bed was transferred through the concrete surface, to heat the living space. Woolridge (1980) concluded that a reduction in the energy requirements was achieved, whilst maintaining thermal comfort.

Fuller (2003) summarised the construction of rock-beds in the 1970's 1980's in Western Australia in table format. Sizes for residential applications ranged from 4.3 m³ to 60 m³, varying in vertical and horizontal types, as well as bi-directional or uni-directional airflow. These are shown in Table 2.8. For commercial applications, the majority were used for greenhouse and experimental facilities, or by research organisations, where vertical designs with uni-directional flow were used (see Table 2.12).

Table 2.12 Rock-bed thermal storage systems used in commercial applications (after Fuller, 2003)

No	Location	Application	Date	Size (m ³)	Type	Status
C1	Highett, Melbourne	Offices Laboratory	1965	32.0	VB	system dismantled
C2	Griffith, NSW	Drying kiln	1969	15.5	VB	kiln dismantled
C3	Griffith, NSW	Greenhouse	1977	10.8	VU	greenhouse dismantled
C4	Griffith, NSW	Greenhouse	1979	40.0	VU	greenhouse dismantled
C5	Griffith, NSW	Greenhouse	1982	6.5	VB	greenhouse dismantled
C6	Mt Wilson, NSW	Greenhouse	1983	62.5	VU	unknown
C7	Kempsey, NSW	Greenhouse	1981	30.0	VU	not working
C8	Coffs Harbour, NSW	Greenhouse	1982	60.0	VU	unknown
C9	Pimpama, Qld	Greenhouse	1981	200.0	HU	unknown
C10	Tatura, Vic	Greenhouse	1984	40.0	VU	not working
C11	Tatura, Vic	Greenhouse	1984	40.0	VU	not working
C12	Mildura	Drying rack	1987	4.5	VU	rack dismantled
C13	Bumley, Vic	Greenhouse	1983	10.0	VU	working
4.1				HU	system dismantled	
3.1				VB	system dismantled	
C14	Canberra, ACT	Greenhouse	1986	25.0	VB	not working
C15	Laura, SA	Greenhouse	1986	11.0	VB	not working

C16	Bunbury, WA	Greenhouse	1983	24.0	VU	unknown
C17	Perth, WA	Office	1981	36.0	VB	not working

Sanderson and Cunningham (1995b) commented that storage tanks with square or rectangular cross-sections, as opposed to cylindrical ones, should be further investigated. Cylindrical cross-sections have undesirable effects, such as flow channelling and the radial dispersion of the temperature field.

Zanganeh *et al.* (2015) state that there are no general design rules for packed bed TES systems. Each unit must be optimised for: (i) its performance i.e. its efficiency and outflow temperature profile, and (ii) its costs i.e. thermal losses, pumping work, excavation and material costs, given the requirements of capacity, charging and discharging, mass flow rate and temperature.

2.4.10 Metrics for packed beds

Metrics are implemented as a performance management tool. The well-known saying: “If you can’t measure it, you can’t manage it” is an excellent description of why metrics is so important. Measurements need to be done correctly and verified, in order to manage the project effectively.

When applying the metrics to packed beds (see Figures 2.10, 2.11, 2.12 and 2.13), the following conclusions of the most important metrics affecting the performance of a packed bed can be drawn. These include porosity, pressure drop, mass flow rate and temperature.

There are four questions that require attention, with respect to the above metrics, namely: (i) What is measured? (ii) Why is it measured? (iii) With what is it measured? and (iv) How is it measured? These questions, together with the metrics applied to packed beds, will be discussed in the following sections.

2.4.10.1 Porosity

Porosity is dependent on the shape, packing and sorting of the storage material used in a packed bed, as discussed in Section 2.4.4, and it is one of the most important properties to take into account, when designing a packed bed. This is because it affects the pressure drop of the system, the mass flow rate and the energy input requirements, which are graphically represented in Figures 2.10, 2.11 and 2.12.

Porosity can be physically measured or calculated, depending on the geometry of particles used. In the case of asymmetrical-shaped materials, Allen (2010) measured the porosity of rocks by placing them in a cylindrically-shaped bucket of known diameter (220 mm high and 282.5 mm in diameter). The cylindrical bucket was filled to 220 mm, where the amount of water represents the volume of voids (V_v) and the cylindrical bucket the total volume (V_t). When applying Equation (2.3), the porosity of the rocks can be calculated. The liquid saturation method used by Allen (2010) was adopted from Löff and Hawley (1948). Allen (2010) commented that this measuring method has the drawback of causing packing disruptions at the edges, due to the flat surface of the bucket, which results in higher porosity values.

When using symmetrical-shaped rocks, such as spheres, the porosity can be calculated without using physical methods. Depending on the packing structure selected, as discussed in Section 2.4.4.2, the packing factor can be calculated according to Equation (2.4). The packing factor results can be applied to Equation (2.5), in order to obtain the porosity. Alternatively, Equation (2.3) can be used, which is very similar.

If a constant porosity is not attained during experimentation, the porosity needs to be recalculated, because of the significant affect that it has on the pressure drop, mass flow rate and energy input requirements. Once the porosity of the system is calculated, the mass flow rate of the system needs to be specified.

2.4.10.2 Fluid flow

The fluid flow in a packed bed can be classified as: (i) flow velocity, $\text{m}\cdot\text{s}^{-1}$, (ii) volumetric flow rate, $\text{m}^3\cdot\text{s}^{-1}$, or (iii) mass flow rate, $\text{kg}\cdot\text{s}^{-1}$. Conversion between the flow classifications can be done with a known fluid density and cross-sectional flow area.

Measuring airflow in an exhaust system is usually done by calculating the average air velocity at a certain point in the system, with a known cross-sectional area. The airflow is calculated as the product of the average velocity and area (Burgess *et al.*, 2004). Devices such as orifice and venturi meters, are also used in airflow measurements, but are rarely used in ventilation systems in the industrial sector (Burgess *et al.*, 2004)

Air flow can be measure by several devices, including: (i) a pitot-static tube, (ii) a Rotating Vane Anemometer (RVA), (iii) a deflecting vane anemometer (velometer), (iv) a Bridled Vane Anemometer (BVA), (v) heated-element anemometers, (vi) a vortex shedding anemometer, (vii) orifice meters, (viii) venturi meters (Burgess *et al.*, 2004), and (ix) a Laminar Flow Element (LFE). The information regarding the vane anemometers are provided in Table 2.13.

Table 2.13 Summary of airflow measuring devices

Rotating vane anemometers are commonly used in the mining industry, and have been proved useful in airflow measurements (Burgess <i>et al.</i> , 2004). The RVA uses a lightweight rotating vane, low-friction bearing to allow rotation at a speed relative to the velocity of the air stream. Velocity measurements are mostly conducted at supply registers, hood faces, exhaust grilles and mine roadways (Burgess <i>et al.</i> , 2004).



Figure 2.24 Rotating vane anemometers
(after Burgess *et al.*, 2004)

The bridled vane anemometer has a constrained wind-mill type impeller. The rotational angle of the impeller is proportional to the air velocity (Burgess *et al.*, 2004). The device is used for rough measurements of registers and HVAC grilles.

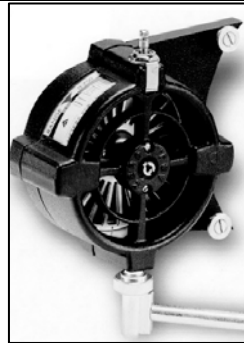


Figure 2.25 Bridled vane anemometer
(after Burgess *et al.*, 2004)

Singh *et al.* (2006) made use of an orifice meter, as well as a U-tube manometer that was inserted in the pipeline to measure the flow rate of air. The flow rate was adjusted, by inserting a control valve in the pipeline.

Kürklü *et al.* (2003) constructed a greenhouse, that was incorporated with a rock-bed TES system. A flow rate of $1\ 100^3\ \text{m}\cdot\text{h}^{-1}$ was used to force the heated air through the rock-bed, produced by a 140 mm head centrifugal fan and drawing 1.1 kW of power. A hot wire anemometer was used to measure the air flow rate in the system.

2.4.10.3 Pressure drop

Fluid pressure is measured as the force per-unit area exerted by a fluid, acting perpendicularly to a contact surface (Heeley, 2005). Fluid systems can be classified as static systems and dynamic systems. In a static system, the fluid is at rest, while in a dynamic system, the fluid is in motion (Heeley, 2005). The pressure in a static system only varies with vertical distance and the pressure in the horizontal plane stays constant, independent of the container shape.

Dynamic systems are more complex and are typically defined as static pressure, dynamic pressure, also known as velocity pressure, and total pressure. The sum of the static pressure and

the dynamic pressure forms the total pressure (Heeley, 2005). Dynamic pressure can be used to calculate the fluid velocity and flow rate in dynamic systems. It is not an easy task to measure the dynamic pressure in the system; hence, the static and total pressure is measured and the static pressure is subtracted from the total pressure to obtain the dynamic pressure. The total pressure measured is known as the stagnation pressure, which is the amount attained when a flowing fluid decelerates to a velocity of zero in an isentropic (frictionless) process (Heeley, 2005).

The pressure drop through a packed bed must be known, in order to estimate the capital and operating costs and to size the blowers or pumps required, to pressurise the fluid flow through the packed bed (Allen *et al.*, 2013).

The simplest and most widely-used model to predict pressure drop inside packed beds was developed by Ergun (1952). However, Allen *et al.* (2013) found that the Ergun equation over-predicts the pressure drop through structured, or randomly packed, beds of smooth spheres at an Ergun Reynolds number greater than ≈ 700 , and reports that previous work found an under-prediction of pressure drop of rock-beds, by a factor of 5. Allen *et al.* (2013) confirmed that the pressure drop during an experimental study of airflow through beds of rough spheres, smooth cylinders, cubes and crushed rock, differs from that of the Ergun equation.

Pressure measurement instruments range from basic liquid tube manometers, to bourdon-tube type gauges, to piezo-electric silicon-based transducers (Heeley, 2005). To ensure accuracy, when measuring dynamic system pressures, the location of the pressure tap must be selected, so that the fluid flow does not influence the measuring process (Heeley, 2005). The pressure tap holes must be situated perpendicularly to the flow, with no obstructions, to cause any disturbance and the tap holes and probes must be as smooth as possible.

Obstructions in a duct should be avoided at all costs, to ensure the flow field is not disturbed. In order to achieve higher accuracy of the measuring pressure in a dynamic system with a Pitot-static tube, Heeley (2005) suggests that there should be a minimum of 10 pipe or duct diameters downstream and two pipe or duct diameters upstream of any obstruction or change in flow path.

2.4.10.4 Temperature

Temperature is used as a measure of the “hotness“ or “coldness” of a material, and is generally not easily defined (Cengel *et al.*, 2002). In order to measure the physiological sensation that humans express qualitatively as: (i) freezing cold, (ii) cold, (iii) warm, (iv) hot, and (v) red-hot, temperature scales were introduced. Temperature scales provide a common basis for temperature measurements and are used in very basic transition states, such as freezing (ice point) and boiling points (steam point) of water (Cengel *et al.*, 2002). The most important temperature scales used today are: (i) the Celsius scale, °C, (ii) the Fahrenheit scale, °F, (iii) the Thermodynamic scale, K, (iv) the Rankine scale, R, and (v) the ideal-gas temperature scale.

Several techniques exist for the measurement of temperature, utilising methods such as: (i) thermoelectricity, (ii) temperature-dependent variations of the resistance of electrical

conductors, (iii) fluorescence, and (iv) spectral characteristics (Childs *et al.*, 2000). The various measurement techniques can be classified into three categories, depending on the nature of contact, that exists between the measuring device and the solid, liquid or gaseous medium of interest. These temperature measurement techniques include invasive, semi-invasive and non-invasive.

The measurement techniques comprise of different equipment. Childs *et al.* (2000) elaborate on the equipment used for temperature measurement, providing a description, the uses, advantages and disadvantages.

Selecting a method and the equipment that suits the particular application, the following need to be considered: (i) the temperature range, (ii) the likely maximum temperature, (iii) the heating rate, (iv) the response, (v) the accuracy, (vi) the stability, (vii) the sensitivity, (viii) the ruggedness, (ix) the service life, (x) the safety, (xi) the environment, and (xii) the contact methods (Childs *et al.*, 2000).

In the greenhouse experimental study conducted by Bouhdjar *et al.* (1996), thermo-hydrographs were used to record temperature and relative humidity, at a 1.5 m height from the ground, inside the greenhouse, and outside. The temperature was also measured at 5 m intervals in the rock-bed, using recorders from MECI Metering Solutions. Two pyrometers were used to obtain the global solar radiation, inside and outside the greenhouse. The ambient air temperature was measured at 0.6 m, 1.5 m, 2.1 m and the soil temperature at 0.3 m, 0.6 m, and 0.9 m.

During the experimental investigation conducted by Kürklü *et al.* (2003), T-type thermocouples were used to measure the inside, outside, rock-bed inlet and outlet temperature. The rock-bed temperatures were measured with K-type thermocouples in the centre of the bed, at bed lengths of 0.5 m, 1.0 m, 1.5 m, 2.0 m and 2.5 m (Kürklü *et al.*, 2003). The data (temperature, relative humidity, solar radiation and air velocity) that were measured, was recorded hourly by with a Delta T data logger for further analysis.

Phueakphum and Fuenkajorn (2010) used thermocouples to monitor the temperature of the following: (i) the rock at the centre of the pit, (ii) the air in the pit, (iii) the air at the end of the tube in the housing model, (iv) the air in the housing model, and (v) the surrounding air. A Digital Strain Meter, TC-31K, was used to measure the temperature every 30 minutes, at the respective points.

Marewo and Henwood (2006) measured the air temperature at various positions along the flow path, using an 8-bit data logger, manufactured by ACR Systems of Canada, which were connected to thermistors sensors, that measure the air temperature (thermistors). The results were used to monitor the performance of the cooling system. The experiment conducted by Marewo and Henwood (2006) recorded temperatures every 15 minutes.

In an experimental study conducted by Srinivasan and Raghunandan (2013), the thermal response of packed beds with low aspect ratios at a high Reynolds number and changing air flow temperature was studied. K-type thermocouples were used to measure the solid and gas

temperature throughout the packed bed. The thermocouple was comprised of a mineral insulated sheath (1.6 mm), together with a leak proof housing at one end. The conductor diameter was 0.23 mm and the accuracy of the thermocouples was more than $\pm 0.5^\circ\text{C}$, in the temperature range of 35°C - 200°C , for which it was calibrated.

The pebble bed TES system, investigated by Zavattoni *et al.* (2011), used six thermocouples, positioned along the height of the TES, as depicted in Figure 2.20 of Table 2.11. The probes provide continuous monitoring and recording during testing. K-type (Chromel-alumel) thermocouples were used with an operative range of -200°C to 1200°C and an uncertainty of 2.5°C , from 40°C to 333°C , as well as $\pm 0.75\%$ of the reading from 333°C to 1200°C . The system had a continuous charging time of 82.5 hours. The bed was at a thermal equilibrium with the surroundings before hot air entering the system was provided by an electric heater.

Singh *et al.* (2006) used T-type (copper-constantan) thermocouples to measure the air and solid temperature at several points along the bed, as displayed in Figure 2.26 (Singh *et al.*, 2006).

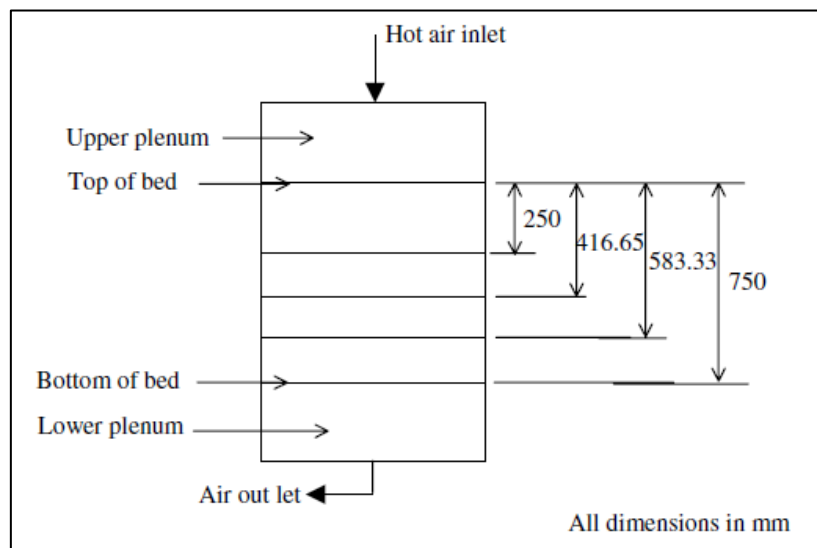


Figure 2.26 Thermocouples placement at different cross-sections in bed (after Singh *et al.*, 2006)

Childs *et al.* (2000) summarised the different temperature techniques and developed a guide to temperature measurement technique identification. It consists of the method, maximum and minimum temperature, response, transient capability, sensitivity, accuracy, high signal, stability/repeatability, low thermal disturbance, commercially available, as well as the relative cost.

When selecting a method of measuring temperature, consideration must be given to the following: (i) the accuracy, (ii) the sensitivity, (iii) the life, (iv) the size, (v) the cost, (vi) the manufacturing constraint, (vii) the dynamic response, (viii) the temperature of operation, and (ix) the robustness (Childs *et al.*, 2000).

The most important measuring parameters in a rock-bed system are the pressure, temperature and mass flow in the system. From these three measuring parameters, many other performance measurements can be obtained; for example, (i) the energy absorption and dissipation rate, which is related to the charging and discharging times, (ii) the energy storage characteristics of the system, (iii) energy requirements, and (iv) system efficiency. Bindra *et al.* (2014) state that the two major components which cause exergy destruction in packed bed TES systems are pressure drop and temperature dispersion, where exergy is the total amount of energy available to do work. Other methods to measure the performance of the packed bed are Computational Fluid Dynamics (CFD) and thermography, which will be discussed in the following sections.

2.4.10.5 Computational Fluid Dynamics

Technological advancements in the last decade, especially in the computational power of computers, allowed researchers to use numerical methods to simulate empirical methods. The utilisation of numerical methods reduces cost, time, and inherently allows research to be conducted more effectively and efficiently. The use of Computation Fluid Dynamics (CFD) software, as a design tool, allows researchers to extract much more data, when compared to empirical methods (Baker, 2011).

CFD is a branch of fluid dynamics, which provides a more cost-effective method to simulate real flows, by numerically solving governing equations (Sayma, 2009). The three fundamental principles that govern the physical characteristics of any fluid flow are: (i) the conservation of mass, (ii) the conservation of energy (First Law of Thermodynamics), and (iii) the conservation of momentum (Newton's second law) (Anderson and Wendt, 1995).

When conducting CFD analysis of packed beds, the Discrete Element Method (DEM) is commonly used, as a tool, to generate packed beds with spherical or non-spherical material (Louw *et al.*, 2012; Nel *et al.*, 2012). DEM is an explicit numerical model, which was introduced by (Cundall and Strack, 1979), to model the mechanical behaviour of the contact interface of the particles, and the particle-particle interaction.

Eppinger *et al.* (2011), Theron (2011) and Van der Merwe (2014) analysed the flow through cylindrical packed beds, with small cylinder to particle diameter ratios, using DEM-CFD of STAR-CCM+[®]. During the analysis, DEM was used to pack the columns and CFD to model the flow through the system. The results obtained from the numerical study, conducted by Theron (2011), correlated well with the empirical data that was used in the DEM study, as well as the empirical data obtained from literature for CFD. Theron (2011) concluded that the STAR-CCM+[®] software package is an acceptable, accurate and reliable tool, to simulate the flow through a packed column, with uncomplicated explicit methods.

Utilising CFD, as a numerical simulation tool in packed beds for TES systems, has gained a lot of interest in recent years. CFD and DEM have been used to study several aspects of packed beds, namely: (i) porosity variations (Zavattoni *et al.*, 2011), (ii) TES materials at elevated temperature (Andreozzi *et al.*, 2012; Zavattoni *et al.*, 2014), (iii) pressure drop predictions

(Louw *et al.*, 2012; Nel *et al.*, 2012), (iv) thermal conductivity (Zavattoni *et al.*, 2012), (v) DEM-CFD coupled modelling for rock particles (Louw, 2014) etc. The literature survey conducted by Louw (2014), concluded that CFD modelling of packed beds only considered spherical particles, and that there was not a definite method to model packed beds with rocks as a TES medium.

2.4.10.6 Thermography

Infrared Thermography (IRT) is a non-destructive technique to evaluate subsurface features, by detecting the temperature variation of the surface. The subsurface features include subsurface anomalies/defects and/or thermal properties (Pramod and Daniele, 2000).

The energy emitted by a surface is proportional to the surface temperature, as presented by the Stefan Boltzmann Law in Equation (2.8) (Borgnakke and Sonntag, 2009):

$$\dot{Q}_{emit} = e * \sigma * A * T_s^4 \quad (2.8)$$

where,

$$\begin{aligned} \dot{Q}_{emit} &= \text{rate of heat transfer by radiation [W]}, \\ e &= \text{emissivity [unitless]}, \\ \sigma &= \text{Stefan-Boltzmann constant [W.m}^{-2}.K^{-4}], \text{ and} \\ T_s &= \text{surface temperature [K]}. \end{aligned}$$

The actual amount that the infrared detector receives is dependent on the emissivity of the object (Meola and Carlomagno, 2004). The scale for emissivity varies between 0 and 1. Emissivity describes the ability of a specific material to emit infrared energy. It is the ratio of the thermal radiation from a surface to the radiation of an ideal black body (emissivity of 1).

When using IRT as an evaluation technique, Pramod and Daniele (2000) comments that care must be taken when neighbouring bodies have very low emissivity values, as it may act as a mirror and reflect energy from other bodies and disturb the actual reading. In order to prevent this, part of the surface may be covered with a high emissivity ($e = 0.9$) flat paint (Pramod and Daniele, 2000).

There are two main IRT methods, namely, active and passive. In active IRT, an external source of energy is required, to provide a temperature difference between the non-defective and defective material that is being studied (Ibarra-Castanedo *et al.*, 2009). There are four different techniques used in active IRT, including: (i) pulsed thermography, (ii) step-heating, (iii) lockin thermography, and (iv) vibrothermography, where each technique is applied to a different situation, depending on the requirements. Quantitative analysis becomes possible, when using active methods, as the properties of the external source are known (Pramod and Daniele, 2000).

Passive IRT requires a temperature difference (usually higher) between the object and the surroundings. When analysing a system, if a temperature difference of 1 to 2°C is found, compared to normal operating conditions, it leads to suspicion, whereas a temperature

difference of 4°C is strong proof of irregular performance (Pramod and Daniele, 2000). Passive IRT is seen as a qualitative method, because it is usually used to identify the irregularities of a system and is based on empirical rules practised by skilled professionals (Pramod and Daniele, 2000).

IRT can be applied in several sectors, including medicine, agriculture, environment, maintenance, non-destructive evaluation, thermofluid dynamics, etc. (Meola and Carlomagno, 2004).

2.5 Conclusions of the Literature Survey

The following section provides the conclusion of the literature survey, the contextualisation of the need, the utilisation of solar energy, and the main conclusions, with respect to the performance effect and metrics of packed beds.

2.5.1 Contextualisation of the need

Humans rely extensively on the conversion of energy, in order to survive and grow. The prevailing methods focus mainly on the conversion of non-renewable sources of energy, through minimising their use, minimising waste and through optimisation. The effects of current energy conversion practices on the equilibrium and sustainability of the earth have given rise to the need to re-investigate and explore alternative energy solutions. Past practices tended to focus on more efficient ways of energy conversion, and the future requires the exploration of the more effective and efficient utilisation of all different available energy sources, in particular, renewable sources.

The Earth Energy Balance indicates a total solar irradiance (solar constant) value of 1367 W.m⁻² (Badescu, 2014), confirming that it as a renewable source, with adequate potential to warrant research. Global horizontal irradiance received in central South Africa provides a potential source of energy with an annual average value of 2000 kWh.m⁻² to 2100 kWh.m⁻² (Vaisala, 2015).

The current electrical load profile in South Africa peaks in the early evening, due to residential loads. The removal of the amount of space heating during this peak period will lower the peak demand. It is necessary for this so called reduced or “clipped” amount of energy from another non-electrical alternative to be sourced. If such a source is renewable, and it can be effectively harnessed, stored, and utilised to provide a load shifting effect, the benefits will include:

- (i) sustained human comfort,
- (ii) economic benefits to the household, and
- (iii) substantial economic benefits to the electrical supplier and the country, within the framework of long-term sustainability.

The sections below will summarise the conclusions that have been drawn from the literature survey.

2.5.2 Solar energy utilisation

- (i) Adequate energy potential in solar radiation is available.
- (ii) The available energy should be harvested, stored and utilised.
- (iii) Appropriate passive harvesting methods are solar thermal collectors in the form of pitched roofs and Trombe-like walls.
- (iv) This study focuses on the Thermal Energy Storage (TES) aspects of the incoming energy contained in air, which is referred to as Heat Transfer Fluid (HTF).
- (v) The most important two characteristics of TES are the amount of energy stored per unit volume (volumetric energy capacity) and the storage duration.
- (vi) Sensible Thermal Energy Storage (STES) systems are typically more cost-effective and simpler, when compared to Thermochemical Energy Storage (TCES) and Latent Thermal Energy Storage (LTES).
- (vii) STES that makes use of water or solid materials as storage media, are well-established, reliable, clearly understood and widely used.
- (viii) The construction and operational cost of the rock-bed system is less than that of the water system and the rock-bed can be used at an elevated temperature ($>100^{\circ}\text{C}$).
- (ix) The implementation of active or passive STES systems in residential buildings may result in the enhancement of energy efficiency, by 30-35%, and thermal efficiency, by 40-60%.

2.5.3 Packed beds

- (i) Packed beds are the most appropriate technology for air-based solar systems.
- (ii) The packing material most often used in packed beds are rocks and pebbles.
- (iii) A rock-bed solar heating system does not normally function at a constant temperature. During the daytime, dependent conditions, such as solar radiation, ambient temperature, collector inlet temperature and load requirements, result in a variation of collector outlet temperature.
- (iv) Cylindrical cross-sections have undesirable effects, such as flow channelling and the radial dispersion of the temperature field.
- (v) The horizontal uni-directional packed bed (as constructed by the CSIRO) discharge energy throughout a space, through radiation and natural convection, instead of utilising forced convection, as with standard vertical/horizontal packed beds.
- (vi) There is currently insufficient research on horizontal packed beds for residential use.
- (vii) No well-structured design rules are available for the design of packed bed TES systems. Each unit must be optimised for: (i) its performance i.e. its efficiency and outflow temperature profile, and (ii) its costs i.e. thermal losses, pumping work, excavation and material costs, given the requirements of capacity, charging and discharging, mass flow rate and temperature.

2.5.4 Performance effects of packed beds

The design-related properties that have the greatest influence on the performance of a packed bed are:

- (i) the porosity,
- (ii) the permeability, and
- (iii) the heat transfer.

2.5.4.1 Porosity

The influence of particle shape on porosity can be summarised as follows:

- (i) Well-rounded particles have a larger porosity than angular particles,
- (ii) An increase in roundness results in a larger porosity and mass flow rate, and a reduced pressure drop and energy requirement. A decrease in roundness has the opposite effect, and
- (iii) An decrease in roundness results in a larger surface area (at a constant volume), which provides better heat transfer and increased system performance. However, the larger surface area has more resistance to flow, and induces larger pressure drops and energy requirements, with a reduction in the mass flow rate. An increase in roundness has the opposite effect.

The influence of packing on porosity can be summarised as follows:

- (i) The more closely packed the particles are, the lower the porosity,
- (ii) A lower porosity has a larger pressure drop, lower mass flow rates and more energy is required. The opposite is true for lower packing (higher porosity),
- (iii) Apparent friction factors of up to 60% more can be obtained when crushed rock (13.5 mm and 26.5 mm) is packed in a co-current direction, relative to the air flow, compared to a cross-flow packing direction, and
- (iv) The minimum ε value of 0.2595 is achieved with a FCC packing arrangement of spherical particles.

The influence of sorting on porosity can be summarised as follows:

- (i) The more sorted the particles are, the higher the porosity,
- (ii) Well-sorted particles have the same size and poorly-sorted particles have different sizes, and
- (iii) Well-sorted particles have a larger porosity, which promotes flow channelling, reduces pressure drop and energy requirements, and increases mass flow rate. The opposite is true for poorly-sorted particles.

2.5.4.2 Permeability

The influence of size on permeability can be summarised as follows:

- (i) Porosity is the same for sorted particles, but not for unsorted particles,
- (ii) The size of the rock particles does not change the porosity,
- (iii) A decrease in particle size covers a larger surface area and has a lower permeability. An increase in surface area increases the heat transfer between fluid and solid, as well as system performance. It also increases the resistance to flow, which increases the pressure drop and energy requirements, and reduces the mass flow rate. The opposite is true for a larger particle size, and
- (iv) A decrease in particle size leads to a lower permeability, which reduces flow channelling and mass flow rate, but increases pressure drop and energy requirements. The opposite is true for a larger particle size.

Conclusion of performance effects of porosity and permeability can be summarised as follows:

- (i) A higher operating efficiency will be obtained for rock-beds that make use of the smallest practical spheres, the longest practical packing lengths and the smallest practical packing dimensions (smallest porosity) normal to the direction of flow,
- (ii) Decreasing the ε of a rock-bed results in an increase of the system's thermal capacity, which prolongs the charging and discharging time,
- (iii) A maximum overall efficiency (outflow energy to input energy and pumping energy for charging and discharging) was found for the smallest particle size,
- (iv) The particle size used in packed beds should be larger than 13 mm, in order to prevent large pressure losses and high energy requirements, and
- (v) Designers should strive to work with the smallest practical spheres.

2.5.4.3 Heat transfer

Summary of the factors that influence heat transfer can be summarised as follows:

- (i) The higher the density of the material, the better are its heat transfer abilities,
- (ii) Storage material with a high specific heat capacity, as well as the capacity to release thermal energy at an adequate rate for the specific application, is essential for a packed bed design,
- (iii) For TES applications, the product of specific heat capacity and density should ideally be greater than $1 \text{ MJ}\cdot\text{m}^{-3}\cdot\text{K}^{-1}$,
- (iv) The thermal conductivity of the storage material only has a small influence, but the volumetric heat capacity is the most important, and
- (v) Implementing rocks as a TES medium offers the following benefits: (i) they are not expensive, (ii) they are not toxic, nor flammable, and (iii) they act both as a storage medium and a heat transfer surface. Other advantages include: (i) the storage media are plentiful and economical, (ii) there is direct heat transfer between the HTF and storage media, (iii) it is applied in a wide temperature range, with the temperature

limited by the melting point of the rocks, (iv) there are no safety concerns, (v) there is no degradation or chemical instability, and (vi) it eradicates harmful and/or corrosive materials.

2.5.5 Performance metrics

- (i) For porosity, the liquid saturation method will be used, due to the asymmetrical-shape of the porous media,
- (ii) Pressure drop will not be considered, due to the low flow rates to be used,
- (iii) Mass flow rate will be measured with a vane probe thermo-anemometer,
- (iv) Temperature will be measured with grounded thermocouple temperature probes,
- (v) Computational Fluid Dynamics, using STAR-CCM+[®] software, will be used as a modelling tool, to reduce repetitive empirical investigation time and costs, and
- (vi) Infrared Thermography (IRT), using a FLIR[®] E63, will be used as a non-destructive technique, to evaluate subsurface features by detecting the temperature variation of the surface on a continuous time cycle, in order to track the temperature wave-front.

3. METHODOLOGY

The need for research into horizontal packed beds, as a means of storing thermal energy for residential space heating, is prevalent. In order to investigate the effect of temperature and mass flow rate in a horizontal packed bed, a research method had to be compiled. A roadmap of the methodology process was developed, as shown in Figure 3.1.

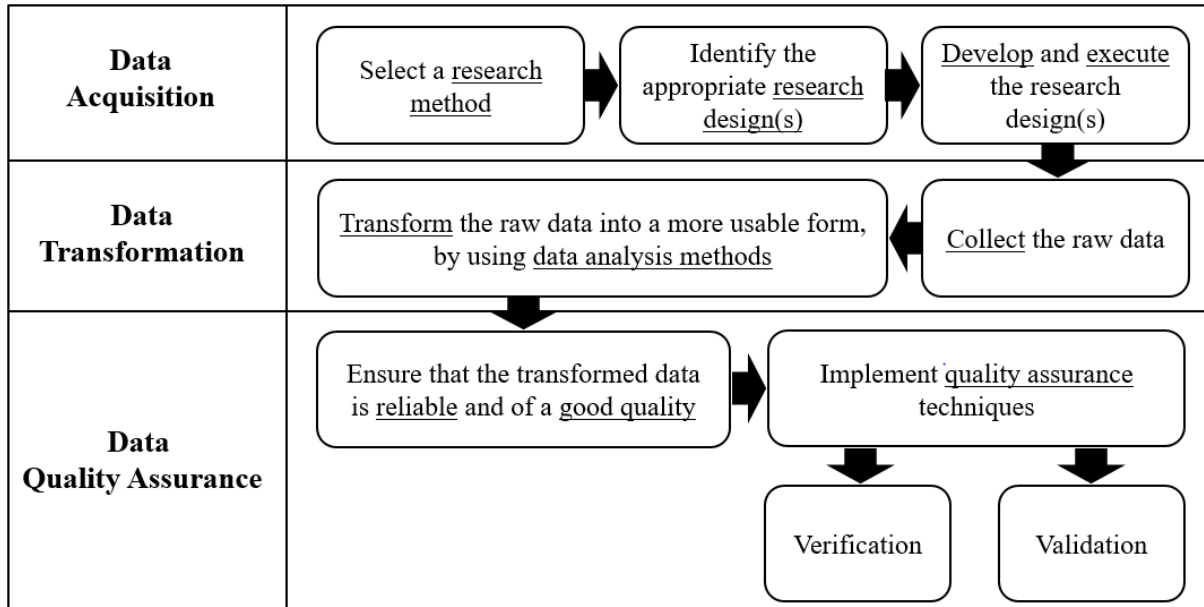


Figure 3.1 Roadmap of the methodology process

The following sections provide the research methods and designs that were used in the study, how they were executed, how the data were analysed and how the quality was ensured.

3.1 Research Methods

A quantitative analysis provides the opportunity to examine the relationship between two or more variables and the influence and patterns thereof (Europe, 2009). The research method involved collecting numerical data from the selected research designs, transforming it into usable statistics and forming conclusions; hence, a quantitative method was selected.

3.2 Research Designs

An empirical and a numerical research design were selected for the study. The empirical research design consisted of an experimental setup, where data were measured, captured and analysed. The numerical research design made use of the commercial software package STAR-CCM+[®], to simulate the results that were obtained from the empirical design. The respective data sets were then compared and analysed.

The literature survey indicated that, until recently, there have been very few CFD analyses of packed beds. It is being used more frequently, due to the technological advancements and the

increase in computational power. No detailed research designs were obtained for uni-directional horizontal packed beds.

The research designs that were selected for the study focussed on the major parameters affecting the performance in packed beds, which were identified in the Literature Survey. These performance effects included the porosity, the permeability and the heat transfer. The pressure drop over the packed bed was not considered, due to the low mass flow rates that were used in the study. The thermal conductivity and the heat transfer coefficient of the storage material were also not measured.

3.3 Empirical Design

The following sections describe the proposed design and construction of an experimental research unit for a horizontal, uni-directional packed bed. The major performance effects are also discussed: what measuring equipment was used to measure them, why it was necessary and how it was measured.

3.3.1 Proposed design

The proposed experimental design was developed with SolidWorks® 2014 Student Edition, as shown in Figures 3.2 and 3.3. The schematic design of each component is provided in Appendix B.

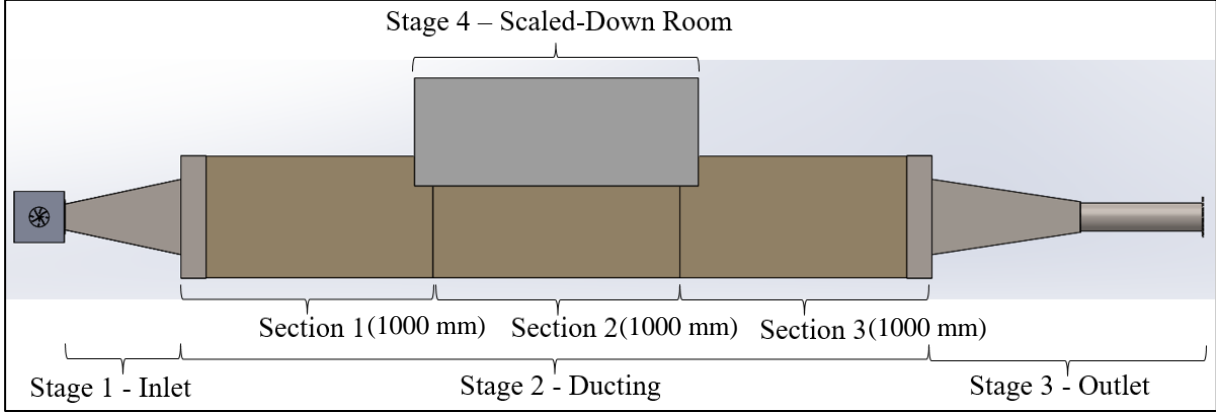


Figure 3.2 Proposed experimental design of a horizontal, uni-directional packed bed

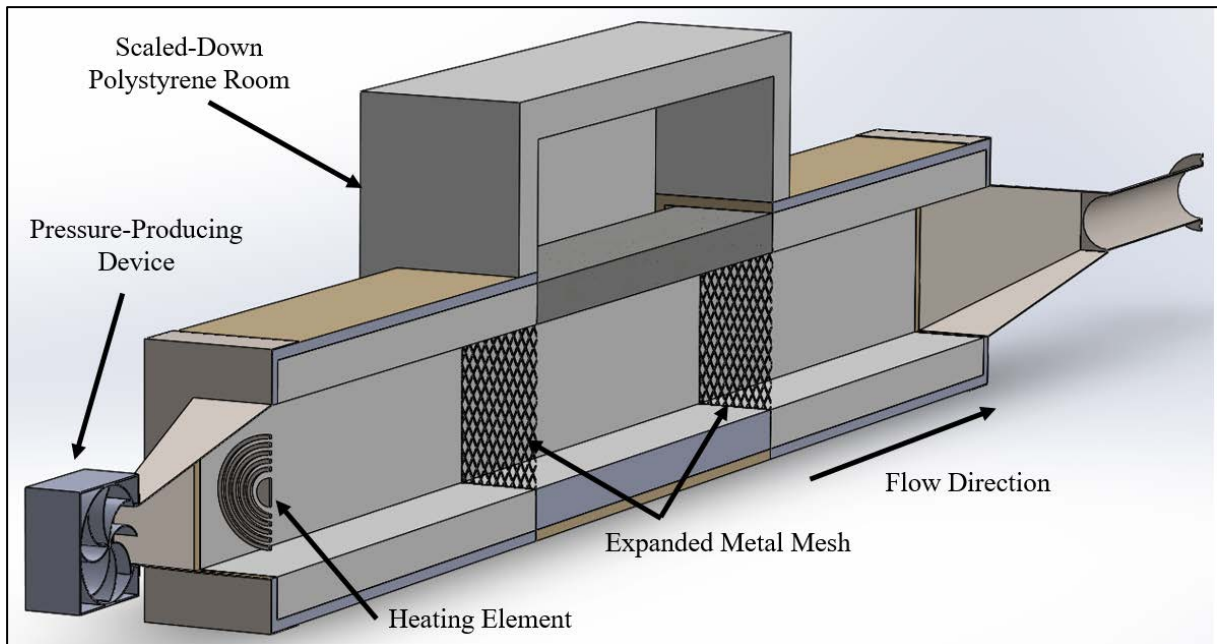


Figure 3.3 Section view of the proposed experimental design

The system is divided into four stages, namely: (i) Stage 1 – the inlet, (ii) Stage 2 – the ducting, (iii) Stage 3 – the outlet, and (iv) Stage 4 – the scaled-down room. A pressure-producing device (PPD), in the form of a fan, is connected to a controller. It is then attached to the inlet of Stage 1, to create the required mass flow rate through the system. A heating element, also connected to a controller, is inserted at the end of Stage 1, to provide a set temperature for the packed bed, as shown in Figure 3.3. The heated air flows from Stage 1 into Stage 2.

Stage 2 is made up of three duct sections. Section 2 is filled with rocks, to form the rock-bed TES system. Sections 1 and 3 is ‘free space’, which allows the air to stabilise, before and after the rock-bed. The heated air flows from Stage 1, through Stage 2, and out of Stage 3, which initiates the charging phase.

During the charging phase, thermal energy is transferred from the air to the rocks, as well as to the concrete slab, which represents a typical floor in a room. Further energy transfer occurs via conduction through the concrete slab, which radiates energy into Stage 4, and results in a temperature increase of the scaled-down room.

The design of Stage 1 is shown in Figures 3.4 and 3.5, where ambient air is drawn through the PPD and heated to a predetermined temperature, before flowing through the packed bed.

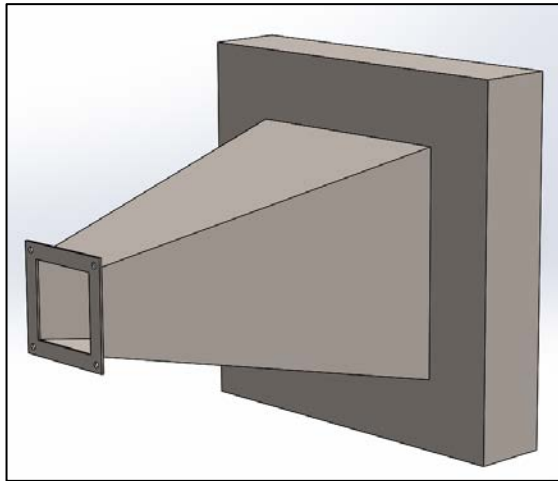


Figure 3.4 Inlet duct design View 1

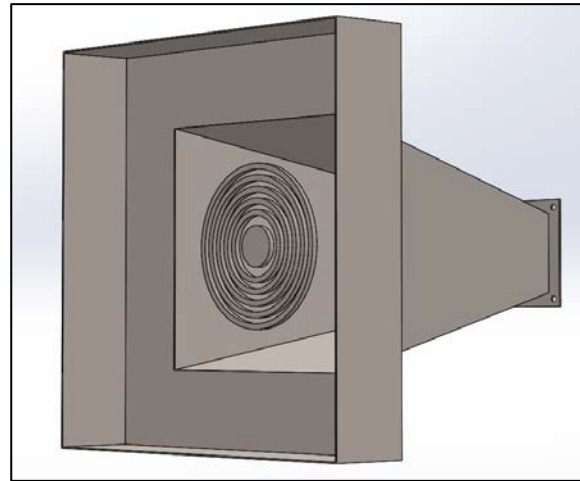


Figure 3.5 Inlet duct design View 2

The PPD is connected to a square 100 mm x 100 mm steel inlet, with a 40 mm flange width. The square inlet expands to a 300 mm x 300 mm square section, to form the inlet duct. The expansion angle selected is based on guidance from the staff at Meriam®, in order to minimise friction and turbulence through the duct. At the end of the 300 mm x 300 mm duct, a flange is added, to increase the size to 490 mm x 490 mm. The flange has an overlap of 100 mm, to firmly fit over Stage 2. At the end of the duct, just before the start of Stage 2, the heating element is inserted, as shown in Figures 3.3 and 3.5. The heating element is connected to a controller, to set the inlet temperature of the packed bed.

Stage 2 consists of three 1000 mm long square channels, each with an inner diameter of 300 mm x 300 mm, which is fairly similar to the diameter that was used in the experimental design of Allen (2010). Insulation on the channel walls is very important, as Allen (2010) noted a significant heat loss through the tunnel walls. To prevent thermal losses to the environment, the channel is constructed from 75 mm high-density polystyrene, with the properties that can be found in Table 3.1:

Table 3.1 Physical properties of polystyrene, that was used as insulation for the packed bed design (after ISOVER, 2015)

Property	Value
Density (kg.m ⁻³) – tolerance ± 10%	30
Thermal conductivity at 10°C (W.m ⁻¹ .K ⁻¹) (mean temperature)	0.033
Compressive strength (kPa) - @ 10% deformation	200
Tensile strength (kPa)	440
Water absorption % volume+	0.5 – 1.5
Temperature limits	-110°C to 70°C

The polystyrene duct is enclosed with 20 mm plywood, to form a strong structure. To ensure good contact between the polystyrene sections, a resin is used to stick them together. The design of Section 1 and Section 3 of Stage 2, is depicted in Figures 3.6 and 3.7.

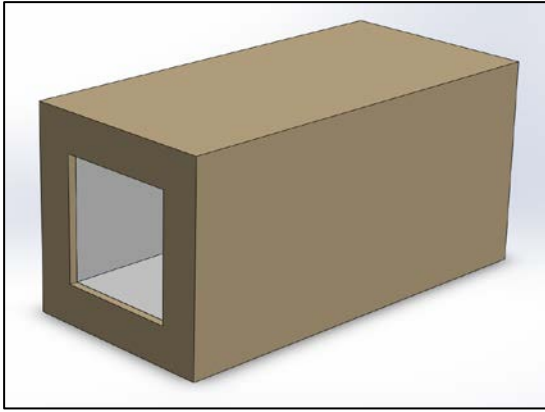


Figure 3.6 Stage 2 duct Section 1 front

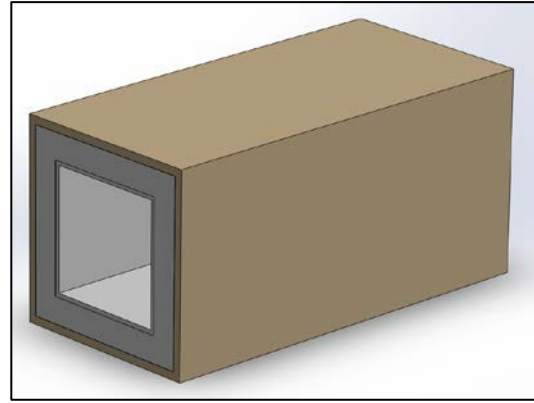


Figure 3.7 Stage 2 duct Section 1 rear

The construction of Section 3, is similar to that of Sections 1 and 3 of Stage 2; however, the top portion of polystyrene and plywood is replaced with a 75 mm concrete slab. This represents the floor in a residential building, as shown in Figure 3.8.

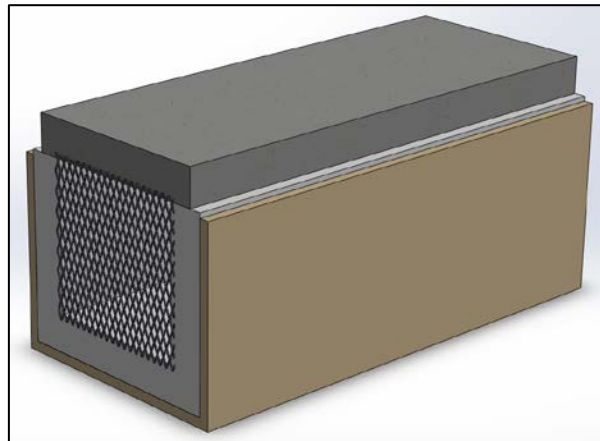


Figure 3.8 Stage 2 rock-bed section with a 75 mm thick concrete slab

The rock-bed section of 1000 mm x 300 mm x 300 mm, is filled with 19 mm crushed dolerite rock. Although spherical shaped concrete particles would be more appropriate, the manufacturing costs outweigh the performance. In order to retain the 19 mm crushed rock, expanded metal mesh of 320 mm x 320 mm is inserted on both sides of the packed bed section.

The outlet duct (Stage 3) is constructed in a similar manner to that of the inlet duct. The 300 mm x 300 mm square section is reduced to a 120 mm x 120 mm square section, which is connected to a pipe of 110 mm in diameter and 500 mm in length. The outlet duct design is depicted in Figures 3.9 and 3.10.

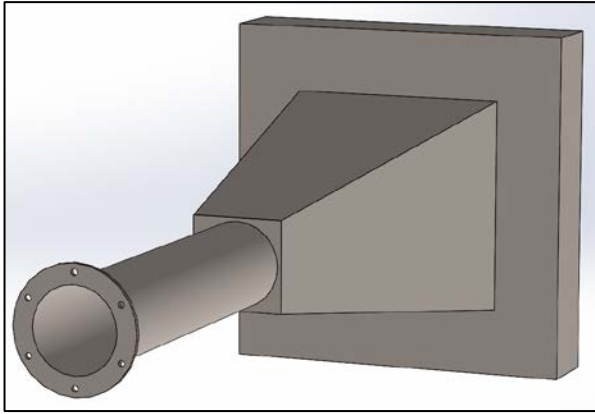


Figure 3.9 Stage 3 outlet duct front view

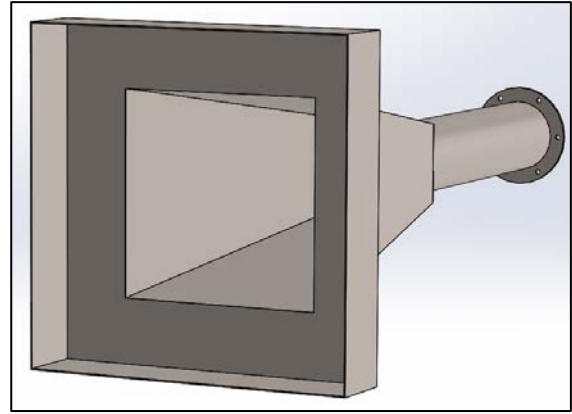


Figure 3.10 Stage 3 outlet duct rear view

Between each of the three stages, as well as the three sections in Stage 2, weather strips are pasted between the sections, to aid as a sealant. Toggle locks are attached to each connecting section and fastened securely, in order to seal the system. This enables the system to be dismantled and inspected separately, for any anomalies.

In order to investigate the effect of the heated concrete slab on the space temperature, a standard room, with a floor area of 40 m^2 ($4 \text{ m} \times 10 \text{ m}$), a wall height of 2.4 m and a volume of 96 m^3 , is scaled-down. The result is a concrete surface area size of 0.4 m^2 ($0.4 \text{ m} \times 1 \text{ m}$), with a wall height of 0.24 m and a volume of 0.096 m^3 . A polystyrene structure is constructed to act as the scaled-down room, as shown in Figures 3.11 and 3.12.

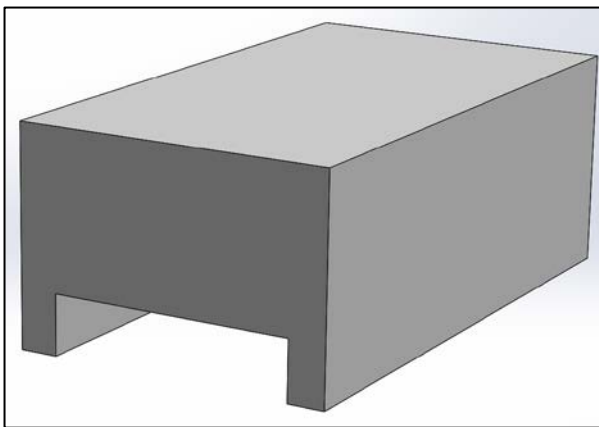


Figure 3.11 Stage 4 room

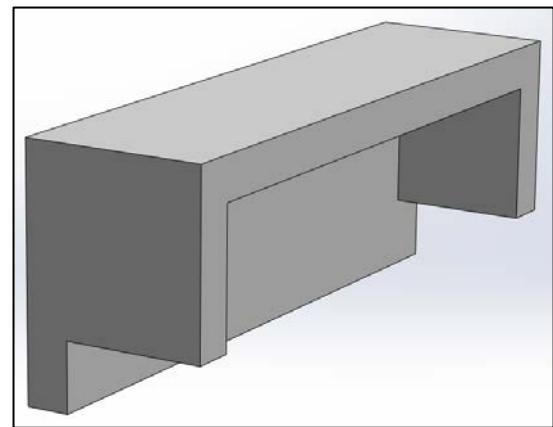


Figure 3.12 Stage 4 room section view

Temperature probes are inserted throughout the test rig, as well as outside the system, to provide the required temperature data. The proposed placement of the temperature probes are provided in Figure 3.13.

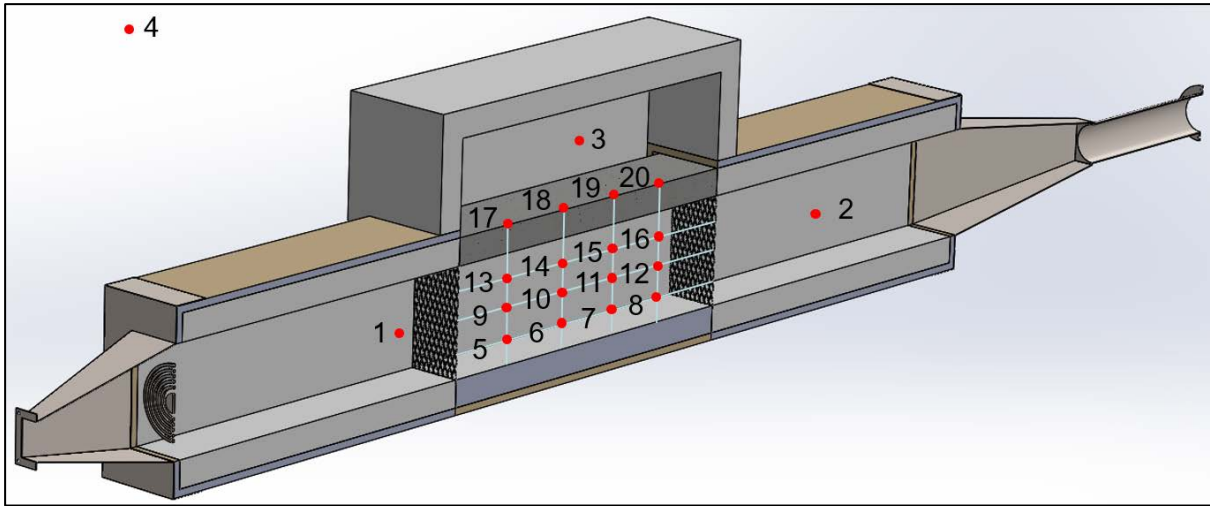


Figure 3.13 Temperature probes proposed placement

The probes are placed on the same vertical plane throughout the duct, but at different horizontal levels. Probes 1 and 2 provides the inlet and outlet temperature of the packed bed. Probe 3 is placed 120 mm above the concrete surface, which represents the increase in the ambient temperature of a standard room. Probe 4 is used as the reference temperature for the room environment. Probes 5 – 16 are evenly spaced throughout the packed bed, to get an accurate representation of how the temperature wave-front progresses through the packed bed. Probes 17 – 20 are placed onto the concrete surface, to get an indication of the thermal energy transfer through the concrete slab. The measured temperature and mass flow rates, provides sufficient data, to analyse the STES for a horizontal uni-directional packed bed. With the proposed design complete, the construction phase could commence.

3.3.2 Construction

The construction phase was completed, according to the proposed design in Section 3.3.1. The required amount and sizes of polystyrene and plywood sections, were calculated, based on the drawings of the proposed design. In order to form the 300 mm x 300 mm duct, the polystyrene sections were stuck together with a resin and left for 24 hours. The plywood sections were placed around the polystyrene duct and fastened with 2.5 mm wood screws, to form a strong structure, as shown in Figures 3.14 and 3.15.



Figure 3.14 Construction of Section 1 and 3

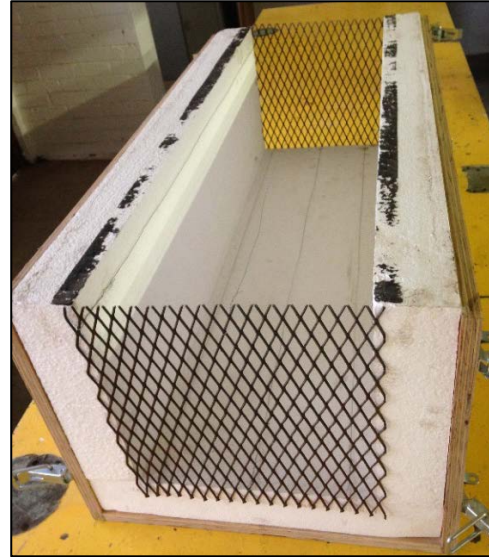


Figure 3.15 Construction of Section 2

Toggle locks were inserted at the connecting sections, as shown in Figure 3.16, in order to form the final unit. Holes were drilled at the positions displayed in the proposed design (see Appendix B), in order to insert the temperature probes for thermal logging, as shown in Figure 3.16.



Figure 3.16 The placement of toggle locks and temperature probes

An expanded metal mesh of 33 mm x 14 mm x 2 mm was selected and cut to a size of 320 mm to 320 mm. The expanded metal was fastened to the ends of Section 2 of Stage 2, to prevent the crushed rock from falling out, as shown in Figure 3.15. The following process was used, in order to fill the packed bed with rocks:

- (i) Markings were made on the sides of Section 2 of Stage 2, at 75 mm, 150 mm and 225 mm from the base.
- (ii) The rocks were poured into the centre of the container and spread out, until a layer was formed, that was level with the 75 mm mark.
- (iii) The first layer of probes was inserted.
- (iv) Step (ii) was repeated, levelling the rocks at the 150 mm mark.
- (v) The second layer of probes was inserted.
- (vi) Step (ii) was repeated, levelling the rocks at the 225 mm mark.
- (vii) The final layer of probes was inserted.
- (viii) Step (ii) was repeated again for a final time, to level the rocks at the 300 mm mark,
- (ix) The concrete surface was placed on top of the rocks.
- (x) A small channel was carved into the concrete surface, to enhance the contact area of the probe onto the concrete surface.
- (xi) The temperature probes were placed into the carved channel and a wood section was fastened onto the concrete surface, to keep the probes in place.
- (xii) Finally, the system was analysed for fenestration before testing.

The rock levelling and the temperature probe placement in the rock-bed and on the concrete surface, is shown in Figures 3.17 and 3.18.



Figure 3.17 Rock levelling and probe placement

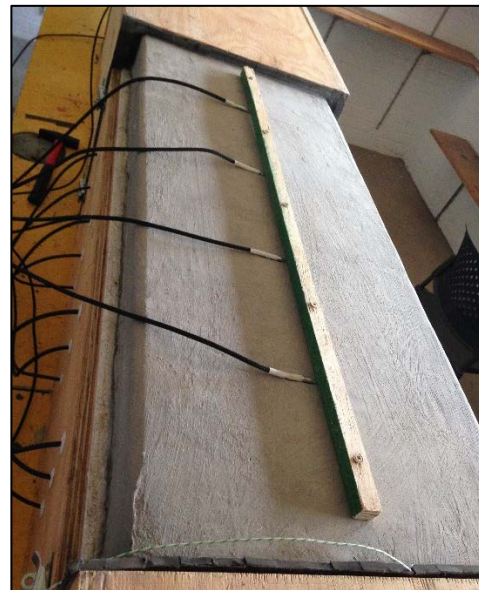


Figure 3.18 Probe placement onto concrete surface

A total mass of 140.924 kg rock was used to fill the channel. The concrete slab was professionally fabricated with 30 MPa cement and 19 mm dolerite stone, the mixture consisting of the following proportions: (i) cement - 16%, (ii) river sand - 36%, (iii) stone - 46%, and (iv) Sika[®] ViscoCrete[®]-20HE plasticiser. Weather strips were placed at each connecting section, to aid in the insulation and air tightness of the structure, as shown in Figure 3.19. The heating element was placed in the inlet duct, just before Stage 2, as shown in Figure 3.20.



Figure 3.19 Weather strips at connecting sections



Figure 3.20 Heating element between Stages 1 and 2

The expanded metal inlet and outlet sections were locally fabricated, based on the design of Appendix B. Silicone was pasted onto all of the connecting pieces, stuck together, and left to dry. The blower was attached to the inlet, as shown in Figure 3.21, and the final assembly of the horizontal uni-directional packed bed is shown in Figure 3.22.



Figure 3.21 Blower attached to the inlet



Figure 3.22 Horizontal uni-directional packed bed experimental setup

3.3.3 Performance metrics

The following chapter contains the main performance metrics for a packed bed, as summarised in Section 2.5.5. The methods and instruments that were used during the empirical study are also discussed. Some of the performance metrics were varied for the empirical design and some were kept constant, in order to reduce the number of variables to be analysed. The data, which were varied during the testing process, were the temperature and mass flow rate. They were selected because they had the greatest influence on the charging and discharging time, as well as the temperature wave-front and energy requirements of the packed bed. The variables that were kept constant throughout the study were the porosity, the permeability and the rock properties.

3.3.3.1 Porosity

The crushed rock particles that were used for testing were asymmetrically-shaped; hence, physical methods were required to measure the porosity. The liquid saturation method was selected. The rocks were placed into a rectangular container, with inner dimensions of 300 mm x 300 mm and 1000 mm in length. This was the exact size of the packed bed system that was used during the empirical method. The rocks were poured into the container in a cross-flow direction, and relative to the air flow, to reduce the friction factor, as suggested by Allen *et al.* (2013). The packing method was conducted as follows:

- (i) Markings were made on the side of the container at 75 mm, 150 mm, 225 mm and 300 mm, from the base of the container.
- (ii) The rocks were poured into the centre of the container and spread out until a layer was formed at the 75 mm mark.
- (iii) Step (ii) was repeated, levelling the rocks at 150 mm.
- (iv) Step (ii) was repeated, levelling the rocks at 225 mm.
- (v) Step (ii) was repeated for a final time, to level the rocks at 300 mm.

Once the container was filled with rocks, water was added, until the rocks were completely submerged, as shown in Figure 3.23.



Figure 3.23 Implementing the liquid saturation method to calculate porosity

The volume of water that was added represented the volume of voids (V_v). As the total volume of the container was known, Equation (2.3) was applied, to calculate the porosity of the packed bed. The physical method that was used to calculate the porosity was conducted three times, to ensure a good average, with the rocks being dried completely before starting each test.

The packing method that was described, to determine the porosity of the packed bed, was similar to the method that was used when filling up the packed bed in the experimental test section. The porosity within the packed bed remained constant throughout the testing process; hence, it was not necessary to recalculate the porosity for every empirical test.

3.3.3.2 Permeability

The permeability is directly related to the size of the storage medium used. Crushed dolerite rock of 19 mm was obtained for testing. The specific size was selected, as it was necessary to have a particle size that was as small as possible. However, Sanderson and Cunningham (1995a) comment that the particle size used in packed beds should be larger than 13 mm, in order to prevent large pressure losses and energy requirements.

3.3.3.3 Rock properties

The properties that affect heat transfer in a packed bed include: (i) the density, (ii) the specific heat capacity, (iii) the thermal conductivity, and (iv) the heat transfer coefficient. Dolerite rock was selected, as it is readily available, it is a natural material, it is used in the residential construction industry, and it is relatively cheap, compared to metal storage media. The thermal conductivity and heat transfer coefficient were not measured for this study, but the density and specific heat capacity were calculated for the 19 mm dolerite rock.

The density of the particles was calculated, using the rocks, a one litre container, water and an electronic scale. The mass of the crushed rock was measured before the water was added, as shown in Figures 3.24 and 3.25.



Figure 3.24 Measuring the mass of rocks in the container



Figure 3.25 Measuring the total mass of rocks and water

Once the mass of the sample size was known, the volume of the crushed rock was calculated, by subtracting the volume of water that was added, to the total volume of the container. As density is defined as the mass per unit volume, the specific density of the dolerite rock was calculated.

The specific heat capacity was calculated, based on the method used by Allen (2010). The container was fabricated from 75 mm high-density polystyrene, in order to reduce the thermal losses to the environment as much as possible. A small hole was made in the lid of the polystyrene container, to measure the temperature in the centre of rocks, as shown in Figure 3.26. The rocks were poured into the container, whilst keeping the temperature probe in the middle.

The temperature of the rocks was measured, which was assumed to be at the current room temperature, before hot water of approximately 60°C was poured into the container. Bricks were placed on top of it, to reduce the thermal losses at the lid, as shown in Figure 3.27. The temperature was constantly monitored until equilibrium was reached.



Figure 3.26 Measuring the mass of the rocks



Figure 3.27 Measuring specific heat capacity of the rocks

Assuming that there were no thermal losses to the environment, the amount of energy gained by the rock was equal to the amount of energy released by the water; hence, Equation (2.2) was converted to Equation (3.1):

$$m_r c_r \Delta T_r = m_w c_w \Delta T_w \quad (3.1)$$

where,

- $c_r = \text{specific heat capacity of rock [kJ.kg}^{-1}.\text{K}^{-1}\text{]},$
- $c_w = \text{specific heat capacity of water [kJ.kg}^{-1}.\text{K}^{-1}\text{]},$
- $m_w = \text{mass of the water [kg]},$
- $m_r = \text{mass of the rock [kg]},$
- $\Delta T_r = \text{temperature difference of rock [K]}, \text{ and}$
- $\Delta T_w = \text{temperature difference of water [K]}.$

All of the temperatures were known, the mass of the water and stones were weighed and the specific heat capacity of water was also known; hence, the specific heat capacity of the dolerite rock could be calculated. The methods used to calculate the density and the specific heat capacity were conducted three times, to obtain a good average. Thermal images were taken, in order to study thermal losses to the environment. Figures 3.28 and 3.29 show the photograph and thermograph of the hot water and rocks.



Figure 3.28 Photograph of hot water and rocks

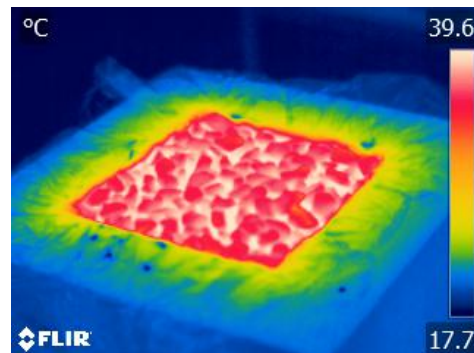


Figure 3.29 Thermograph of hot water and rocks

The polystyrene cover was placed onto the polystyrene container, in order to calculate the specific heat capacity, as shown in Figures 3.30 and 3.31.



Figure 3.30 Photograph of polystyrene container

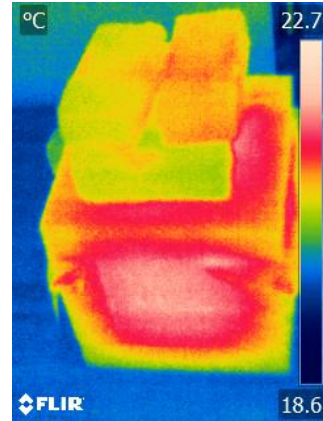


Figure 3.31 Thermograph of container

Figure 3.31 shows the thermal patterns on the container, with a maximum temperature of 22.7°C and ambient conditions at 18.6°C.

3.3.3.4 Flow rate

To charge the packed bed with thermal energy, a pressure-producing device was required, to provide flow through the system. Equipment was also required to measure the mass flow rate through the packed bed and to calculate the amount of thermal energy entering the system. The flow rates that were selected for testing are summarised in Table 3.2.

Table 3.2 Summary of the flow rates used, with a duct size of 300 mm x 300 mm

Superficial velocity, U , $\text{m}\cdot\text{s}^{-1}$	0.463	0.611	0.768	0.916
Volume flow rate, \dot{V}_f , $\text{m}^3\cdot\text{s}^{-1}$	0.042	0.055	0.069	0.083
Volume flow rate, \dot{V}_{fl} , $\text{m}^3\cdot\text{h}^{-1}$	149.854	197.920	248.814	296.881
Mass flow rate, \dot{m} , $\text{kg}\cdot\text{h}^{-1}$	151.353	199.900	251.302	299.849

To accurately measure the mass flow rate through the system, an LV 110 vane probe thermo-anemometer was selected. The operating principle of the anemometer makes use of the Hall effect sensor. A Dual Hall effect sensor captures the signals of magnetic field polarity transition. The signals are converted to electrical frequency, which is proportional to the rotational velocity of the vane probe.

The vane anemometer has a vane probe diameter of 100 mm, as well as an edge diameter on the face of the vane probe anemometer of 103 mm, with an expanding angle. The circular outlet and inlet steel pipe has an inner diameter of 110.3 mm. A 110 mm UPVC drainage pipe was fitted into both circular steel pipes of 110.3 mm, in order to reduce the final inner diameter to

104 mm. The reduction in area allowed the vane anemometer to fit securely into the inlet and outlet sections and to provide accurate and reputable results. The velocity values from Table 3.2 were converted, in order to accommodate the 100 mm vane probe diameter, as shown in Table 3.3.

Table 3.3 Summary of the flow rates used, with a vane probe diameter of 100 mm

Superficial Velocity, U , $\text{m}\cdot\text{s}^{-1}$	5.3	7.0	8.8	10.5
Volume flow rate, \dot{V}_f , $\text{m}^3\cdot\text{s}^{-1}$	0.042	0.055	0.069	0.083
Volume flow rate, \dot{V}_{fL} , $\text{m}^3\cdot\text{h}^{-1}$	149.854	197.920	248.814	296.881
Mass flow rate, \dot{m} , $\text{kg}\cdot\text{h}^{-1}$	151.353	199.900	251.302	299.849

The vane anemometer can measure air velocity from $0.3 \text{ m}\cdot\text{s}^{-1}$ to $35 \text{ m}\cdot\text{s}^{-1}$. It has an accuracy of $\pm 3\%$ of the reading $\pm 0.1 \text{ m}\cdot\text{s}^{-1}$, in the range of $0.3 \text{ m}\cdot\text{s}^{-1}$ to $3 \text{ m}\cdot\text{s}^{-1}$ (resolution of $0.01 \text{ m}\cdot\text{s}^{-1}$), and an accuracy of $\pm 1\%$ of the reading $\pm 0.3 \text{ m}\cdot\text{s}^{-1}$, in the range of $3.1 \text{ m}\cdot\text{s}^{-1}$ to $35 \text{ m}\cdot\text{s}^{-1}$ (resolution of $0.1 \text{ m}\cdot\text{s}^{-1}$). Airflow can also be measured from 0 to $99999 \text{ m}^3\cdot\text{h}^{-1}$, with an accuracy of $\pm 3\%$ of the reading $\pm 0.3 \times \text{area} (\text{cm}^2)$. The selection was based on the accuracy and the ease of use.

Preliminary pressure drop calculations over the packed bed were carried out, in order to establish the size of the PPD required for testing. The Reynolds number of the particles was also calculated, to determine the flow regime of the air. The preliminary calculations are summarised in Appendix C.

A backward-curved, single intake, gas blower for condensing boilers was selected, in order to achieve the required pressure and mass flow rates for the packed bed. The inlet section of Stage 1 was designed to have a cross-sectional diameter of 100 mm, in order to fit the pressure-producing device. The technical data of the pressure-producing device is provided in Appendix D.

3.3.3.5 Temperature

Thermal energy was required to charge the packed bed. The energy was provided by a heating element placed in the inlet duct. The temperature wave-front, through the packed bed, was tracked by several temperature probes, which were placed at predetermined positions, as indicated in Figure 3.13.

A 20 mm, 2000 W, spiral coil heating element was purchased and connected to a controller, which allowed the inlet temperature to be varied, and it was set to the desired temperature. The inlet temperature was varied between 40°C and 55°C , in increments of 5°C , for different testing conditions.

The accurate measurement of the temperature through the system was essential, as the temperature data were used for the heat transfer analysis of the packed bed. Temperature probes

and thermal loggers were obtained. The temperature probes are tested at the South African National Accreditation System (SANAS) testing facility, with an accuracy of less than 0.3°C and a maximum error of 0.5°C. Four temperature probes can be connected to a logger. The standard inputs for the loggers are: (i) four temperatures, (ii) four CT's, (iii) two pulses, and (iv) power on/off events (according to power supplied to unit).

The temperature probes were placed in the packed bed at predetermined positions, as previously described in Section 3.3.2. The data received by the loggers were sent telemetrically to a central server, which the user had access to. The temperature measurement provided part of the data required to do the energy analysis, by tracking the temperature wave-front progression through the rock-bed, as well as the conduction through the concrete slab and the radiation into space.

3.3.3.6 Thermography

A thermal camera, FLIR® E60, was used to detect any thermal losses from the system and to track the temperature wave-front progression through the concrete slab. Thermal images were taken at the end of the charging phase, in order to identify the major energy losses. A second set of images was taken, specifically of the concrete slab, when the discharge phase was complete, so that the surface temperature could be compared to that of the temperature probes on the concrete surface. Emissivity of the thermal camera was not set to that of the concrete surface and kept at the custom value of 0.95.

3.3.4 Test procedure

The empirical method was comprised of 16 tests, over a period of 32 days, which covered four pre-selected temperatures, each with four mass flow rates. For testing, the flow was measured in velocity ($\text{m}\cdot\text{s}^{-1}$) and converted to a mass flow rate ($\text{kg}\cdot\text{h}^{-1}$). These tests consisted of a charging phase of eight hours, which started from 08:00 until 16:00 in the afternoon, followed by a discharge phase of 16 hours, from 16:00 until 08:00 the following day. The data logging process that was followed is shown in Table 3.4.

Table 3.4 Testing procedure for the empirical design

Test Number	1.1	1.2	1.3	1.4	2.1	2.2	2.3	2.4
Inlet Temperature (°C)	40	40	40	40	45	45	45	45
Inlet mass flow rate, kg.h ⁻¹	151.4	199.9	251.3	299.9	151.4	199.9	251.3	299.9
Charge Start	8:00	8:00	8:00	8:00	8:00	8:00	8:00	8:00
Charge End / Discharge Start	16:00	16:00	16:00	16:00	16:00	16:00	16:00	16:00
Discharge End	8:00	8:00	8:00	8:00	8:00	8:00	8:00	8:00
Test Number	3.1	3.2	3.3	3.4	4.1	4.2	4.3	4.4
Inlet Temperature (°C)	50	50	50	50	55	55	55	55
Inlet mass flow rate, kg.h ⁻¹	151.4	199.9	251.3	299.9	151.4	199.9	251.3	299.9
Charge Start	8:00	8:00	8:00	8:00	8:00	8:00	8:00	8:00
Charge End / Discharge Start	16:00	16:00	16:00	16:00	16:00	16:00	16:00	16:00
Discharge End	8:00	8:00	8:00	8:00	8:00	8:00	8:00	8:00

The data loggers that were used for the empirical tests logged the temperature data every five minutes and telemetrically sent it to a server every 60 minutes. The data could also be viewed in real time on the display screen of the loggers.

The testing procedure was as follows:

- (i) Prior to testing, the pressure-producing device was set to an inlet velocity of approximately 4.8 m.s^{-1} at 16:00, in order to achieve a thermal equilibrium within the packed bed.
- (ii) The polystyrene housing was placed over the concrete slab at 07:50.
- (iii) All the probes and connecting pieces were checked until 07:55, when the flow rate through the system was changed, according to the requirements of the test number.
- (iv) All tests started at exactly 08:00, to initiate the charging phase.
- (v) The temperature control box was switched on at 08:00, with the required temperature set for the inlet of the packed bed.
- (vi) The inlet temperature (Probe 1 in Figure 3.13) was monitored every 30 minutes, in order to maintain a constant inlet temperature.
- (vii) The charging phase continued for eight hours, from 08:00 until 16:00.
- (viii) At 15:50, thermal images were taken all around the test system, to identify the areas of possible fenestration and heat loss.
- (ix) The heating element was switched off at 16:00 and the mass flow rate was reduced, to approximately 137.07 kg.h^{-1} .
- (x) The PPD was kept on for five minutes, to allow the heating element to cool down, so as not to cause any damage to the polystyrene within the system.
- (xi) At 16:05, the PPD was switched off and the discharge cycle was started.
- (xii) The discharge cycle continued for eight hours, until the following day at 08:00.
- (xiii) At 08:00 the polystyrene housing was removed and placed next to the packed bed,

- (xiv) Thermal images were taken, to identify the distribution of the energy pattern across the concrete slab, as well as its specific temperature, after the eight-hour discharging cycle.
- (xv) After the thermal images were taken, the flow rate through the system was increased and the PPD was kept on for approximately two hours, to remove the stored heat within the system.
- (xvi) At 16:00, the PPD was set to the conditions as described in (i), and the process was repeated for the other tests.

The results of the charging and discharging of the Thermal Energy Storage (TES) system were logged and analysed. The empirical method provided a means of physically calculating the data to be analysed. A numerical method was required to validate the results obtained from the empirical investigation.

3.4 Numerical Design

The accurate numerical simulation of an empirical investigation is highly dependent on the simulation setup. The CFD numerical model was developed, using the commercial software package, STAR-CCM+®, Version 11.04. The following section provides an overview of the CFD simulation setup and execution, in order to model the effects of changing the inlet temperature and mass flow rate on the thermal energy transfer, the temperature wave-front and the charging and discharging time of the system. The general sequence of operations in the CFD analysis is depicted in Figure 3.32.

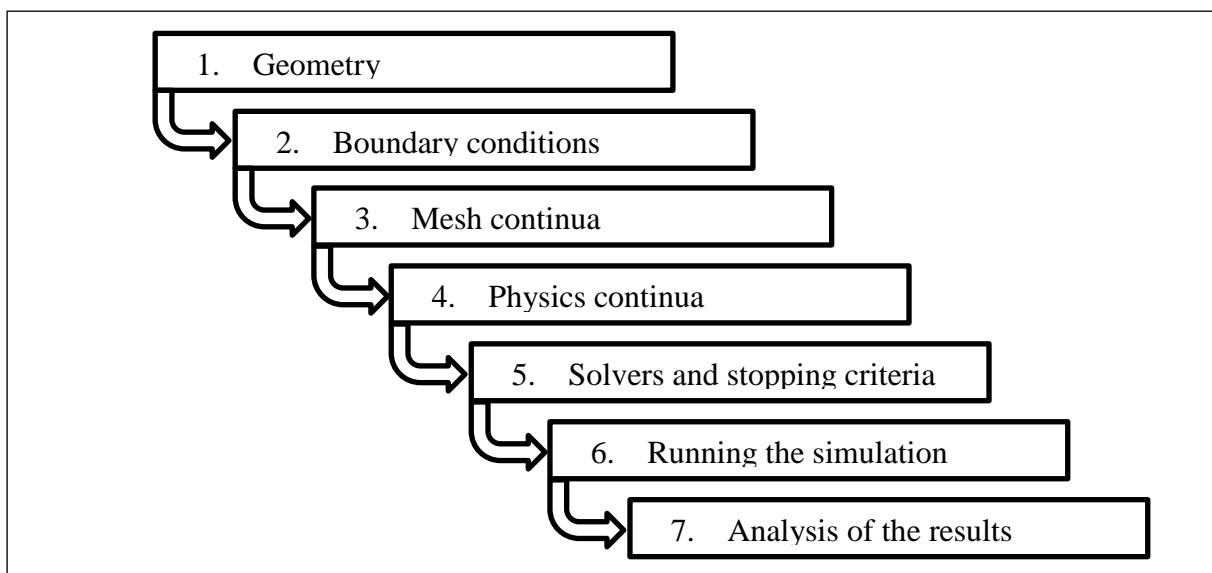


Figure 3.32 General sequence of operation in a STAR-CCM+ analysis (adapted from CD-Adapco, 2016)

3.4.1 Geometry

The geometry used for the CFD analysis, in STAR-CCM+[®], could either be imported from a native CAD file, where the fluid is extracted, in order to be used as the geometry, or developed within STAR-CCM+[®], using the 3D-CAD model. The integrated 3D-CAD model was used, based on the simplicity of the packed bed geometry and also to make use of an alternative CAD package. The geometry of the horizontal, uni-directional packed bed, which was designed in the STAR-CCM+[®] 3D-CAD model, is shown in Figure 3.33.

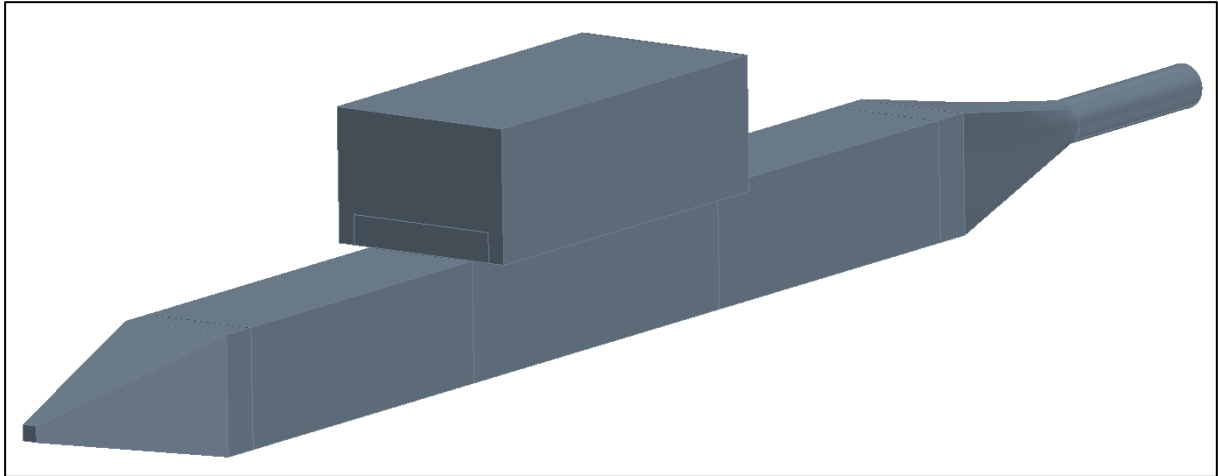


Figure 3.33 Geometry of a horizontal, uni-directional packed bed for CFD analysis

The boundary surfaces were defined by using the “split by patch” method for each face of a part surface. The geometry parts provide a three-dimensional representation of the model, whereas the computational model (to which physics is applied) is defined in terms of regions, boundaries and interfaces (CD-Adapco, 2016).

3.4.2 Boundary conditions

The geometry parts were assigned to regions, where a region was created for each part and a boundary for the surface of each part. The region and boundary types that were created are summarised in Table 3.5.

Table 3.5 Summary of region and boundary types used in the CFD setup

Regions	Region Type	Boundaries	Boundary Types
1_Upstream	Fluid Region	IF_Upstream-Heater	Wall
		Inlet	Velocity Inlet
		Metal	Wall
1_Upstream_Duct	Fluid Region	IF_Heater-Duct	Wall
		IF_Upstream-Centre	Wall
		Poly_Wood	Wall
1_Upstream_Heater	Fluid Region	IF_Heater-Duct	Wall
		IF_Upstream-Heater	Wall
		Poly_Wood_Metal	Wall
2_Centre	Porous Region	IF_Concrete-Centre	Wall
		IF_Downstream-Centre	Wall
		IF_Upstream-Centre	Wall
		Poly_Wood	Wall
3_Downstream	Fluid Region	IF_Downstream-Centre	Wall
		Metal	Wall
		Outlet	Pressure Outlet
		Poly_Wood	Wall
		Poly_Wood_Metal	Wall
4_Concrete	Solid Region	IF_Concrete-Centre	Wall
		IF_Concrete-Room	Wall
		Poly	Wall
5_Room	Fluid Region	IF_Concrete-Room	Wall
		Poly	Wall

All the boundary types were set to ‘walls’, except the inlet and the outlet, which were set to ‘velocity inlet’ and ‘pressure outlet’, respectively. The interface types, which were used in the CFD setup, are summarised in Table 3.6.

Table 3.6 Summary of interface types used in CFD setup

Interfaces	Interface Type
1_Upstream/1_Upstream_Heater	Internal Interface
1_Upstream_Duct/1_Upstream_Heater	Internal Interface
1_Upstream_Duct/2_Centre	Porous Baffle Interface
2_Centre/3_Downstream	Porous Baffle Interface
2_Centre/4_Concrete	Contact Interface
4_Concrete/5_Room	Contact Interface

The interfaces between the upstream/downstream and centre pieces, were set to the porous baffle interface, to indicate the transition from the fluid to the porous region. Contact interfaces

were selected for both sides of the concrete slab, as conduction occurs between the porous region and the room. With the required boundary conditions set for the model, the mesh could be applied.

3.4.3 Mesh continua

The mesh continua consisted of models, reference values and volumetric control values, which were selected, based on the descriptions provided in the following sections.

3.4.3.1 Models

A new mesh continuum was created and the following models were selected, for the CFD simulation:

- (i) A surface remesher.
- (ii) A polyhedral mesher.
- (iii) A prism layer mesher.

3.4.3.2 Reference values

The reference values were continuously changed, until the results that were obtained were independent of the mesh resolution. The results of the mesh independence study are summarised in Appendix E. The following reference values were selected:

- (i) The base size was changed from 1 m to 15 mm.
- (ii) The prism layer thickness - size types were changed to absolute.
- (iii) The absolute size was changed to 5 mm.
- (iv) The surface growth rate was changed to 1.1.
- (v) The surface size > relative minimum size > percentage of base was changed to 50.

3.4.3.3 Volumetric control

There were no volumetric controls added to the mesh continua. The detailed setup of the mesh, for the regions, boundaries and interfaces, are summarised in Appendix F.

3.4.4 Physics continua

The physics continua required two physics types, namely, air and a solid. The following sections describe the physics models selected, the reference values that were changed, the initial conditions that were set and the physics that was used for the regions and boundaries, in each model.

3.4.4.1 Physics 1 Air

The models, reference values and initial conditions for air were selected, as described in the following sections.

3.4.4.1.1 Models

The models that were selected for the physics continuum of air, include:

- (i) Exact Wall Distance (auto select),
- (ii) Gas – Air,
- (iii) Gradients (auto select),
- (iv) Gravity,
- (v) Ideal Gas,
- (vi) Implicit Unsteady,
- (vii) K-Epsilon Turbulence,
- (viii) Realizable K-Epsilon Two-Layer (auto select),
- (ix) Reynolds-Averaged Navier-Stokes (auto select),
- (x) Segregated Flow,
- (xi) Segregated Fluid Temperature,
- (xii) Three Dimensional,
- (xiii) Turbulent, and
- (xiv) Two-Layer All y^+ Wall Treatment (auto select).

The implicit unsteady solver was selected, due to the segregated flow. The explicit unsteady solver is usually used for coupled energy, namely, for inviscid and laminar viscous regime models. Steady state conditions were not considered, as they converge to a solution, and the investigation is specifically time-dependant; hence, the unsteady model was selected.

3.4.4.1.2 Reference values

The reference values were selected, based on the location of the empirical model, which was situated in Bloemfontein, Free State, South Africa, with the following values:

- (i) Altitude 1422 m,
- (ii) Density 1.01 kg.m^{-3} , and
- (iii) Pressure 85270 Pa.

3.4.4.1.3 Initial Conditions

The only initial condition that was set, was that of the static temperature. The following field function was created, in order to change the static temperature of the air, when dealing with the different conditions of the empirical model:

Static Temperature > Field Function > A_StaticTempAir.

3.4.4.2 Physics 2 Concrete

The models, reference values and initial conditions for concrete were selected, as described in the following sections.

3.4.4.2.1 Models

The models of the physics continua for concrete were selected, as listed below. The default properties of concrete, from the STAR-CCM+ library, were used for the study:

- (i) Constant density.
- (ii) Gradients (auto select).
- (iii) Segregated Solid Energy.
- (iv) Solid – Concrete (Properties kept constant).
- (v) Implicit Unsteady.
- (vi) Three Dimensional.

A sensitivity analysis was conducted on some of the variables in the system and the thermal conductivity value of the concrete was changed from the default value of $0.53 \text{ W.m}^{-1}.\text{K}^{-1}$, provided by the STAR-CCM+[®] library, to $1.4 \text{ W.m}^{-1}.\text{K}^{-1}$ for a concrete stone mix. The sensitivity analysis will be discussed in Chapter 4.

3.4.4.2.2 Reference values

No reference values were set for the physics continua of concrete.

3.4.4.2.3 Initial Conditions

The initial conditions of the concrete were set, based on the average value of the data from the four surface probes on the concrete of the empirical method. The following field function was created, in order to input the required surface temperature for each numerical setup:

Static Temperature > Field Function > A_StaticTempConcrete.

A detailed layout of the setup of the regions, boundaries and interfaces of the physics continua are summarised in Appendix G.

3.4.5 Field functions

Field functions were created in order to change specific variables at one place, and not to sequentially work through the whole tree-structure, to change them. The field functions that were used in the numerical study are summarised in Table 3.7.

Table 3.7 Field functions that were used in the numerical setup

Field Function	Type	Value	Unit
A_AmbientTemperatureTable	Scalar	See (i) below	K
A_HeatingElementEnergySource	Scalar	See (ii) below	W
A_HeatingLocalSource	Scalar	See (iii) below	W
A_HeatingTemperatureTable	Scalar	See (iv) below	K
A_HeatTransferCoefficient_Metal	Scalar	6.665	W.m ⁻² .K ⁻¹
A_HeatTransferCoefficient_Poly	Scalar	0.398	W.m ⁻² .K ⁻¹
A_HeatTransferCoefficient_Poly_Wood	Scalar	0.390	W.m ⁻² .K ⁻¹
A_HeatTransferCoefficient_Poly_Wood_Metal	Scalar	0.390	W.m ⁻² .K ⁻¹
A_PorousInertialResistance	Scalar	667.858	kg.m ⁻⁴
A_PorousInertialResistanceMesh	Scalar	2.723	kg.m ⁻⁴
A_StaticTempAir	Scalar	T+273.15	K
A_StaticTempConcrete	Scalar	T+273.15	K
A_ThermalResistance_Metal	Scalar	0.150	m ² .K.W ⁻¹
A_ThermalResistance_Poly	Scalar	2.513	m ² .K.W ⁻¹
A_ThermalResistance_Poly_Wood	Scalar	2.561	m ² .K.W ⁻¹
A_ThermalResistance_Poly_Wood_Metal	Scalar	2.561	m ² .K.W ⁻¹
A_VelocityInlet	Scalar	26.016	m.s ⁻¹

Some of the field functions required definitions, in order to execute the input data that were provided correctly, as shown in (i) – (iv) below:

- (i) Field Function > A_AmbientTemperatureTable >
 - Definitions > interpolateTable(@Table("AmbientSecondsKelvin"), "column0", LINEAR, "column1", \$Time)
- (ii) Field Function > A_HeatingElementEnergySource >
 - Definitions > (-1*\${MassFlowatInletReport}) *1003.62* ((\${A_HeatingTemperatureTable}) - \${A_StaticTempAir})
- (iii) Field Function > A_HeatingLocalSource >
 - \${Centroid}[0]<0.674058 && \${Centroid}[0]>0.62553 && \${Centroid}("Laboratory.Cylindrical 1")[0]<(0.2032/2) ? \${A_HeatingElementEnergySource}:0
- (iv) Field Function > A_HeatingTemperatureTable >
 - Type > Scalar
 - Definitions > interpolateTable(@Table("HeatingSecondsKelvin"), "column0", LINEAR, "column1", \$Time)

The A_HeatingLocalSource that was created represents the heating element, that was used in the empirical study. Dimensions were given to the local source, in the shape of a cylinder, and an energy value was allocated as 'A_HeatingElementEnergySource'. The value of the energy source, in watts, was calculated by means of Equation (3.2):

$$\dot{Q} = \dot{m}c_p\Delta T \quad (3.2)$$

where,

\dot{Q} = rate of heat transfer [W], and
 \dot{m}_{air} = mass flow rate of air [kg.s⁻¹].

Taking into account the mass flow rate through the packed bed, which was automatically generated by a report (MassFlowInletReport), the specific heat capacity of air, selected as 1003.62 J.kg⁻¹.K⁻¹ and the temperature difference. The temperature difference (ΔT) was the difference between a pre-generated heating table (A_HeatingTemperatureTable) and the static air temperature (A_StaticTemprAir).

The static air temperature was used as the inlet temperature, because when the ambient temperature is used as the inlet, the required heating inlet temperature is not achieved, due to the ambient temperature changing diurnally. The pre-generated heating table consisted of temperature values at 300 second time intervals, in order to simulate the heating inlet curve of the empirical design. Appendix H describes the process followed, to select the correct temperature for the heating element.

The empirical testing was not conducted in a controlled environment; hence, heat transfer coefficient and thermal resistance values were required for all the materials used in construction. A summary of the values that were used in the numerical study are shown in Table 3.7, with the complete calculations in Appendix I.

The velocity values that were used in the numerical study, were changed accordingly, based on the inlet diameter of 100 mm x 100 mm. The values in the field functions were changed, depending on the empirical results that needed to be modelled.

The porous inertial and viscous resistance values were required, as input to the numerical model. These values were calculated for the porous region, as well as the expanded metal mesh. The porous viscous resistance values were selected as zero, whereas the porous inertial resistance values were calculated, depending on the flow rate through the packed bed. These calculations are summarised in Appendix J.

3.4.6 Tables

During the empirical tests, the ambient temperature in the testing facility constantly changed throughout the course of the day. The heat provided to the packed bed was also not instantaneous, as the heating element heated up gradually, before providing the required temperature. Hence, for the numerical study, the empirical values of the ambient conditions, as well as the inlet temperature values of the packed bed, had to be used. The tables were created in STAR-CCM+ and the path was set to the specific data file, which was in the form of a comma-separated values (CSV) file. The CSV field contained two columns. The first column consisted of time in seconds, starting at zero seconds, in intervals of 300 seconds (five minutes).

The second column was the temperature in K, at each time step. The heating table was created in a similar way and using the values developed, as described in Appendix H.

3.4.7 Solvers and stopping criteria

The time-step that was used for the implicit unsteady solver was set to one second, from the initial 0.001 second. The number of inner iterations were changed from five to 10.

The maximum physical time was set to 28800 seconds (eight hours) for the charging phase. When the charging phase was complete, some conditions were changed and the discharge phase continued up to 86400 seconds (24 hours); hence, a charging time of eight hours was allowed, with a discharge time of 16 hours.

3.4.8 Derived parts, scenes and reports

Several point probes were created as derived parts, according to the proposed placement in Figure 3.13. From the point probes, a geometry scene was created, in order to graphically represent the placement of the point probes. The names given to Probes 1-20 are summarised in Table 3.8. Probe 4 was not used in the CFD simulation setup as a point probe, as it falls out of the geometry scope; however, it provided the ambient temperature data in the empirical investigation, which was used as input for the numerical ambient conditions (environmental).

Table 3.8 Probe descriptions for numerical investigation

1	T_Inlet	6	T_1.2	11	T_2.3	16	T_3.4
2	T_Outlet	7	T_1.3	12	T_2.4	17	T_4.1
3	T_Space	8	T_1.4	13	T_3.1	18	T_4.2
4	N/A	9	T_2.1	14	T_3.2	19	T_4.3
5	T_1.1	10	T_2.2	15	T_3.3	20	T_4.4

Reports were created for each of the point probes in Table 3.8. Based on Equation (2.2), a mass flow report was also required, to calculate the amount of energy that the heat source must provide, at the inlet of the rock-bed.

3.4.9 Monitors and plots

From the reports, monitors and plots were developed, to acquire the numerical data, which were then compared with the empirical data. The point probes were grouped together and plots were created, as shown in Table 3.9.

Table 3.9 Summary of plots created for the specific point probes

Level_0	T_Inlet, T_Outlet, T_Space
Level_1	T_1.1, T_1.2, T_1.3, T_1.4
Level_2	T_2.1, T_2.2, T_2.3, T_2.4
Level_3	T_3.1, T_3.2, T_3.3, T_3.4
Level_4	T_4.1, T_4.2, T_4.3, T_4.4
Mass Flow at Inlet Monitor Plot	

With the numerical setup complete, the testing procedure of the simulations could be compiled.

3.4.10 Running the simulation

The empirical testing procedure that was discussed in Section 3.3.4 consisted of 16 tests. Four of the empirical tests were selected, in order to cover a range of the main temperature and mass flow rate fields. The four empirical tests that were selected, in order to be numerically simulated, were comprised of test numbers 1.1, 2.2, 3.3 and 4.4.

The numerical setup was conducted, as discussed in Sections 3.4.1 to 3.4.9. For each of the numerical test cases, the respective field functions were changed, according to the respective values that were used in each empirical test. The simulations were conducted on the High Performance Computing Unit (HPCU) at the University of the Free State.

The charging phase continued to a solution time of 28800 seconds, which amounted to approximately 21 hours of real-time. Once the charging phase was complete, the discharge phase had to continue; however, a few changes were required, namely:

- (i) the velocity inlet, at the inlet boundary had to be changed to a stagnation inlet,
- (ii) the physics conditions of the upstream heater had to be changed to none, and
- (iii) the pressure outlet, at the outlet boundary had to be changed to a stagnation inlet.

The boundary conditions of the inlet and outlet, which were changed to a stagnation inlet, prevented any airflow through the packed bed. The energy of the upstream heater was set to none, to prevent any heat being generated by the heating element, during the discharge phase. With the implemented changes, the discharge phase continued from 28800 seconds up to 86400 seconds (16 hours discharge), which took approximately 41 hours to complete. A total of 62 hours of computing time was required to complete one of the four tests.

Once the empirical and numerical research designs had been developed and executed correctly, the obtained raw data needed to be transformed into a more usable form, by using data analysis methods.

3.5 Data Analysis Methods

The data analysis methods focussed on the empirical and numerical data that were obtained from the respective research designs. The raw data that had not yet been processed, needed to be transformed into a more usable form, by using data analysis methods. The data were categorised into empirical performance effects data, empirical test data and numerical test data. The data analysis process and categorisation are shown in Figure 3.34.

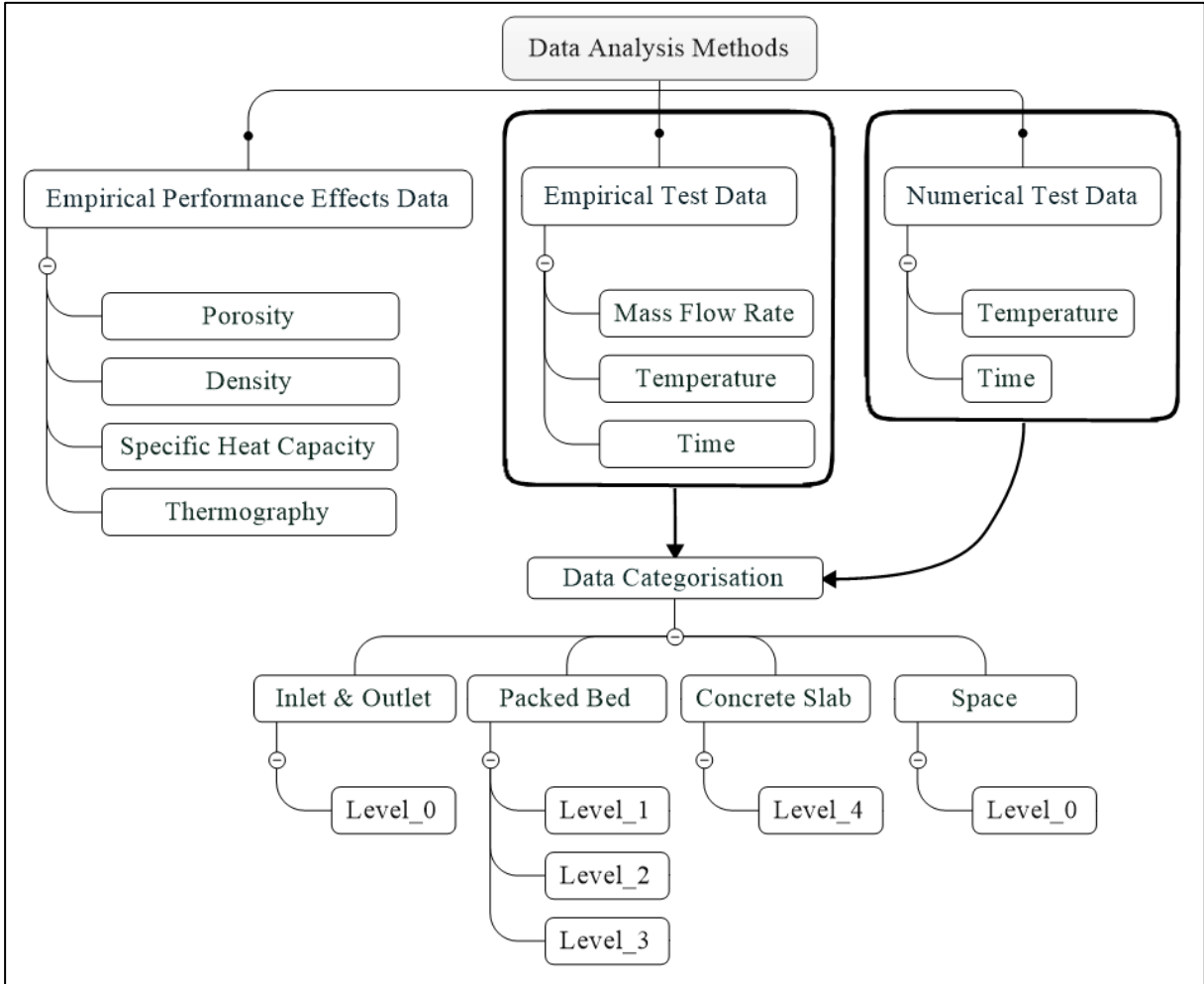


Figure 3.34 Data analysis process and categorisation

3.5.1 Empirical performance effects data

The porosity of the packed bed, the density of the rock and the specific heat capacity of the rock were identified as design-related properties, which have a substantial influence on the performance of a packed bed. The results that were collected from the design-related properties did not require specific data analysis methods to be implemented, as the methods that were used to obtain the data were described in Section 3.3.3; however, the verification of the data was required, as they were used as an input to the numerical design. The thermal image data were used to identify major energy losses in the system and to compare with the surface temperatures that were obtained after the discharge phase.

3.5.2 Empirical test data

The testing procedure of the horizontal, uni-directional packed bed, provided a significant amount of temperature data, with each test that was conducted. The data sets were categorised into the following sections, namely: (i) the inlet and outlet, (ii) the packed bed, (iii) the concrete slab, and (iv) the space, in order to analyse the data more effectively. An energy balance of the packed bed was also conducted. The charging phase was from 0 – 28800 seconds and the discharge phase was from 28800 – 86400 seconds.

The 16 tests that were conducted, were given specific names, in order to identify the test conditions. For example, test E_40_250 was an empirical test, with an inlet temperature of 40°C and a mass flow rate of 250 kg.h⁻¹; hence, the letter represents either an empirical test – E, or a numerical test – N. The first set of values represents the temperature data, which are either 40°C, 45°C, 50°C or 55°C and the second pair of values represents the mass flow rate, 150 kg.h⁻¹, 200 kg.h⁻¹, 250 kg.h⁻¹ or 300 kg.h⁻¹. For the empirical test data, the letter prefix was not used, as only empirical data were considered.

For each of the data categories, graphs of temperature vs time were plotted. The inlet temperature data were kept constant and the mass flow rate was then varied. The opposite was also done, keeping the mass flow rate constant and varying the temperature data. The result trends, the anomalies and the variance were then analysed. The difference between the inlet temperature and the maximum temperature obtained for the outlet, as well as the packed bed, the concrete slab and the space temperature, were compared for a range of mass flow rates and the initial temperature of the specific categories. This provided the opportunity to study the influence of the temperature at $t = 0$ on the system's performance.

The packed bed contained 16 temperature probes, four on each level, with the concrete surface also having four probes. The average was calculated for the probes on each level, in order to obtain a uniform temperature over the specific layer. The temperature wave-front was also tracked through the packed bed and the concrete slab, by using the point probes at each level. The thermal image data that were captured for the respective tests, were also used to compare with the empirical data sets.

The energy distribution of the inlet and outlet, the packed bed, the concrete slab and the space area was calculated, using Equation (2.2). The energy input was calculated for each component from time $t = 0$, until the maximum value was obtained. The thermal energy that was lost, was then calculated, until the discharge phase was complete. The results provided the ability of the packed bed to store and retain thermal energy. The results of the scaled-down room provided a good estimate of the thermal energy distribution that could be expected. The thermal energy data of the different sections were used to develop an energy balance of the packed bed.

3.5.3 Numerical test data

The plots that were created in the STAR-CCM+[®] workspace, were comprised of the temperature data of Level_0, Level_1, Level_2, Level_3 and Level_4. The summary of the

specific point probes that were allocated to each level are provided in Table 3.9. The plots were exported as CSV files and the data were filtered, to obtain the temperature data every 300 seconds, which correlated exactly with the empirical temperature measurement cycle of 300 seconds. The data were transferred to a Microsoft Excel® workspace, where the numerical data were compared with the empirical data for validation.

3.6 Quality Assurance

The processed data that were obtained, after the data analysis methods had been applied, included: (i) the porosity, (ii) the specific heat capacity, (iii) the density, (iv) the mass flow rate, and (v) the temperature. To ensure that the transformed data is reliable and of a good quality, verification and validation was required.

3.6.1 Verification

The verification of the results involved verifying that the selected research designs (empirical and numerical) were executed and implemented in the right way, in order to obtain accurate results that could be validated.

3.6.2 Validation

Validation involved comparing the empirical data that were obtained, with data from literature, as well as the results that were acquired from the thermographs and the numerical design.

The numerical data were categorised according to the data categorisation of Figure 3.34. The empirical and numerical data were used to develop graphs and to compare the trends in the data sets. The percentage error between the empirical results and the numerical results was calculated, by implementing Equation (3.3).

$$\% \text{ error} = \frac{\text{Exact value} - \text{Approximate value}}{\text{Exact value}} \times 100 \quad (3.3)$$

where,

$$\begin{aligned} \text{Exact value} &= \text{empirical results } [^{\circ}\text{C}], \text{ and} \\ \text{Approximate value} &= \text{numerical results } [^{\circ}\text{C}]. \end{aligned}$$

The percentage error calculations provided the results that were needed to evaluate the accuracy and validity of the numerical design that was developed. Calculations were also conducted for the thermal image data of the concrete surface and the concrete surface probes.

3.7 Conclusions of the Methodology

The methodology chapter provided a step-by-step process of how the research project was executed. The roadmap of how the methodology was conducted was summarised in Figure 3.1. A quantitative research method was selected, which involved transforming data into usable

statistics and forming conclusions. Both an empirical and a numerical research design were selected, in order to get sufficient data to analyse.

The empirical research design was comprised of the proposed design of the horizontal, uni-directional packed bed, followed by the construction phase. The most important performance metrics of the packed bed were identified, and it was shown how they were measured and what instruments were used. The testing procedure of the empirical design was discussed, and how the data was sourced.

The numerical design required the complete setup of a simulation, using CFD. The geometry was developed and the boundary conditions were specified. The mesh and physics continua were established and the necessary field functions, tables and solvers were set, in order to execute the simulation in the correct way. The numerical design used some of the results from the empirical design as input.

The raw data were collected from the empirical design, and transformed into a more usable form, by using data analysis methods. Data analysis methods were developed, in order to obtain the empirical performance effects data, the empirical test data and the numerical test data.

The transformed data were verified and validated, in order to ensure reliable and good quality data. Verification focussed more on whether the developed research designs were executed properly, in order to get the correct results. The data were validated by comparing the empirical data with the data from literature and by also comparing the numerical data with the empirical data.

4. RESULTS AND DISCUSSION

The following chapter provides the results and discussion of the empirical and numerical tests that were conducted. A verification of the research designs was undertaken, followed by an analysis of the empirical test data of the horizontal, uni-directional packed bed. A comparison of the empirical data with the numerical data is also presented.

4.1 Verification

A verification for both the empirical and numerical research designs was undertaken, in order to ensure that the methods that were developed, were implemented correctly.

4.1.1 Empirical method

The empirical method was followed, as described by the research design in Section 3.3. A few ‘test runs’ were carried out, in order to operate the system in the correct way. It was noted that the empirical system was not as air-tight as required. A summary of the inlet and outlet mass flow rates that were obtained for each test, is provided in Table 4.1.

Table 4.1 Inlet and outlet mass flow rate values of the empirical tests

Inlet mass flow rate, kg.h ⁻¹	151.35	199.90	251.30	299.85
Outlet mass flow rate, kg.h ⁻¹	139.93	185.62	234.17	279.86
% error	7.55	7.14	6.82	6.67

The loss of between 6.67% and 7.55% in mass flow rate between the inlet and outlet, was as a result of the connecting pieces between the sections of the packed bed. Although toggle logs, weather strips, silicon and thermography were used to identify and reduce fenestration, it was not sufficient. During the analysis of the results, the inlet mass flow rates were rounded to the nearest 10 and presented as 150 kg.h⁻¹, 200 kg.h⁻¹, 250 kg.h⁻¹ and 300 kg.h⁻¹.

4.1.2 Numerical method

The numerical method was executed, according to the guidelines that were developed in Section 3.4. As the numerical tests were conducted, the results were continuously monitored and adjustments were made, if required. After the first numerical run, it was noted that the numerical results, correlated well with the empirical results. The mesh independence study indicated that mesh resolution was sufficient for the numerical model, as provided in Appendix E. The inner iterations that were set to 10, were adequate, as it is generally accepted that the residual data must reduce to three orders of magnitude (below 0.001), except for the energy component.

A sensitivity analysis was done for the numerical simulation on four variables, namely: (i) the porosity of the packed bed, (ii) the specific heat capacity of the rock, (iii) the thermal conductivity of the concrete slab, and (iv) the resistance values of the materials that were used for the packed bed. It was found that the variable that had a significant effect, was the thermal

conductivity of the concrete slab. The default value of $0.53 \text{ W}\cdot\text{m}^{-1}\cdot\text{K}^{-1}$, provided by the STAR-CCM+[®] library, was changed to $1.4 \text{ W}\cdot\text{m}^{-1}\cdot\text{K}^{-1}$ for a concrete stone mix. The numerical curves of the space and concrete data followed the empirical curves much better. More information on the sensitivity analysis is provided in Appendix K.

4.2 Empirical Test Data

The empirical test data were divided into four sections, namely, the inlet and outlet, the packed bed, the concrete slab and the space. The empirical data were analysed, to investigate the effect of changing the inlet temperature and mass flow rate, on the thermal energy transfer, the temperature wave-front, as well as the charging and discharging time of the system.

4.2.1 Inlet and outlet

The empirical data of the inlet and outlet temperature probes are provided in Figures 4.1 and 4.2, for the different mass flow rates. The inlet and outlet temperature data were only considered for the charging phase.

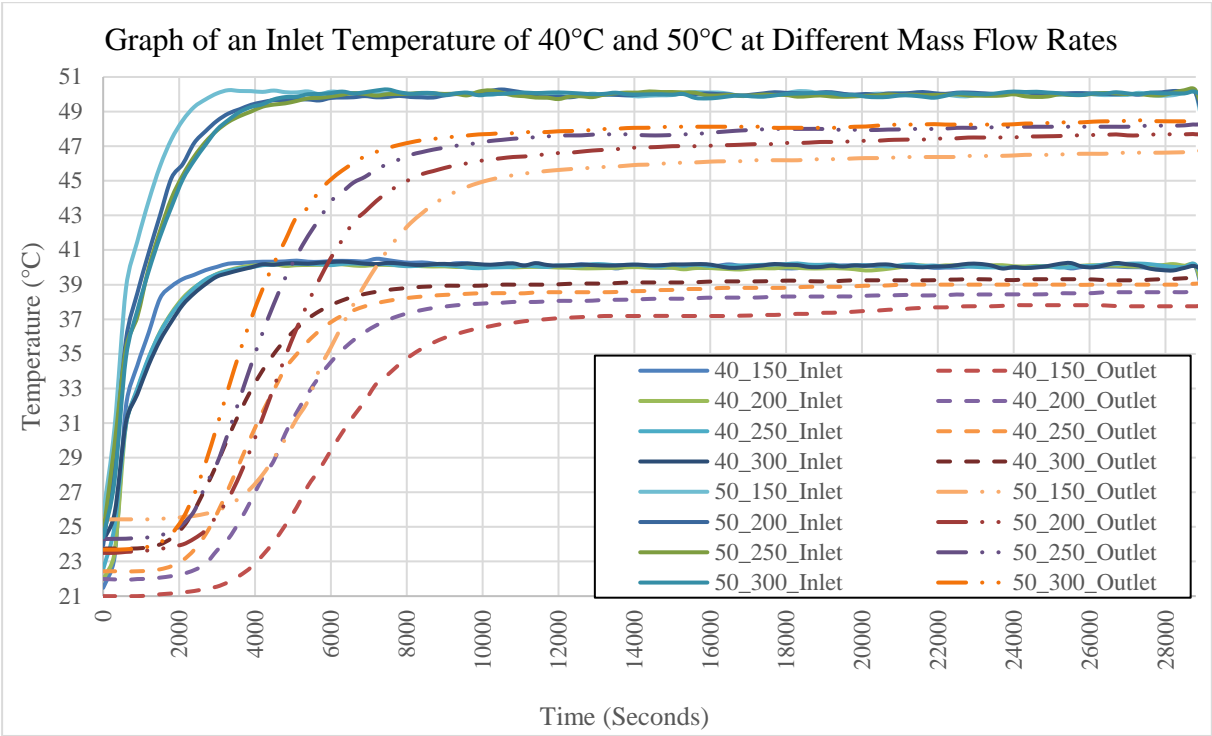


Figure 4.1 Graph of an inlet temperature of 40°C and 50°C at different mass flow rates

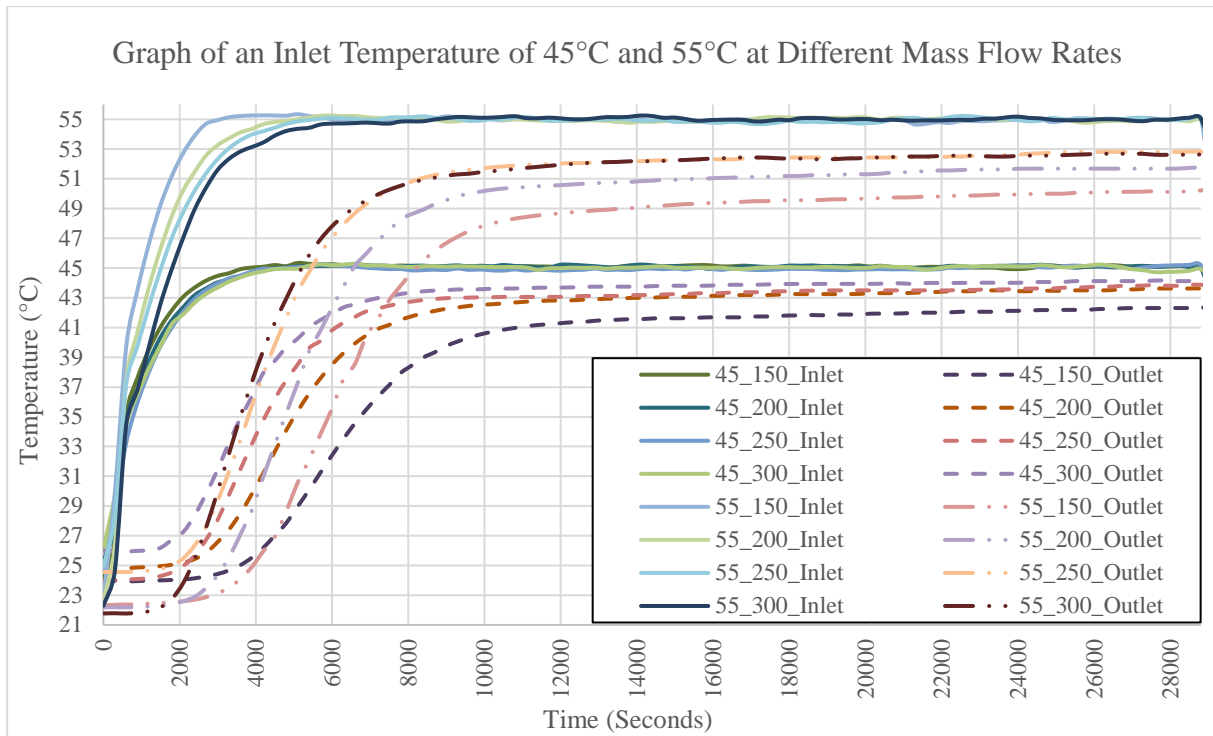


Figure 4.2 Graph of an inlet temperature of 45°C and 55°C at different mass flow rates

The inlet curve data of all the tests follow a similar trend, reaching the required inlet temperature between 4000 and 6000 seconds. The higher the inlet temperature, the longer it takes to reach a plateau, as expected. The increase in mass flow rate from 150 kg.h⁻¹ to 300 kg.h⁻¹, at selected temperatures, resulted in an average reduction in the charging time of 750 seconds per 50 kg.h⁻¹ increase (refer to Table 18.1 in Appendix L).

The packed bed was deemed charged, when the outlet temperature did not increase by more than 0.01°C in 300 seconds. The outlet curve lagged the inlet curve by approximately 4800 – 9000 seconds, before the gradient reduced to close to zero. From 9000 seconds to the end of the charging cycle, the outlet temperature increased, on average, by approximately 0.283°C.h⁻¹, for all the tests that were conducted; hence, the system can be charged to more than 90% in 9000 seconds of the total charging cycle. This amounted to two-and-a-half hours of the total eight-hour charging cycle. This posed the question of whether the extra five-and-a-half hours of charging time and energy requirements are worth the extra 10% of charging capacity.

The increase in the inlet temperature, results in a larger temperature difference between the outlet temperature curves that were obtained at a specific mass flow rate. The higher inlet temperature increases the gradient of the outlet temperature curves, which implies that more energy is transferred from the air to the rocks, in a shorter period of time. Figures 4.3 to 4.6 provide the inlet and outlet temperature data, with fixed mass flow rates and varying inlet temperatures.

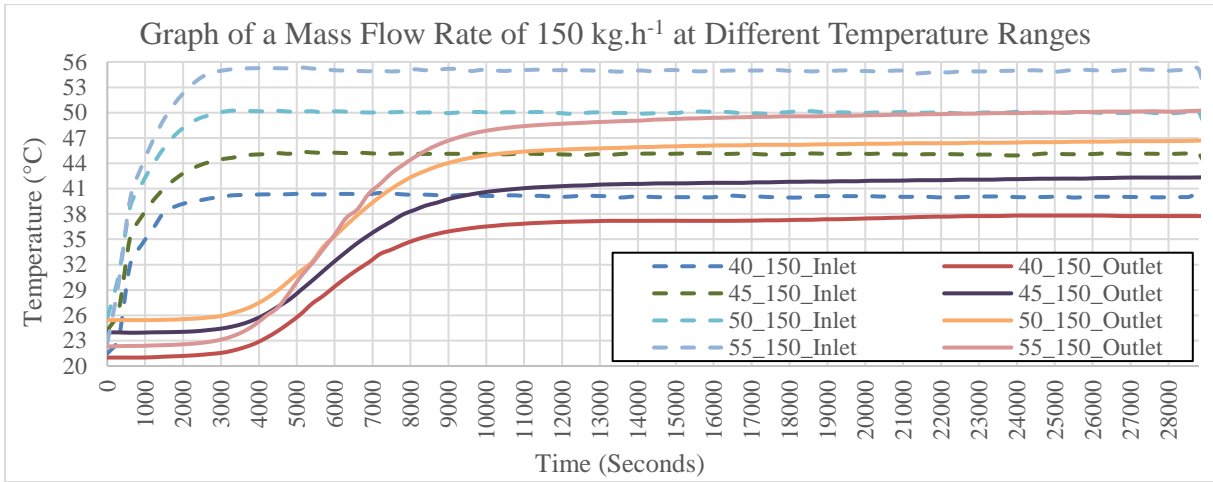


Figure 4.3 Graph of a mass flow rate of 150 kg.h⁻¹ at different temperature ranges

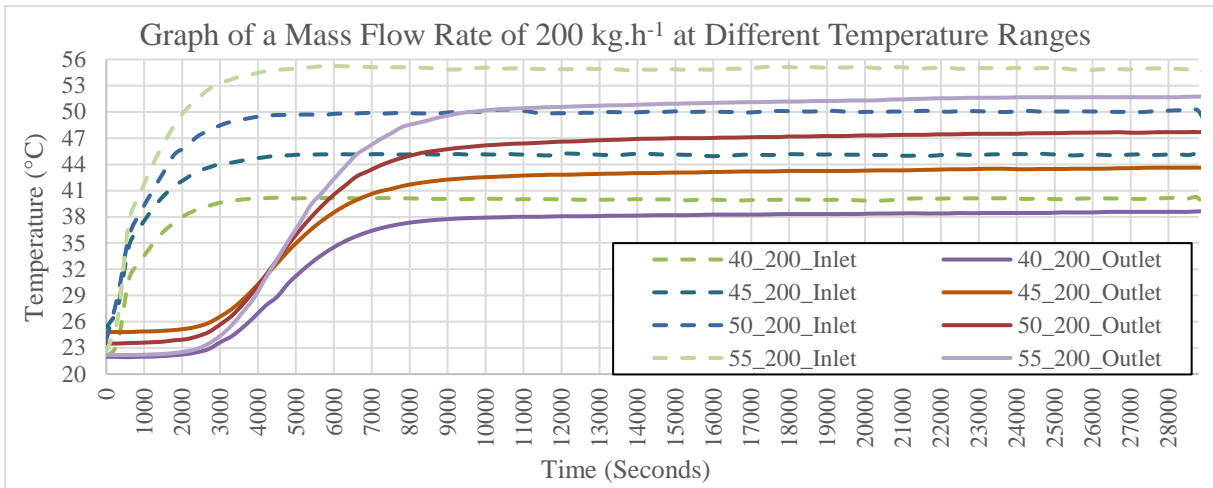


Figure 4.4 Graph of a mass flow rate of 200 kg.h⁻¹ at different temperature ranges

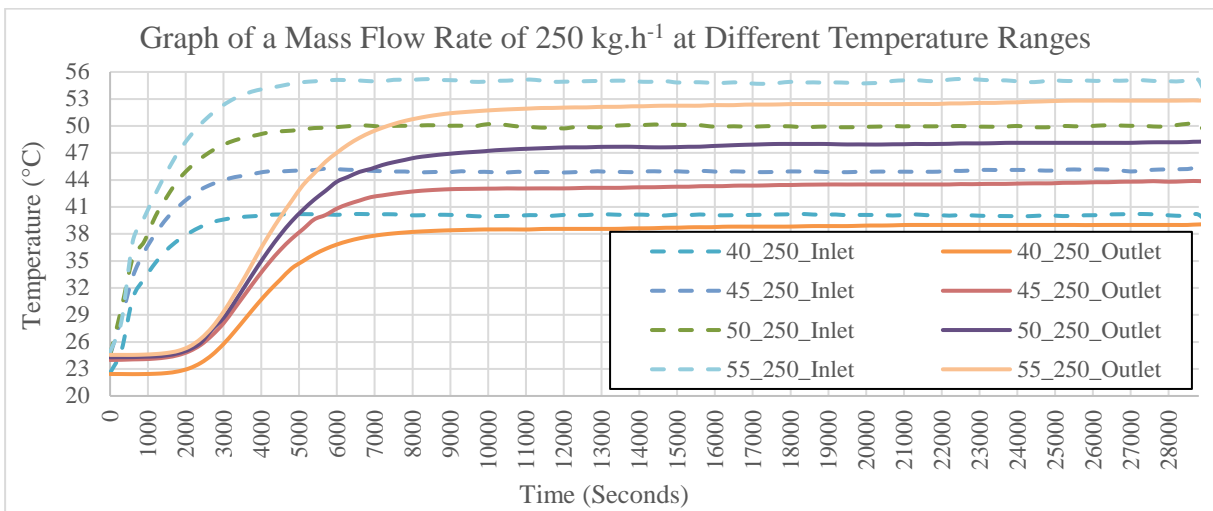


Figure 4.5 Graph of a mass flow rate of 250 kg.h⁻¹ at different temperature ranges

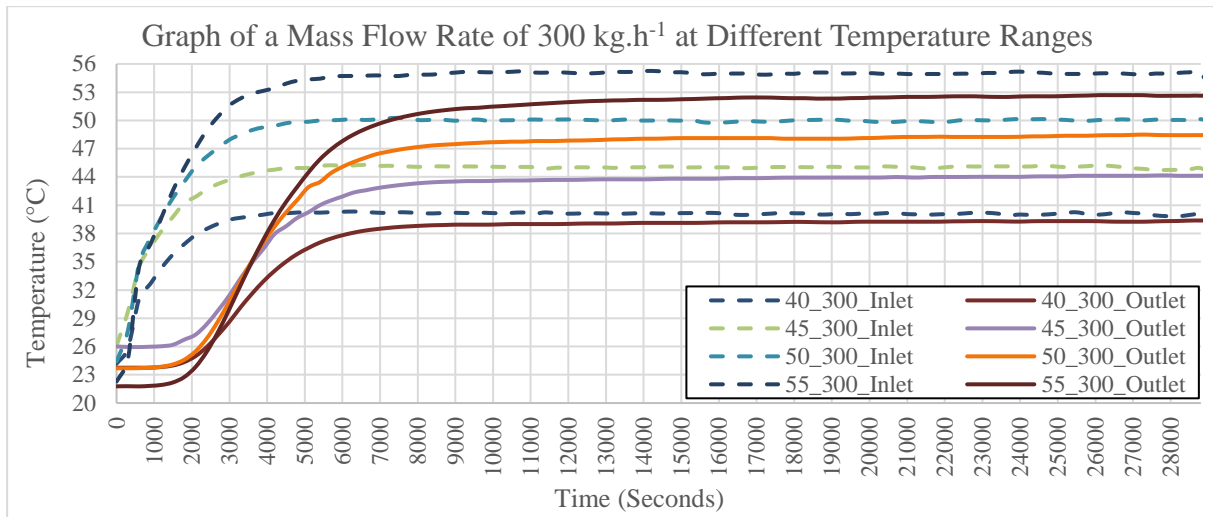


Figure 4.6 Graph of a mass flow rate of 300 kg.h^{-1} at different temperature ranges

The results indicate that, as the inlet temperature increases from 40°C to 55°C for a selected mass flow rate, the following effects are noted, namely:

- (i) the temperature wave-front moves through the packed bed quicker, because the temperature lines of the inlet and outlet, for a specific temperature (example 40°C), come closer together between 4000 and 9000 seconds, and the time that it takes for the outlet temperature to reach the plateau, decreases,
- (ii) the outlet temperature curves get closer to the inlet temperature curves, and
- (iii) an average reduction of the charging time of 500 seconds per 5°C increase for selected mass flow rates (refer to Table 18.2 in Appendix L).

The reduction in charging time implied that the temperature wave-front moved through the packed bed at a higher rate, with more energy being transferred from the air to the rocks.

Figure 4.7 provides a summary of the difference between the inlet temperature and maximum outlet temperature for a range of mass flow rates, as well as the ambient temperature at $t = 0$, during each test that was conducted.

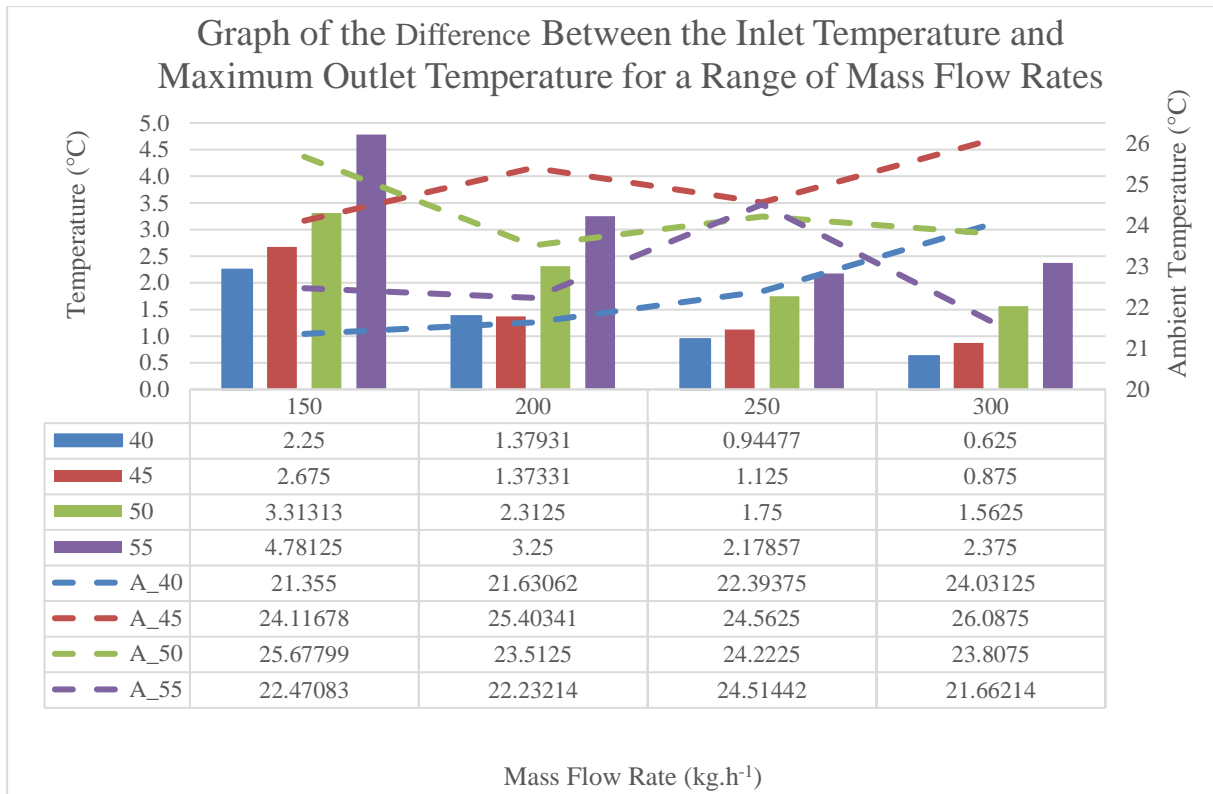


Figure 4.7 The difference between the inlet temperature and maximum outlet temperature for a range of mass flow rates

The results of Figure 4.7 show that, as the mass flow rate increases, the difference between the actual inlet temperature and the outlet temperature decreases. The opposite is true when increasing the inlet temperature of the packed bed. The temperature difference of 55°C and 300 kg.h⁻¹ (55_300) is higher than for the same inlet temperature of 55°C and a lower mass flow rate of 250 kg.h⁻¹ (55_250). This was unexpected; however the ambient temperature (A_55) for Test 55_250 was 2.85°C higher than the ambient temperature of Test 55_300. Figure 4.8 shows the amount of energy that was used as input to the packed bed for each test, the amount that was lost during the charging phase, as well as the energy that was available at the outlet.

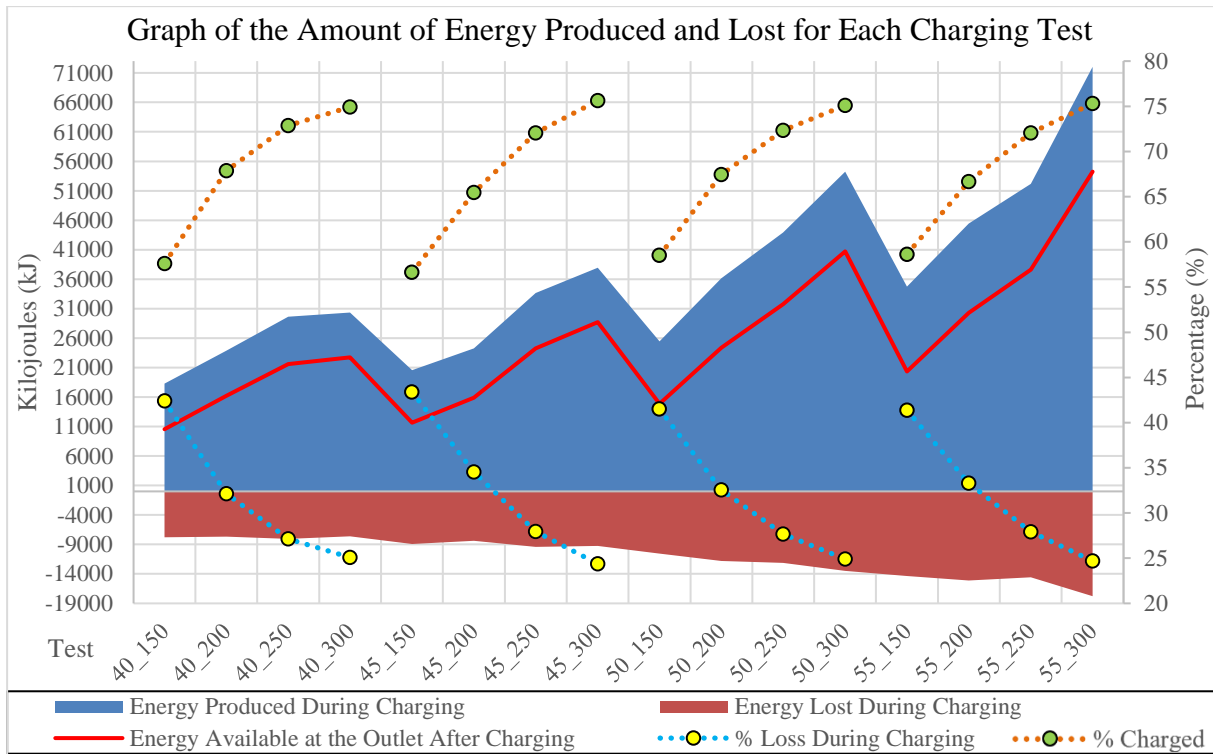


Figure 4.8 Graph of the amount of energy produced and lost for each charging test

The minimum amount of energy that was supplied to the packed bed was 18305.28 kJ for Test 40_150 and the maximum 72023.82 kJ for Test 55_300. The results show that the energy that was lost during charging phase increased, with an increase in the inlet temperature and mass flow rate. The energy that was available at the outlet was calculated, taking into account the lower mass flow rate at the outlet.

The percentage charged, as well as the percentage loss during the charging cycle, stayed fairly constant with an increase in the inlet temperature from 40°C to 55°C, at selected mass flow rates. However, with an increase in mass flow rate from 150 kg.h⁻¹ to 300 kg.h⁻¹, at selected inlet temperatures, the percentage charged increases, whereas the percentage loss during charging decreases. These results indicate that as the mass flow rate increases, more energy is stored within the packed bed, and less losses occur. It must be noted that the percentage loss during the charging phase was calculated, based on the energy lost during charging to the energy produced during charging. The minimum amount that the packed bed was charged was 56.609% (45_150) and the maximum was 75.622% (45_300). On average, the packed bed was charged to 68.067% of the available capacity.

4.2.2 Packed bed

The temperature wave-front that moves through the packed bed is depicted in Figure 4.9. An inlet temperature of 40°C was selected, with a mass flow rate of 150 kg.h⁻¹. The charging data was only used up to 12000 seconds, when the temperature in the packed bed was stable.

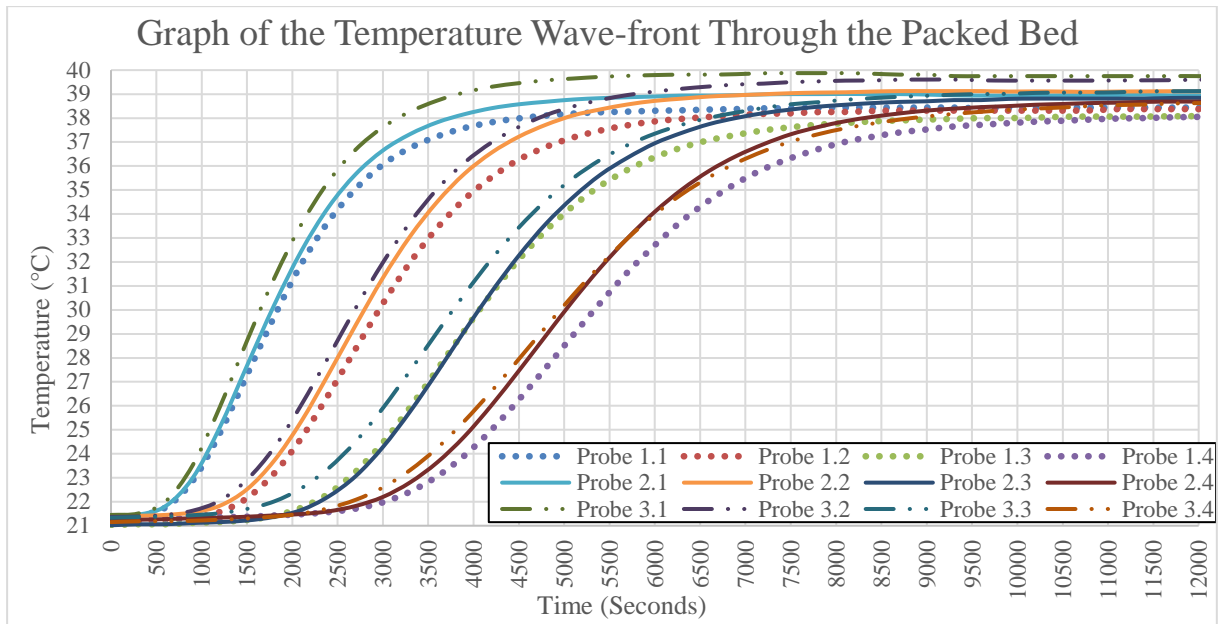


Figure 4.9 Graph of the temperature wave-front through the packed bed

The results indicate that the probes that are the closest to the inlet (1.1, 2.1 and 3.1) increase in temperature first, followed by the temperature probes situated further inside the packed bed. The temperature wave-front curves lag one another by approximately 1200 seconds. The graph also shows that the temperatures in Level_3 are generally higher than for Level_2 and Level_1, which was expected, due to thermal stratification. Figure 4.10 shows the average temperature data for all the thermocouples in each layer and of all the mass flow rates for the inlet temperatures of 40°C, 45°C, 50°C and 55°C, as illustration.

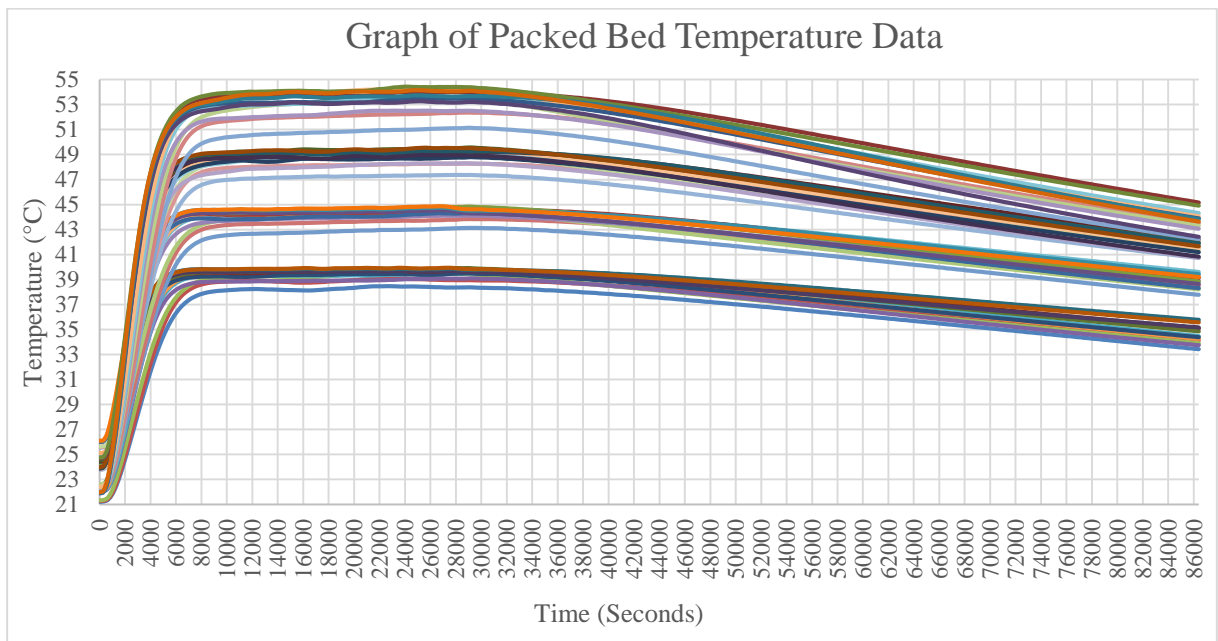


Figure 4.10 Graph of the packed bed temperature data

The data show very similar curves for the inlet temperatures, with larger deviations as the inlet temperature is increased. The data from Figure 4.10 are categorised into the temperature layers Level_1, Level_2 and Level_3, as shown in Figures 4.11, 4.12 and 4.13.

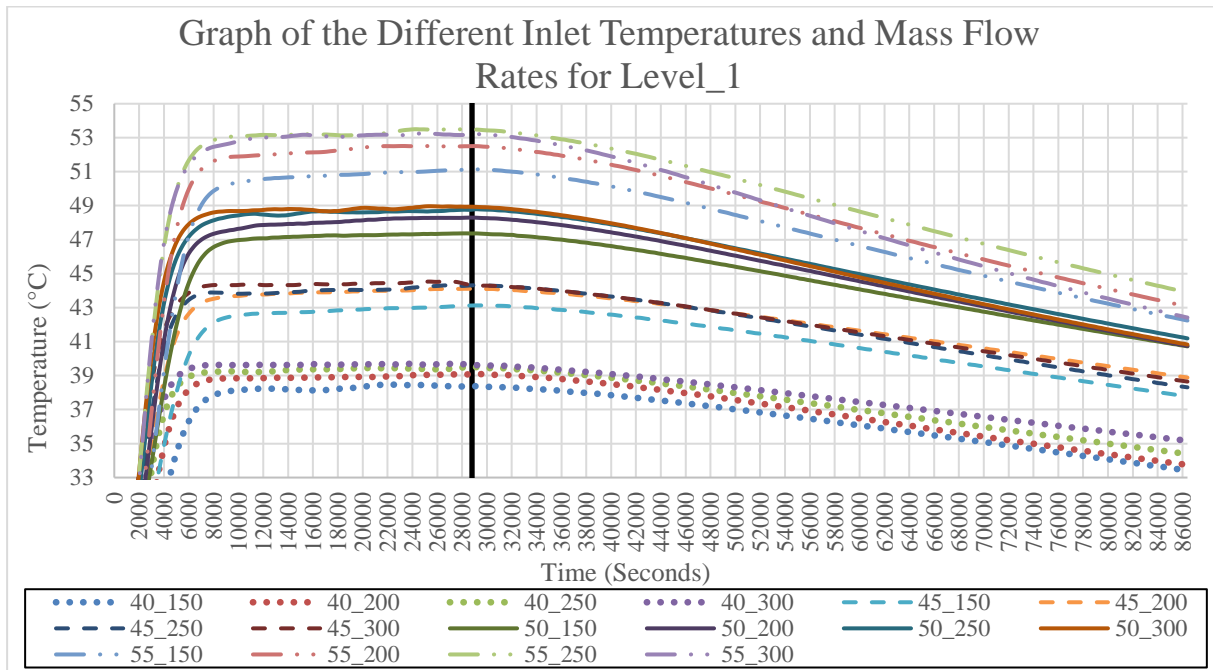


Figure 4.11 Graph of the different inlet temperatures and mass flow rates for Level_1

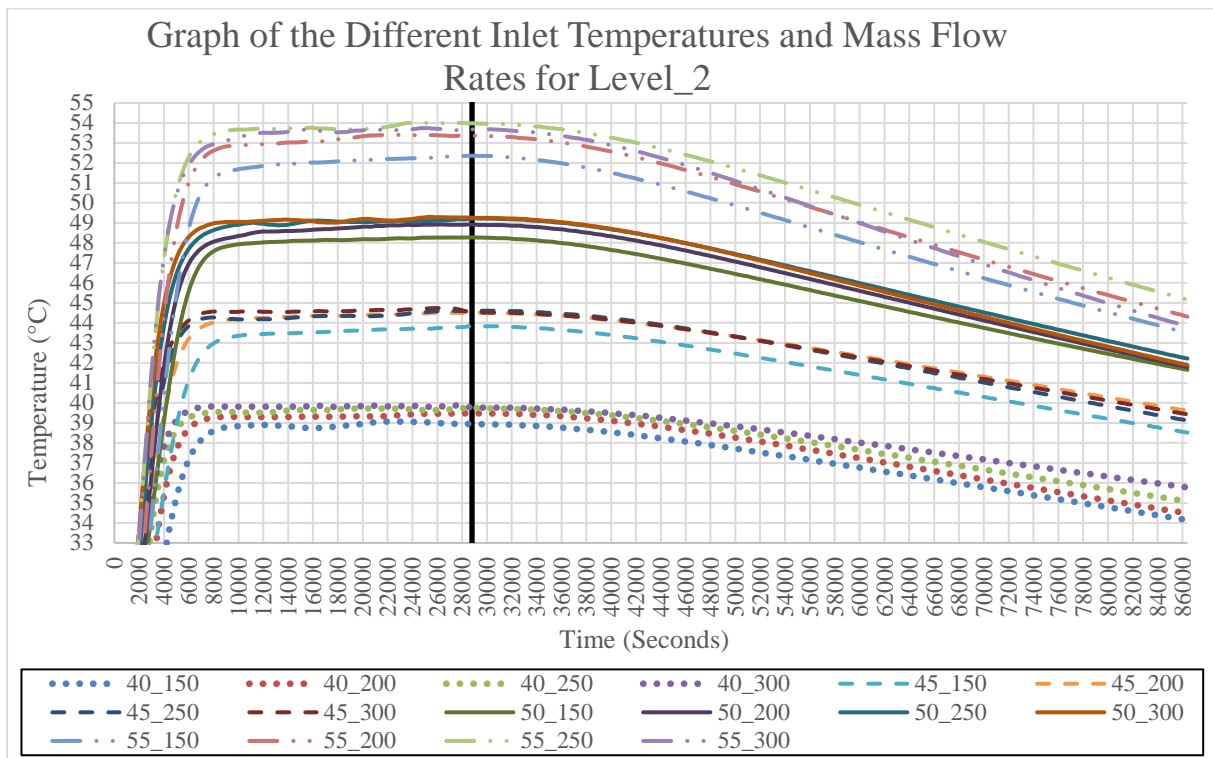


Figure 4.12 Graph of the different inlet temperatures and mass flow rates for Level_2

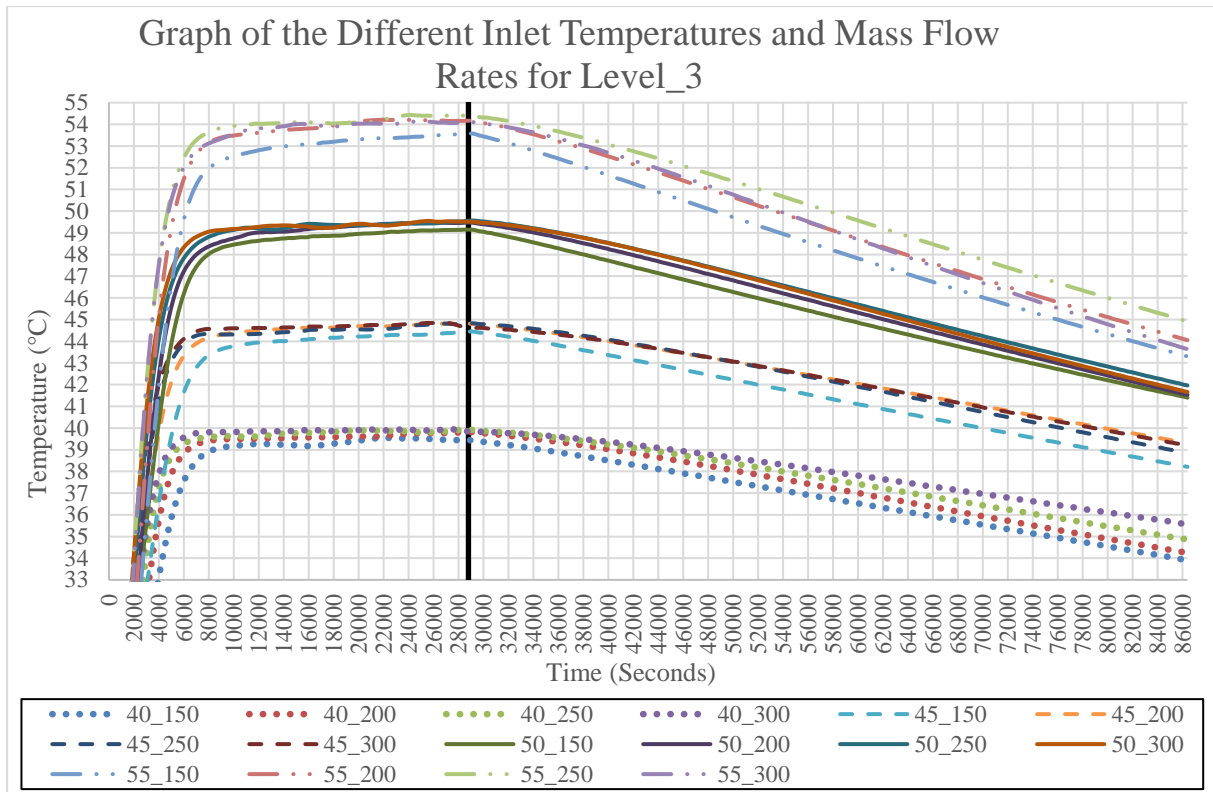


Figure 4.13 Graph of the different inlet temperatures and mass flow rates for Level_3

The results show that for each inlet temperature data set, the temperature lines tend to get closer to one another when moving from Level_1 to Level_3, for the charging phase. The temperature curves are also closer to the inlet temperatures that were used.

For the discharge phase, the data which converged during the charging phase at the higher levels (Level_2 and Level_3), started to diverge. At approximately 40000 seconds (11200 seconds into discharge), the data curves followed a similar pattern to Level_1. When the discharge phase was complete, the temperature of Level_2 was higher than the temperature data of Level_3. This was due to the core of the packed bed retaining the thermal energy and the thermal energy being lost to the environment and the concrete slab. Figures 4.14, 4.15 and 4.16 show the difference between the inlet temperature and the maximum packed bed temperature for a range of mass flow rates, for the respective levels.

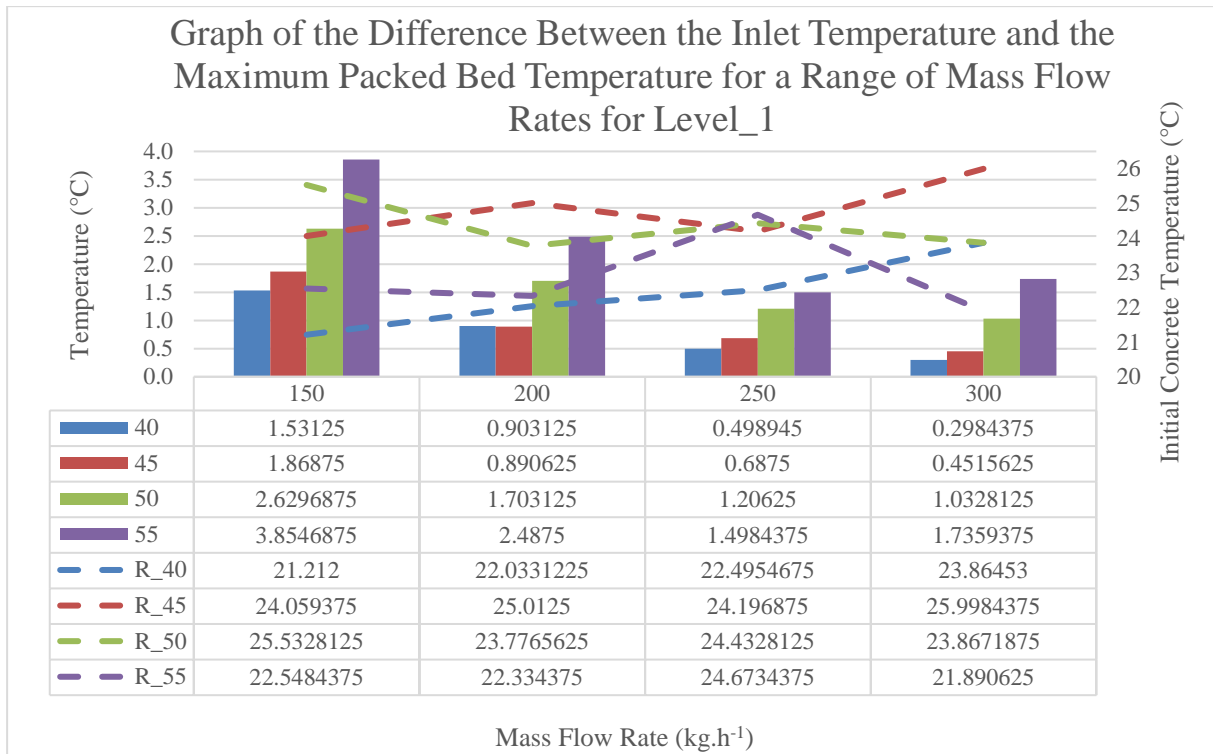


Figure 4.14 Graph of the difference between the inlet temperature and the maximum packed bed temperature, for a range of mass flow rates for Level_1

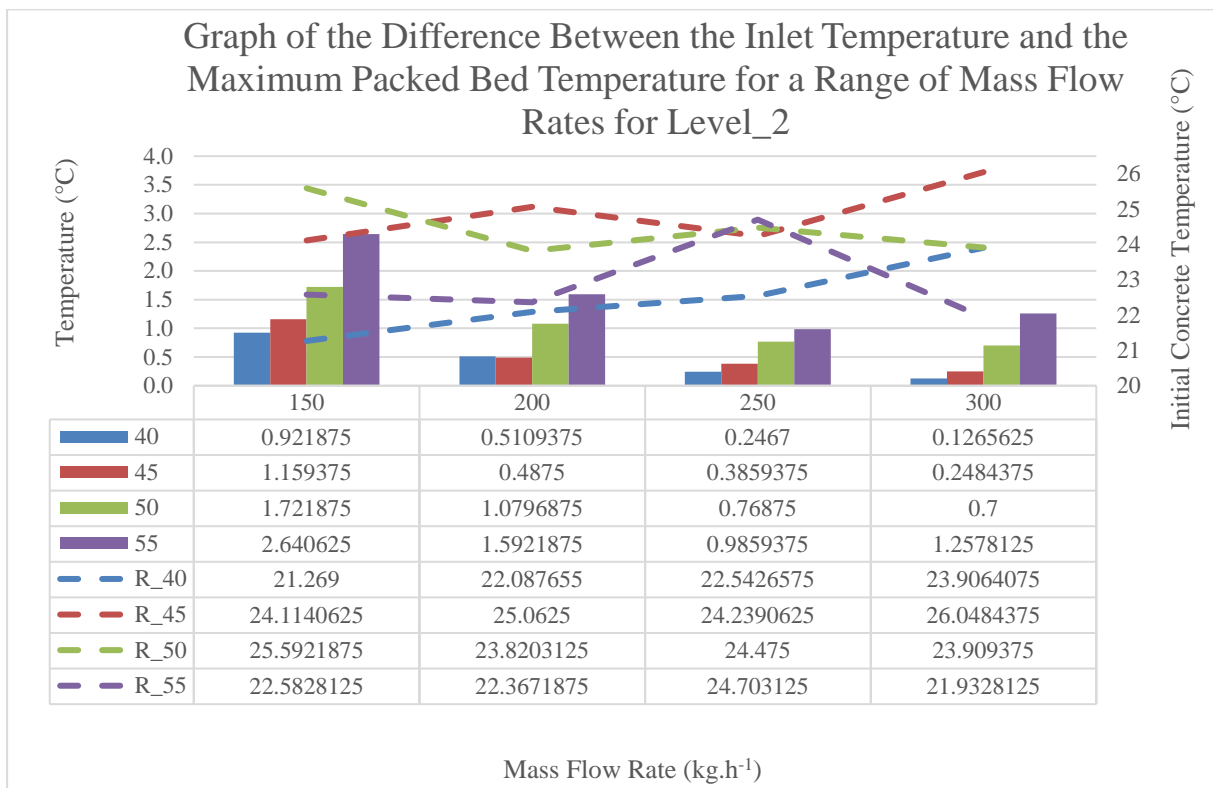


Figure 4.15 Graph of the difference between the inlet temperature and the maximum packed bed temperature, for a range of mass flow rates for Level_2

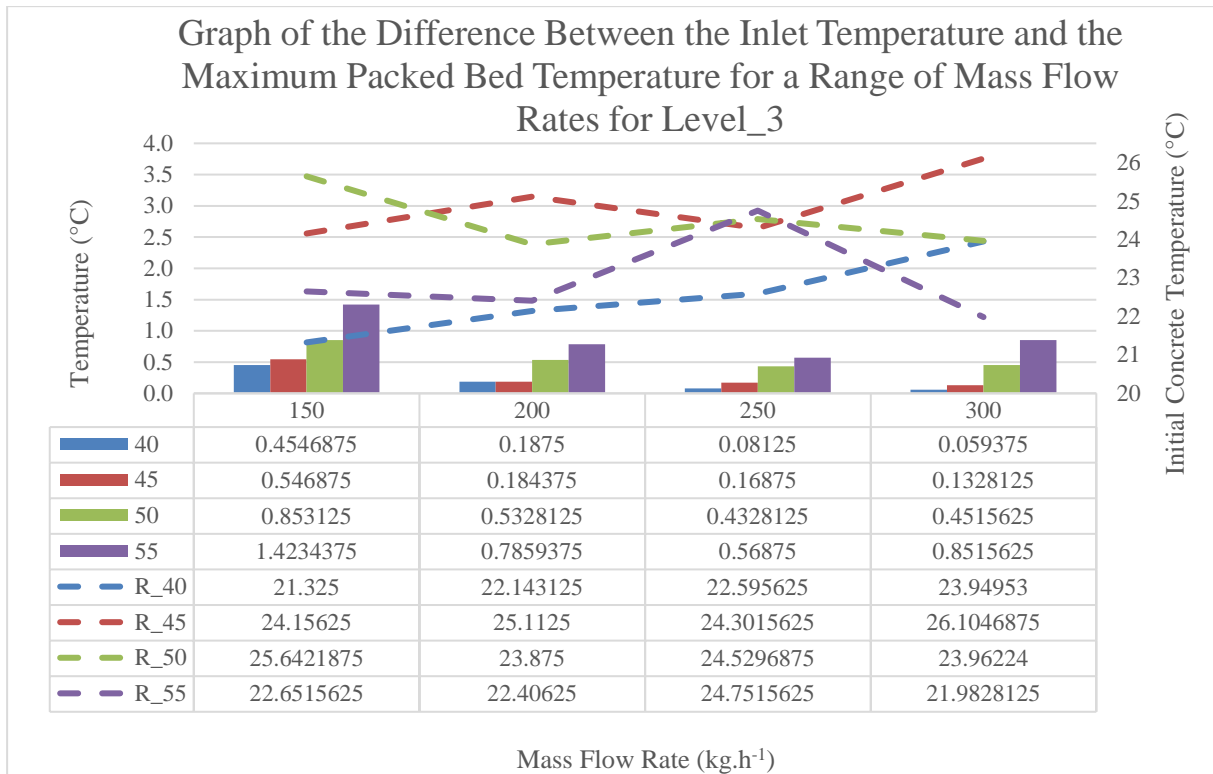


Figure 4.16 Graph of the difference between the inlet temperature and the maximum packed bed temperature, for a range of mass flow rates for Level_3

The results show that, with an increase in mass flow rate through the packed bed, the difference between the maximum temperatures that were obtained in the packed bed and the inlet temperature decreases. The smallest temperature differences were obtained for Level_3. Higher values were obtained for a mass flow rate of 300 kg.h⁻¹, at inlet temperatures of 50°C and 55°C. Figures 4.21 and 4.22 show the photograph and thermograph of the temperature probes in the packed bed and scaled-down room (space).

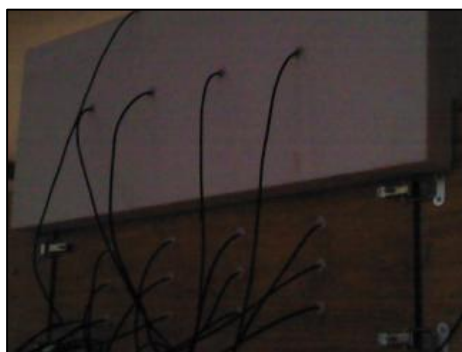


Figure 4.17 Photograph of probes

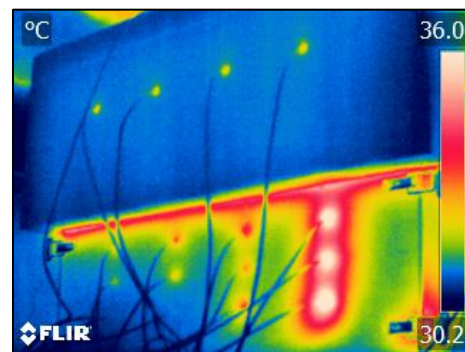


Figure 4.18 Thermograph of probes

The thermograph indicates that temperatures of approximately 36°C were obtained, for the first vertical layer of temperature probes at an inlet temperature of 50°C and mass flow rate of 150 kg.h⁻¹. The amount of thermal energy lost in the initial stages of the packed bed is significant; however, the losses subside when moving down-stream.

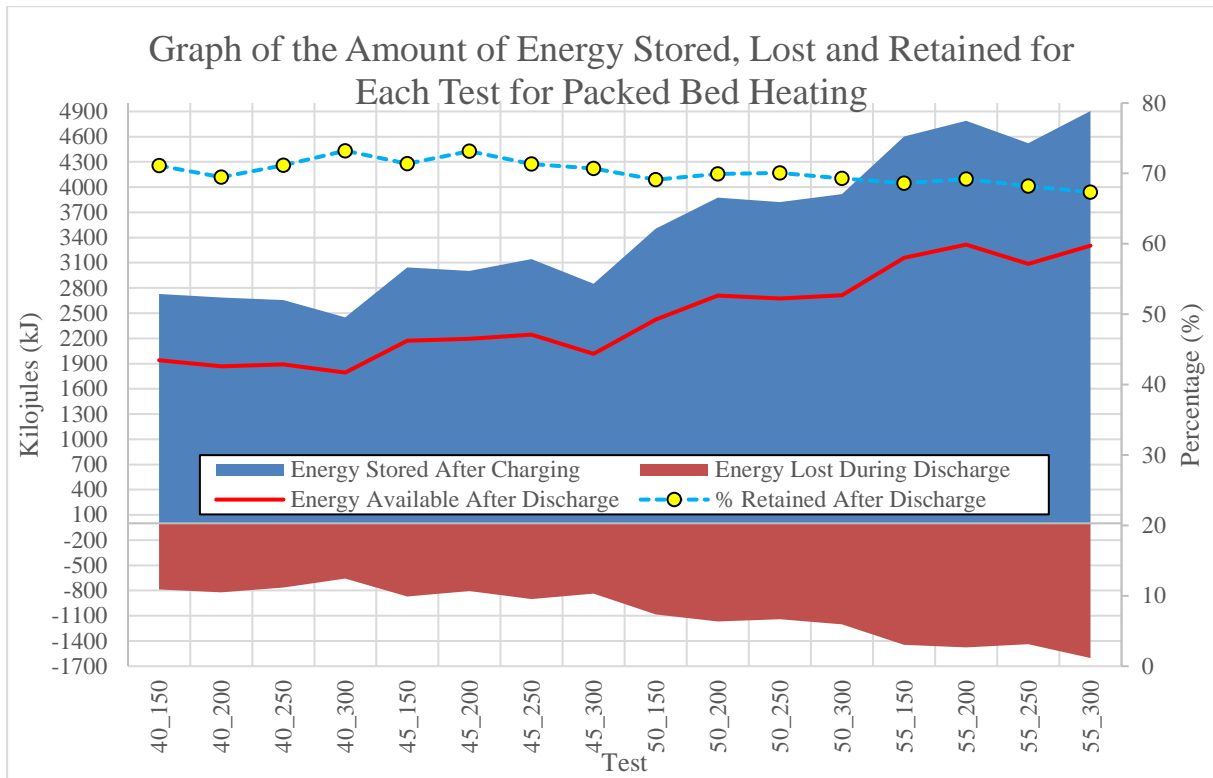


Figure 4.19 Graph of the amount of energy stored, lost and retained for each test for packed bed heating

The results show that with an increase in the inlet temperature and mass flow rate, the energy that is stored after discharge and lost during discharge, as well as the energy that is available after the discharge cycle, increases. The percentage energy that was retained after the discharge cycle decreased slightly with the larger inlet temperatures and mass flow rates. This is expected, as the larger temperature difference between the packed bed and the ambient temperature, promotes energy transfer. The minimum amount of energy retained by the packed bed after the 16-hour discharge cycle was 67.329% and the maximum 73.223%. For all the tests that were conducted, the average energy that was retained by the packed bed was approximately 70.211%.

4.2.3 Concrete slab

The temperature wave-front through the concrete slab can be presented by the individual temperature probes for each test that was conducted. Figure 4.20 shows the temperature wave-front that moves through the concrete slab at an inlet temperature of 40°C and a mass flow rate of 150 kg.m⁻¹.

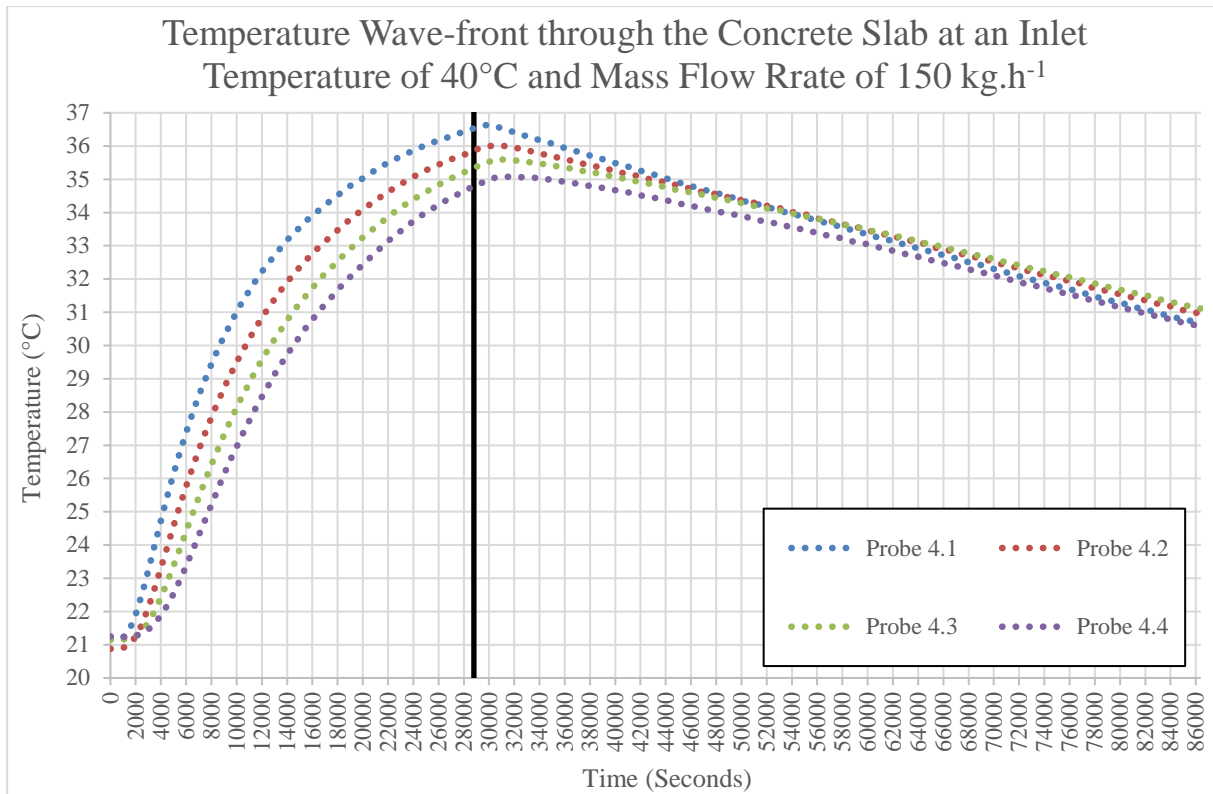


Figure 4.20 Temperature wave-front through the concrete slab

The temperature of the first probe increases first and, as the temperature wave-front moves through the concrete surface, the temperature at each point increases. After the maximum temperature was reached for each probe, the data converged during the discharge phase. The rate at which the temperature wave-front passes through the concrete slab, is dependent on the inlet temperature and the mass flow rate. For the data analysis, an average of the four temperature probes on the concrete surface was used, as shown in Figures 4.21 and 4.22.

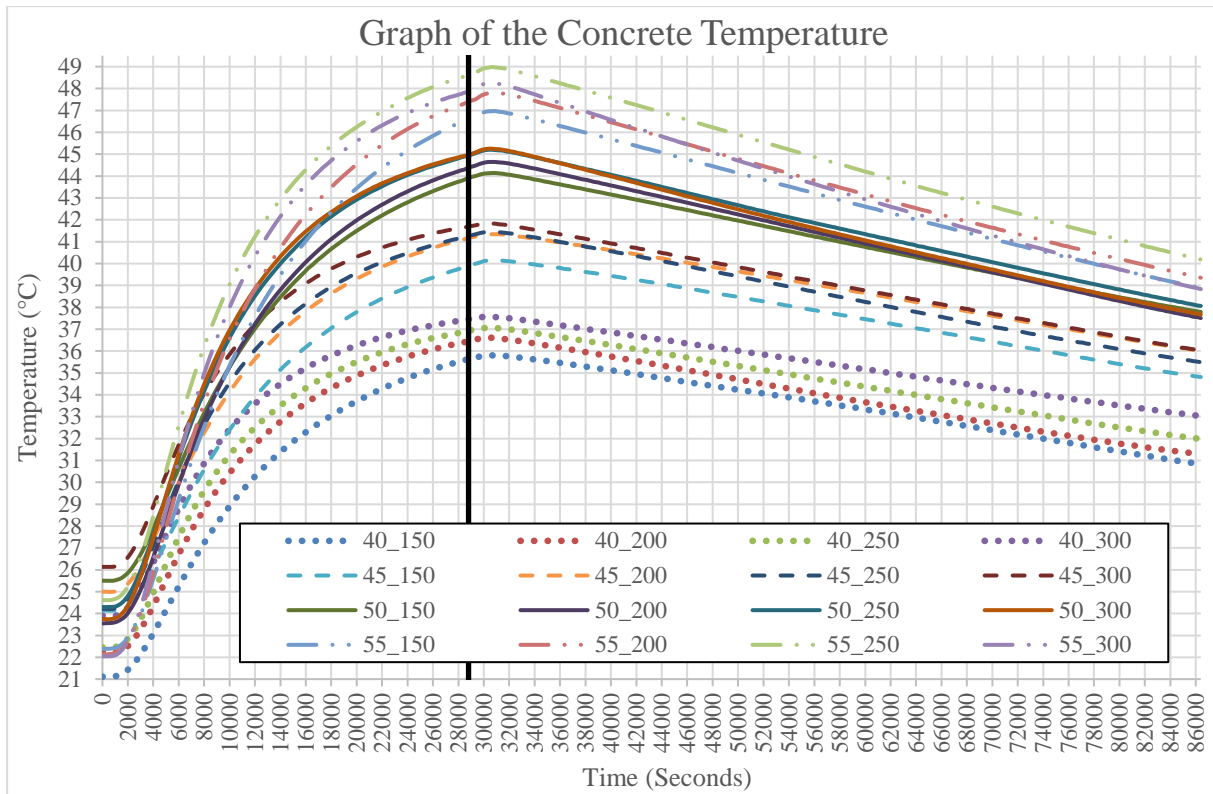


Figure 4.21 Graph of the concrete temperature of the packed bed

The temperature data for the charging and discharging phase follows a similar pattern. The surface temperature increases with an increase in mass flow rate and inlet temperature. The data converges more, with an increase in the inlet temperature during the discharge phase. When the charging phase is complete, the maximum temperature that was obtained on the concrete surface occurred between 30000 and 30900 seconds, which is a lag-time of between 20 and 35 minutes.

The tests with an inlet temperature of 45°C follow a very similar pattern, during the charging phase. During discharge, the gradient of the temperature lines increase slightly, from a high mass flow rate, to a lower mass flow rate. For the inlet temperature of 45°C, Test 45_200 gets very close to the temperature data of 45_250 during the charging phase. During discharge, Test 45_200 crosses the line of 45_250 and at the end of discharge, gets very close to the data of 45_300. A similar tendency is seen with an inlet temperature of 50°C during the charging phase; however, during the discharge phase, the temperature lines change dramatically, but converge at the end of the discharge phase. The tests at 55°C also indicate a similar pattern; however, the temperature data of test 55_250 is already higher than that of 55_300 and it continues throughout the discharge phase. Figure 4.22 takes into account the maximum temperature that was reached by the concrete surface and the inlet temperature that was selected, as well as the initial concrete surface temperature at $t = 0$.

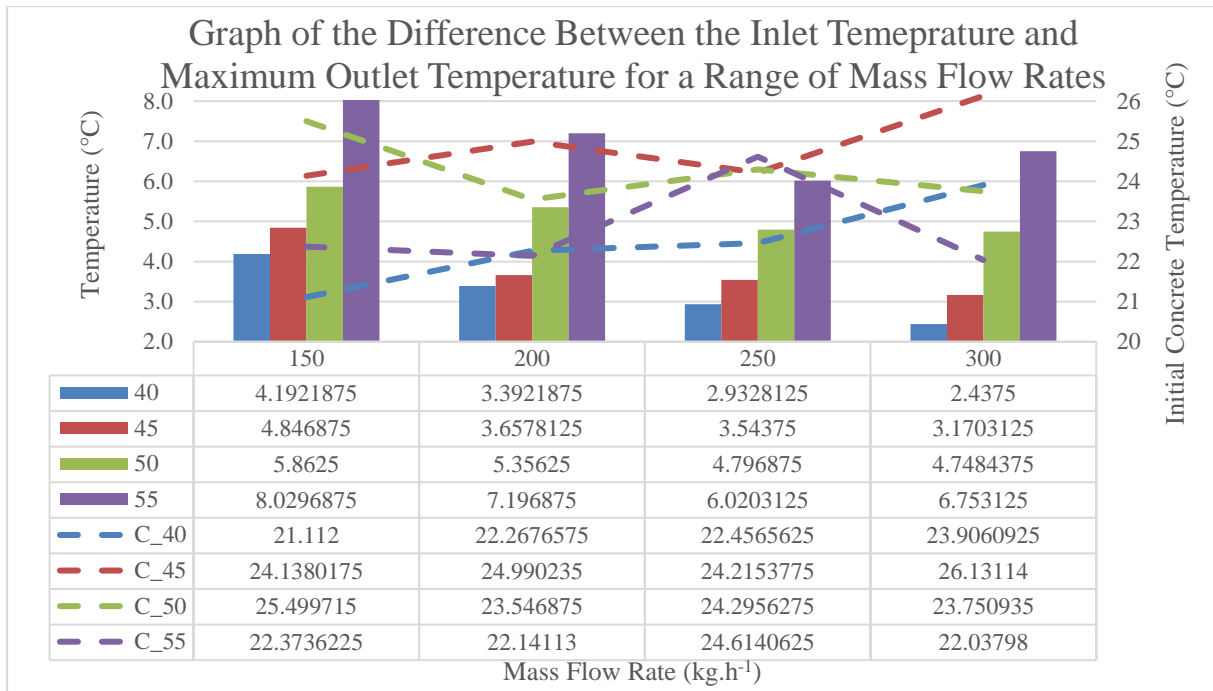


Figure 4.22 Graph of the difference between the inlet temperature and the maximum outlet temperature for a range of mass flow rates and concrete temperature

The results show that, with an increase in the inlet temperature and inlet mass flow rate, the difference between the inlet temperatures and the maximum outlet temperatures also increase. This is not the case with the inlet temperatures of 50°C and 55°C, where the difference is larger for the mass flow rate of 300 kg.h⁻¹, compared to the mass flow rate of 250 kg.h⁻¹. The larger difference is attributed to the ambient temperature. The temperature wave-front through the concrete slab can be graphically presented by temperature data from the probes; however, it cannot actually be seen. Figure 4.23 shows a photograph of the concrete slab, during the initial stages of the charging phase. Figure 4.24 shows a thermograph of the exact same concrete slab. The thermal images offer the opportunity to actually ‘see’ the temperature wave-front, as it progresses through the concrete slab.

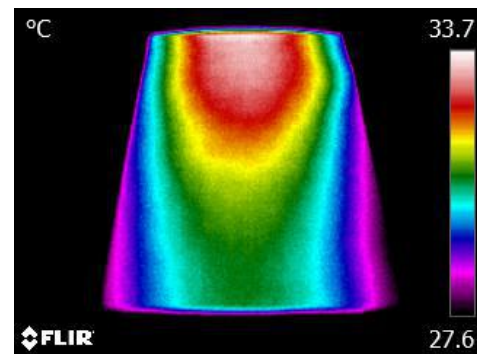


Figure 4.23 Photograph of concrete slab Figure 4.24 Thermograph of concrete slab

Figures 4.25 and 4.26 provide the photograph and thermograph of the concrete slab from the side.



Figure 4.25 Photograph of concrete slab, side view

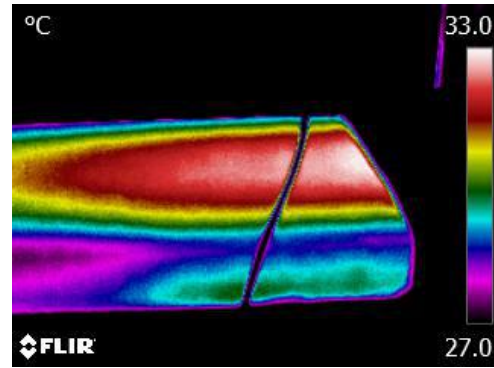


Figure 4.26 Thermograph of concrete slab, side view

The temperature wave-front moves through the core of the concrete slab first, before it progresses through the rest of the slab, until the final temperature profile is visible after discharge, as shown in Figure 4.27.

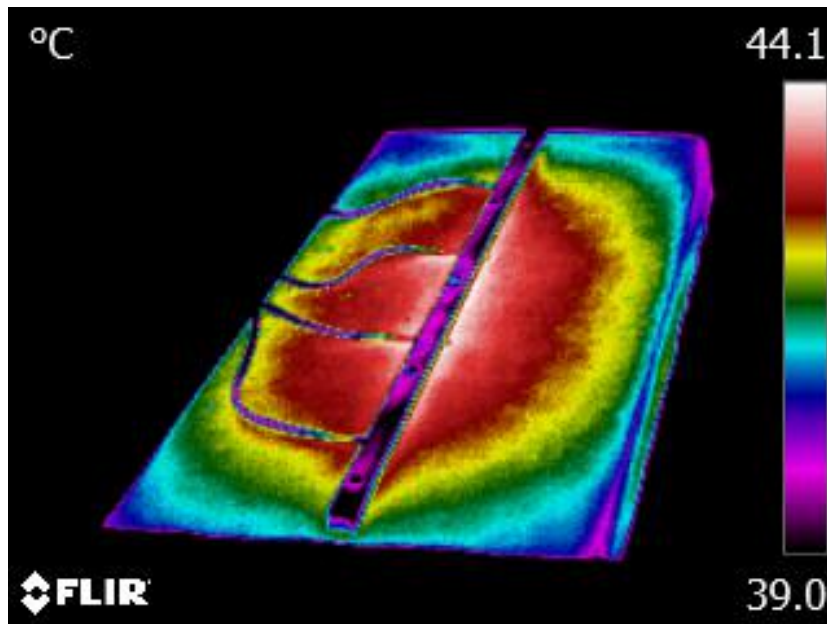


Figure 4.27 Thermograph of the concrete slab after the discharge phase

Figure 4.28 shows the amount of energy produced by the concrete surface during the respective tests. The thermograph of the slab, after discharge, shows that the thermal energy was stored in the core of the packed bed, as well as the concrete surface, and that the thermal energy first dissipated from the sides of the slab and moved progressively to the centre.

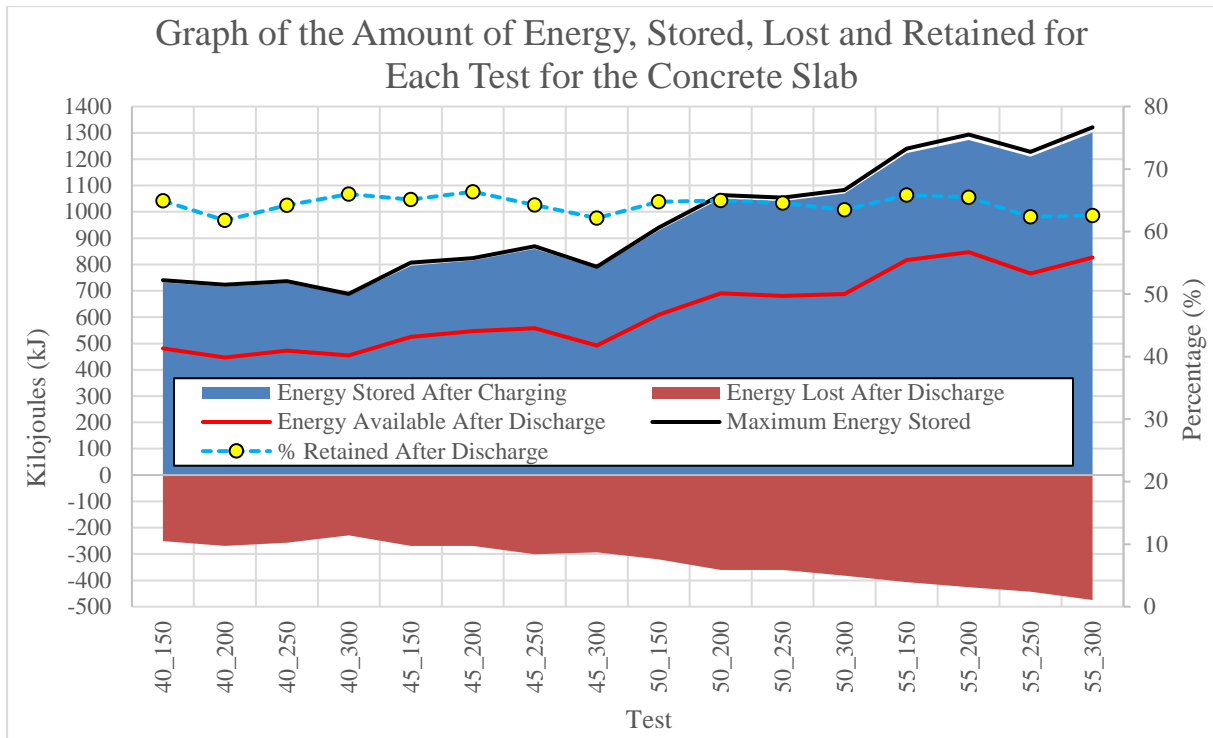


Figure 4.28 Graph of the amount of energy produced and lost for each test of the concrete surface

The amount of energy stored, lost and the amount that is available after discharge increases, with an increase in the mass flow rate and inlet temperature. The maximum energy that is stored in the concrete slab, occurs 20 – 35 minutes into the discharge phase. This results in an average energy increase of approximately 1.202% for the concrete surface. The data trends are very similar to those of the packed bed, although the ability to retain the thermal energy is slightly worse; however, a minimum retention capacity of 61.790% and a maximum of 66.371% was achieved, with an average thermal retention of 64.302%.

4.2.4 Space

The space temperature data of the packed bed is shown in Figure 4.29. The space temperature provided the data of how efficiently the packed bed system actually worked.

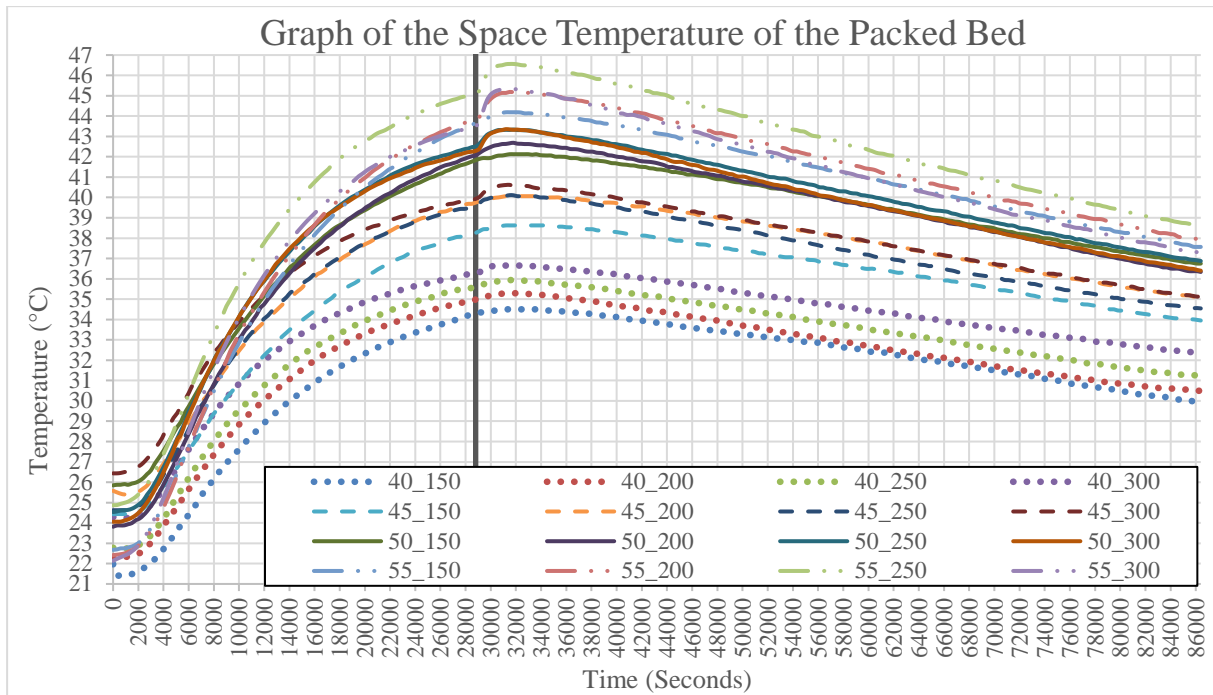


Figure 4.29 Space temperature data of the packed bed

The temperature curves of the space temperature was similar to that of the concrete slab; however, the temperatures were lower. The charging phase for the respective data sets follows very similar curves, until the charging phase is complete. The maximum space temperatures are reached between 30900 and 32100 seconds. This shows a lag-time of between 35 and 55 minutes from when the charging phase was complete. This indicates that, as the concrete surface reaches its maximum after a lag time of between 20 to 35 minutes, the maximum space temperature is initiated. The initial space temperature data, the difference between the inlet temperature and the maximum space temperature for a range of mass flow rates, are provided in Figure 4.30.

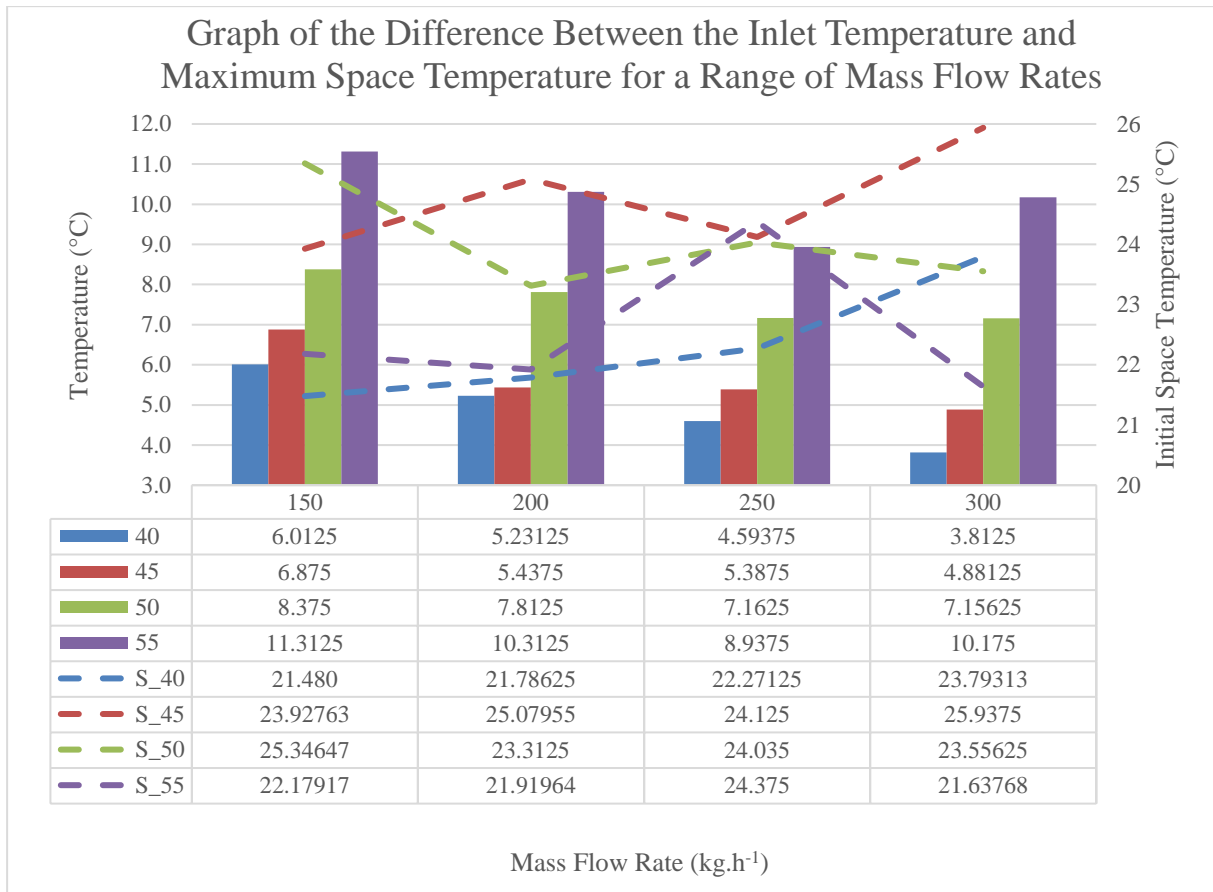


Figure 4.30 Graph of the difference between the inlet temperature and the maximum space temperature for a range for mass flow rates

The inlet temperature of 40°C shows that, as the mass flow rate increases, the space temperature moves closer to the selected inlet temperature.

The inlet temperature of 45°C had a higher temperature for the mass flow rate of 200 kg.h⁻¹, than the mass flow rate of 250 kg.h⁻¹, during discharge. The initial space temperature of test 40_200 is higher than that of Test 40_250. The same results are obtained for the inlet temperature of 50°C.

The inlet temperature of 55°C shows that the initial space temperature, at a flow rate of 250 kg.h⁻¹, is 2.74°C higher than for the flow rate of 300 kg.h⁻¹. Figure 4.31 shows the maximum space temperature that was achieved during each test, compared to the ambient temperature conditions at the specific space temperature.

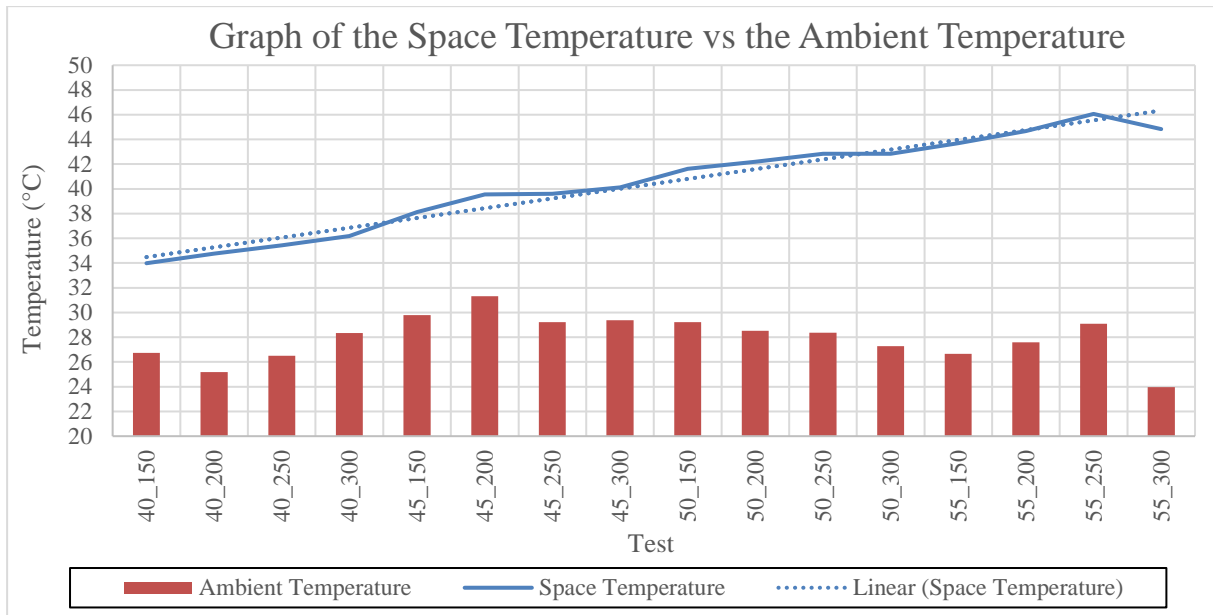


Figure 4.31 Graph of the space temperature vs the ambient temperature

The results indicate that the higher inlet temperatures and mass flow rates provide a reasonable increase in the space temperature, with an average increase of 0.79°C per test. The first Test, 40_150, provided an increase of 7.25°C for the space temperature, whereas the final Test, 55_30, delivered a temperature increase of 20.85°C above the ambient conditions.

Figure 4.32 shows a photograph of the contact section between the polystyrene and the packed bed, and Figure 4.33 shows the thermograph of the same section, both showing the thermal losses out of the scaled-down room.

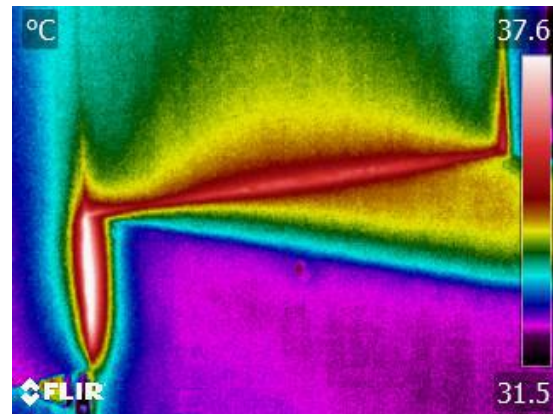


Figure 4.32 Photograph of thermal losses Figure 4.33 Thermograph of thermal losses

The thermograph show that a temperature of 37.6°C is reached at the contact region, just before the end of the charging phase (Time of day - 15:54), for an inlet temperature of 55°C and a mass flow rate of $300\text{ kg}\cdot\text{h}^{-1}$. A fair amount of thermal energy was lost at the contact surface between the polystyrene scaled-down room section and the packed bed. This was because the polystyrene section had been continuously removed, in order to take the thermographs of the

concrete surface; hence, it could not be kept insulated at the contact sections. The amount of energy transferred into the space area, as well as the amount lost, is depicted in.

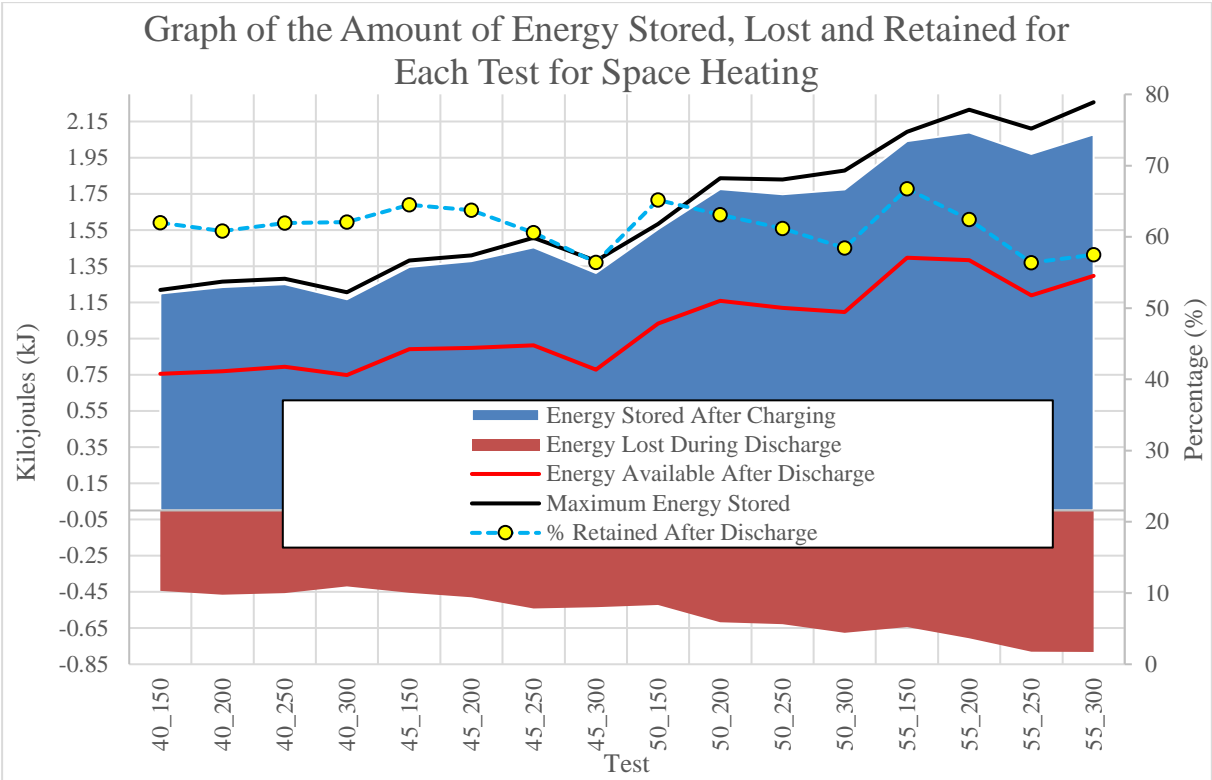


Figure 4.34 Graph of the amount of energy produced and lost for each test for space heating

The amount of energy absorbed during the charging phase was much less than that of the packed bed and the concrete slab, because of the lower density of air; however, the ability to retain thermal energy was mostly dependant on the 75 mm high-density polystyrene. Nevertheless, the scaled-down room reached its maximum energy content approximately 35 – 55 minutes into the discharge phase, with an average increase of approximately 3.764% for the lag-time period (from the end of the charging phase, to the maximum energy content achieved). The minimum energy increase was 1.573% and the maximum 7.871%.

The ability of the space section to retain thermal energy, varies considerably for the different tests. On average, the percentage retention of 64.432% was achieved after the discharge cycle.

4.2.5 Energy Balance

The energy balance of the charging phase of the horizontal, uni-directional packed bed, with an inlet temperature of 40°C and mass flow rate of 150 kg.h⁻¹ is shown in Figure 4.35.

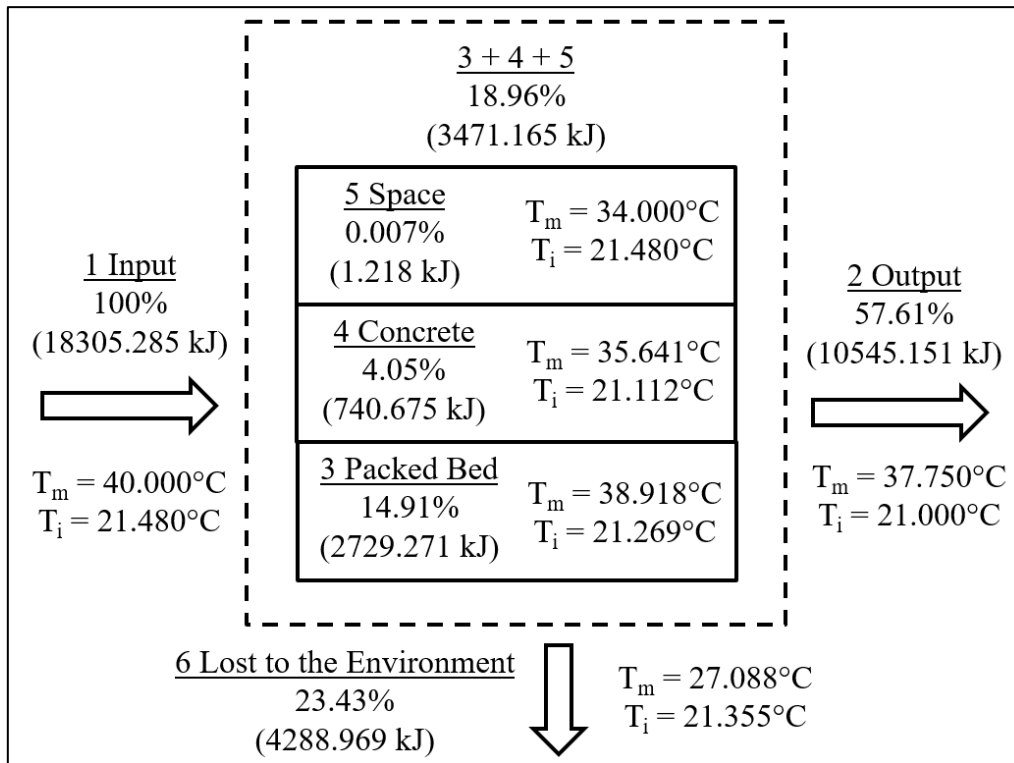


Figure 4.35 The energy balance of the horizontal, uni-directional packed bed, with an inlet temperature of 40°C and mass flow rate of 150 kg.h⁻¹

The energy balance shows that of the 100% of energy flowing into the system, 57.61% of the energy flows out, 18.96% is stored and 23.43% is lost to the environment. The amount of energy that was stored was made up of 14.91% for the packed bed, 4.05% for the concrete slab and a mere 0.007% for the space. This shows that of the 100% of thermal energy (18305.285 kJ) coming into the system, only 0.007% (1.218 kJ) is finally obtained in the space section.

The performance of the system appears to be low; however, it must be noted that the available energy in the space region was calculated, based on the results of the charging phase alone and that the energy that was released during the discharge phase, was not accounted for. There was no energy supplied to the packed bed during the discharge phase and the available energy that was stored within it, as well as the concrete slab, was continuously transferred to the space region and the environment (losses). Although a reduction in the space temperature occurred during the discharge phase, the temperature drop of the space region would have been much greater, had it not been for the TES system. It should also be taken into account that for all the tests that were conducted, the system was charged, and then fully discharged before the next test commenced. This testing procedure does not utilise the stored energy within the packed bed for the next charging session, which will lower the temperature gradients and increase the thermal energy transfer in the system, due to the initial temperatures being higher. The energy balance data of the different tests are summarised in Appendix M.

4.3 Validation

The validation of the results involved comparing the following data sets, namely: (i) the empirical performance effects data, with similar data from literature, (ii) the empirical temperature data of concrete, with the thermographs of the respective concrete surfaces, and (iii) the empirical test data, with the numerical data, which were simulated for the horizontal, uni-directional packed bed.

4.3.1 Empirical vs. literature

The empirical data that were compared with the values obtained from literature, were for the porosity of the packed bed and the rock properties. The rock properties included the density and the specific heat capacity.

4.3.1.1 Porosity

The porosity of the packed bed was calculated and described in Section 3.3.3.1. Table 4.2 provides a summary of the results that were obtained.

Table 4.2 Summary of the results obtained for the porosity of the packed bed

Test Number:		1	2	3	
Mass of water	m_w	38.560	37.730	38.910	kg
Volume of water	V_w	0.0386	0.0377	0.0389	m^3
Total volume	V_t	0.0873	0.0867	0.0873	m^3
Porosity	ε	0.4417	0.4352	0.4457	
Average porosity of the packed bed = 0.4409					

The average porosity of the packed bed was calculated to be 0.4409. The value is in range with the values proposed by Kaviani (2012), namely, 0.44 – 0.49, for crushed rock.

4.3.1.2 Rock properties

The density of the 19 mm dolerite rock particles that were used as the TES material, was calculated according to the method described in Section 3.3.3.3. Table 4.3 provides a summary of the results that were obtained.

Table 4.3 Summary of the results obtained for the density of the rocks

Test Number:		1	2	3	4	5	
Mass of rocks	m_r	1.348	1.355	1.229	1.128	1.275	kg
Mass of rocks and water	m_{r+w}	1.845	1.827	1.665	1.538	1.740	kg
Mass of water	m_w	0.497	0.472	0.436	0.410	0.465	kg
Total volume	V_t	985.000	957.000	871.000	807.000	915.000	cm^3
Volume of water	V_w	497.000	472.000	436.000	410.000	465.000	cm^3

Volume of rocks	V_r	488.000	485.000	435.000	397.000	450.000	cm^3
Density of rocks	ρ_r	2762.295	2793.814	2825.287	2841.310	2833.333	kg.m^3
Average density of the rocks = 2811.208 kg.m^3							

An average density of 2811.208 kg.m^3 was obtained. This falls well between the values obtained by Allen (2010) of 2657 kg.m^3 , for a dolerite, which was extracted south of Kenhardt, in the Northern Cape, and that obtained by Jones (2003) of 2960 kg.m^3 , for a Karoo dolerite.

Table 4.4 provides a summary of the results that were obtained to calculate the specific heat capacity of the rocks that were used in the packed bed.

Table 4.4 Summary of the results obtained for the specific heat capacity of the rocks

Test Number:		1	2	3	
Mass of rocks	m_r	8.044	8.808	7.522	kg
Mass of rocks and water	m_{r+w}	10.702	11.802	10.554	kg
Mass of water	m_w	2.658	2.994	3.032	kg
Initial temperature of rocks	T_r	24.375	19.188	19.25	$^{\circ}\text{C}$
Initial temperature of water	T_w	62.063	64.375	65.313	$^{\circ}\text{C}$
Temperature of rocks and water	T_{r+w}	44.813	45.931	46.679	$^{\circ}\text{C}$
Specific heat capacity of water	$c_w @20$	4.182	4.182	4.182	$\text{kJ.kg}^{-1}.\text{K}^{-1}$
Specific heat capacity of rocks	c_r	1.166	0.980	1.145	$\text{kJ.kg}^{-1}.\text{K}^{-1}$
Average specific heat capacity of the rocks = 1097.321 $\text{J.kg}^{-1}.\text{K}^{-1}$					

The tests concluded that an average specific heat capacity value of 1097.321 $\text{J.kg}^{-1}.\text{K}^{-1}$ was obtained for the 19 mm dolerite rocks, at an average temperature of between 30 $^{\circ}\text{C}$ and 35 $^{\circ}\text{C}$ (difference between initial and final). It must also be borne in mind that the specific heat capacity of rocks, increase quite rapidly with temperature. The specific heat capacity obtained by Allen (2010) was 839 $\text{J.kg}^{-1}.\text{K}^{-1}$. The difference in the results, was partly due to the area from which the rocks were obtained and mainly the experimental uncertainty and error, such as water mass measurement or stratification. Özkahraman *et al.* (2004) suggested that the product of specific heat capacity and density, for TES applications, should ideally be greater than 1 $\text{MJ.m}^{-3}.\text{K}^{-1}$. The heat capacity (the product of specific heat capacity and density) of the rocks amounts to 3.085 $\text{MJ.m}^{-3}.\text{K}^{-1}$.

4.3.2 Empirical vs. thermography

The empirical and thermography data that were used for validation, were obtained at the end of the discharge cycle. The empirical data of the surface probes consisted of four data points, from which the maximum temperature data were extracted. The thermography data were comprised of four to six thermographs per test, each containing the maximum surface temperature of the concrete slab. An example of the thermal images that were captured is depicted in Figure 4.36.

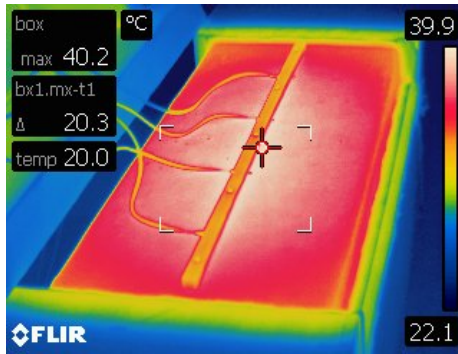


Figure 4.36 A thermograph of the concrete slab, at an inlet temperature of 55°C and a mass flow rate of 300 kg.h⁻¹

The temperature data of the concrete surface probes and the average results of the thermographs are shown in Figure 4.37.

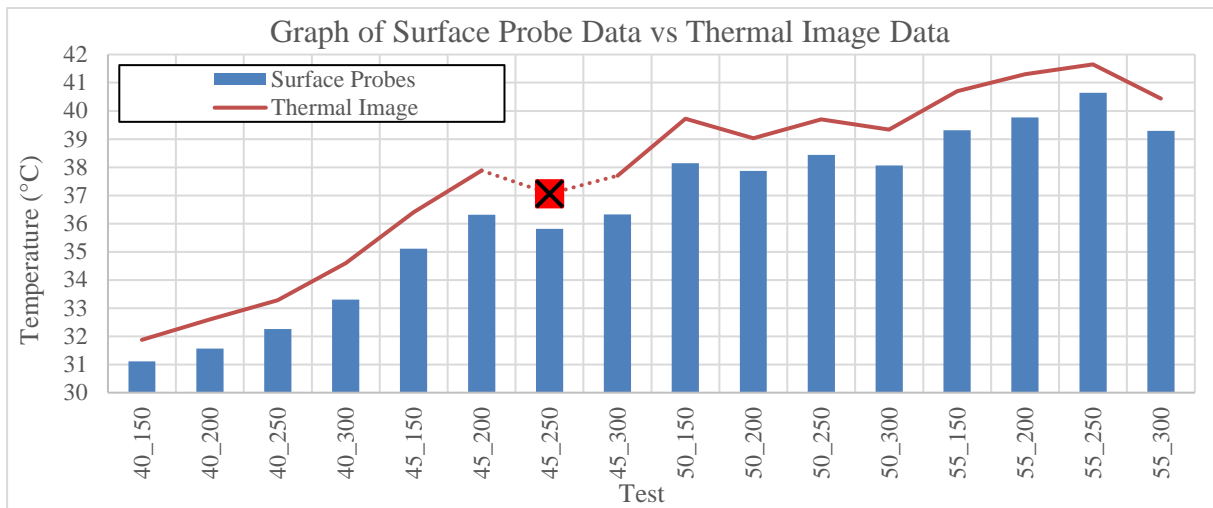


Figure 4.37 Graph of surface probe data vs thermal image data

The “x” in the data set, was because there was no thermal image data for the specific test; however, the average difference between the surface probe data and the thermal image data, was used to complete the data curve, in order to study the trends in the data. The results indicate that the trend of the temperature measured by the probes and thermal camera were similar. The thermal image data was, on average, 1.247°C higher than the surface probe data. The lower surface probe results could have been caused by the surface probes not making full contact with the concrete surface or the emissivity setting on the thermal camera that was used at 0.95. The average percentage error between the surface probes and thermal images amounted to 3.302%.

4.3.3 Empirical vs. numerical

The results of the empirical data had to be compared with the results of the numerical data, in order to evaluate the accuracy and validity of the numerical design that was developed.

4.3.3.1 Inlet and outlet

The data of the inlet and outlet temperatures were only considered for the charging phase, as the discharge temperature data for the inlet and outlet probes were not required. The inlet temperature data of the empirical and numerical designs are presented in Figure 4.38.

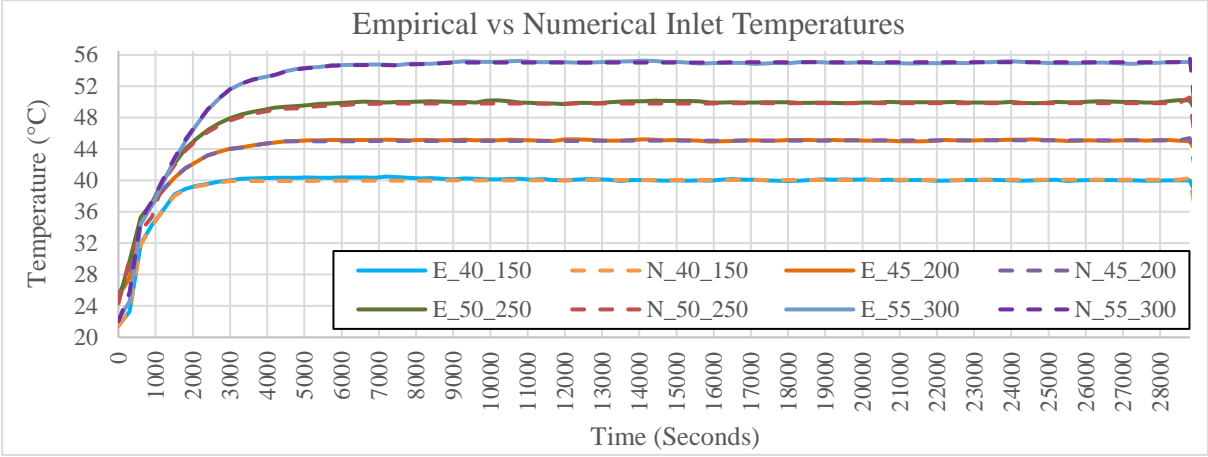


Figure 4.38 Empirical vs numerical inlet temperatures

The results indicate that the numerical data curves follow the empirical data curves very well. This was because a heating table was developed, as an inlet to the numerical model, in order to mimic the shape of the empirical curve. The development of the heating table is described in Appendix H. Figure 4.39 provides the percentage error between the inlet temperatures of the empirical and numerical data.

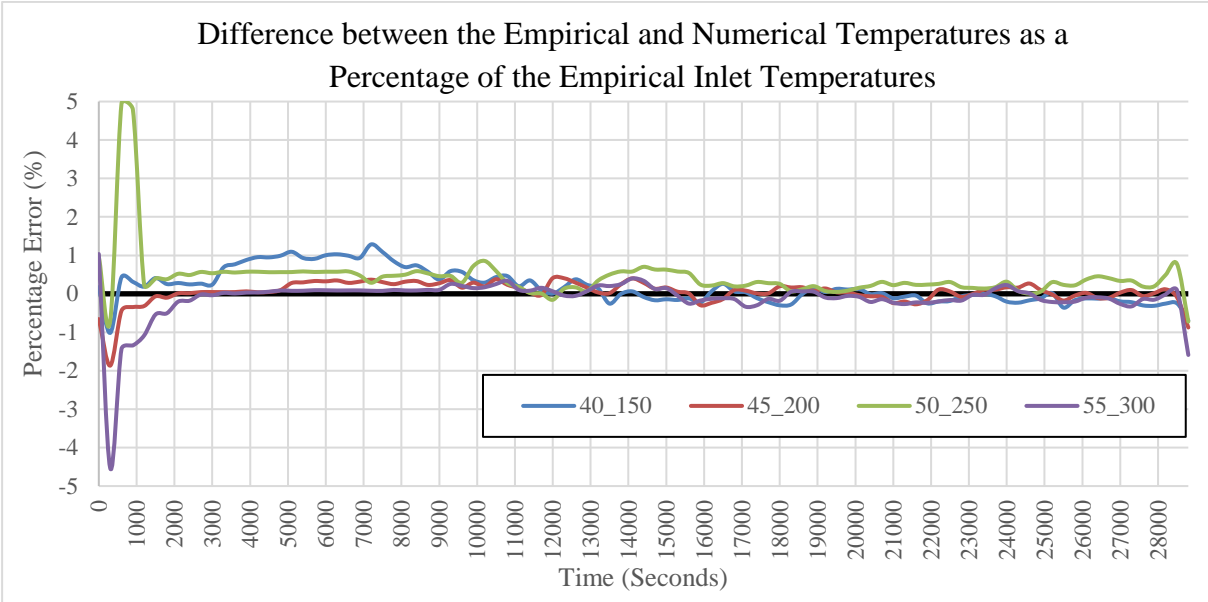


Figure 4.39 Difference between the empirical and numerical temperatures as a percentage of the empirical inlet temperatures

The results from the graph indicate that the percentage error, during the first 900 seconds (15 minutes), was close to 5% for the Test cases 50_250 and 55_300. This was due to the initial steep gradient of heating at the start of each test. The data stabilised, as the heating process continued. An average percentage error of 0.138% was achieved for the inlet temperature data. Figure 4.40 shows a comparison of the outlet temperature data of the empirical and numerical results.

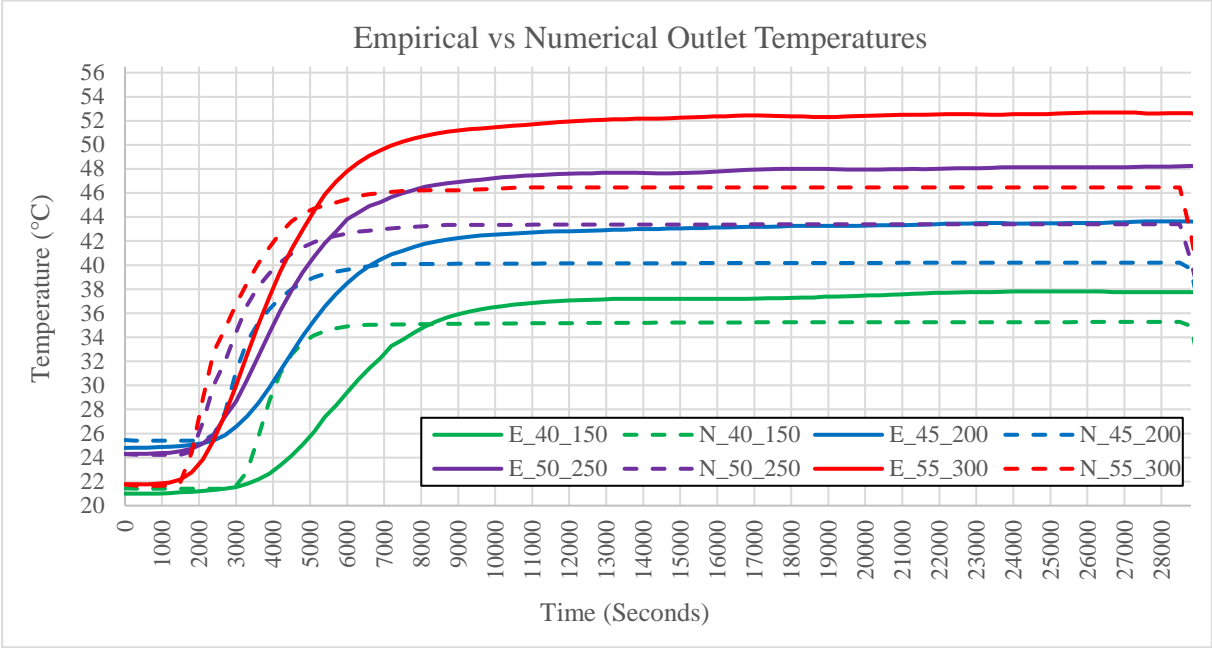


Figure 4.40 Empirical vs numerical data of the outlet temperatures

The curves of the numerical data followed a similar pattern; however, the numerical outlet temperature reached a plateau in a shorter period of time, which can be attributed to the leakage losses in the empirical design. The maximum outlet temperature of the numerical tests was lower, compared to the empirical tests. With an increase in the inlet temperature and mass flow rate, the temperature difference between the numerical and empirical data moved further apart. This could be due to the thermal conductivity of the material not being tested, as values from literature was used, which could result in a larger loss of thermal energy at higher mass flow rates and temperatures. Figure 4.41 shows the percentage error that was obtained for the outlet temperatures of the empirical and numerical data.

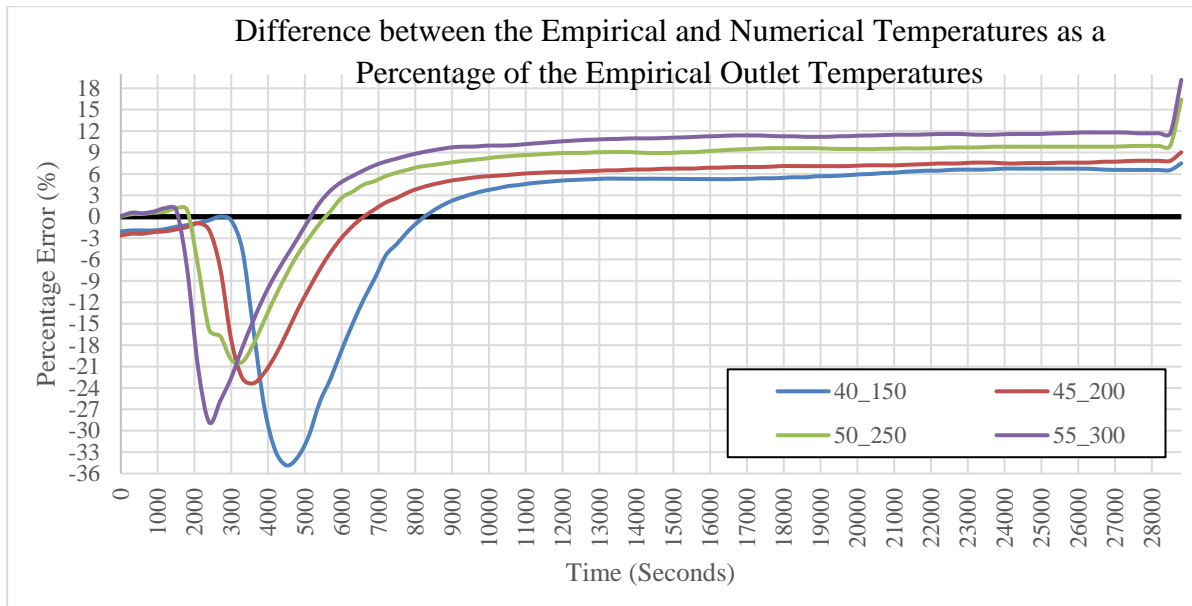


Figure 4.41 Difference between the empirical and numerical temperatures as a percentage of the empirical outlet temperatures

The error stayed constant for the first 1500 seconds (25 minutes) and then the numerical data under-predicted the temperature by up to -34.85%. The data stabilised from 12000 seconds and gradually increased, until the charging phase was complete. The error increased as the inlet temperature and mass flow rate increased for each test. Table 4.5 provides a summary of the percentage error of the numerical model for the inlet and outlet temperature data for the charging phase.

Table 4.5 Summary of the percentage error of the numerical model for the inlet and outlet temperature data

Test	Inlet				Outlet			
	40_150	45_200	50_250	55_300	40_150	45_200	50_250	55_300
Average 0-28800	0.185	0.046	0.432	-0.112	0.782	3.148	5.694	6.970
28800	-0.696	-0.876	-0.724	-1.590	7.488	9.042	16.413	19.181

The average percentage error for the inlet and outlet curves, as well as the final results at the end of the charging phase, tend to be more accurate for the lower inlet temperatures and mass flow rates.

4.3.3.2 Packed bed

The temperature data of the packed bed involved the charging and discharging phase. The following graphs represent the average temperature data and percentage error of Level_1, Level_2 and Level_3.

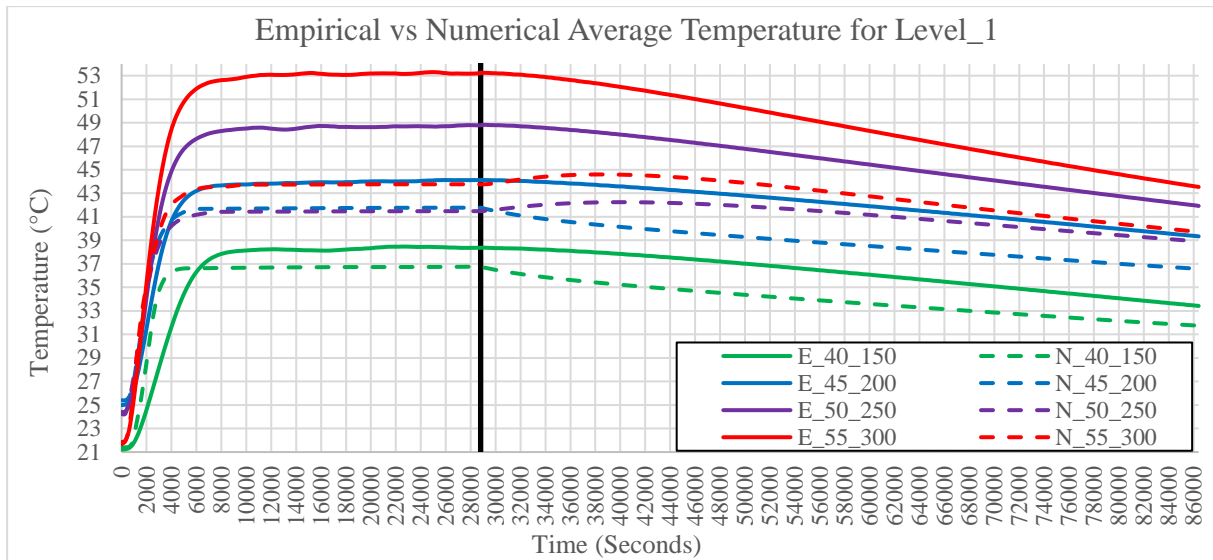


Figure 4.42 Empirical vs numerical average temperature for Level_1

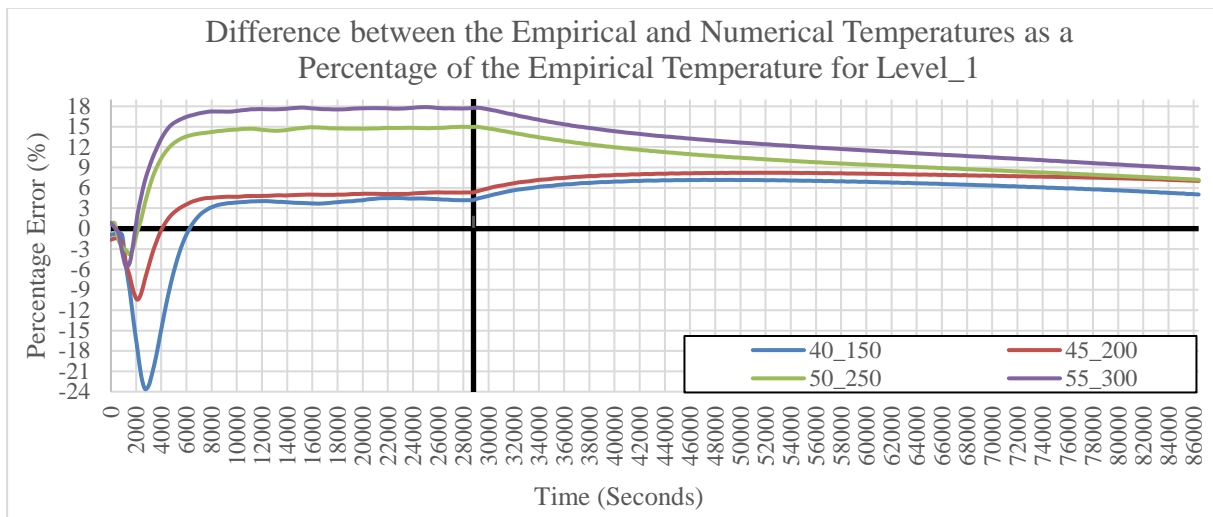


Figure 4.43 Difference between the empirical and numerical temperatures as a percentage of the empirical temperature for Level_1

Figure 4.42 indicates that the numerical curves for Tests 40_150 and 45_200 follow a similar pattern, compared to the empirical results, and under-predicts the temperature by approximately 2°C. However, the numerical curves of Tests 50_250 and 55_300 show that the increase in the inlet temperature and mass flow rate provides a much lower temperature, compared to the empirical curves. In the discharge phase, the numerical curves of Tests 50_250 and 55_300 actually increase slightly. The percentage error for the lower temperatures and mass flow rates (40_150 and 45_200) are higher during the initial stage of the charging phase, but it decreases, as the charging phase continues. During the discharge phase, the error of the tests converges to a final percentage error value of between 5.027% and 8.778%.

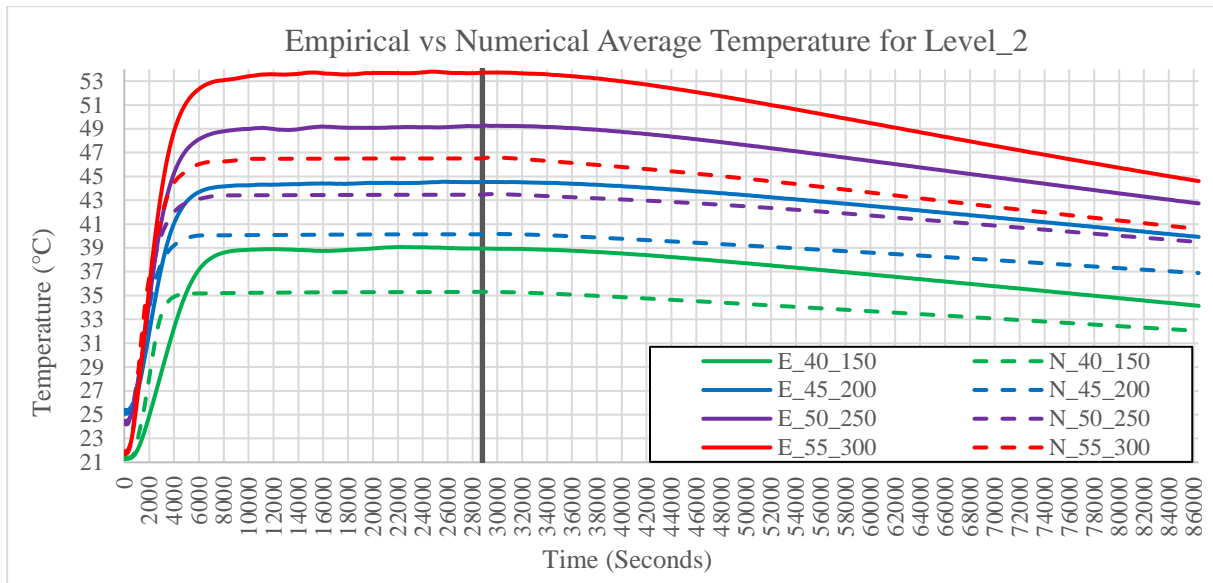


Figure 4.44 Empirical vs numerical average temperature for Level_2

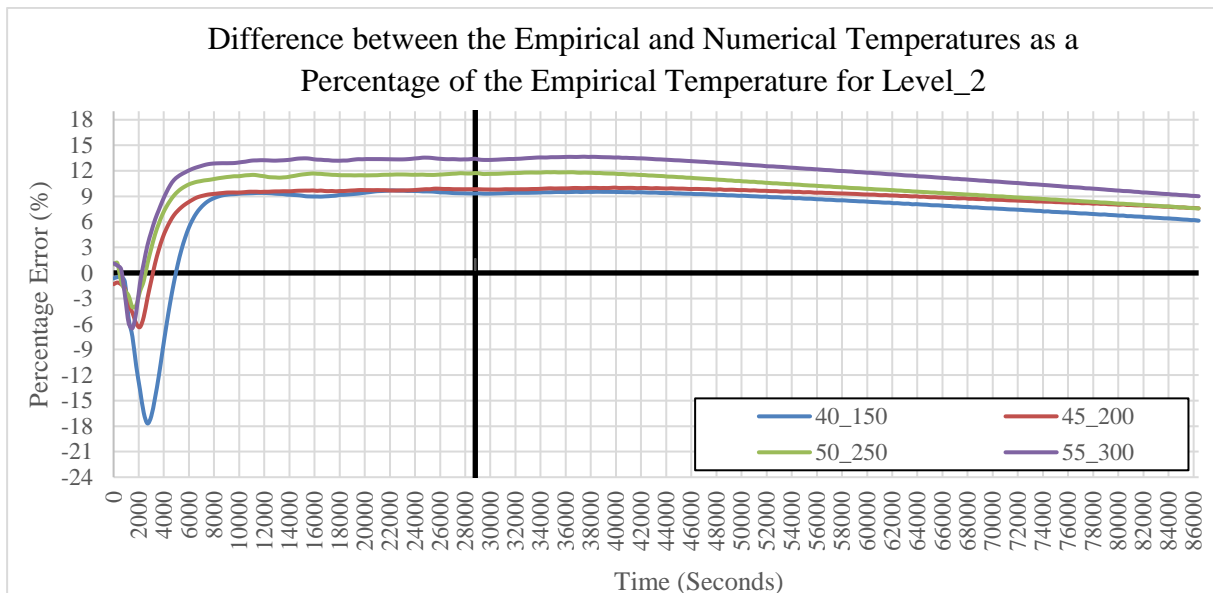


Figure 4.45 Difference between the empirical and numerical temperatures as a percentage of the empirical temperature for Level_2

The percentage error is initially high during the charging phase, but it starts to stabilise between 9% and 14% and slowly converges during the discharge phase, to between 6.139% and 9.011%.

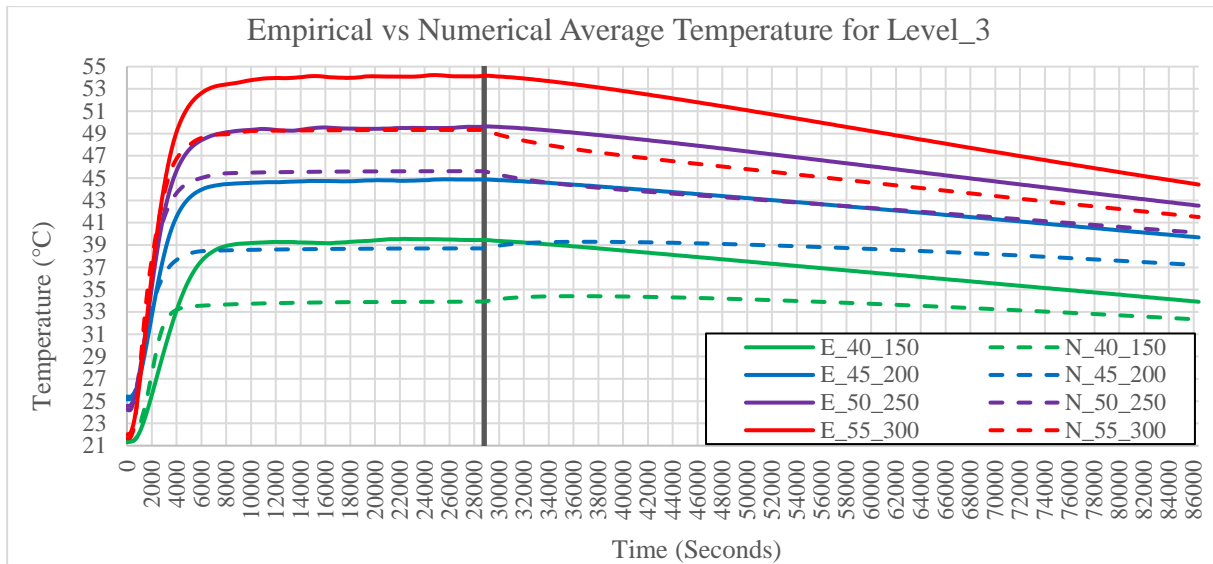


Figure 4.46 Empirical vs numerical average temperature for Level_3

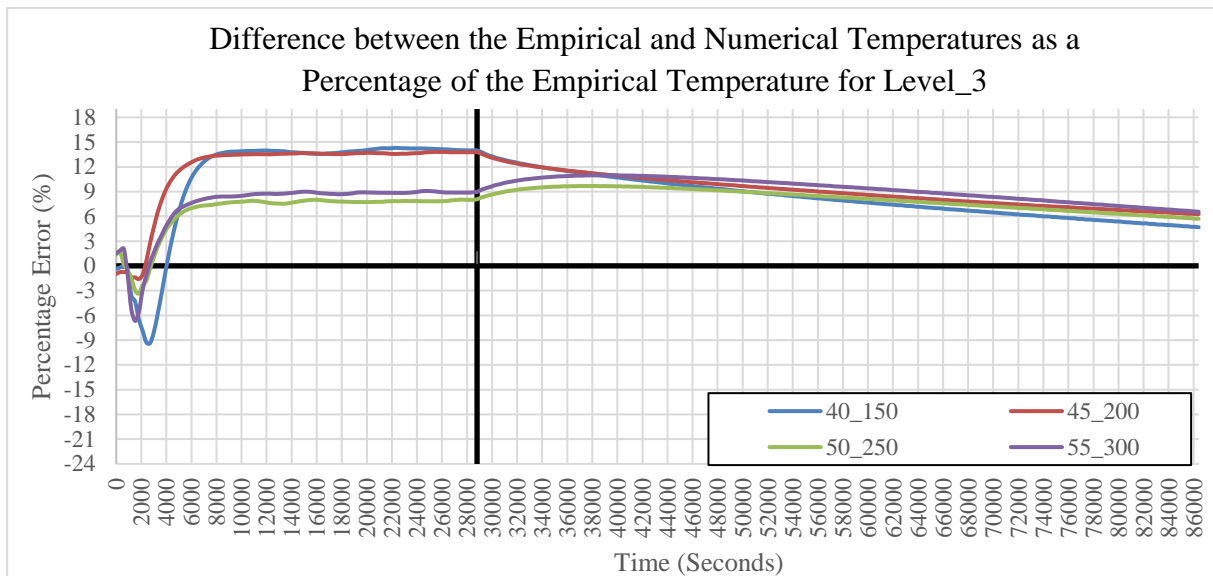


Figure 4.47 Empirical vs numerical percentage error for Level_3 average temperatures

The percentage error of Test 40_150 and 45_200 are larger than Tests 50_250 and 55_300, during the charging phase. The percentage error of Tests 40_150 and 45_200 decrease during discharge, while it increases for Tests 50_250 and 55_300. The data converges to a percentage error of between 4.678% and 6.560%. Figure 4.48 shows a comparison of the numerical data for the different levels in the packed bed.

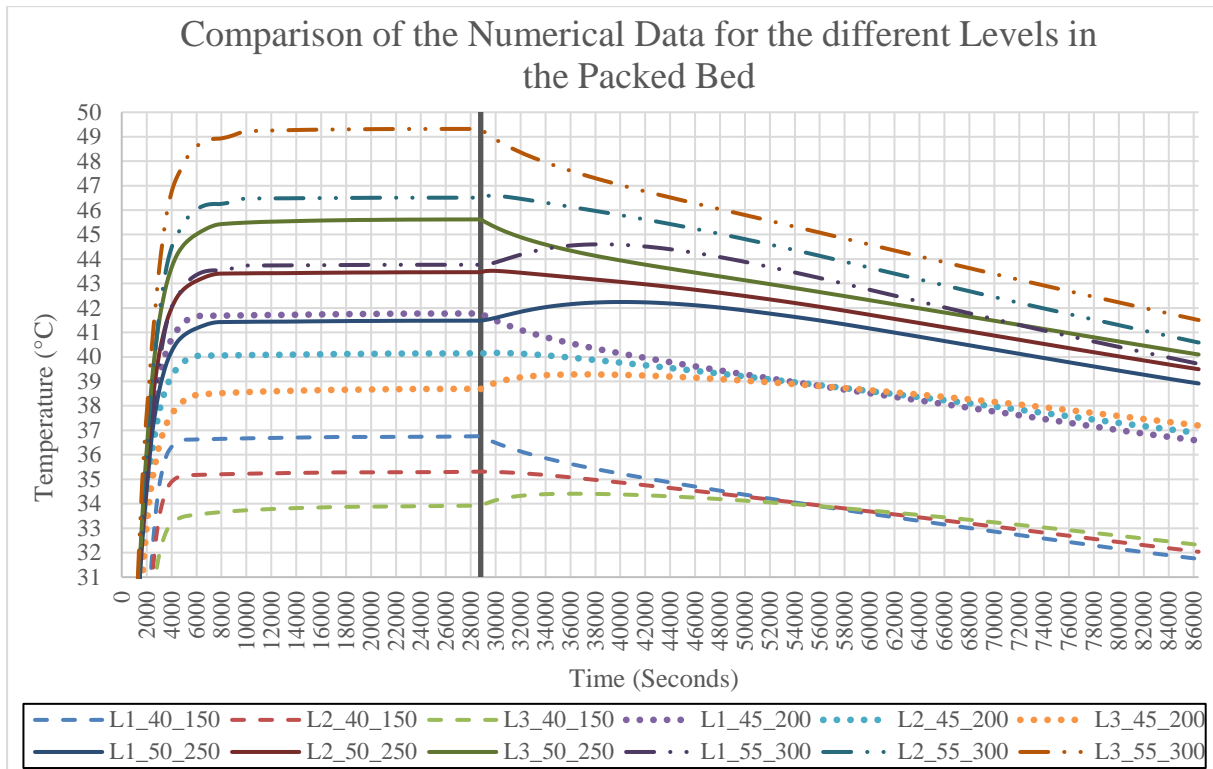


Figure 4.48 Comparison of the numerical data for the different levels in the packed bed

The results indicate that for each test that was conducted, a similar pattern was observed. During the charging phase, a bigger distribution of the levels occurs, as the inlet temperature and mass flow rate increases. The values tend to converge during the discharge phase; however, the distribution at higher mass flow rates and inlet temperatures, prevents the values from converging.

An interesting phenomenon occurred during the charging phase, as the temperature and mass flow rate decreased for each test. During Tests 50_250 and 55_300, the highest temperatures were for Level_3 and the lowest for Level_1, as one would expect (thermal stratification); however, when examining Tests 40_150 and 45_200, the highest temperatures were for Level_1 and the lowest for Level_3. This could be due to the environmental boundary conditions that were set, and that a larger amount of energy was extracted with the lower mass flow rates. Figure 4.49 and Figure 4.50 depicts the velocity profile and temperature profile, at 28800 seconds (end of the charging phase), with an inlet temperature of 45°C and a mass flow rate of 200 kg.h⁻¹.

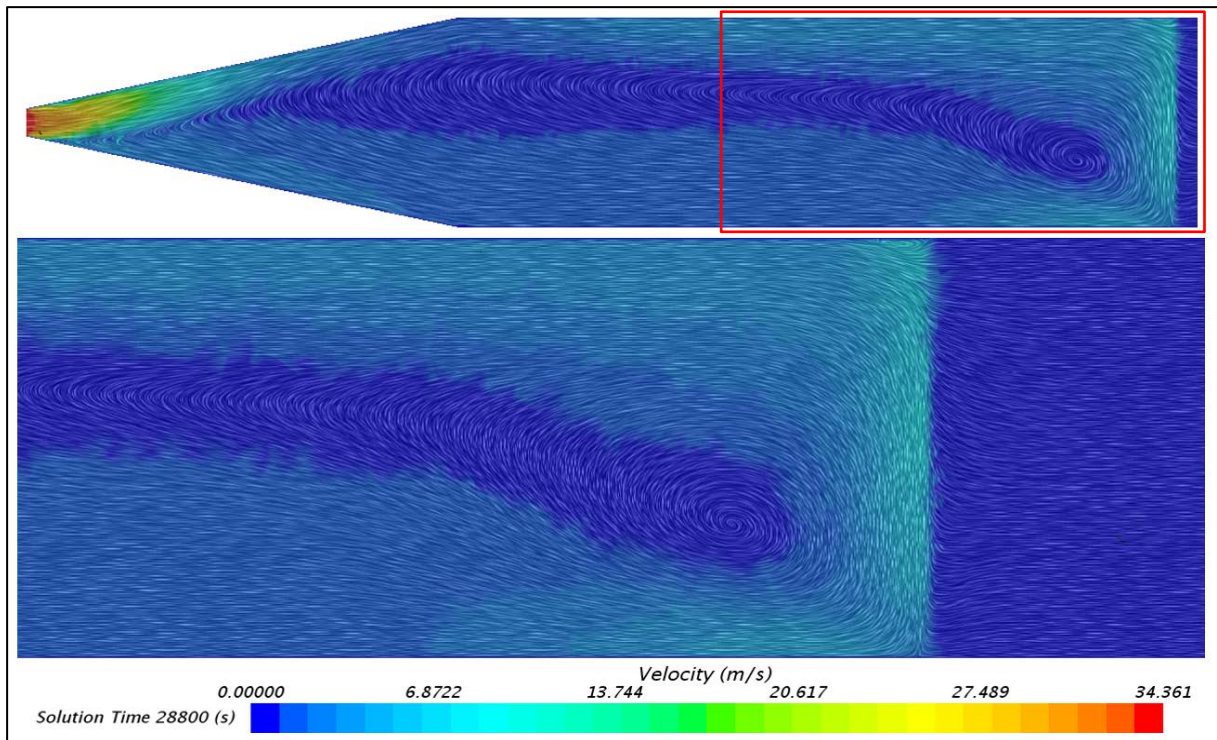


Figure 4.49 Air stream velocity profile at an inlet temperature of 45°C and a mass flow rate of 200 kg.h⁻¹

The velocity profile indicate a distinctive layer just before it hits the rock bed, with a central recirculating region forming just before the packed bed.

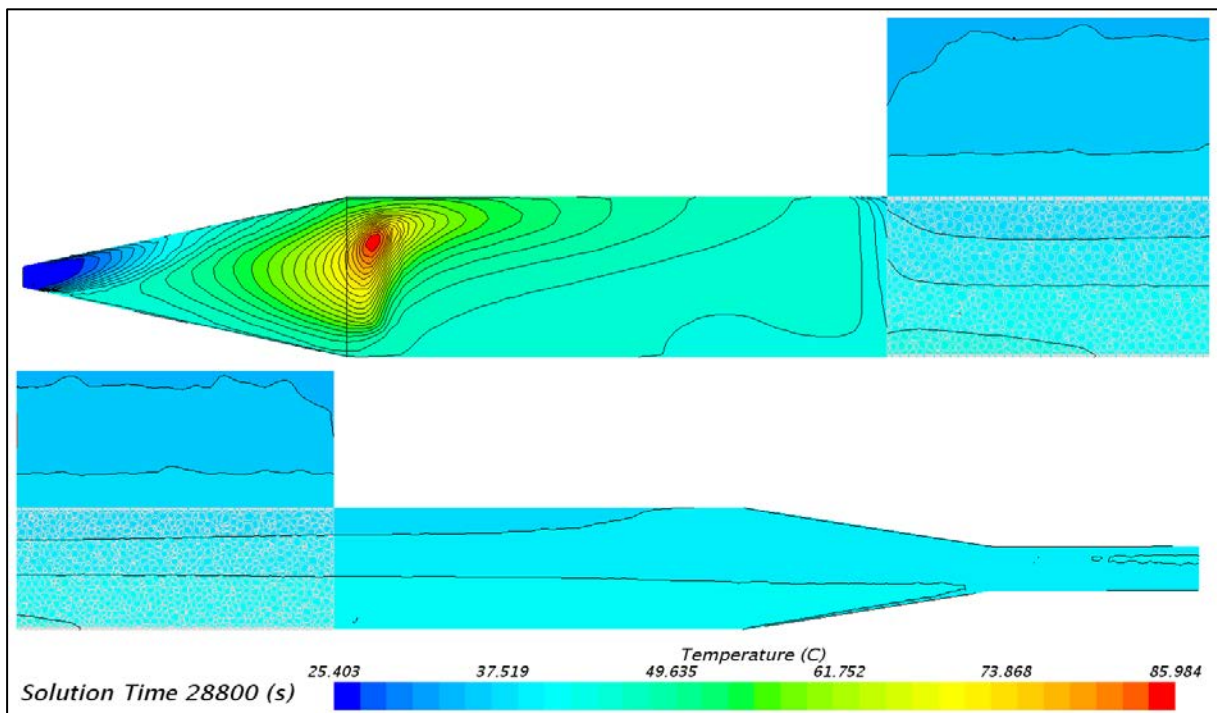


Figure 4.50 Temperature profile through packed bed at an inlet temperature of 45°C and a mass flow rate of 200 kg.h⁻¹

The temperature profile shows how the lower temperature is drawn from the top left hand corner of the packed bed (a cold region is visible) through the top region of the packed bed. The temperature profiles just before the packed bed are drawn straight through the packed bed; hence, the lower temperatures at Level_3.

Table 4.6 provides a summary of the percentage error of the numerical model for the packed bed. Each test case was investigated at each level within the packed bed. The average percentage error was calculated for the charging phase, the discharging phase, as well as the whole charging and discharging cycle. The percentage error values were selected at the end of the charging and discharge phases.

Table 4.6 Summary of the percentage error of the numerical model for the packed bed

	Level_1			
Test	40_150	45_200	50_250	55_300
Average 0-28800 (s)	0.816	3.362	12.648	15.317
28800 (s)	4.204	5.332	14.975	17.784
Average 29100-86400 (s)	6.411	7.701	10.053	12.161
Average 0-86400 (s)	4.533	6.245	10.924	13.221
86400 (s)	5.026	7.014	7.180	8.778
	Level_2			
Test	40_150	45_200	50_250	55_300
Average 0-28800 (s)	5.929	7.760	9.701	11.299
28800 (s)	9.333	9.844	11.736	13.416
Average 29100-86400 (s)	8.314	9.147	10.032	11.809
Average 0-86400 (s)	7.514	8.682	9.921	11.638
86400 (s)	6.139	7.588	7.582	9.011
	Level_3			
Test	40_150	45_200	50_250	55_300
Average 0-28800 (s)	10.706	11.703	6.539	7.299
0-28800 (s)	13.985	13.773	8.067	8.957
Average 29100-86400 (s)	8.272	9.056	8.090	9.274
Average 0-86400 (s)	9.089	9.945	7.570	8.611
86400 (s)	4.678	6.260	5.708	6.560

For Level_1 and Level_2, the numerical simulation was the most accurate for an inlet temperature of 40°C and a mass flow rate of 150 kg.h⁻¹ at the end of the discharge, with a percentage error of 5.026% for Level_1 and 6.139% for Level_2. The data from Level_3 was more accurate, with an inlet temperature of 50°C and a mass flow rate of 250 kg.h⁻¹, and a percentage error of 5.708%.

4.3.3.3 Concrete slab

The empirical and numerical results of the concrete surface temperatures are presented in Figure 4.51, followed by the percentage error distribution in Figure 4.52.

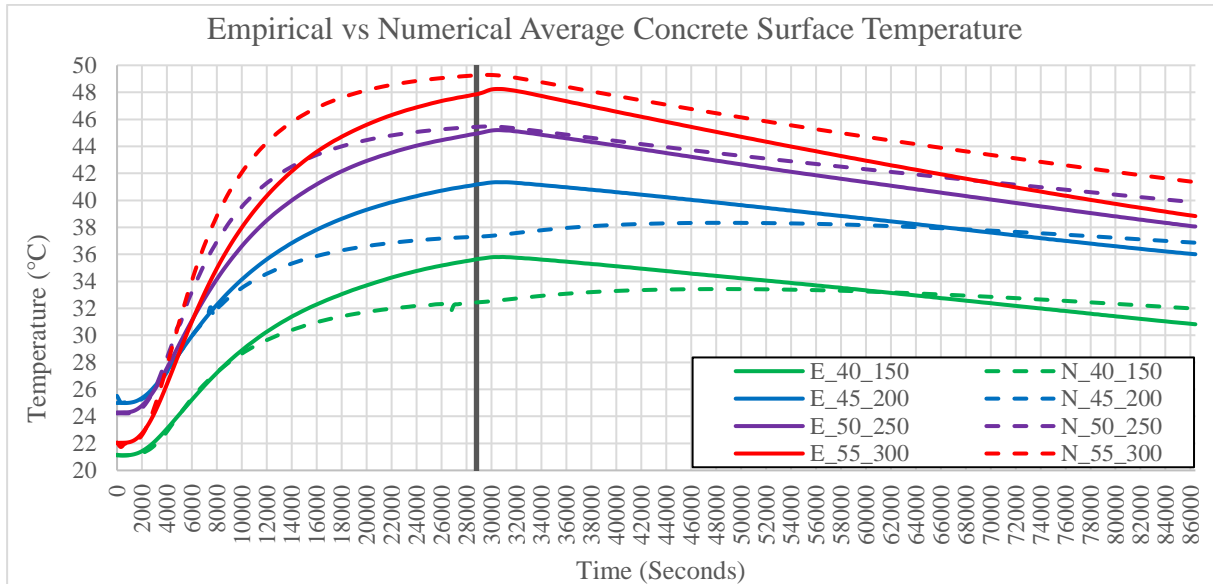


Figure 4.51 Empirical vs numerical average concrete surface temperature

During the charging phase, the numerical results of Tests 40_150 and 45_200 track the empirical results well at first, followed by a reduction in temperature. The curve gradually increases until it reaches approximately 66,000 seconds, where the numerical temperature curve crosses the empirical temperature curve. For the Tests 50_250 and 55_300, the numerical curve constantly stays above that of the empirical results.

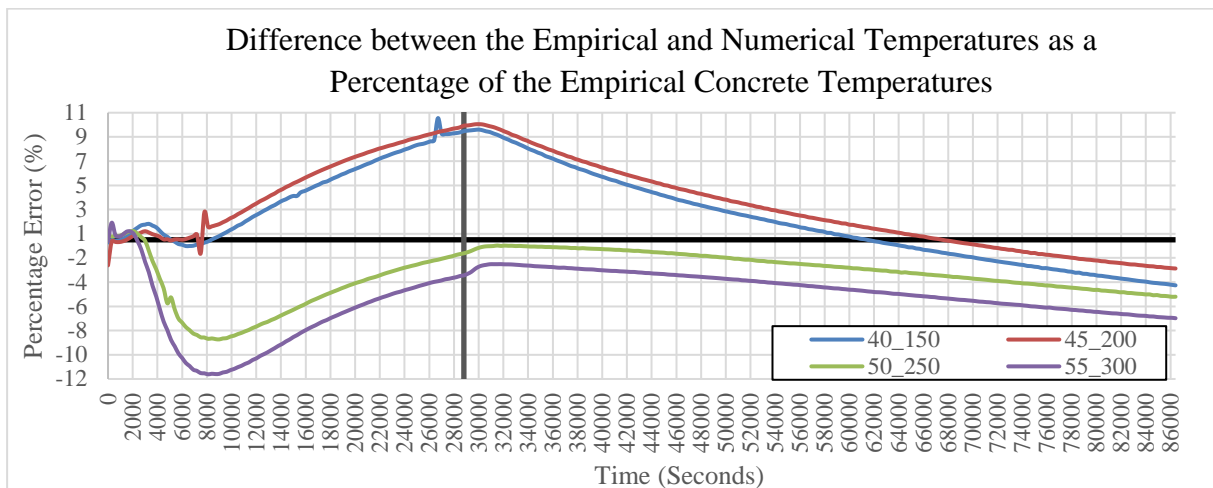


Figure 4.52 Empirical vs numerical percentage error of the concrete surface temperature

The percentage error data indicates that the lower temperature and mass flow rate tests (40_150 and 45_200) under-predict the temperature data late in the charging phase, whereas Tests

50_250 and 55_300 under-predict the data early in the charging phase. The percentage error tends to increase, as the inlet temperature and mass flow rate increases. At the end of the discharge state, all of the numerical temperature results were greater than the empirical results, with an error percentage of between -2.373% and -6.481%. The most accurate numerical result occurred at the end of the discharge, in the test with an inlet temperature of 45°C and a mass flow rate of 200 kg.h⁻¹, achieving a percentage error of -2.373%. The results are summarised in Table 4.7.

Table 4.7 Summary of the percentage error of the numerical model for the concrete slab

Test	40_150	45_200	50_250	55_300
Average 0-28800 (s)	3.646	4.223	-4.112	-6.166
28800 (s)	8.976	9.433	-1.115	-2.940
Average 29100-86400 (s)	1.394	2.357	-2.263	-4.023
Average 0-86400 (s)	2.150	2.984	-2.884	-4.742
86400 (s)	-3.764	-2.372	-4.703	-6.481

At the end of the discharge state, all of the numerical temperature results were greater than the empirical results, with an error percentage of between -2.373% and -6.481%. The most accurate numerical result at the end of discharge, was for the test with an inlet temperature of 45°C and a mass flow rate of 200 kg.h⁻¹, achieving a percentage error of -2.373%. The numerical model seemed to be more accurate, with the low inlet temperature of 40°C and a mass flow rate of 150 kg.h⁻¹; however, the concrete slab was predicted much better by Tests 50_250 at the end of the charging phase (-1.115%) and for the discharge phase, Test 45_200 was the most accurate (-2.372%). This is most likely due to more thermal stratification that occurs at lower flow rates.

4.3.3.4 Space

The results of the space temperature for the empirical and numerical data are shown in Figure 4.53, while the percentage error is depicted in Figure 4.54.

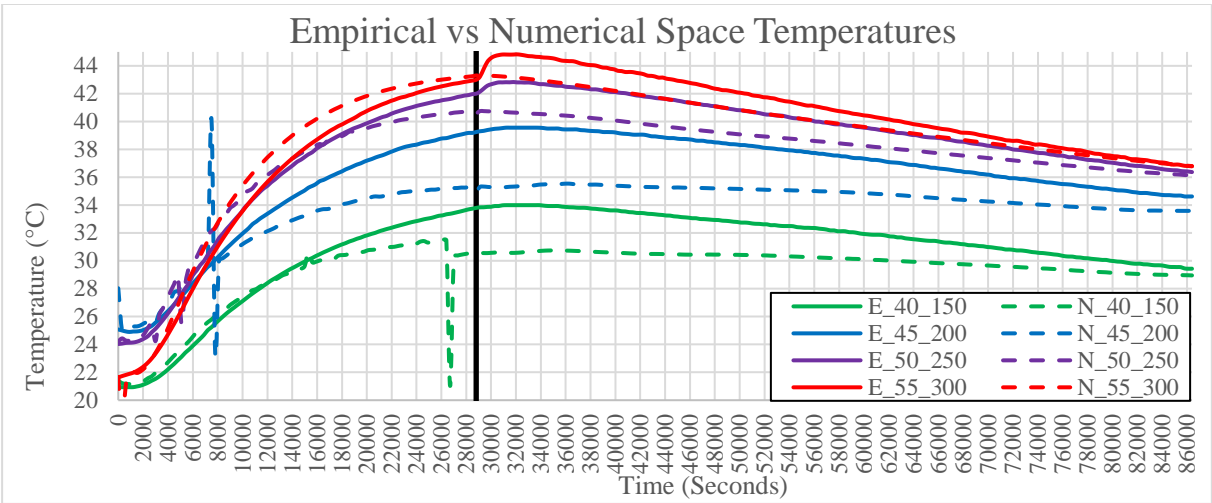


Figure 4.53 Empirical vs numerical results of the space temperatures

The charging phase shows the numerical data over- and under-predicting the empirical data, until the charging phase is complete. At the start of the discharge phase, the empirical and numerical results tend to increase to their maximum values. A steep increase to the maximum temperature data is seen for the empirical Tests E_50_250 and E_55_300.

The numerical temperature data for all the tests during discharge are lower than the empirical data; however, the empirical data has a steeper gradient than that of the numerical data. This could be attributed to the thermal losses of the empirical scaled-down room, at the contact surfaces between the polystyrene and the packed bed, as well as the ability of the numerical model to retain the thermal energy better. The gradient of the numerical data tends to increase with an increase in the inlet temperature and mass flow rate.

The outliers that are depicted in Figure 4.53 only occurred during the charging phase for the space region. No spikes occurred for the inlet, outlet, packed bed, or concrete slab. A reference value was provided as the starting temperature of the space regions, which was obtained from the empirical data sets. Several tests were conducted (even with the exact same input parameters), and in some instances, the spikes occurred early in the simulation, and only later in some of the other simulations. These spikes can be attributed to numerical noise. The outliers are taken into account for the percentage error; however, the temperature axis in Figure 4.54, was adjusted to focus on the more relevant error data.

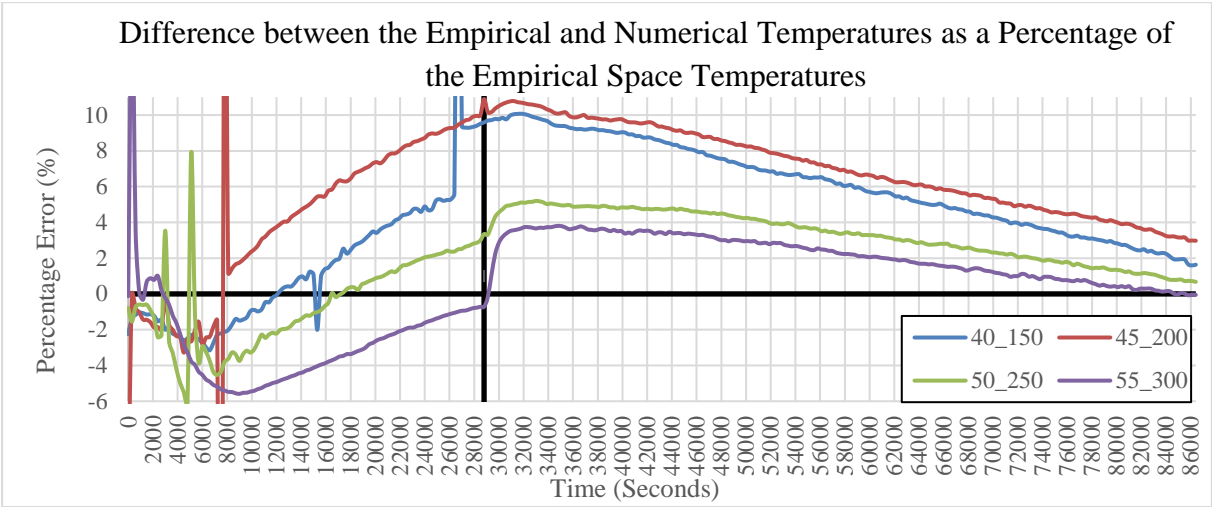


Figure 4.54 Empirical vs numerical percentage error for space temperature

The numerical space temperature results all started with a higher temperature, compared to the empirical results, and they gradually decreased, until the percentage error was above zero. At the end of the charging phase, the percentage error for the higher inlet temperature and mass flow rates (50_250 and 55_300) were significantly less, compared to the tests with lower values (40_150 and 45_200). The lower percentage error of Tests 50_250 and 55_300, provided a percentage error of less than 1% at the end of the discharge state. The percentage error of Test 40_100 was lower, compared to Test 45_200, although the data shows that the higher the inlet

temperature and the mass flow rate, the more accurate the space temperature data. A summary of the percentage error of the numerical model for the space data is presented in Table 4.8.

Table 4.8 Summary of the percentage error of the numerical model for space data

Test	40_150	45_200	50_250	55_300
Average 0-28800 (s)	1.796	3.900	-0.556	-2.642
28800 (s)	9.590	10.892	3.346	-0.717
Average 29100-86400 (s)	6.108	7.041	3.295	2.117
Average 0-86400 (s)	4.661	5.987	2.003	0.520
86400 (s)	1.633	2.973	0.677	-0.051

The space data was the final thermal energy transfer stage of the horizontal, uni-directional packed bed. The most accurate test for the average of the charging phase was Test 50_250, with a percentage error of -0.556%. Thereafter, Test 55_300 was the most accurate for the end of the charging phase (-0.717%), the average of the discharge phase (2.117%), the average of the charging and discharging phase (0.520%), as well as the final temperature state of the space temperature probe, which had a percentage error of just -0.051%. For all the tests that were conducted, a maximum 2.973% error was achieved for the final temperature state; hence, the numerical model predicted the final temperature state of the space relatively well, although the general trend was not that well predicted.

4.4 Conclusions of the Results

The following section provides the conclusions of the results obtained from the verification of the empirical and numerical methods and the empirical test data, as well as the validation of the empirical results against those found in the literature, thermography and the numerical design.

4.4.1 Verification

The verification of the empirical and numerical results concluded that:

- (i) the empirical design was not as air-tight as required, with a loss of between 6.67% and 7.55% for the different mass flow rates due, due to fenestration,
- (ii) the use of toggle locks, weather strips, silicon and thermography, to identify and reduce fenestration, was not sufficient,
- (iii) a mesh independence study indicated that the selected mesh resolution was adequate, and that the end-states of the numerical results, correlated well with the empirical results, although the trends were not generally well followed,
- (iv) a qualitative convergence test indicated that the residual data reduced to three orders of magnitude (below 0.001), except for the energy component,
- (v) the sensitivity analysis identified a key variable that influenced the numerical model significantly, which resulted in the numerical curves of the space and concrete data

- following the empirical curves much better, with a percentage error of less than 1% for the final space temperature of the numerical model, and
- (vi) the empirical and numerical methods that were developed were implemented and executed in the correct way.

4.4.2 Empirical test data

The empirical test data of the inlet, outlet, packed bed, concrete surface and space, resulted in the following conclusions:

4.4.2.1 Inlet and outlet

- (i) The increase in the mass flow rate from 150 kg.h^{-1} to 300 kg.h^{-1} , at selected temperatures, resulted in an average reduction in the charging time of 750 seconds, per 50 kg.h^{-1} increase.
- (ii) The increase in the inlet temperature from 40°C to 55°C , for a selected mass flow rate, resulted in an average reduction in the charging time of 500 seconds per 5°C increase.
- (iii) After 9000 seconds, till the end of the charging cycle, the outlet temperature increased, on average, by approximately 0.283°C , for all the tests that were conducted.
- (iv) The packed bed could be charged to more than 90% in two-and-a-half hours of the total eight-hour charging time.
- (v) The higher the inlet temperature, the longer it took for the inlet curve to reach a plateau, and a larger temperature difference occurred between the outlet temperature curves at specific mass flow rates.
- (vi) The temperature wave-front moved quicker through the packed bed, with the temperature lines coming closer together between 4000 and 9000 seconds. The time it took for the outlet temperature to reach the plateau also decreased.
- (vii) A reduction in the charging time resulted in the temperature wave-front moving through the packed bed at a higher rate, with more energy being transferred from the air to the rocks.
- (viii) The initial ambient-, packed bed-, concrete- and space temperatures had a significant effect on the thermal performance of the system.
- (ix) The percentage charged, as well as the percentage loss during the charging cycle, stayed fairly constant with an increase in the inlet temperature from 40°C to 55°C , at selected mass flow rates. However, with an increase in mass flow rate from 150 kg.h^{-1} to 300 kg.h^{-1} , at selected inlet temperatures, the percentage charged increased, whereas the percentage loss during charging decreased.
- (x) As the mass flow rate increased, more energy was stored within the packed bed, and less losses occurred.

4.4.2.2 Packed bed

- (i) With an increase in the mass flow rate through the packed bed, the difference between the maximum temperatures in the packed bed and the inlet temperatures decreased.
- (ii) At the end of the discharge phase, the temperature of Level_2 was higher than the temperature of Level_3, because the core of the packed bed retained the thermal energy in Level_2, while it was lost to the environment and the concrete slab in Level_3.
- (iii) The thermographs showed that a substantial amount of thermal energy was lost at the first vertical layer of temperature probes (Figure 4.18).
- (iv) With an increase in the inlet temperature and mass flow rate, the energy that was stored after discharge, and lost during discharge, as well as the energy that was available after the discharge cycle, increased.
- (v) The minimum amount of energy that was retained by the packed bed after the 16-hour discharge cycle was 67.329%, and the maximum was 73.223%. For all the tests, the average energy that was retained by the packed bed was approximately 70.211%.

4.4.2.3 Concrete slab

- (i) The temperature wave-front progressively moved through the packed bed, increasing the temperature of each probe. After the maximum temperature for each probe was reached, the data converged during the discharge phase.
- (ii) With an increase in the inlet temperature and inlet mass flow rate, the difference between the inlet temperatures and the maximum outlet temperatures also increased.
- (iii) The thermograph indicated that the temperature wave-front moved through the core of the concrete slab first, during the charging phase, before it progressed through the rest of the slab, until the final temperature profile was visible.
- (iv) The thermograph showed that most of the energy was retained in the core of the concrete slab after the discharge phase, as the energy had dissipated on the sides and had progressively moved to the core.
- (v) The maximum surface temperature and energy that was stored in the concrete slab, occurred 20 – 35 minutes into the discharge phase, which resulted in an average energy increase of approximately 1.202% for the concrete surface, after the charging phase was complete.
- (vi) The data trends were very similar to those of the packed bed, although the ability to retain the thermal energy was slightly lower; however, a minimum retention capacity of 61.790% and a maximum of 66.371% were achieved, with an average thermal retention of 64.302%.

4.4.2.4 Space

- (i) The results indicated that the higher inlet temperatures and mass flow rates provided a reasonable increase in the space temperature, with an average increase of 0.79°C per test. The first test, Test 40_150, provided an increase of 7.25°C for the space

temperature, whereas the final test, Test 55_30, delivered a temperature increase of 20.85°C above the ambient conditions.

- (ii) The thermograph indicated that a considerable amount of thermal energy was lost at the contact surface between the polystyrene scaled-down room section and the packed bed.
- (iii) The amount of energy absorbed during the charging phase was much less than that of the packed bed and the concrete slab, because of the lower air density. The ability to retain thermal energy was mostly dependant on the 75 mm high-density polystyrene.
- (iv) The scaled-down room reached its maximum temperature and energy content approximately 35 – 55 minutes into the discharge phase, which was directly after the concrete lag-time of between 20 and 35 minutes.
- (v) The ability of the space section to retain thermal energy varied considerably for the different tests. On average, a retention of 64.432% was achieved after the discharge cycle.

4.4.2.5 Energy balance

- (i) The performance of the horizontal, uni-directional packed bed was not as expected, due to the very low energy output (in the space region), compared to the total energy input, as depicted in the energy balance (Figure 4.35); however, it must be noted that the system was charged for all the tests, and then it was fully discharged before the next test commenced.
- (ii) This testing procedure does not utilise the stored energy within the packed bed for the next charging session. If it is continuously operated, a higher starting temperature in the packed bed will occur, which will lower the temperature gradients and increase the thermal energy transfer in the system.
- (iii) The available energy in the space region was calculated based on the results of the charging phase alone and the energy that was released during the discharge phase, was not accounted for.
- (iv) There was no energy supplied to the packed bed during the discharge phase and the available energy that was stored within it, as well as the concrete slab, was continuously transferred to the space region and the environment (losses).
- (v) Although a reduction in the space temperature occurred during the discharge phase, the temperature drop of the space region would have been much greater, had it not been for the TES system.

4.4.3 Validation

The empirical results were validated against the results from literature, thermography and the numerical design.

4.4.3.1 Empirical vs literature

- (i) The porosity, density and specific heat capacity values that were calculated, compared well with the values obtained in literature.
- (ii) The heat capacity (the product of the specific heat capacity and density) of the rocks amounted to $3.085 \text{ MJ.m}^{-3}.\text{K}^{-1}$.

4.4.3.2 Empirical vs thermography

- (i) The thermal image data was, on average, 1.247°C higher than the surface probe data.
- (ii) The surface probes did not make full contact with the concrete surface, which could have resulted in the lower temperatures.

4.4.3.3 Empirical vs numerical

The following outcomes were summarised for the inlet and outlet results:

- (i) The heating table that was developed as the input to the numerical model, correlated well with the empirical inlet temperature data, with an average percentage error of 0.138%.
- (ii) An increase in the inlet temperature and mass flow rate, resulted in a larger temperature difference between the numerical and empirical curves for the outlet data.
- (iii) The average percentage error for the inlet and outlet curves, as well as the final results at the end of the charging phase, were inclined to be more accurate for the lower inlet temperatures and mass flow rates.

The following outcomes were summarised for the packed bed results:

- (i) As the inlet temperature and mass flow rate increased during the discharge phase, a larger distribution between the levels occurred.
- (ii) The tests with higher inlet temperatures and mass flow rates (Tests 50_250 and 55_300) predicted the thermal stratification from low to high temperatures in the correct order, namely, Level_1, Level_2 and Level_3, whereas the tests with lower inlet temperatures and mass flow rates (40_150 and 45_200) did not predict the thermal stratification correctly, with the highest temperature being at Level_1 and the lowest at Level_3.
- (iii) For Level_1 and Level_2, the numerical simulation was the most accurate for an inlet temperature of 40°C and a mass flow rate of 150 kg.h^{-1} .
- (iv) The data from Level_3 was more accurate, with an inlet temperature of 50°C and a mass flow rate of 250 kg.h^{-1} .

The following outcomes were summarised for the concrete slab results:

- (i) The percentage error data indicate that the lower temperature and mass flow rate tests (40_150 and 45_200) under-predict the temperature data late in the charging phase, whereas Tests 50_250 and 55_300 under-predict the data early in the charging phase.
- (ii) At the end of the discharge state, all of the numerical temperature results were greater than the empirical results.

The following outcomes were summarised for the space temperature:

- (i) The charging phase showed the numerical data over- and under-predicted the empirical data, until the charging phase was complete.
- (ii) At the start of the discharge phase, the empirical and numerical results tended to increase to their maximum values and, at the end of the discharge cycle, the numerical data were lower than the empirical data.
- (iii) At the end of the charging phase, the percentage error for the higher inlet temperature and mass flow rates (Tests 50_250 and 55_300) were significantly less than the tests with lower values (40_150 and 45_200).
- (iv) For all the tests, a maximum error of 2.973% was achieved for the final temperature state and a minimum of -0.051%; hence, the final temperature state of the space was predicted well by the numerical model.

5. CONCLUSIONS AND RECOMMENDATIONS

The goal of the study was to conduct a thorough literature research study on the theory of thermal energy storage in a packed bed, as well as to design and construct an experimental research unit for a horizontal, uni-directional packed bed. The study was also aimed at investigating the effects of changing the inlet temperatures and mass flow rates on the thermal energy transfer, the temperature wave-front, as well as the charging and discharging time of the system. The effects were modelled by using CFD, and the empirical results were compared with the numerical results through validation and verification. The following sections will provide the main conclusions pertaining to the study, followed by some recommendations for future work.

5.1 Conclusions

In South Africa, there is adequate energy potential available from solar radiation for it to be harvested, stored and utilised. The appropriate passive harvesting methods that were identified were solar thermal collectors in the form of pitched roofs and Trombe-like walls. It was established that the two most important characteristics of TES are the amount of energy stored per unit volume (volumetric energy capacity) and the storage duration. The literature indicated that STES systems are typically more cost-effective and simpler, when compared to TCES and LTES. They are also well-established, reliable, clearly understood and widely used. It was found that the construction and operational cost of a rock-bed system is less than that of the water system and can also best be used at elevated temperatures greater than 100°C. The implementation of active or passive STES systems in residential buildings may result in a 30-35% enhancement of energy efficiency and a 40-60% enhancement of thermal efficiency.

Packed beds were identified as being the most appropriate technology for air-based solar systems, with rocks being the most suitable packing material. Horizontal uni-directional packed beds discharge energy throughout a space, by means of radiation and natural convection, instead of utilising forced convection, as in vertical packed beds. It was found that there is currently insufficient research available on horizontal packed beds and that no well-structured design rules are available for the design of packed bed TES systems, as each unit must be optimised for its performance i.e. efficiency and outflow temperature profile, and its costs i.e. thermal losses, pumping work, excavation and material costs, given the requirements of capacity, charging and discharging, mass flow rate and temperature.

The design-related properties that were identified to have the greatest influence on the performance of a packed bed were porosity, permeability and heat transfer. The critical factors of each of the performance effects were highlighted in the literature survey. The most important metrics that affect the performance of a packed bed were identified as the porosity, the pressure drop, the mass flow rate and the temperature. The metrics were addressed and the respective measurement equipment was identified. The literature survey provided a fundamental understanding of packed beds, the performance effects, as well as the performance metrics.

The empirical design was comprised of the design and construction of an experimental research unit for a horizontal, uni-directional packed bed. The proposed design provided a step-by-step process, in order to execute the construction with ease. Data from the thermal camera indicated that the design was not as air-tight as it was initially thought to be, due to a difference in the flow rate between the inlet and the outlet of the packed bed. Thermal losses were also identified at the inlet of the probe point, in the initial stages of the packed bed, as well as at the contact regions of the polystyrene structure, which represented the scaled-down room and the horizontal packed bed structure.

The empirical test data found that the initial ambient-, packed bed-, concrete- and space temperatures had a significant effect on the thermal performance of the system. An increase in mass flow rate, from 150 kg.h^{-1} to 300 kg.h^{-1} at selected temperatures, resulted in an average reduction in the charging time of 750 seconds per 50 kg.h^{-1} increase. An increase in the inlet temperature from 40°C to 55°C for a selected mass flow rate, resulted in an average reduction in the charging time of 500 seconds per 5°C increase. It was established that the packed bed could be charged to more than 90% of its capacity in two-and-a-half hours of the total eight-hour charging time.

The percentage charged, as well as the percentage loss during the charging cycle, stayed fairly constant with an increase in the inlet temperature from 40°C to 55°C , at selected mass flow rates. However, with an increase in mass flow rate from 150 kg.h^{-1} to 300 kg.h^{-1} , at selected inlet temperatures, the percentage charged increases, whereas the percentage loss during charging decreases. These results indicate that as the mass flow rate increases, more energy is stored within the packed bed, and less losses occur

It was found that the maximum surface temperature and energy that was stored in the concrete slab had a lag-time of approximately 20 – 35 minutes after the charging phase was complete. This resulted in an average energy increase of approximately 1.202% after the charging phase was complete. The scaled-down room reached its maximum temperature and energy content approximately 35 – 55 minutes into the discharge phase, which was directly after the concrete lag-time. The average energy increase of the space was 3.764%, which was more than the concrete slab.

The increase in the inlet temperatures and mass flow rates resulted in an average increase in the space temperature of 0.79°C for each test that was conducted. The test with an inlet temperature of 40°C and a mass flowrate of 150 kg.h^{-1} provided an increase of 7.25°C for the space temperature, whereas the final temperature of 55°C and mass flow rate of 300 kg.h^{-1} , delivered a temperature increase of 20.85°C above the ambient conditions.

The energy balance found that the performance of the horizontal, uni-directional packed bed, was not as expected, with an energy input of 100%, which resulted in a space energy output of below 0.01%. However, the thermal calculations that were done, focussed on the thermal energy transfer, as a result of the charging phase alone and that the energy that was released during the discharge phase, was not accounted for. There was no energy supplied to the packed

bed during the discharge phase and the available energy that was stored within it, as well as the concrete slab, was continuously transferred to the space region and the environment (losses). Although a reduction in the space temperature occurred during the discharge phase, the temperature drop of the space region would have been much greater, had it not been for the TES system. It must be noted that the system was first charged for all the tests, and then fully discharged before the next test commenced. This testing procedure did not utilise the retained energy within the packed bed for the next charging session. The retained energy was, on average, 70.211% of the maximum thermal energy after the 16-hour discharge cycle. The retained energy will lower the temperature gradients between the starting temperature of the system (rock bed, concrete slab and space temperature) and it will increase the thermal energy transfer and the overall thermal performance of the system, as the system was completely discharged for each run during the empirical tests.

The accurate numerical simulation of an empirical investigation was highly dependent on the simulation setup. The CFD numerical model was developed, using the commercial software package, STAR-CCM+® Version 11.04. A general sequence of operations for the CFD simulation setup and analysis was followed, in order to model the effects of the empirical design and to assess and compare the numerical results with the empirical results. The mesh independence study indicated that the selected mesh size was adequately selected, in order to obtain results that are not effected by the mesh resolution. The end-state of the numerical results, correlated well with the empirical results, although some variation did occur during the charging and discharging phases. The inner iterations that were set to 10, were sufficient for the residual data. Sensitivity analyses that were conducted on several variables, identified a key variable, which was subsequently adjusted to a more appropriate value. This increased the accuracy of the numerical model and resulted in a percentage error of less than 1% for the final space temperature.

It was found that the porosity, density and specific heat capacity values that were calculated for use as input to the numerical model, compared well with the values obtained in literature. The heat capacity (the product of the specific heat capacity and density) of the rocks amounted to $3.085 \text{ MJ.m}^{-3}.\text{K}^{-1}$.

The thermal camera was a valuable asset in the identification of thermal losses throughout the packed bed, tracking the temperature wave-front through the concrete slab and providing surface temperature values. The thermographs indicated that a substantial amount of thermal energy was lost at the first vertical layer of temperature probes, as well as at the contact surface between the polystyrene scaled-down room section and the packed bed. It was established that the temperature wave-front first moved through the core of the concrete slab during the charging phase, before progressing through the rest of the slab, until the final temperature profile was visible from the thermographs. It was found that the concrete slab retained most of the energy in the core after the discharge phase, as the energy had dissipated on the sides and had progressively moved to the core. The thermal image data was, on average, 1.247°C higher than the surface probe data. The surface probes did not make full contact with the concrete surface, which could have resulted in the lower temperatures.

It was concluded that the heating table that was developed as the input to the numerical model, correlated well with the empirical inlet temperature data, with an average percentage error of 0.138%. The numerical model for the inlet and outlet curves, the packed bed and the concrete surface, were inclined to be more accurate for the lower inlet temperatures and mass flow rates, whereas the space temperature data, were more accurate at higher inlet temperatures and mass flow rates. An increase in the inlet temperatures and mass flow rates, resulted in a larger temperature difference between the numerical and empirical curves for the outlet data, as well as between the different temperature layers of the packed bed.

The thermal stratification in the packed bed was correctly predicted, using the test data with an inlet temperature and mass flow rate of 50°C and 250 kg.h⁻¹, and 55°C and 300 kg.h⁻¹, respectively. However, the tests with an inlet temperature and mass flow rate of 40°C and 150 kg.h⁻¹, and 45°C and 200 kg.h⁻¹, did not predict the thermal stratification correctly, with the highest temperature being at Level_1 and the lowest at Level_3. It was found that the final temperature states of the space region, for all the tests that were conducted, had a maximum error of 2.973% and a minimum of -0.051%; hence, the final temperature state of the space was predicted well by the numerical model.

The numerical design, provided a good platform to simulate higher and lower mass flow rates and inlet temperature data. The curves of the numerical model did not always follow a similar pattern to that of the empirical data, although the final temperature state of the space was quite accurate. The energy flow balance of the horizontal, uni-directional packed bed indicates very low efficiencies; however, if the system were completely passive and continuously made use of the retained energy in the packed bed for each charging cycle, it could become a viable option to be implemented in the residential sector.

5.2 Recommendations

The following recommendations are made for future studies:

- (i) The temperature must be determined that will be available in pitched roofs and Trombe-like walls, to see whether the amount of thermal energy will be sufficient for the packed bed.
- (ii) A financial analysis must be carried out on the viability of the horizontal, uni-directional packed bed, for residential use, based on the construction material, as well as the labour and energy requirements.
- (iii) Fenestration and thermal losses must be prevented, to increase the efficiency of the system.
- (iv) The effect of charging the packed bed to only two-and-a-half hours (90% of charging capacity) of the initial eight-hour charging cycle must be tested and compared.
- (v) The mass flow rate must be increased, in order to get closer to the full charging capacity of the packed bed. These results can also be used to find the optimal flow rates out of a financial perspective, with respect to the charging capacity.

- (vi) The overall thermal performance of the horizontal, uni-directional packed bed must be investigated, making use of the retained energy within the packed bed that is available after each discharge cycle (not making use of forced discharge, as with the tests that were conducted in current study). This will provide a continuous charging cycle on a daily basis, increasing the charging capacity.
- (vii) Testing must be done at a constant room temperature. This will allow the ambient temperature, the packed bed, the concrete slab and the space area to start from a reference temperature. The room temperature will also aid in conducting tests for different weather conditions, for example, during the summer and the winter.
- (viii) Low flow rates must be investigated for the numerical studies, to identify the cause of the higher temperatures that are found in the lower regions of the packed bed, and the lower temperature that are found in the higher regions of the packed bed.
- (ix) The use of DEM must be investigated and compared with the results obtained for the porous region of the packed bed.
- (x) More numerical tests must be conducted on the data of the empirical results, and the effect of changing only the inlet temperature or mass flow rate for the numerical models must be studied, to see which has the largest effect on the results.
- (xi) A numerical design must be developed to simulate the thermal energy transfer in a Trombe-like wall, so that it can be used as input to the packed bed.

6. REFERENCES

- Abhat, A. 1983. Low temperature latent heat thermal energy storage: Heat storage materials. *Solar Energy* 30 (4): 313-332.
- Alam, T, Saini, R and Saini, J. 2014. Packed bed solar energy storage: A state-of-art review. *International Global Journal for Engineering Research* 9 (1): 1-6.
- Allen, K. 2010. Performance characteristics of packed bed thermal energy storage for solar thermal power plants. Unpublished thesis, Faculty of Engineering, University of Stellenbosch., Stellenbosch.
- Allen, K, von Backström, T and Kröger, D. 2013. Packed bed pressure drop dependence on particle shape, size distribution, packing arrangement and roughness. *Powder Technology* 246: 590-600.
- Allen, K, von Backström, T and Kröger, D. 2014a. Packed rock bed thermal storage in power plants: Design considerations. *Energy Procedia* 49: 666-675.
- Allen, K, von Backström, T, Kröger, D and Kisters, A. 2014b. Rock bed storage for solar thermal power plants: Rock characteristics, suitability, and availability. *Solar Energy Materials and Solar Cells* 126: 170-183.
- Anderson, JD and Wendt, J. 1995. *Computational Fluid Dynamics*. Springer, 72 Chaussee de Waterloo, 1640 Rhode-Saint-Genese, Belgium.
- Andreozzi, A, Buonomo, B, Manca, O, Mesolella, P and Tamburrino, S.2012. Numerical investigation on sensible thermal energy storage with porous media for high temperature solar systems. *Journal of Physics: Conference Series*, 012150. IOP Publishing, Conference Centre of Poitiers, Futuroscope, France.
- Arce Maldonado, P, Medrano Martorell, M, Gil, A, Oró Prim, E and Cabeza, LF. 2011. Overview of thermal energy storage (TES) potential energy savings and climate change mitigation in Spain and Europe. *Applied Energy* 88 (8): 2764–2774.
- ASHRAE. 2001. *2001 American Society of Heating, Refrigerating and Air-Conditioning Engineers Handbook: Fundamentals*. ASHRAE, 2001, 1791 Tullie Circle, Atlanta, Georgia, United States of America.
- Askeland, D, Fulay, P and Wright, W. 2011. *The Science and Engineering of Materials, SI Edition*. Cengage Learning, 200 First Stamford Place, Suite 400, Stamford, CT 06902, United States of America.
- Badescu, V. 2014. *Modeling Solar Radiation at the Earth's Surface*. Springer, Splaiul Independenței 313, Bucharest 060042, Romania.
- Baker, MJ. 2011. CFD simulation of flow through packed beds using the finite volume technique. Unpublished thesis, Engineering, University of Exeter, Exeter, United Kingdom.

- Bales, C, Gantenbein, P, Hauer, A, Henning, H-M, Jaenig, D, Kerskes, H, Núñez, T and Visscher, K. 2005. *Thermal Properties of Materials for Thermo-Chemical Storage of Solar Heat*. Solar heating and cooling programme Interanional Energy Agency, Solar Energy Research Center SERC, Högskolan Dalarna, SE-78188 Borlänge, Sweden.
- Barlev, D, Vidu, R and Stroeve, P. 2011. Innovation in concentrated solar power. *Solar Energy Materials and Solar Cells* 95 (10): 2703-2725.
- Barton, N. 2013. Simulations of air-blown thermal storage in a rock bed. *Applied Thermal Engineering* 55 (1): 43-50.
- Beken, BB, G. 1984. Passive solar heating. [Internet]. Iklim Ltd Sti. Available from: http://www.iklimnet.com/save/passive_solar_heating.html. [Accessed: 20-06-2016].
- Belusko, M, Saman, W and Bruno, F. 2004. Roof integrated solar heating system with glazed collector. *Solar Energy* 76 (1): 61-69.
- Berg, RR. 1970. Method for determining permeability from reservoir rock properties. *Gulf Coast Association of Geological Societies* 20: 303-317.
- Bindra, H, Bueno, P and Morris, JF. 2014. Sliding flow method for exergetically efficient packed bed thermal storage. *Applied Thermal Engineering* 64 (1): 201-208.
- Bindra, H, Bueno, P, Morris, JF and Shinnar, R. 2013. Thermal analysis and exergy evaluation of packed bed thermal storage systems. *Applied Thermal Engineering* 52 (2): 255-263.
- Borgnakke, C and Sonntag, RE. 2009. *Fundamentals of Thermodynamics*. John Wiley and Sons, Inc., 111 River Street, Hoboken, NJ 07030-5774, United States of America.
- Bouhdjar, A, Belhamel, M, Belkhiri, F and Boulbina, A. 1996. Performance of sensible heat storage in a rockbed used in a tunnel greenhouse. *Renewable Energy* 9 (1): 724-728.
- Burgess, WA, Ellenbecker, MJ and Treitman, RD. 2004. *Ventilation for Control of the Work Environment, Second Edition*. John Wiley and Sons, Inc., 111 River Street, Hoboken, NJ 07030-5774, United States of America.
- Cabeza, LF. 2014. *Advances in Thermal Energy Storage Systems: Methods and Applications*. Elsevier Ltd., 80 High Street, Sawston, Cambridge, CB22 3HJ, United Kingdom.
- Cárdenas, B and León, N. 2013. High temperature latent heat thermal energy storage: Phase change materials, design considerations and performance enhancement techniques. *Renewable and Sustainable Energy Reviews* 27: 724-737.
- CD-Adapco. 2016. *STAR-CCM+ User Guide, Version 11.04*. New York, United States of America.
- Cengel, YA, Boles, MA and Kanoğlu, M. 2002. *Thermodynamics: An Engineering Approach*. McGraw-Hill, 1221 Avenue of the Americas, New York, NY 10020, United States of America.

- Central, T-F. 2010. Solar heating and cooling. [Internet]. 2010. Available from: [http://www.thermalfluidscentral.org/encyclopedia/index.php/Solar Heating and Cooling](http://www.thermalfluidscentral.org/encyclopedia/index.php/Solar_Heating_and_Cooling). [Accessed: 20-06-2016].
- Chen, B, Zhao, J, Chen, C and Zhuang, Z. 2006. Experimental investigation of natural convection in Trombe wall systems. *Envelope Technologies for Building Energy Efficiency* 2 (3): 5.
- Chidambaram, L, Ramana, A, Kamaraj, G and Velraj, R. 2011. Review of solar cooling methods and thermal storage options. *Renewable and Sustainable Energy Reviews* 15 (6): 3220-3228.
- Childs, P, Greenwood, J and Long, C. 2000. Review of temperature measurement. *Review of Scientific Instruments* 71 (8): 2959-2978.
- Choudhury, C, Chauhan, P and Garg, H. 1995. Economic design of a rock bed storage device for storing solar thermal energy. *Solar Energy* 55 (1): 29-37.
- Crabtree, GW and Lewis, NS. 2007. Solar energy conversion. *Physics Today* 60 (3): 37-42.
- Cundall, PA and Strack, OD. 1979. A discrete numerical model for granular assemblies. *Geotechnique* 29 (1): 47-65.
- da Silva, W. 2016. Milestone in solar cell efficiency by UNSW Engineers. [Internet]. Media Office, UNSW Sydney NSW 2052 Australia. Available from: <http://newsroom.unsw.edu.au/news/science-tech/milestone-solar-cell-efficiency-unsw-engineers>. [Accessed: 20-06-2016].
- Delgado, J. 2006. A critical review of dispersion in packed beds. *Heat and Mass Transfer* 42 (4): 279-310.
- Eppinger, T, Seidler, K and Kraume, M. 2011. DEM-CFD simulations of fixed bed reactors with small tube to particle diameter ratios. *Chemical Engineering Journal* 166 (1): 324-331.
- Ergun, S. 1952. Fluid flow through packed columns. *Chemical Engineering Progress* 48 (2): 89-94.
- Europe, A. 2009. Types of research. [Internet]. eZ Publish. Available from: <http://www.alzheimer-europe.org/Research/Understanding-dementia-research/Types-of-research/The-four-main-approaches>. [Accessed: 15-07-2016].
- Farid, MM, Khudhair, AM, Razack, SAK and Al-Hallaj, S. 2004. A review on phase change energy storage: Materials and applications. *Energy Conversion and Management* 45 (9): 1597-1615.
- Fath, HE. 1998. Technical assessment of solar thermal energy storage technologies. *Renewable Energy* 14 (1): 35-40.

- Florida Solar Energy Center Cocoa, F. 2006. *Solar Water and Pool Heating Manual*. University of Central Florida, University of Central Florida, 12443 Research Parkway, Orlando, FL 32826.
- Fraser, H. 1935. Experimental study of the porosity and permeability of clastic sediments. *The Journal of Geology* 43 (8): 910-1010.
- Fuller, R. 2003. Operational experiences with rockbed storage systems. *ANZSES 2003: Destination Renewables: From Research to Market: 41st Annual Conference of the Australian and New Zealand Solar Energy Society*, 19-25. Australian and New Zealand Solar Energy Society, University of Melbourne, Victoria, Australia.
- Gao, R, Li, A, Zhang, O and Zhang, H. 2011. Comparison of indoor air temperatures of different under-floor heating pipe layouts. *Energy Conversion and Management* 52 (2): 1295-1304.
- Graton, LC and Fraser, H. 1935. Systematic packing of spheres: With particular relation to porosity and permeability. *The Journal of Geology* 43 (8): 785-909.
- Green, MA. 2000. Photovoltaics: Technology overview. *Energy Policy* 28 (14): 989-998.
- GSA, GoSA. 2008. Where energy is used in the home. [Internet]. Government of South Australia. Available from: <https://www.sa.gov.au/topics/water-energy-and-environment/energy/saving-energy-at-home/check-and-reduce-your-energy-use/energy-use-at-home>. [Accessed: 27-06-2016].
- Hänchen, M, Brückner, S and Steinfeld, A. 2011. High-temperature thermal storage using a packed bed of rocks—heat transfer analysis and experimental validation. *Applied Thermal Engineering* 31 (10): 1798-1806.
- Heeley, D. 2005. *Understanding Pressure and Pressure Measurement*. Freescale Semiconductor, Technical Information Center, CH370, 1300 N. Alma School Road, Chandler, Arizona 85224, United States of America.
- Hoffmann, A and Finkers, H. 1995. A relation for the void fraction of randomly packed particle beds. *Powder Technology* 82 (2): 197-203.
- Huang, B, Chang, J, Petrenko, V and Zhuk, K. 1998. A solar ejector cooling system using refrigerant R141b. *Solar Energy* 64 (4): 223-226.
- Ibarra-Castanedo, C, Piau, J-M, Guilbert, S, Avdelidis, NP, Genest, M, Bendada, A and Maldague, XP. 2009. Comparative study of active thermography techniques for the nondestructive evaluation of honeycomb structures. *Research in Nondestructive Evaluation* 20 (1): 1-31.
- InnovateUs. 2006. What are the factors affecting Solar radiation? [Internet]. Available from: <http://www.innovateus.net/science/what-are-factors-affecting-solar-radiation>. [Accessed: 08-04-2015].

- Irshad, K, Habib, K and Thirumalaiswamy, N. 2015. Performance evaluation of PV-trombe wall for sustainable building development. *Procedia CIRP* 26: 624-629.
- ISOVER, S-G. 2015. Expanded polystyrene. [Internet]. Available from: <http://www.isover.co.za/products/expanded-polystyrene>. [Accessed: 23-10-2015].
- Ji, J, Yi, H, He, W and Pei, G. 2007. PV-Trombe wall design for buildings in composite climates. *Journal of Solar Energy Engineering* 129 (4): 431-437.
- Jones, M. 2003. Thermal properties of stratified rocks from Witwatersrand gold mining areas. *The Journal of The South African Institute of Mining and Metallurgy* 35 (1): 173-183.
- Kalaiselvam, S and Parameshwaran, R. 2014. *Thermal Energy Storage Technologies for Sustainability: Systems Design, Assessment and Applications*. Elsevier Inc., 32 Jamestown Road, London NQ1 7BY, United Kingdom.
- Kaviany, M. 2012. *Principles of Heat Transfer in Porous Media*. Springer Science & Business Media, Springer-Verlag New York, Inc., 175 Fifth Avenue, New York, NY 10010, United States of America.
- Khudhair, AM and Farid, MM. 2004. A review on energy conservation in building applications with thermal storage by latent heat using phase change materials. *Energy Conversion and Management* 45 (2): 263-275.
- Kürklü, A, Bilgin, S and Özkan, B. 2003. A study on the solar energy storing rock-bed to heat a polyethylene tunnel type greenhouse. *Renewable Energy* 28 (5): 683-697.
- Lin, W, Ma, Z, Sohel, MI and Cooper, P. 2014. Development and evaluation of a ceiling ventilation system enhanced by solar photovoltaic thermal collectors and phase change materials. *Energy Conversion and Management* 88: 218-230.
- Liping, W and Angui, L. 2006. A numerical study of Trombe wall for enhancing stack ventilation in buildings. *The 23rd Conference on Passive and Low Energy Architecture*, Geneva, Switzerland.
- Löf, G and Hawley, R. 1948. Unsteady-state heat transfer between air and loose solids. *Industrial and Engineering Chemistry* 40 (6): 1061-1070.
- Louw, AD, Nel, RG and Gauché, P. 2012. A DEM-CFD approach to predict the pressure drop through an air-rock bed thermal energy storage system: Part 2 of 2. *Southern African Solar Energy Conference*, Protea Hotel, Technopark, Stellenbosch, South Africa.
- Louw, ADR. 2014. Discrete and porous computational fluid dynamics modelling of an air-rock bed thermal energy storage system. Unpublished thesis, Stellenbosch University, Stellenbosch, South Africa.
- Marewo, G and Henwood, D. 2006. A mathematical model for supplying air-cooling for a building using a packed bed. *Building Services Engineering Research and Technology* 27 (1): 11-26.

- Meola, C and Carlomagno, GM. 2004. Recent advances in the use of infrared thermography. *Measurement Science and Technology* 15 (9): R27.
- Moran, MJ, Shapiro, HN, Boettner, DD and Bailey, MB. 2010. *Fundamentals of Engineering Thermodynamics*. John Wiley and Sons, 111 River Street, Hoboken, NJ 07030, United States of America.
- Mueller, GE. 2010. Radial porosity in packed beds of spheres. *Powder Technology* 203 (3): 626-633.
- N'Tsoukpoe, KE, Liu, H, Le Pierrès, N and Luo, L. 2009. A review on long-term sorption solar energy storage. *Renewable and Sustainable Energy Reviews* 13 (9): 2385-2396.
- Nel, RG, Louw, AD and Coetzee, C. 2012. A DEM-CFD approach to predict the pressure drop through an air-rockbed thermal storage system: Part 1. *Southern African Solar Energy Conference*, Protea Hotel, Stellenbosch, South Africa.
- Ozbalta, TG and Kartal, S. 2010. Heat gain through Trombe wall using solar energy in a cold region of Turkey. *Scientific Research and Essays* 5 (18): 2768-2778.
- Özkahraman, H, Selver, R and Işık, E. 2004. Determination of the thermal conductivity of rock from P-wave velocity. *International Journal of Rock Mechanics and Mining Sciences* 41 (4): 703-708.
- Pérez-Lombard, L, Ortiz, J and Pout, C. 2008. A review on buildings energy consumption information. *Energy and Buildings* 40 (3): 394-398.
- Phueakphum, D and Fuenkajorn, K. 2010. A rock fills based solar thermal energy storage system for housing. *Science Asia* 36: 237-243.
- Pinel, P, Cruickshank, CA, Beausoleil-Morrison, I and Wills, A. 2011. A review of available methods for seasonal storage of solar thermal energy in residential applications. *Renewable and Sustainable Energy Reviews* 15 (7): 3341-3359.
- Pintaldi, S, Perfumo, C, Sethuvenkatraman, S, White, S and Rosengarten, G. 2015. A review of thermal energy storage technologies and control approaches for solar cooling. *Renewable and Sustainable Energy Reviews* 41: 975-995.
- Pramod, KR and Daniele, I. 2000. *Trends in Optical Non-destructive Testing and Inspection*. Elsevier, Inc., Michigan, United States of America.
- Rabani, M, Kalantar, V, Dehghan, AA and Faghieh, AK. 2015. Experimental study of the heating performance of a Trombe wall with a new design. *Solar Energy* 118: 359-374.
- Radosavljević, J, Lambić, M and Pavlović, TM. 2004. Thermodynamic designing of a solar block of flats with a tromb's wall with ventuce holes. *Facta Universitatis-Series: Physics, Chemistry and Technology* 3 (1): 27-34.

- Saber, EM, Lee, SE, Manthapuri, S, Yi, W and Deb, C. 2014. PV (photovoltaics) performance evaluation and simulation-based energy yield prediction for tropical buildings. *Energy* 71: 588-595.
- Sanderson, T and Cunningham, G. 1995a. Packed bed thermal storage systems. *Applied Energy* 51 (1): 51-67.
- Sanderson, T and Cunningham, G. 1995b. Performance and efficient design of packed bed thermal storage systems. Part 1. *Applied Energy* 50 (2): 119-132.
- Sayma, A. 2009. *Computational Fluid Dynamics*. Ventus Publishing ApS, Falkoner Alle 7, 2000 Frederiksberg, Denmark.
- Schumann, TE. 1929. Heat transfer: A liquid flowing through a porous prism. *Journal of the Franklin Institute* 208 (3): 405-416.
- Shepherd, RG. 1989. Correlations of permeability and grain size. *Groundwater* 27 (5): 633-638.
- Singh, H, Saini, R and Saini, J. 2010. A review on packed bed solar energy storage systems. *Renewable and Sustainable Energy Reviews* 14 (3): 1059-1069.
- Singh, H, Saini, R and Saini, J. 2013. Performance of a packed bed solar energy storage system having large sized elements with low void fraction. *Solar Energy* 87: 22-34.
- Singh, R, Saini, R and Saini, J. 2006. Nusselt number and friction factor correlations for packed bed solar energy storage system having large sized elements of different shapes. *Solar Energy* 80 (7): 760-771.
- Srinivasan, R and Raghunandan, B. 2013. Experiments on thermal response of low aspect ratio packed beds at high Reynolds numbers with varying inflow temperature. *Experimental Thermal and Fluid Science* 44: 323-333.
- Stazi, F, Di Perna, C, Filiaci, C and Stazi, A. 2008. The solar wall in the italian climates. *World Academy of Science, Engineering and Technology* 37: 31-39.
- Suman, S, Khan, MK and Pathak, M. 2015. Performance enhancement of solar collectors—A review. *Renewable and Sustainable Energy Reviews* 49: 192-210.
- Theron, WGJ. 2011. Numerical analysis of the flow distribution within packed columns using an explicit approach. Unpublished thesis, School of Mechanical and Nuclear Engineering, Potchefstroom Campus of the North-West University, South Africa.
- Todorović, R, Banjac, M and Gojak, M. 2015. Theoretical and experimental study of heat transfer in wall heating panels. *Energy and Buildings* 98: 66-73.
- Todorović, RI, Banjac, MJ and Vasiljević, BM. 2014. Analytical and experimental determination of the temperature field on the surface of wall heating panels. *Thermal Science* 19 (2): 68-68.

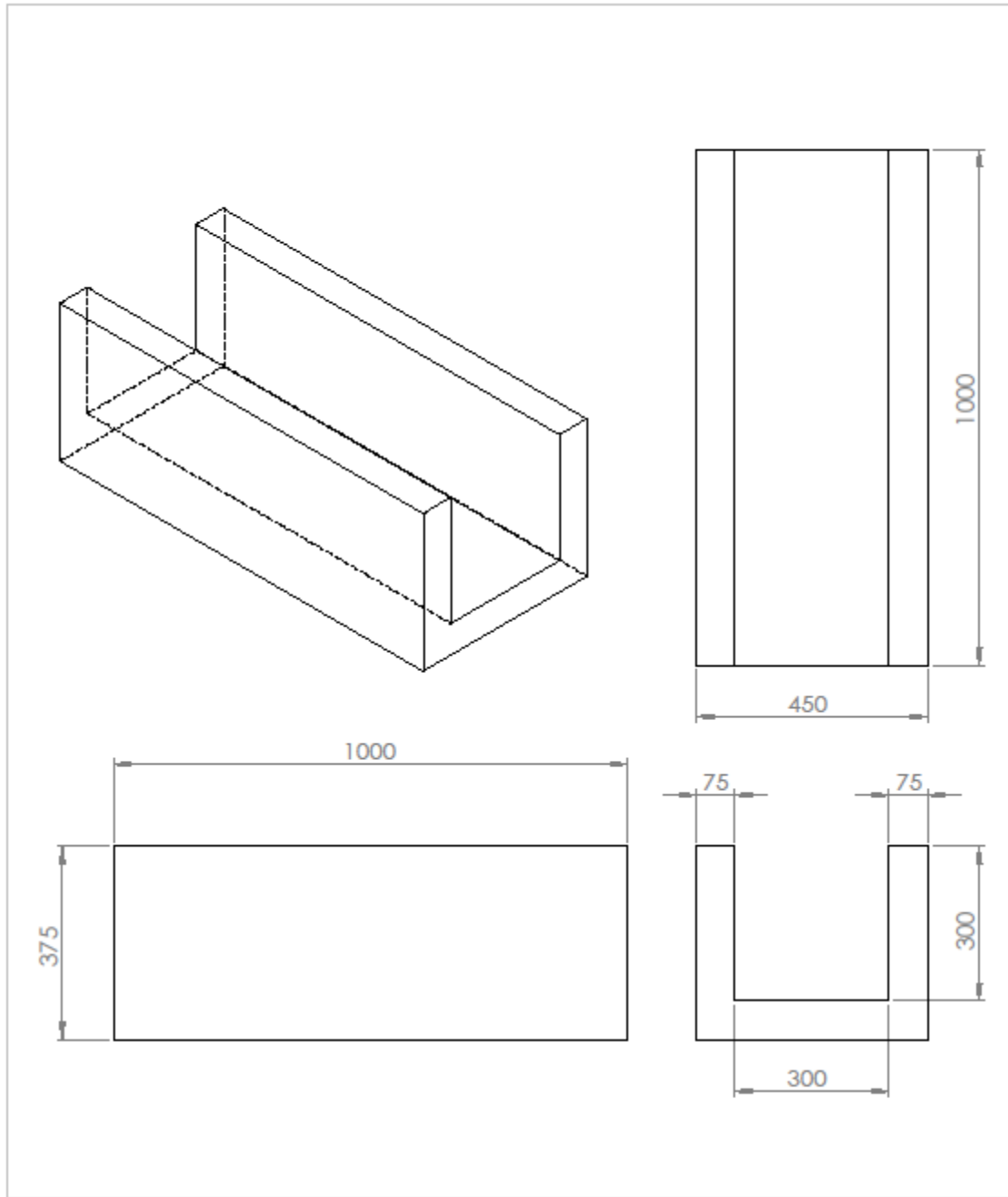
- Toolbox, TE. 2016. Thermal conductivity of some common materials and gases. [Internet]. Available from: http://www.engineeringtoolbox.com/thermal-conductivity-d_429.html. [Accessed: 03-09-2016].
- Vaisala, T. 2015. Glossary of technical renewable energy terminology. [Internet]. Available from: <http://www.3tier.com/en/support/glossary/#ghi>. [Accessed: 13-08-2015].
- Van der Merwe, WJS. 2014. Analysis of flow through cylindrical packed beds with small cylinder diameter to particle diameter ratios. Unpublished thesis, School of Mechanical and Nuclear Engineering, Potchefstroom Campus of the North-West University, South Africa.
- Wang, W, Tian, Z and Ding, Y. 2013. Investigation on the influencing factors of energy consumption and thermal comfort for a passive solar house with water thermal storage wall. *Energy and Buildings* 64: 218-223.
- Woolridge, MW, LW.1980. Summary of major results from first winter of operation of the CSIRO LEC house. *1980 Airah Conference in Melbourne*, 23-34. Australian Refrigeration, Air Conditioning and Heating, Melbourne, Australia.
- Zanganeh, G, Pedretti, A, Haselbacher, A and Steinfeld, A. 2015. Design of packed bed thermal energy storage systems for high-temperature industrial process heat. *Applied Energy* 137: 812-822.
- Zavattoni, S, Barbato, M, Pedretti, A and Zanganeh, G.2011. CFD simulations of a pebble bed thermal energy storage system accounting for porosity variations effects. *SolarPaces-2011*, Granada Congress Centre, Granada, Spain.
- Zavattoni, S, Barbato, M, Pedretti, A, Zanganeh, G and Steinfeld, A.2012. Effective thermal conductivity and axial porosity distribution of a rock-bed TES system: CFD modeling and experimental validation. *SolarPACES Conference, September*, 11-14.
- Zavattoni, S, Barbato, M, Pedretti, A, Zanganeh, G and Steinfeld, A. 2014. High temperature rock-bed TES system suitable for industrial-scale CSP plant—CFD analysis under charge/discharge cyclic conditions. *Energy Procedia* 46: 124-133.
- Zhai, X, Qu, M, Li, Y and Wang, R. 2011. A review for research and new design options of solar absorption cooling systems. *Renewable and Sustainable Energy Reviews* 15 (9): 4416-4423.
- Zhang, H, Baeyens, J, Degrève, J and Cacères, G. 2013. Concentrated solar power plants: review and design methodology. *Renewable and Sustainable Energy Reviews* 22: 466-481.
- Zhang, Z, Sun, Z and Duan, C. 2014. A new type of passive solar energy utilization technology—The wall implanted with heat pipes. *Energy and Buildings* 84: 111-116.

7. APPENDIX A: RESIDENTIAL SECTOR ELECTRICITY CONSUMPTION

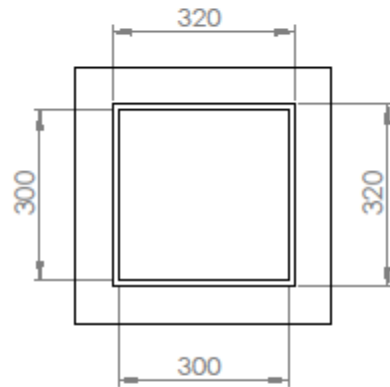
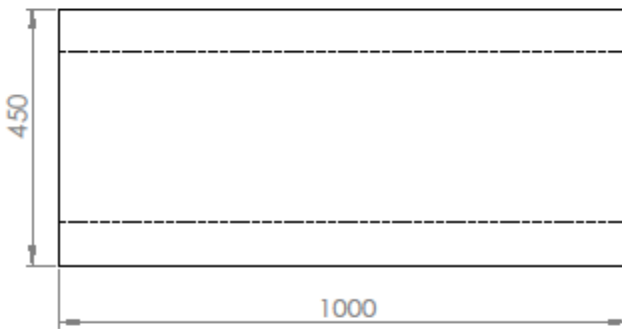
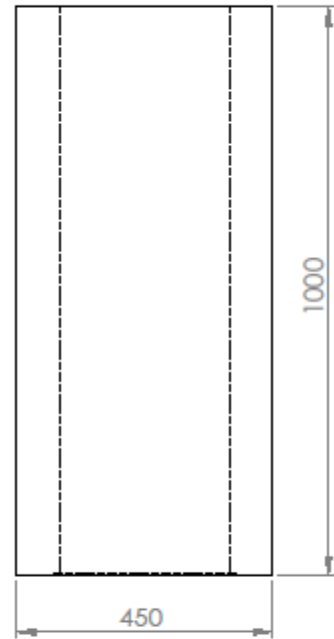
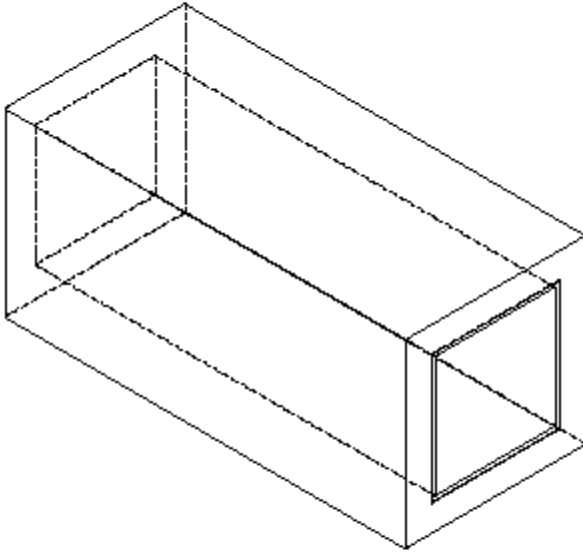
Table 7.1 Estimated U.S. residential sector electricity consumption by end use in 2014
(after EIA, 2009)

Estimated U.S. residential sector electricity consumption by end use, 2014			
End use	Exajoule (10 ¹⁸ Joule)	Billion kilowatthours	Share of total
Space cooling	0.686	190	13%
Lighting	0.538	149	11%
Water heating	0.475	132	9%
Space heating	0.454	125	9%
Refrigeration	0.380	106	8%
Televisions and related equipment	0.317	88	6%
Clothes dryers	0.211	60	4%
Furnace fans and boiler circulation pumps	0.148	42	3%
Computers and related equipment	0.116	34	2%
Cooking	0.116	31	2%
Dishwashers	0.095	28	2%
Freezers	0.084	22	2%
Clothes washers	0.032	8	1%
Other uses	1.414	393	28%
Total consumption	5.064	1,407	

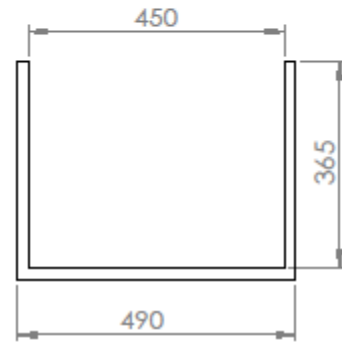
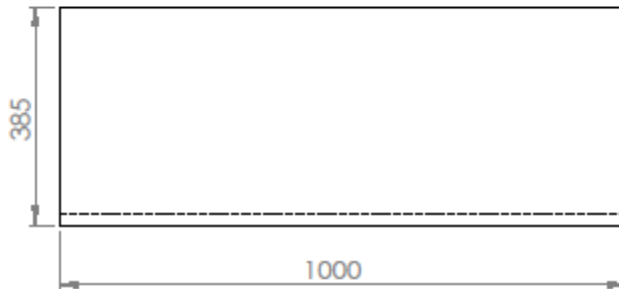
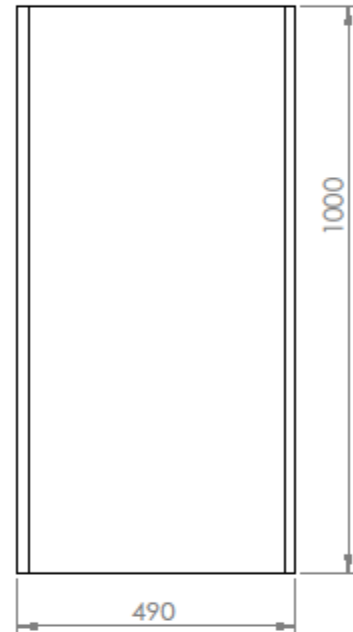
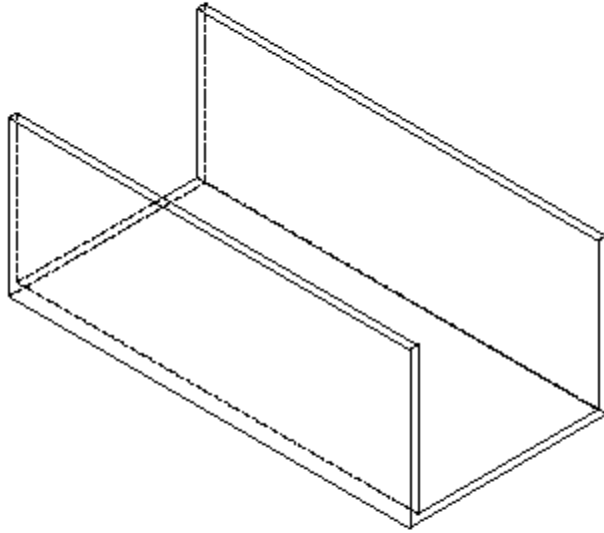
8. APPENDIX B: PACKED BED DESIGN DRAWINGS



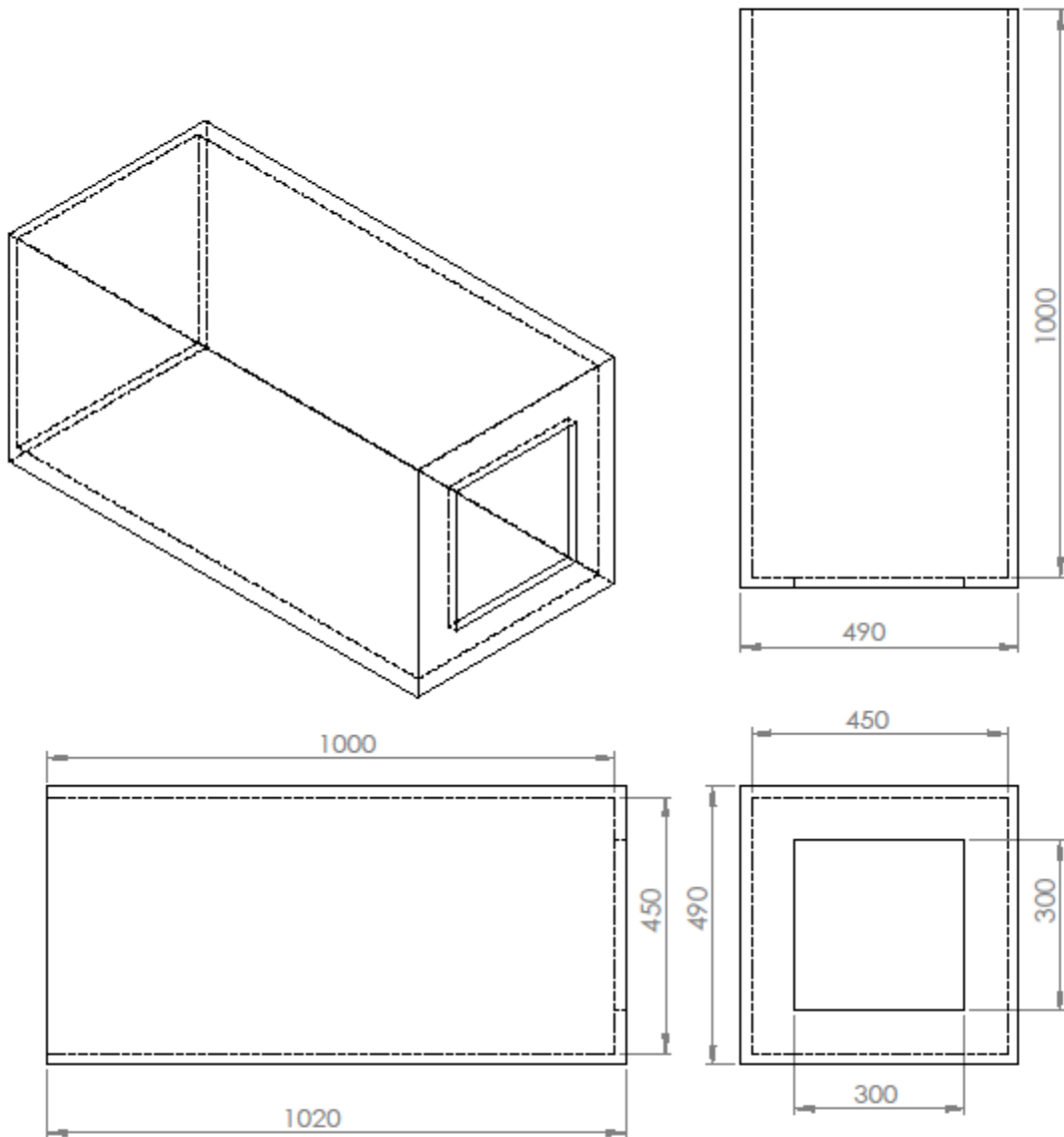
UNLESS OTHERWISE SPECIFIED: DIMENSIONS ARE IN MILLIMETERS SURFACE FINISH: TOLERANCES: LINEAR: ANGULAR:		FINISH:	DEBUR AND BREAK SHARP EDGES		DO NOT SCALE DRAWING	REVISION																														
<table border="1"> <thead> <tr> <th>NAME</th> <th>SIGNATURE</th> <th>DATE</th> <th></th> <th></th> </tr> </thead> <tbody> <tr> <td>DRAWN</td> <td></td> <td></td> <td></td> <td></td> </tr> <tr> <td>CHK'D</td> <td></td> <td></td> <td></td> <td></td> </tr> <tr> <td>APP'VD</td> <td></td> <td></td> <td></td> <td></td> </tr> <tr> <td>MFG</td> <td></td> <td></td> <td></td> <td></td> </tr> <tr> <td>G.A.</td> <td></td> <td></td> <td></td> <td></td> </tr> </tbody> </table>					NAME	SIGNATURE	DATE			DRAWN					CHK'D					APP'VD					MFG					G.A.					TITLE: POLYSTYRENE CENTRE	
NAME	SIGNATURE	DATE																																		
DRAWN																																				
CHK'D																																				
APP'VD																																				
MFG																																				
G.A.																																				
SolidWorks Student Edition. For Academic Use Only.					DWG NO.	A4																														
WEIGHT:					SCALE:1:10	SHEET 1 OF 1																														



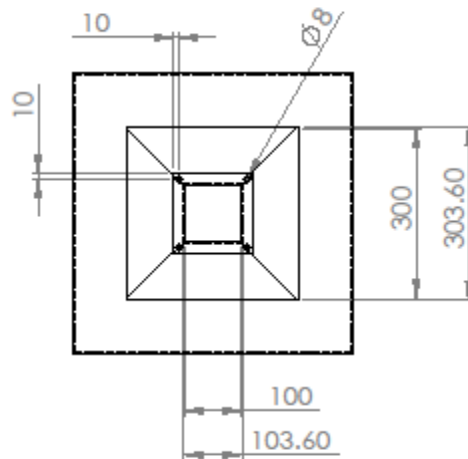
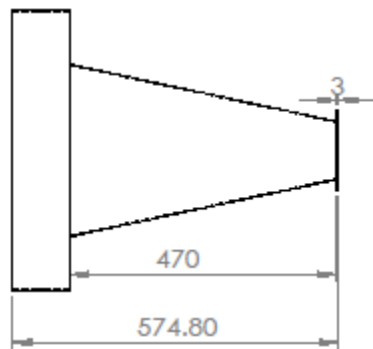
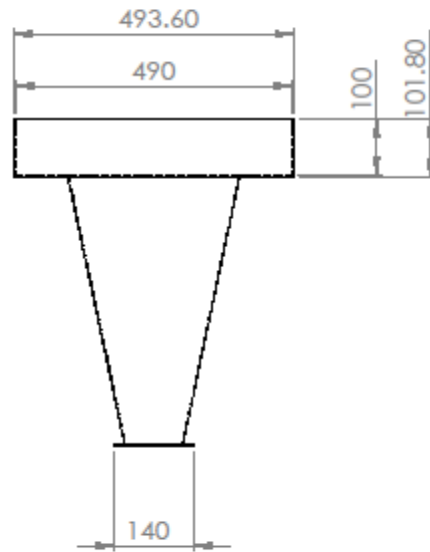
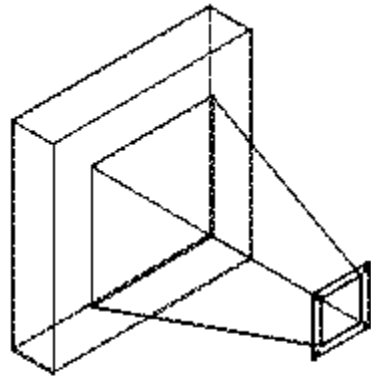
UNLESS OTHERWISE SPECIFIED: DIMENSIONS ARE IN MILLIMETERS SURFACE FINISH: TOLERANCES: LINEAR: ANGULAR:				FINISH:	DEBUR AND BREAK SHARP EDGES	DO NOT SCALE DRAWING	REVISION	
DRAWN	NAME	SIGNATURE	DATE			POLYSTYRENE INLET & OUTLET		
CHK'D								
APP'D								
MFG	SolidWorks Student Edition.							
G.A.	For Academic Use Only.							
						DWG NO.	A4	
				WEIGHT:		SCALE:1:10	SHEET 1 OF 1	



UNLESS OTHERWISE SPECIFIED: DIMENSIONS ARE IN MILLIMETERS SURFACE FINISH: TOLERANCES: LINEAR: ANGULAR:		FINISH:	DEBUR AND BREAK SHARP EDGES		DO NOT SCALE DRAWING	REVISION
DRAWN	NAME	SIGNATURE	DATE		TITLE: WOOD CENTRE	
CHK'D						
APP'VD						
MFG						
G.A.						
SolidWorks Student Edition. For Academic Use Only.				MATERIAL:	DWG NO.	A4
WEIGHT:				SCALE:1:10	SHEET 1 OF 1	

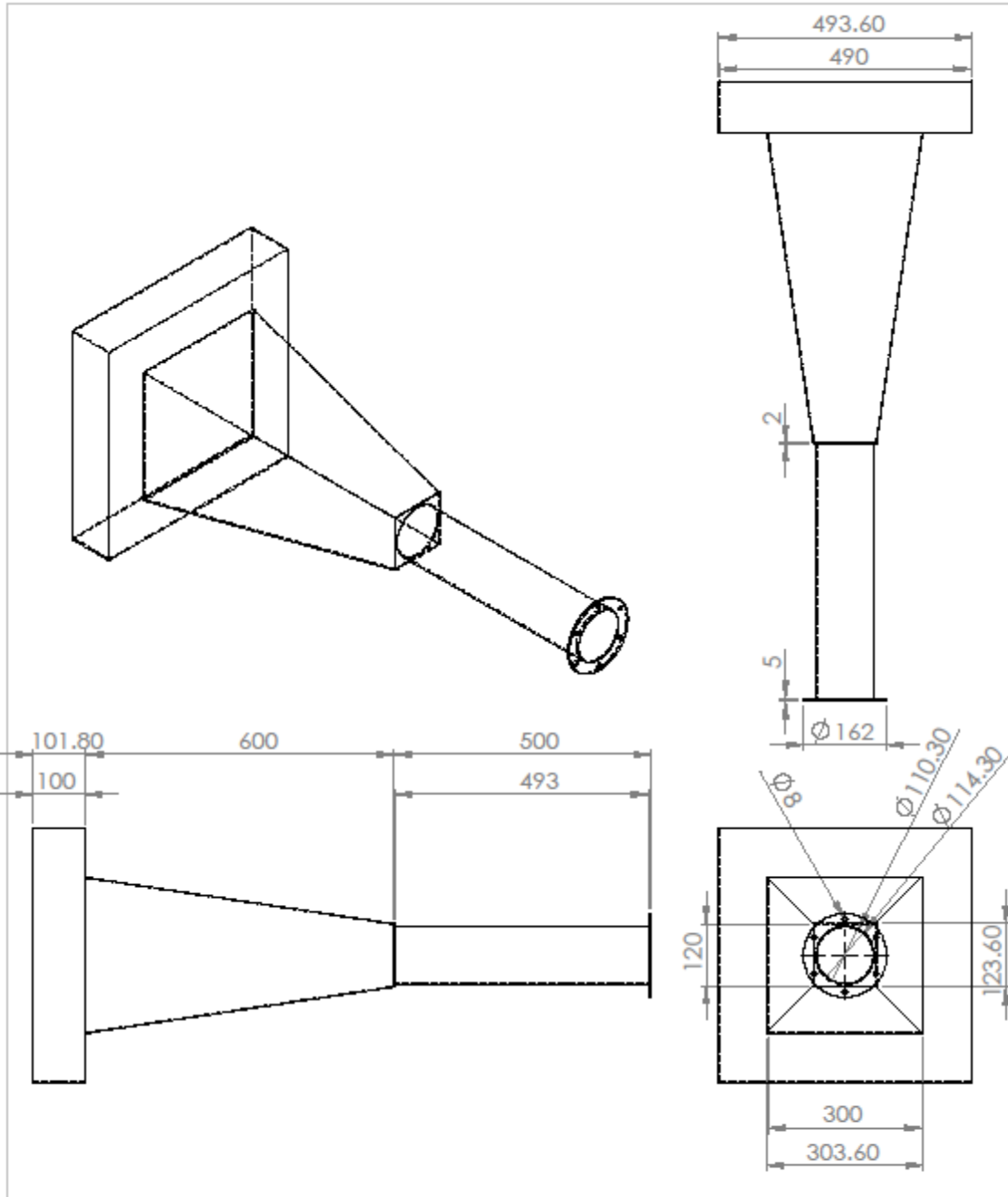


UNLESS OTHERWISE SPECIFIED: DIMENSIONS ARE IN MILLIMETERS SURFACE FINISH: TOLERANCES: LINEAR: ANGULAR:			FINISH:	DEBUR AND BREAK SHARP EDGES	DO NOT SCALE DRAWING	REVISION
DRAWN	NAME	SIGNATURE	DATE		TITLE: WOOD INLET & OUTLET	
CHK'D						
APP'VD						
MFG	SolidWorks Student Edition.				DWG NO.	A4
G.A.	For Academic Use Only.					
				WEIGHT:	SCALE:1:10	SHEET 1 OF 1



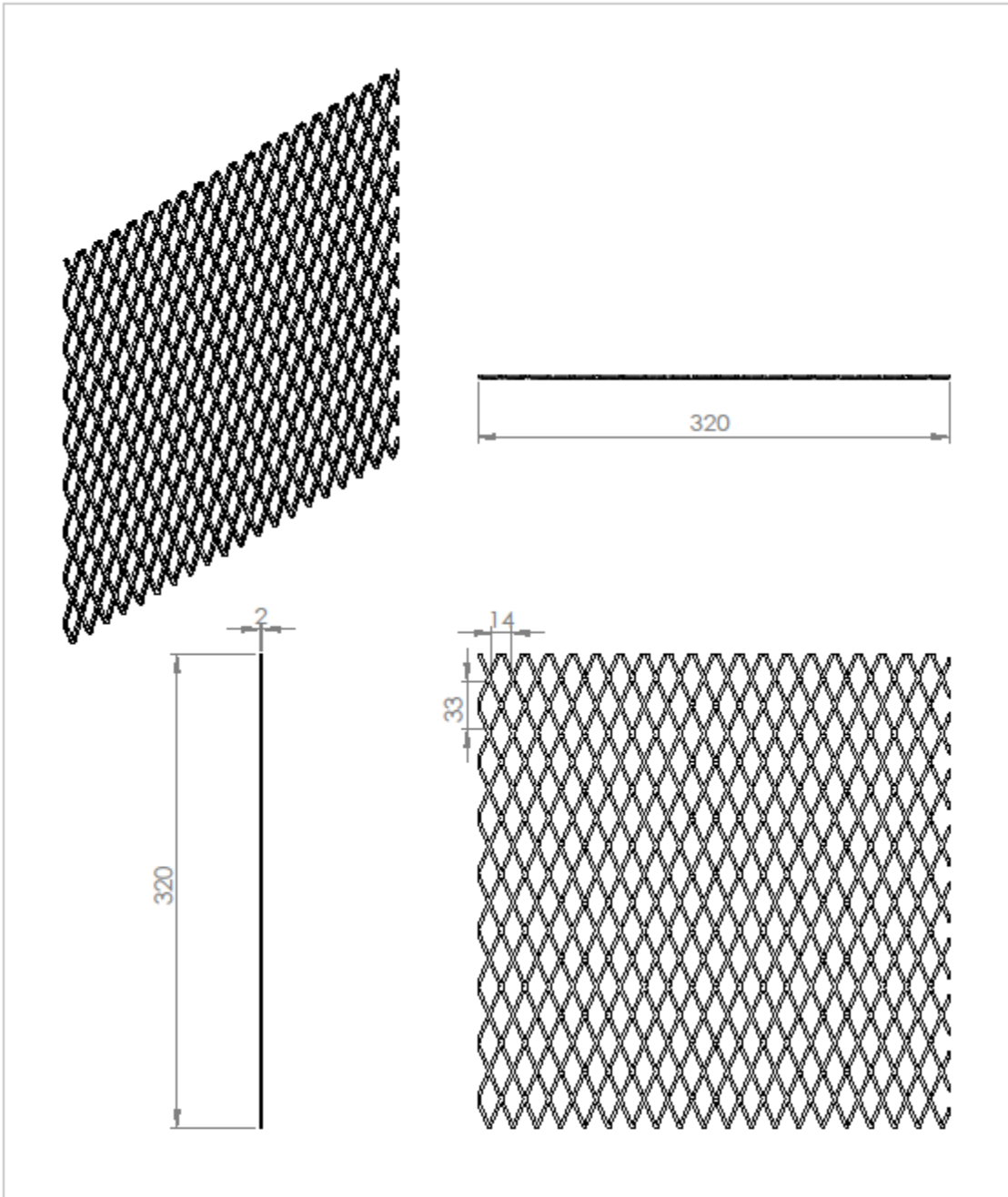
UNLESS OTHERWISE SPECIFIED: DIMENSIONS ARE IN MILLIMETERS		FINISH:		DEBUR AND BREAK SHARP EDGES		DO NOT SCALE DRAWING		REVISION	
SURFACE FINISH:									
TOLERANCES:									
LINEAR:									
ANGULAR:									
NAME		SIGNATURE		DATE		TITLE:			
DRAWN						DUCT DESIGN INLET			
CHK'D									
APP'VD									
MFG									
G.A.						DWG NO.		A4	
						SCALE:1:10		SHEET 1 OF 1	
				WEIGHT:					

**SolidWorks Student Edition.
For Academic Use Only.**

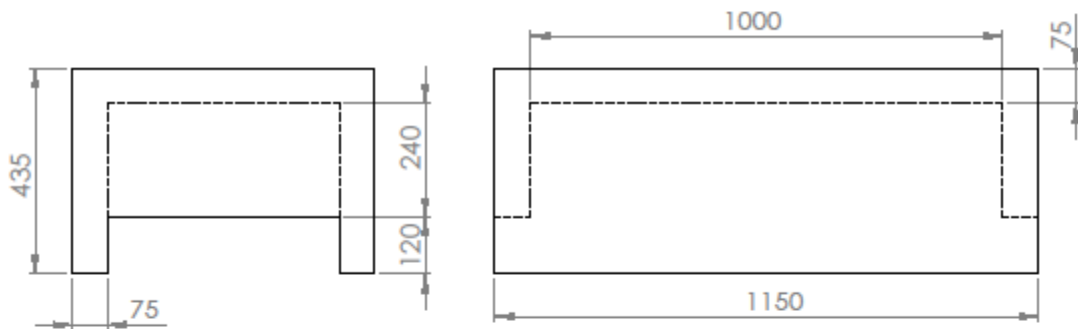
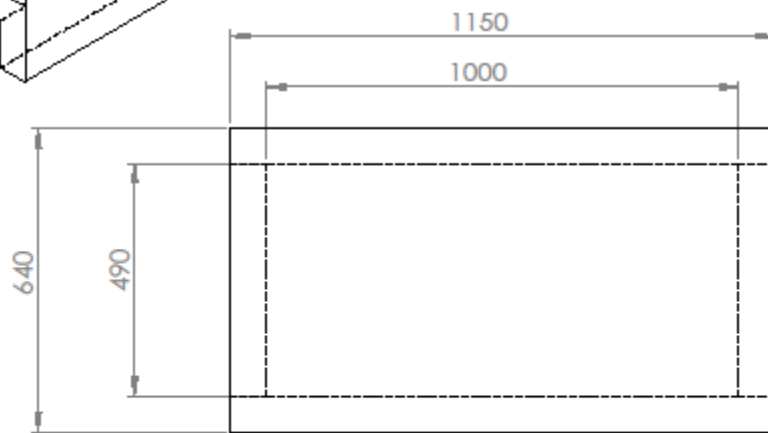
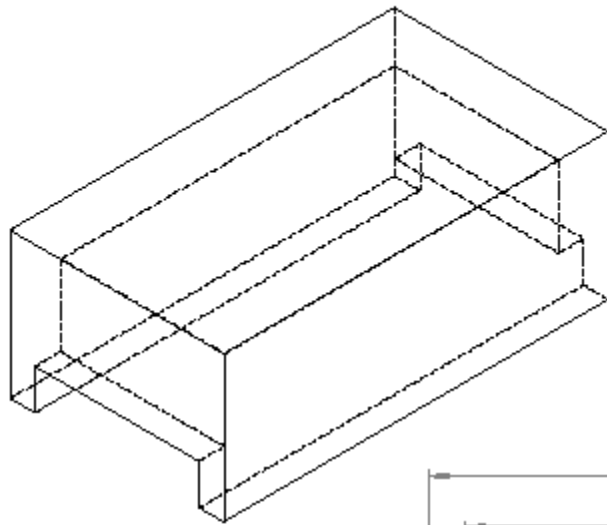


UNLESS OTHERWISE SPECIFIED: DIMENSIONS ARE IN MILLIMETERS SURFACE FINISH: TOLERANCES: LINEAR: ANGULAR:		FINISH:		DEBUR AND BREAK SHARP EDGES		DO NOT SCALE DRAWING		REVISION	
DRAWN		SIGNATURE		DATE		TITLE: DUCT DESIGN OUTLET			
CHK'D									
APP'VD									
MFG									
G.A.						DWG NO.		A4	
						SCALE:1:10		SHEET 1 OF 1	
						WEIGHT:			

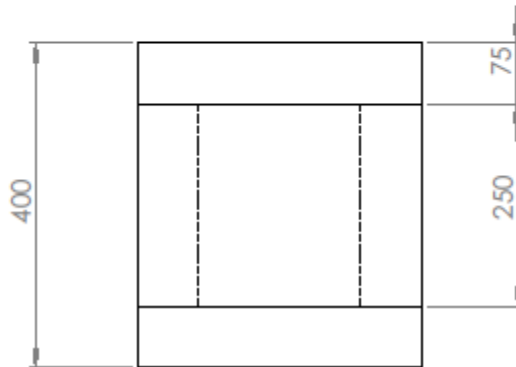
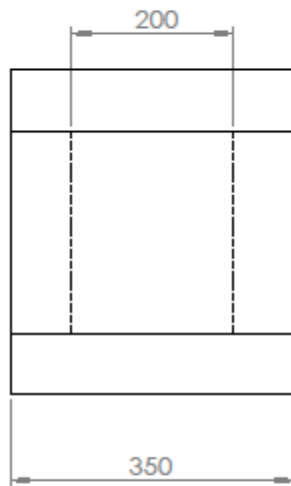
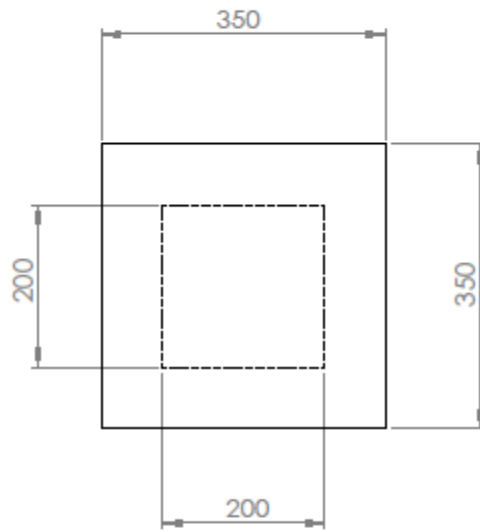
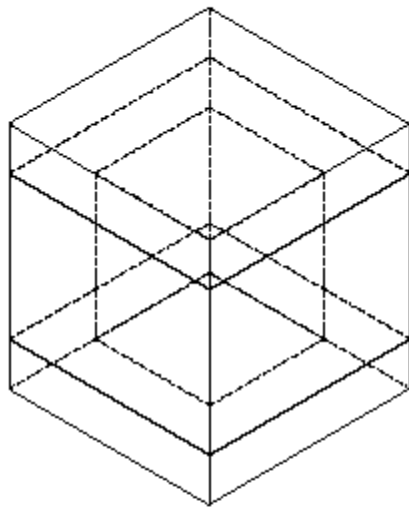
**SolidWorks Student Edition.
For Academic Use Only.**



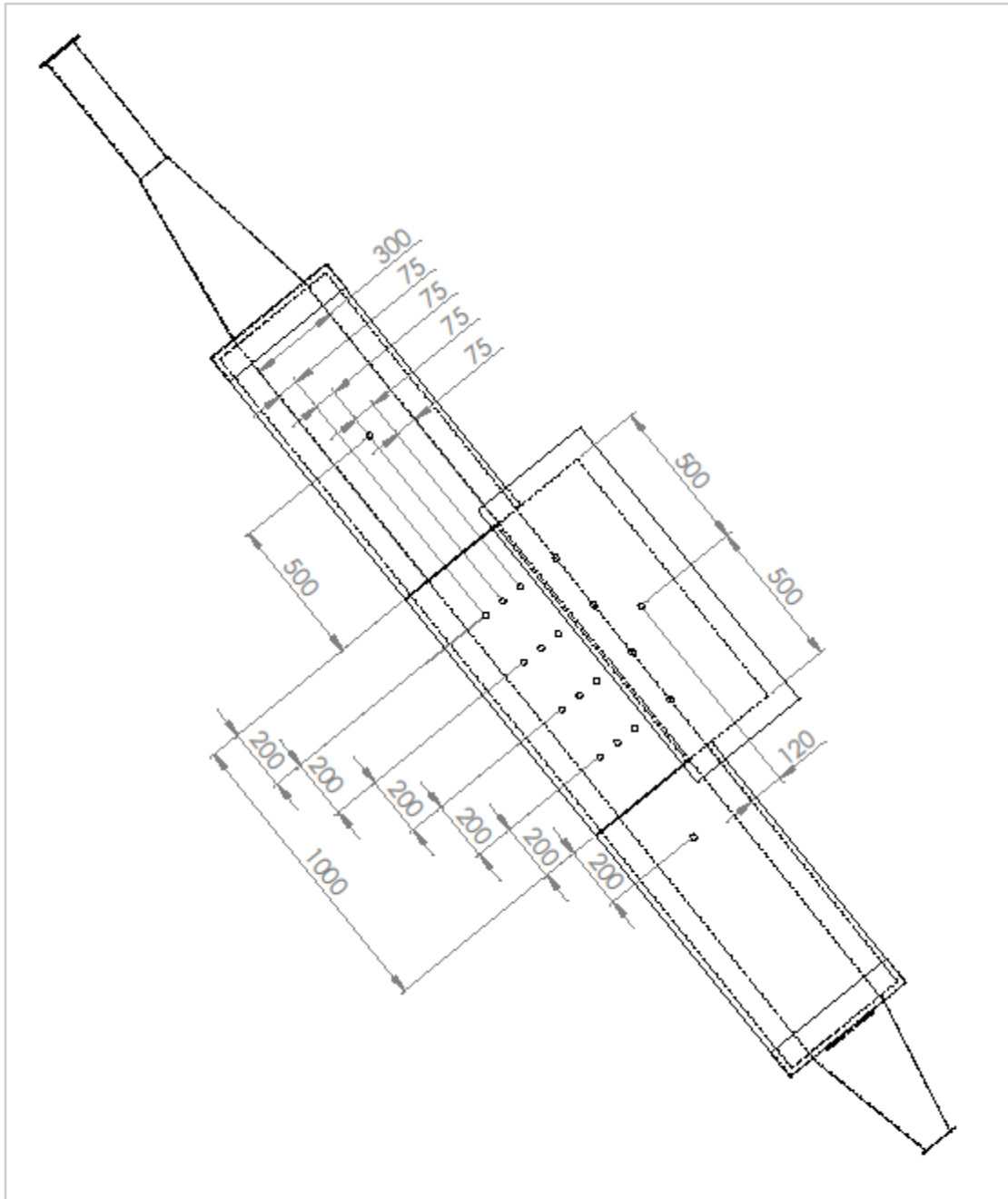
UNLESS OTHERWISE SPECIFIED: DIMENSIONS ARE IN MILLIMETERS SURFACE FINISH: TOLERANCES: LINEAR: ANGULAR:				FINISH:	DEBUR AND BREAK SHARP EDGES	DO NOT SCALE DRAWING	REVISION
DRAWN	NAME	SIGNATURE	DATE			TITLE: EXPANDED METAL	
CHK'D							
APP'VD							
MFG	SolidWorks Student Edition.					DWG NO.	
G.A.	For Academic Use Only.						A4
				WEIGHT:		SCALE:1:3.5	SHEET 1 OF 1



UNLESS OTHERWISE SPECIFIED: DIMENSIONS ARE IN MILLIMETERS		FINISH:		DEBUR AND BREAK SHARP EDGES		DO NOT SCALE DRAWING		REVISION	
SURFACE FINISH:									
TOLERANCES:									
LINEAR:									
ANGULAR:									
DRAWN		NAME	SIGNATURE	DATE	TITLE: POLYSTYRENE COVER				
CHK'D									
APP'VD									
MFG		SolidWorks Student Edition.			DWG NO.				
G.A.		For Academic Use Only.			A4				
		WEIGHT:			SCALE:1:12		SHEET 1 OF 1		



UNLESS OTHERWISE SPECIFIED: DIMENSIONS ARE IN MILLIMETERS SURFACE FINISH: TOLERANCES: LINEAR: ANGULAR:		FINISH:	DEBUR AND BREAK SHARP EDGES		DO NOT SCALE DRAWING	REVISION
DRAWN	NAME	SIGNATURE	DATE		TITLE: POLYSTYRENE CONTAINER	
CHK'D						
APP'VD						
MFG						
G.A.	SolidWorks Student Edition. For Academic Use Only.			MATERIAL:	DWG NO.	A4
			WEIGHT:		SCALE:1:7	SHEET 1 OF 1



UNLESS OTHERWISE SPECIFIED: DIMENSIONS ARE IN MILLIMETERS		FINISH:		DEBUR AND BREAK SHARP EDGES		DO NOT SCALE DRAWING		REVISION	
SURFACE FINISH:									
TOLERANCES:									
LINEAR:									
ANGULAR:									
	NAME	SIGNATURE	DATE			TITLE: TEMPERATURE PROBES PLACEMENT			
DRAWN									
CHK'D									
APP'VD									
MFG	SolidWorks Student Edition.								
G.A.	For Academic Use Only.					DWG NO.		A4	
				WEIGHT:		SCALE:1:17		SHEET 1 OF 1	

9. APPENDIX C: PRESSURE DROP CALCULATIONS

The pressure drop and particle Reynolds number calculations were calculated for the rock-bed with a duct diameter of 300 mm x 300 mm, using the values summarised in Table 9.1.

Table 9.1 Summary of the values used to calculate the pressure drop and particle Reynolds number

	Value	Unit
ρ_a	1.01	kg.m. ⁻³
x	0.019	m
ε	0.44	%
U	0.9162979	m.s ⁻¹
κ	0.0000184	Pa.s
L	1	m
C_v	0.7	unitless
A	0.0643103	m ²

The calculations were conducted, based on the maximum flow velocity through the packed bed. The pressure drop over the packed bed was calculated, using the Ergun (1952) equation as shown in Equation (9.1).

$$\frac{-\Delta P}{L} = 150 \frac{\kappa U(1 - \varepsilon)^2}{x^2 \varepsilon^3} + 1.75 \frac{\rho_f U^2(1 - \varepsilon)}{x \varepsilon^3} \quad (9.1)$$

where,

$\Delta P = \text{change in pressure [Pa]}$,

$\kappa = \text{dynamic viscosity [Pa.s]}$,

$U = \text{superficial velocity [m.s}^{-1}\text{]}$,

$x = \text{spherical equivalent particle diameter [m]}$, and

$\rho_f = \text{density of fluid [kg.m}^{-3}\text{]}$.

The total pressure drop over the packed bed was calculated to be 1695.23 Pa. The pressure drop over the expanded metal mesh was also calculated, using Equation (9.2).

$$\Delta P = \left(\frac{\dot{V}_f}{C_v A} \right)^2 \left(\frac{\rho_f}{2} \right) \quad (9.2)$$

where,

$C_v = \text{flow coefficient [unitless]}$, and

$\dot{V}_f = \text{volumetric flow rate [m}^3\text{.s}^{-1}\text{]}$.

The maximum pressure drop over the expanded metal mesh was calculated to be 2.3067 Pa. The particle Reynolds number from Ergun (1952) was used to determine the flow regime through the packed bed, based on the flow values used in the study, as shown in Equation (9.3):

$$Re^* = \frac{xU\rho_f}{\kappa(1 - \varepsilon)} \quad (9.3)$$

where,

$Re^* = \text{particle Reynolds number [unitless]}$.

The minimum and maximum particle Reynolds numbers calculated, were 855.687 and 1695.229, respectively.

10. APPENDIX D: PRESSURE-PRODUCING DEVICE DETAILS

G1G170-AB53-03

EC centrifugal fan

backward-curved, single-intake
with housing (flange), Gas blower for condensing boilers



ebm-papst Mulfingen GmbH & Co. KG
Bachmühle 2 · D-74673 Mulfingen
Phone +49 7938 81-0
Fax +49 7938 81-110
info1@de.ebmpapst.com
www.ebmpapst.com

United partnership · Headquarters Mulfingen
Antragsnr. (court of registration) Stuttgart · HRA 590344
General partner Elektrobau Mulfingen GmbH · Headquarters Mulfingen
Antragsnr. (court of registration) Stuttgart · HRB 590142



Nominal data

Type	G1G170-AB53-03	
Motor	M1G074-CF	
Phase		1~
Nominal voltage	VAC	230
Frequency	Hz	50/60
Method of obtaining data		fa
Speed	min ⁻¹	5830
Power consumption	W	360
Current draw	A	1.6
Min. ambient temperature	°C	-25
Max. ambient temperature	°C	55
Min. temp. of flow medium	°C	-25
Max. temp. of flow medium	°C	+80

nl = Max. load ne = Max. efficiency fs = Free air cs = Customer specification ca = Customer equipment
Subject to change

Data according to ErP Directive

		Actual	Req. 2015			
01 Overall efficiency η_{ES}	%	58.8	45	09 Power consumption P_{ed}	KW	0.3
02 Measurement category		A		09 Air flow q_v	m ³ /h	285
03 Efficiency category		Static		09 Pressure increase p_{es}	Pa	2000
04 Efficiency grade N		74.8	61	10 Speed n	min ⁻¹	6220
05 Variable speed drive		Yes		11 Specific ratio*		1.02

Data obtained at optimum efficiency level.
The ErP data is determined using a motor-impeller combination in a standardized measurement setup.

* Specific ratio = $1 + p_{es} / 100\ 000\ Pa$

LU47508



G1G170-AB53-03

EC centrifugal fan

backward-curved, single-intake
with housing (flange), Gas blower for condensing boilers

Technical description

Weight	4.47 kg
Fan size	170 mm
Rotor surface	Painted black
Cover material	Polyflam RPP 374-ND C51 (UL 97-V0)
Impeller material	Sheet aluminum
Housing material	Die-cast aluminum
Direction of rotation	Clockwise, viewed toward rotor
Degree of protection	IP20
Insulation class	"B"
Max. permitted ambient temp. for motor (transport/storage)	+80 °C
Min. permitted ambient temp. for motor (transport/storage)	-40 °C
Installation position	Any
Cooling hole/opening	On rotor side
Mode	S1
Premixing	If gas is premixed in the blower, then a special blower must be used. Please consult us about this.
Motor bearing	Ball bearing
Technical features	<ul style="list-style-type: none">- PFC, active- PWM control input- Motor current limitation- Tach output- Thermal overload protection for motor
EMC immunity to interference	According to EN 61000-6-2 (industrial environment)
EMC circuit feedback	According to EN 61000-3-2/3
EMC interference emission	According to EN 61000-6-3 (household environment)
Touch current according to IEC 60990 (measuring circuit Fig. 4, TN system)	≤ 3.5 mA
Electrical hookup	With plug
Motor protection	Thermal overload protector (TOP) internally connected
Approval	UL 507; CSA C22.2 No. 113



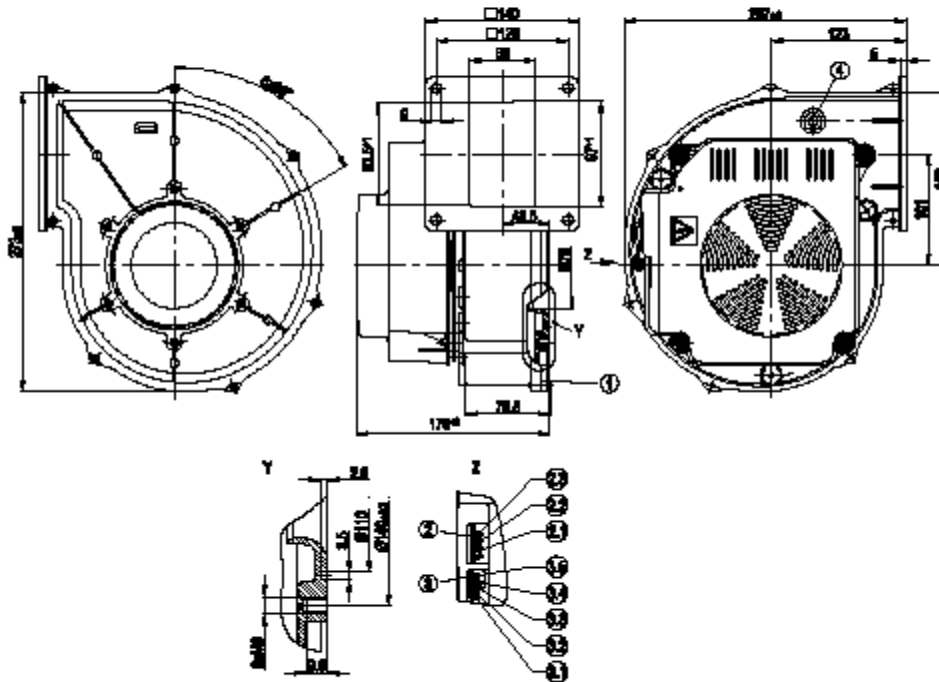
G1G170-AB53-03

EC centrifugal fan

backward-curved, single-intake

with housing (flange), Gas blower for condensing boilers

Product drawing



1	Housing side parts sealed with NBR round cord (pentane-resistant)
2	View Z
2	3-pole header, mating connector (not included in scope of delivery): tyco no. 350 766-1, socket: tyco no. 926 884-1
2.1	L
2.2	N
2.3	PE
3	5-pole header, mating connector (not included in scope of delivery): Molex no. 39-01-4050; socket: Molex no. 39-00-0059
3.1	(+)
3.2	Speed monitoring
3.3	not used
3.4	PWM input
3.5	(-)
4	Pressure tap possible



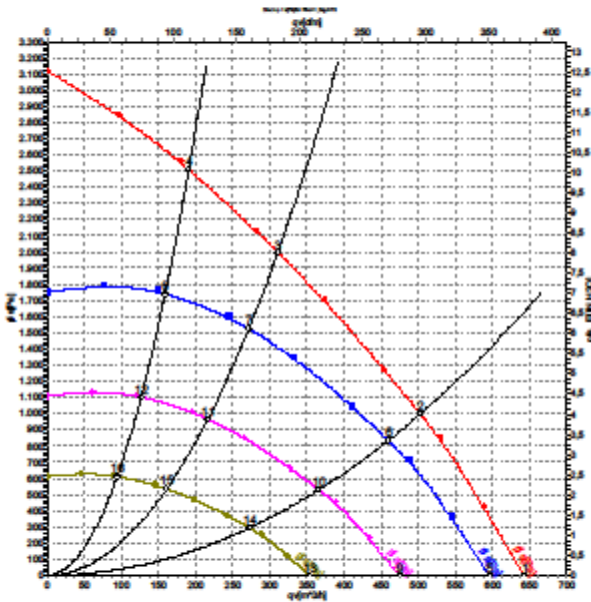
G1G170-AB53-03

EC centrifugal fan

backward-curved, single-intake

with housing (flange), Gas blower for condensing boilers

Curves: Air performance 50 Hz



Measurement LU-57526-1

Air performance measured according to ISO 5007 installation category A. For detailed information on the measurement setup, contact ebm-papst. Intake sound level: Sound power level according to ISO 13347 / sound pressure level measured at 1 m distance from fan axis. The values given are valid under the specified measuring conditions and may vary due to conditions of installation. For deviations from the standard configuration, the parameters have to be checked on the installed unit.

Measured values

	U	f	n	P _{ed}	I	q _v	P _h
	V	Hz	min ⁻¹	W	A	m ³ /h	Pa
1	230	50	5830	360	1.60	645	0
2	230	50	5905	346	1.52	505	1000
3	230	50	6175	308	1.35	310	2000
4	230	50	6480	268	1.18	190	2500
5	230	50	5400	287	1.26	595	0
6	230	50	5400	265	1.16	460	838
7	230	50	5400	206	0.91	270	1527
8	230	50	5400	156	0.68	160	1747
9	230	50	4300	145	0.63	475	0
10	230	50	4300	134	0.59	365	531
11	230	50	4300	104	0.46	215	968
12	230	50	4300	79	0.34	125	1108
13	230	50	3200	60	0.26	355	0
14	230	50	3200	55	0.24	270	294
15	230	50	3200	43	0.19	160	536
16	230	50	3200	32	0.14	95	614

U = Power supply I = Frequency n = Speed P_{ed} = Power consumption I = Current draw q_v = Air flow P_h = Pressure increase



11. APPENDIX E: MESH INDEPENDENCE STUDY

The mesh independence study was done, in order to make sure that the results that were obtained, were independent of the mesh resolution. Low resolution meshes often lead to unstable and inaccurate solutions, while dense meshes require more computational power.

Due to transient flow, a single point value was not selected for the mesh independence study, but a vertical line that was situated 3.1 m from the inlet, in the downstream section of the packed bed. The vertical line provides the temperature data along the height of the outlet channel, exactly at the position where the outlet temperature probe was placed. The vertical line that was used to capture the temperature profile is shown in Figure 11.1.

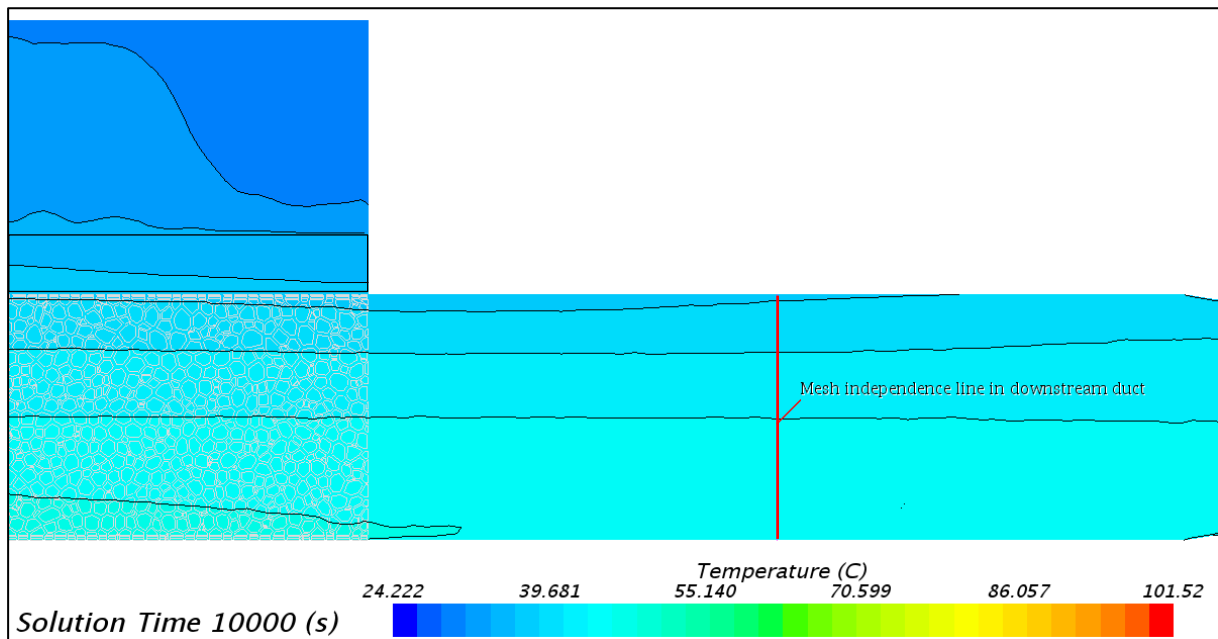


Figure 11.1 Mesh independence study placement

Simulation number 3.3 was selected at random, with a mass flow rate of $250 \text{ kg}\cdot\text{h}^{-1}$ and an inlet temperature of 50°C . The stopping criteria for the simulation was set to 10 000 seconds. This provides sufficient time for the outlet temperature to reach a steady gradient, as shown in Figure 4.40. The base size that was selected for the mesh, was 15 mm, which amounted to 214 261 cells. To test for mesh independence, the number of cells were increased and decreased by 1.5 times the original amount. These values are summarised in Table 11.1.

Table 11.1 Mesh independence base size and cell count

Base Size (mm)	Cell Count
13	345 610
15	214 261
21	106 373

The simulations were run, each with the respective base size. An XY plot was created in STAR-CCM+®, in order to extract the respective data sets. The temperature and channel height data sets were plotted, using Microsoft Excel® scatter plot (smooth lines), as shown in Figure 11.2.

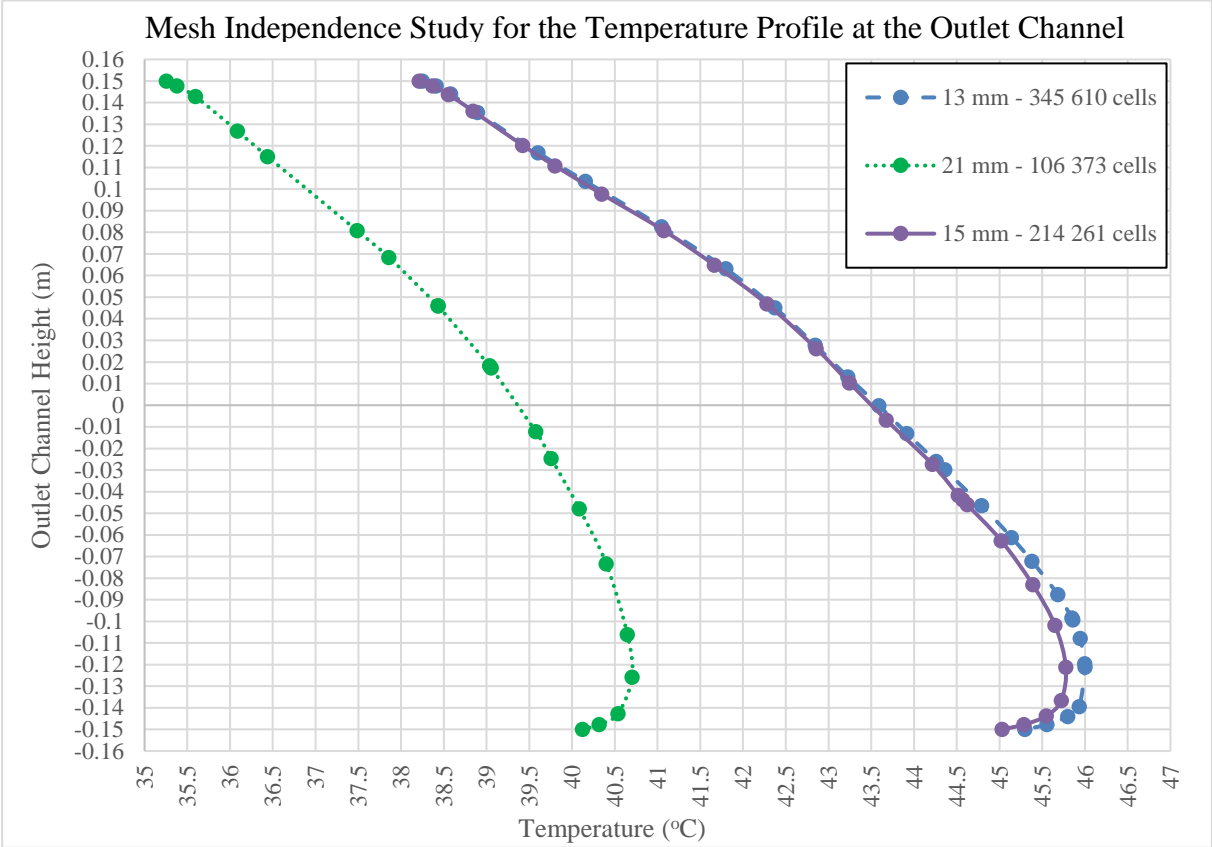


Figure 11.2 Mesh independence study for different cell amounts

The outlet channel height (y-axis) is the 300 mm duct, with the centre being at zero. The data shows that the curves all follow a similar trend. Starting at the top (0.15 m), the temperature is at its lowest, due to energy escaping through the environmental boundary conditions that were set. The temperature gradually increases with a decrease in the vertical position, reaching its maximum close to the boundary layer, where energy is lost through the environmental boundary conditions and the temperature starts to decrease. With the time-step selected at 10000 seconds, it is still in the very early stages of the charging phase, which will result in the curves slowly inverting and displaying a higher temperature in the top regions.

The data indicates that the very coarse mesh of 106 373 cells did not capture the temperature gradient line as well as the original cell size used (15 mm, 214 261 cells). A difference of more than 5% between the two curves is apparent. When comparing the 15 mm grid size with the refined grid size of 13 mm, a very similar trend is displayed, with a maximum difference being far less than 5% (approximately 0.55%).

The results indicate that the selected base size of 15 mm with a cell count of 214 261 is sufficient to capture the temperature profile in the numerical model.

12. APPENDIX F: MESH DEVELOPMENT FOR REGIONS, BOUNDARIES AND INTERFACES

Table 12.1 Mesh for regions and boundaries

Regions	Mesh Conditions	Boundaries	Mesh Conditions and Values
1_Upstream	Customize prism mesh > <u>use default values</u>	IF_Upstream-Heater	-
		Inlet	<ul style="list-style-type: none"> • Mesh conditions > custom surface size > <u>check box</u> • Mesh values > <u>relative to base</u> • Mesh values > relative minimum size > <u>10</u> • Mesh values > relative target size > <u>15</u>
		Metal	-
1_Upstream_Duct	Customize prism mesh > <u>use default values</u>	IF_Heater-Duct	-
		IF_Upstream-Centre	-
		Poly_Wood	-
1_Upstream_Heater	Customize prism mesh > <u>use default values</u>	IF_Heater-Duct	-
		IF_Upstream-Heater	-
		Poly_Wood_Metal	-
2_Centre	Customize prism mesh > <u>use default values</u>	IF_Concrete-Centre	-
		IF_Downstream-Centre	-
		IF_Upstream-Centre	-
		Poly_Wood	-
3_Downstream	Customize prism mesh > <u>use default values</u>	IF_Downstream-Centre	-
		Metal	-
		Outlet	-
		Poly_Wood	-

		Poly_Wood_MEtal	-
4_Concrete	Customize prism mesh > <u>disable</u>	IF_Concrete-Centre	-
		IF_Concrete-Room	-
		Poly	-
5_Room	Customize prism mesh > <u>use default values</u>	IF_Concrete-Room	-
		Poly	-

Table 12.2 Mesh for interfaces

Interfaces	Mesh Conditions
1_Upstream/1_Upstream_Heater	-
1_Upstream_Duct/1_Upstream_Heater	
1_Upstream_Duct/2_Centre	
2_Centre/3_Downstream	-
2_Centre/4_Concrete	Interface Prism Layer Option > Grow Prisms From Interface > <u>Check box</u>
4_Concrete/5_Room	Interface Prism Layer Option > Grow Prisms From Interface > <u>Check box</u>

13. APPENDIX G: PHYSICS DEVELOPMENT FOR REGIONS, BOUNDARIES AND INTERFACES

Table 13.1 Physics for regions and boundaries

Regions	Physics Conditions and values	Boundaries	Physics Conditions and values
1_Upstream	-	IF_Upstream-Centre	-
		Inlet	<ul style="list-style-type: none"> • Physics values > static temperature > method > field function > A_StaticTempAir • Physics values > velocity magnitude > method > field function > A_VelocityInlet
		Metal	<ul style="list-style-type: none"> • Physics conditions > thermal specifications > condition > environment • Physics values > ambient temperature > method > field function > A_AmbientTemperature_Table • Physics values > heat transfer coefficient > method > field function > A_HeatTransferCoefficient_Metal • Physics values > thermal Resistance > method > field function > A_ThermalResistance_Metal
1_Upstream_Duct	-	IF_Heater-Duct	-
		IF_Upstream-Centre	-
		Poly_Wood	<ul style="list-style-type: none"> • Physics conditions > thermal specifications > condition > environment • Physics values > ambient temperature > method > field function > A_AmbientTemperatureTable • Physics values > heat transfer coefficient > method > field function > A_HeatTransferCoefficient_Poly_Wood

			<ul style="list-style-type: none"> Physics values > thermal resistance > method > field function > A_ThermalResistance_Poly_Wood
1_Upstream_Heater	<ul style="list-style-type: none"> Physics conditions > energy source option > total heat source Physics values > field function > A_HeatingLocalSource 	IF_Heater-Duct	-
		IF_Upstream-Centre	-
		Poly_Wood_Metal	<ul style="list-style-type: none"> Physics conditions > thermal specifications > condition > environment Physics values > ambient temperature > method > field function > A_AmbientTemperature_Table Physics values > heat transfer coefficient > method > field function > A_HeatTransferCoefficient_Poly_Wood_Metal Physics values > thermal resistance > method > field function > A_ThermalResistance_Poly_Wood_Metal
2_Centre	<ul style="list-style-type: none"> Physics conditions > turbulence specifications > intensity + length scale Physics values > porosity > 0.44 Physics values > porous inertial resistance > isotropic tensor > isotropic component > field function > A_PorousInertialResistance Physics values > porous viscous resistance > isotropic tensor isotropic component > $0 \text{ kg.m}^{-3}.\text{s}^{-1}$ 	IF_Concrete-Centre	-
		IF_Downstream-Centre	-
		IF_Upstream-Centre	-
		Poly_Wood	<ul style="list-style-type: none"> Physics conditions > thermal specifications > condition > environment Physics values > ambient temperature > method > field function > A_AmbientTemperature_Table Physics values > heat transfer coefficient > method > field function > A_HeatTransferCoefficient_Poly_Wood Physics values > thermal resistance > method > field function > A_ThermalResistance_Poly_Wood

	<ul style="list-style-type: none"> • Physics values > solid density > 2811.208 kg.m⁻³ • Physics values > solid specific heat capacity > 1097.321 J.kg⁻¹.K⁻¹ • Physics values > solid thermal conductivity > isotropic tensor > isotropic component > 3 W.m⁻¹.K⁻¹ [value used in the numerical analysis by Allen (2010)] • Physics values > turbulent length scale > 1 m 		
3_Downstream	-	IF_Downstream-Centre	-
		Metal	<ul style="list-style-type: none"> • Physics conditions > thermal specifications > condition > environment • Physics values > ambient temperature > method > field function > A_AmbientTemperature_Table • Physics values > heat transfer coefficient > method > field function > A_HeatTransferCoefficient_Metal • Physics values > thermal resistance > method > field function > A_ThermalResistance_Metal
		Outlet	<ul style="list-style-type: none"> • Physics values > static temperature > method > field function > A_StaticTempAir • Physics values > pressure > value > 0.0 Pa
		Poly_Wood	<ul style="list-style-type: none"> • Physics conditions > thermal specifications > condition > environment • Physics values > ambient temperature > method > field function > A_AmbientTemperature_Table

			<ul style="list-style-type: none"> • Physics values > heat transfer coefficient > method > field function > A_HeatTransferCoefficient_Poly_Wood • Physics values > thermal resistance > method > field function > A_ThermalResistance_Poly_Wood
		Poly_Wood_Metal	<ul style="list-style-type: none"> • Physics conditions > thermal specifications > condition > environment • Physics values > ambient temperature > method > field function > A_AmbientTemperature_Table • Physics values > heat transfer coefficient > method > field function > A_HeatTransferCoefficient_Poly_Wood_Metal • Physics values > thermal resistance > method > field function > A_ThermalResistance_Poly_Wood_Metal
4_Concrete	-	IF_Concrete-Centre	-
		IF_Concrete-Room	-
		Poly_Wood	<ul style="list-style-type: none"> • Physics conditions > thermal specifications > condition > environment • Physics values > ambient temperature > method > field function > A_AmbientTemperature_Table • Physics values > heat transfer coefficient > method > field function > A_HeatTransferCoefficient_Poly_Wood • Physics values > thermal resistance > method > field function > A_ThermalResistance_Poly_Wood
5 - R	-	IF_Concrete-Room	-

		Poly	<ul style="list-style-type: none"> • Physics conditions > thermal specifications > condition > environment • Physics values > ambient temperature > method > field function > A_AmbientTemperature_Table • Physics values > heat transfer coefficient > method > field function > A_HeatTransferCoefficient_Poly • Physics values > thermal resistance > method > field function > A_ThermalResistance_Poly
--	--	------	--

Table 13.2 Physics for interfaces

Interfaces	Physics Conditions and Values
1_Upstream/1_Upstream_Heater	-
1_Upstream_Duct/1_Upstream_Heater	-
1_Upstream_Duct/2_Centre	<ul style="list-style-type: none"> • Physics conditions > baffle thermal option > <u>conducting</u> • Physics values > porosity > value > <u>0.71455889</u> * • Physics values > porous inertial resistance > field function > <u>A_PorousInertialResistanceMesh</u> • Physics values > thermal resistance > field function > <u>A_ThermalResistance_Metal</u>
2_Centre/3_Downstream	<ul style="list-style-type: none"> • Physics conditions > baffle thermal option > <u>conducting</u> • Physics values > porosity > value > <u>0.71455889</u> * • Physics values > porous inertial resistance > field function > <u>A_PorousInertialResistanceMesh</u> • Physics values > thermal resistance > field function > <u>A_ThermalResistance_Metal</u>
2_Centre/4_Concrete	-
4_Concrete/5_Room	-
<p>* Porosity of mesh region upstream/downstream = Total area (90000 mm²) – Mesh area (25689.7 mm²) = Open area (64310.3 mm²)</p> <p>Porosity = $\frac{\text{Open area (64310.3 mm}^2\text{)}}{\text{Total area (90000 mm}^2\text{)}} = 0.71455889$</p>	

14. APPENDIX H: GENERATING THE HEATING TABLE

The energy source (heating element) that provides the required temperature to the rock-bed, needs a certain temperature difference, in order to provide the watt output of the element. Before the numerical curve could be fitted to the empirical curve, the inlet temperature had to be obtained, which will provide a constant temperature at the inlet of the rock-bed.

The simulation was set up according to the methods described in Section 3.4. The empirical data were plotted to provide the curve for the numerical heating input values to follow, as shown in Figure 14.1. An inlet temperature of 40°C was required.

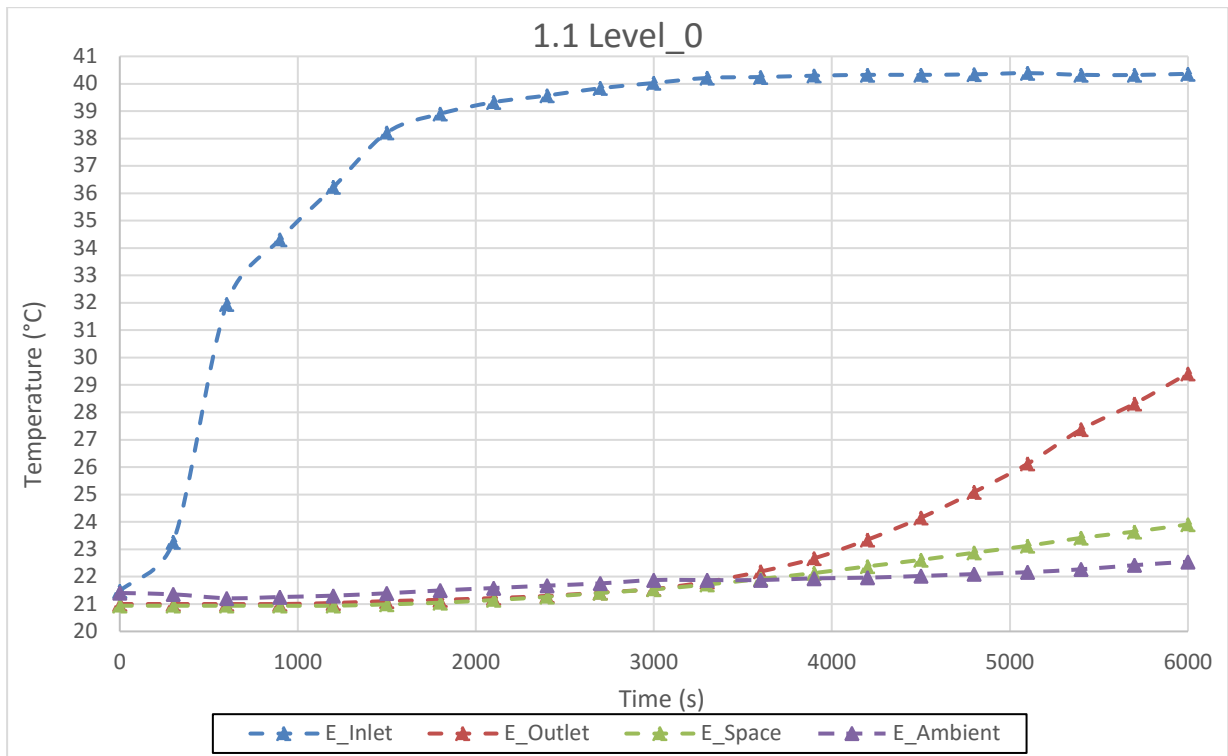


Figure 14.1 Empirical results of the inlet temperature before the packed bed

The heating element energy source in the numerical setup consisted of the ambient temperature and a heating temperature. In order to obtain the heating temperature, several simulations had to be conducted, to get to the required temperature of 40°C for the numerical inlet temperature, as shown in Figure 14.2.

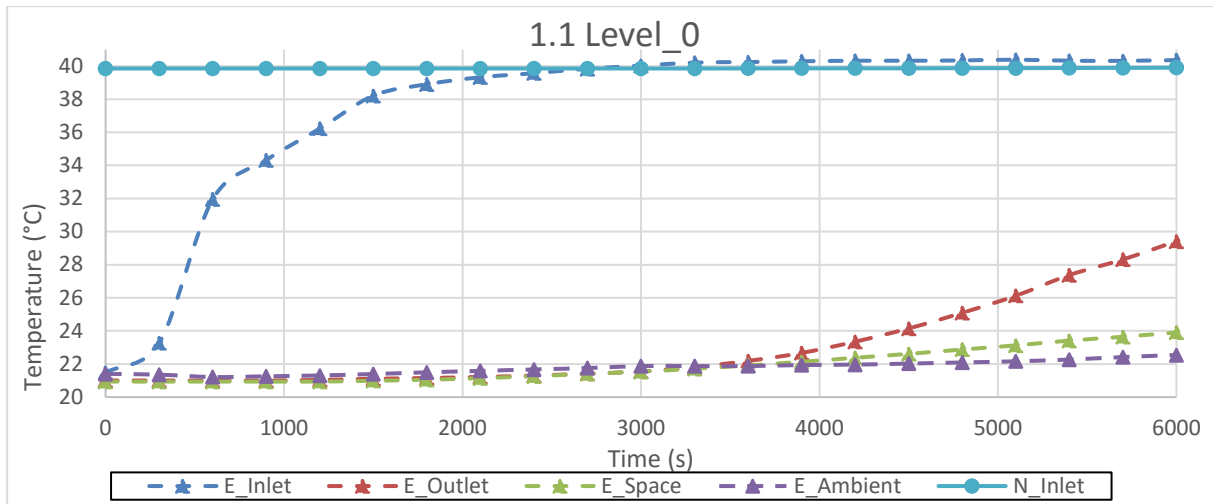


Figure 14.2 Finding the numerical inlet temperature

The heating temperature that was required to provide an inlet temperature of 40°C was determined to be 111°C. This allowed a sufficient temperature difference between the heating temperature and the static ambient temperature, to provide the required watt output of the simulated heating element.

Once the heating temperature was obtained, a heating table was developed, in order to fit the inlet curve of the numerical results to that of the empirical results. This provided the exact inlet temperature in the packed bed for the numerical study. The starting point was at zero seconds, and the end point of the curve, where 40°C was achieved, was at 3000 seconds. Table 14.1 provides the extrapolation method that was developed to predict a shape of the numerical curve that is similar to that of the empirical curve, based on the different end points.

Table 14.1 Method of extrapolation based on empirical results

1	2	3	4	5	6	7	8
Time	Emp. (°C)	Num. (°C)	18.547 (°C)	E%		N%	89.195 (°C)
0	21.480	21.805	1.790	9.651	must =	9.651	8.608
300	23.270	30.413	8.680	46.799	must =	46.799	41.742
600	31.950	72.155	2.369	12.771	must =	12.771	11.391
900	34.319	83.547	1.906	10.278	must =	10.278	9.167
1200	36.225	92.714	1.989	10.722	must =	10.722	9.564
1500	38.214	102.278	0.689	3.714	must =	3.714	3.312
1800	38.903	105.590	0.424	2.285	must =	2.285	2.038
2100	39.326	107.628	0.243	1.311	must =	1.311	1.169
2400	39.569	108.797	0.269	1.452	must =	1.452	1.295
2700	39.839	110.093	0.189	1.017	must =	1.017	0.907
3000	40.027	111.000	-0.000	-0.002	must =	0.000	0.000
3300	40.027	111.000					

The first column consists of the time that the heating temperature required to achieve the inlet temperature of 40°C. The empirical results were used from zero to 3300 seconds. The numerical value at zero seconds, in Column 2, is similar to that of the empirical value; however, it must always be larger than the static air temperature, otherwise the thermal calculations for the heating element source will not work. The final temperature value of 111°C at 3000 seconds was selected as the final temperature state, as it provided the inlet temperature of 40°C, as discussed above. The extrapolation method that was developed works on a percentage basis.

The value of 18.547°C was calculated by taking the difference between the empirical maximum (40.027°C) and the minimum (21.480°C). The value of 89.195°C in Column 9 was calculated in a similar way, based on the numerical maximum (111°C) and the minimum (21.805°C). The values in Columns 4 and 8 were calculated by taking the difference between the temperature values at each time-step of 300 seconds. For example, between the time-step of zero and 300 seconds, the difference between the empirical values, at the specific time-steps (23.27°C - 21.348°C), equalled 1.79°C, as shown in Column 4 at time zero. This was completed until 3000 seconds was reached, for both the empirical and numerical data.

The values in Column 5 and 7 were calculated as a percentage of the temperature value between each time-step and the difference between the maximum and minimum temperature values. For example, using the empirical values in Column 4, $1.79^{\circ}\text{C} / 18.54741^{\circ}\text{C} * 100 = 9.651\%$. This was completed for the rest of the empirical time-steps, as well as the numerical data.

For the extrapolation method to work correctly, the empirical percentage (E%) values in Column 5 must almost be equal to the numerical percentage (N%) values in Column 7; hence, the add-in, SOLVER.XLAM of Microsoft Excel®, was used. The SOLVER.XLAM add-in started at 2700 seconds and progressed up to zero seconds. For each time-step, the objective (N% Column 7), was set to a value of E% (Column 5), by changing the variable cells in Column 3. Working through each time-step, from the bottom to the top, the extrapolated values used in the numerical setup were calculated. The values of the empirical temperatures, as well as the extrapolated numerical data, were plotted on a graph, as shown in Figure 14.3.

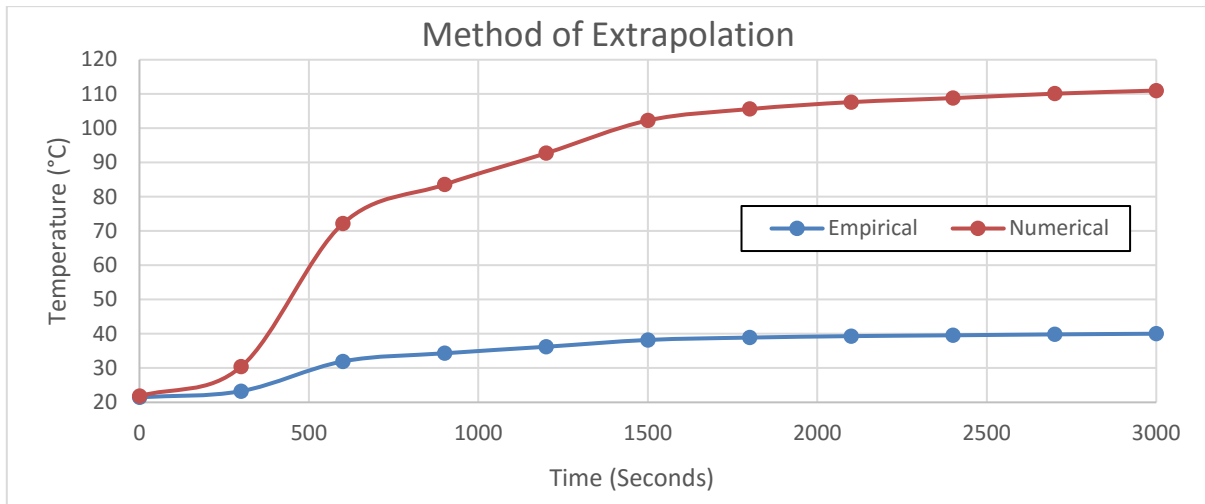


Figure 14.3 Empirical and numerical extrapolation data

The extrapolated numerical data were tabulated to serve as the input file of the simulation. The numerical results from the simulation were plotted to the empirical data, as shown in Figure 14.4.

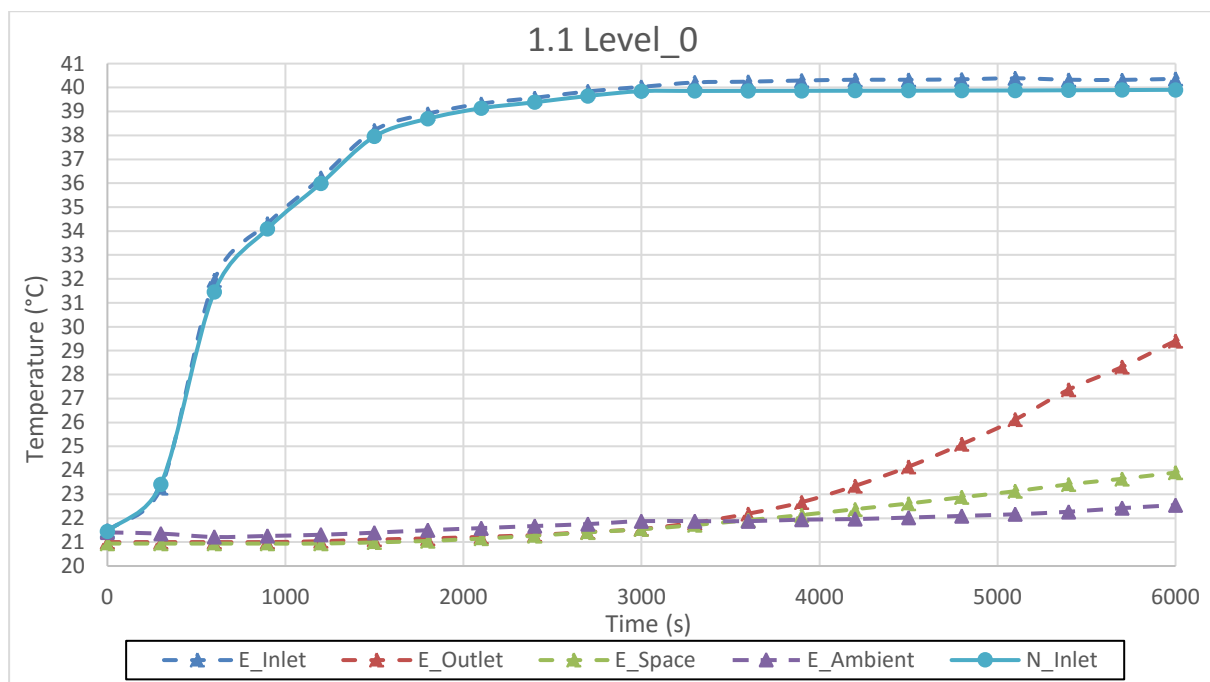


Figure 14.4 Extrapolation method results compared with the empirical results

Generating the heating table as an input file for each simulation required the inlet temperature to be used in the numerical study. The extrapolation method was then used to generate the correct values to be used in the numerical study and to obtain the best fit curve for the numerical data. The methods described above were used for all the simulations that were conducted during the study.

15. APPENDIX I: HEAT TRANSFER AND THERMAL RESISTANCE CALCULATIONS

The empirical setup was not situated in a controlled environment. The ambient conditions varied throughout the day and the materials used in construction had different degrees of thermal resistance. The thermal conductivity values of the materials used in construction, as well as the thickness of the material, are summarised in Table 15.1.

Table 15.1 Summary of thermal resistance values of selected materials

Material	Conductivity, λ ($\text{W}\cdot\text{m}^{-1}\cdot\text{K}^{-1}$)	Source	Thickness, Δx (m)	Thermal resistance, R ($\text{m}^2\cdot\text{K}\cdot\text{W}^{-1}$)
Carbon steel	54.000	Toolbox (2016)	0.0018	3.3333×10^{-5}
Polystyrene	0.033	ISOVER (2015)	0.0750	2.27272727
Wood	0.130	Toolbox (2016)	0.0180	0.13846154

Resistance values can be added together, if the heat transfer values need to be calculated for different layers of materials. The empirical design consists of sections containing a combination of materials, namely: (i) metal, (ii) polystyrene, (iii) polystyrene and wood, and (iv) polystyrene, wood and metal. Hence, the values in Table 15.1 can be added, depending on the layers of material used. A surface air film was also considered for the inside surface of the materials, as well as on the outside surface of the empirical system.

Table 15.2 Summary of the thermal resistance values for a combination of materials

Material	R – inside air film ($\text{m}^2\cdot\text{K}\cdot\text{W}^{-1}$)	R – material ($\text{m}^2\cdot\text{K}\cdot\text{W}^{-1}$)	R – outside air film ($\text{m}^2\cdot\text{K}\cdot\text{W}^{-1}$)	$\sum R$ ($\text{m}^2\cdot\text{K}\cdot\text{W}^{-1}$)
Metal	0.03	3.3333×10^{-5}	0.12	0.1500333
Poly	0.12	2.27272727	0.12	2.5127272
Poly_Wood	0.03	2.411188811	0.12	2.5611888
Poly_Wood_Metal	0.03	2.411222145	0.12	2.5612221

The values of the inside and outside air films were obtained from the ASHRAE (2001). The value of 0.12 was selected for the inside air film of the polystyrene, as the polystyrene container that represents the scaled-down room does not have any moving air within it. The thermal conductance values were also required for the materials, which are the inverse of the thermal resistance values. The thermal conductance values are summarised in Table 15.3.

Table 15.3 Summary of the thermal resistance and conductance values for a combination of materials

Material	$\sum R$ ($m^2.K.W^{-1}$)	Thermal conductance, U, ($W.m^{-2}.K^{-1}$)
Metal	0.1500333	6.665186
Poly	2.5127272	0.397974
Poly_Wood	2.5611888	0.390444
Poly_Wood_Metal	2.5612221	0.390439

The thermal resistance and conductance values allowed the numerical design to simulate the energy loss through the materials, as close as possible, to that of the empirical design.

16. APPENDIX J: POROUS INERTIAL RESISTANCE CALCULATIONS

The porous inertial resistance for the packed bed (porous region) was calculated, using Equations (16.1) and (16.2).

$$P_i = \frac{\Delta P}{U^2 L} \quad (16.1)$$

where,

$P_i = \text{porous inertial resistance [kg.m}^{-4}\text{].}$

$$\frac{\Delta P}{L} = -(P_i |U| + P_v) U \quad (16.2)$$

where,

$P_v = \text{porous viscous resistance [kg.m}^{-3}\text{.s}^{-1}\text{].}$

The porous inertial resistance was calculated for the different flow velocities that were used during the empirical design, with a bed length of 1 m. The predicted pressure drop values in the test model, which was calculated in Appendix C, was used to determine the pressure drop in the porous test model, as summarised in Table 16.1.

Table 16.1 Porous inertial resistance calculations

Velocity (m.s ⁻¹)	Actual Pressure Drop in Test Model (Pa)	Pressure drop in Porous Test Model (Pa)	Porous Inertial Resistance (kg.m ⁻⁴)	Viscous Inertial Resistance (kg.m ⁻³ .s ⁻¹)
0.46251	142.86657	142.86657	667.85801	0.0
0.61087	243.70478	243.70478	653.09023	0.0
0.76794	379.59923	379.59923	643.67291	0.0
0.91630	535.45052	535.45052	637.74345	0.0

The values of the actual test model and the porous test model were changed accordingly, until the curve of pressure drop vs. velocity followed a similar pattern, as depicted in Figure 16.1.

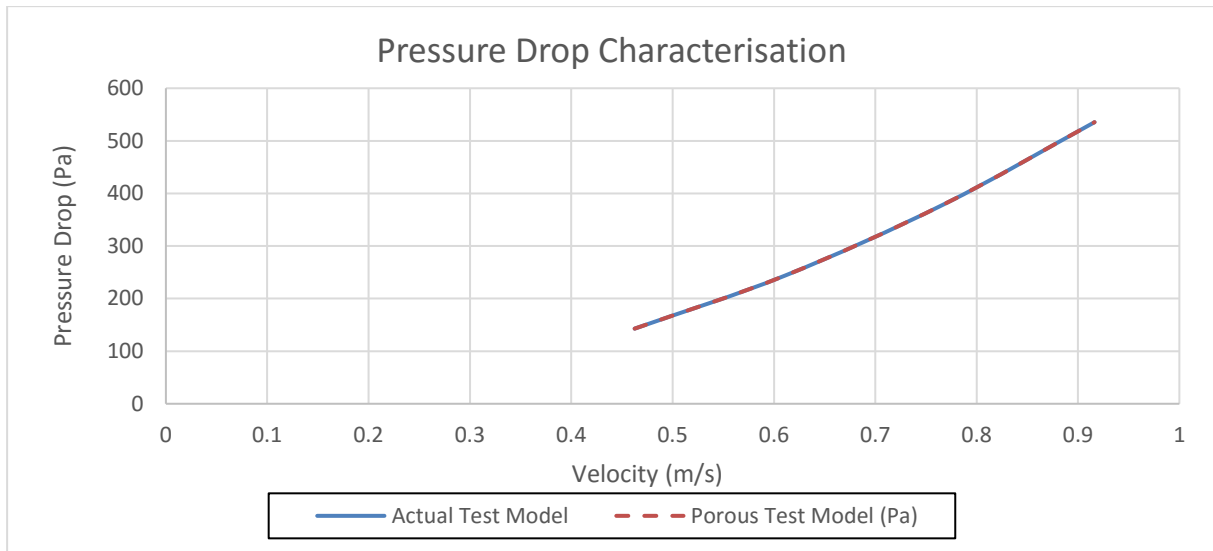


Figure 16.1 Pressure drop characterisation of pressure vs velocity

The porous inertial resistance over the expanded metal mesh was calculated in a similar way, as shown in Equation (16.3).

$$\Delta P = -(P_{im}|U| + P_{vm})U \quad (16.3)$$

where,

P_{im} = porous inertial resistance mesh [unitless], and
 P_{vm} = porous viscous resistance mesh [$m.s^{-1}$].

The porous inertial resistance was calculated for the different flow velocities that were used during the empirical design. The actual pressure drop values in the test model, which were calculated in Appendix C, were used to determine the pressure drop over the porous baffle test model, as summarised in Table 16.2.

Table 16.2 Porous inertial resistance calculations for porous baffle

Velocity ($m.s^{-1}$)	Actual Brattice Model (Pa)	Porous Baffle Test Model (Pa)	Porous Inertial Resistance (unitless)	Viscous Inertial Resistance Mesh ($m.s^{-1}$)
0.462512252	0.587704895	0.588	2.75	0
0.61087	1.02519	1.02618		
0.76794	1.62022	1.62178	2.72277	
0.91630	2.30667	2.30890	Input for STAR-CCM+	

The porous inertial resistance value was constantly changed, until a perfect relationship between the actual model and the test model was achieved, as shown in Figure 16.2.

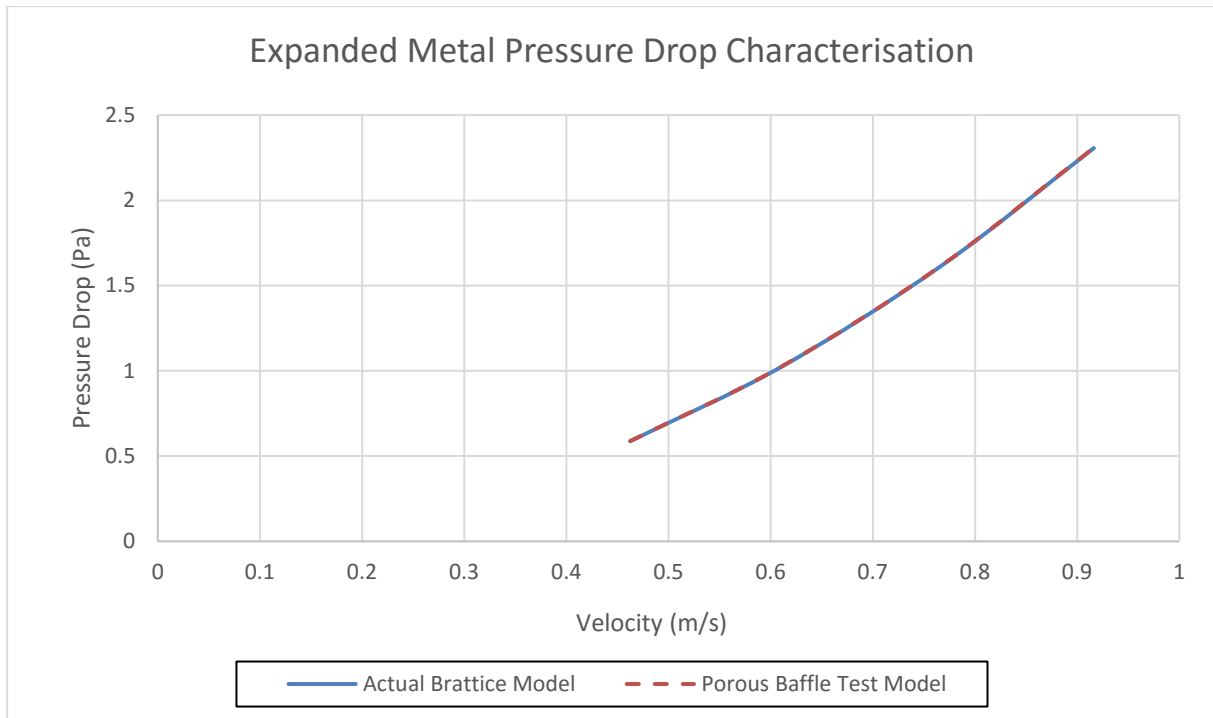


Figure 16.2 Expanded metal pressure drop characterisation

The porous inertial value of 2.75 was divided by the density of air, in order to obtain the final porous inertial resistance value of 2.72, that was to be used as input to the numerical model.

17. APPENDIX K: SENSITIVITY ANALYSIS OF SELECTED VARIABLES

A sensitivity analysis on the numerical simulation was conducted on four variables, namely: (i) the porosity of the packed bed, (ii) the specific heat capacity of the rock, (iii) the resistance values of the construction materials that were used, and (iv) the thermal conductivity of the concrete slab. The intention of the sensitivity analysis is to indicate how large the influence of changing each variable has on the numerical results.

A baseline was selected, with an inlet temperature of 40°C and a mass flow rate of 199.9 kg.h⁻¹. The following graphs compare the empirical data with the numerical data for Level_0, Level_1, Level_2, Level_3 and Level_4.

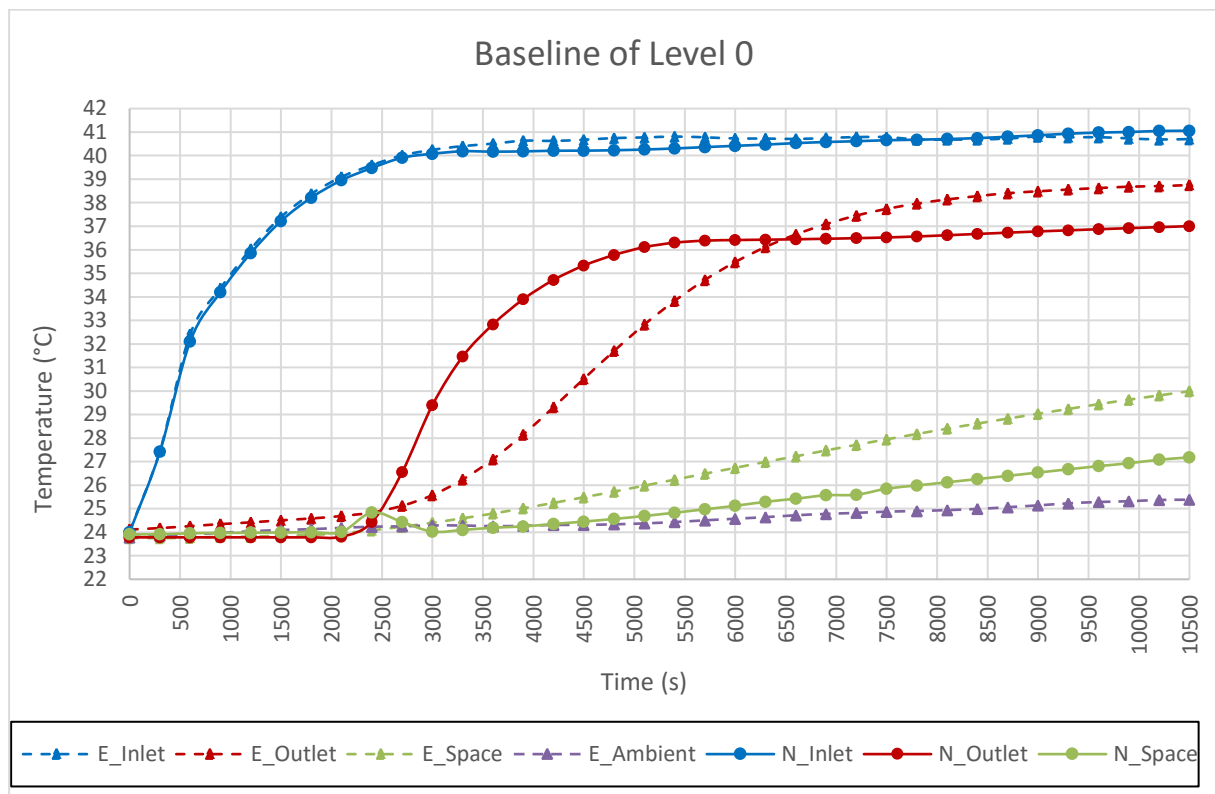


Figure 17.1 Graph of empirical vs numerical data of the baseline for Level 0

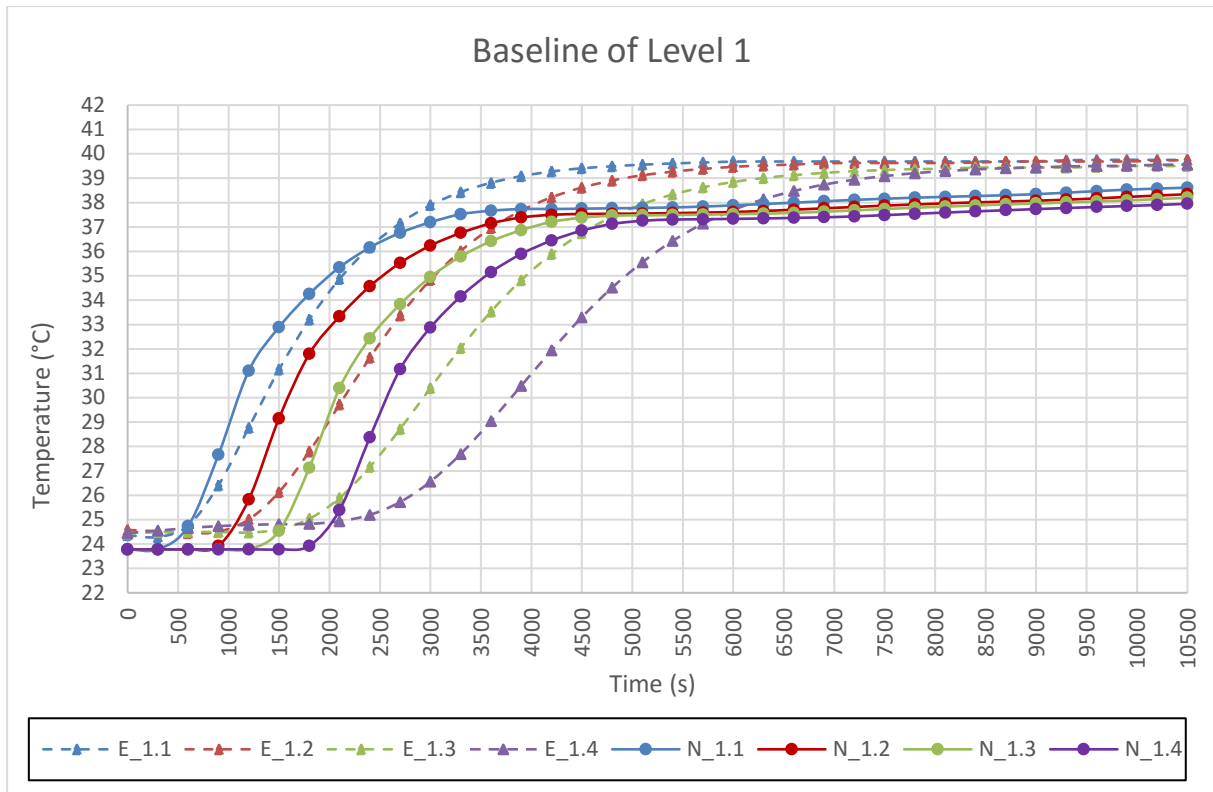


Figure 17.2 Graph of empirical vs numerical data of the baseline for Level 1

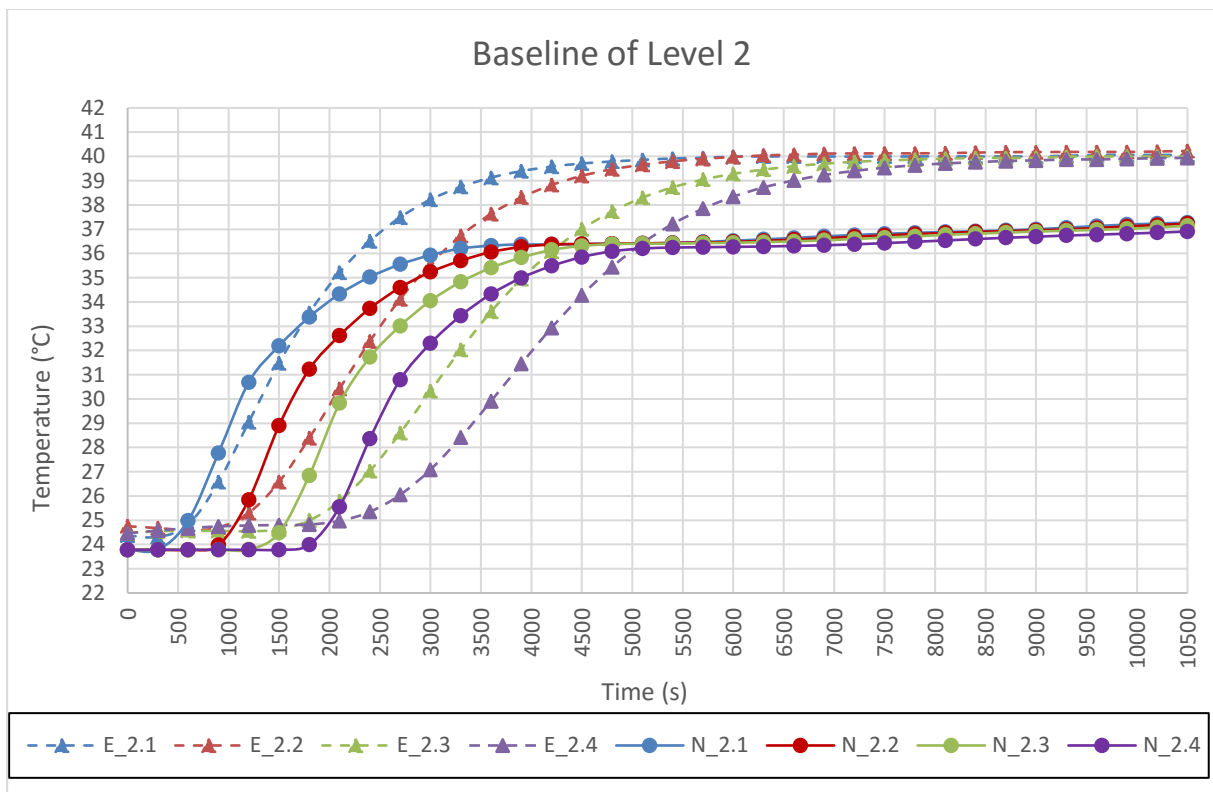


Figure 17.3 Graph of empirical vs numerical data of the baseline for Level 2

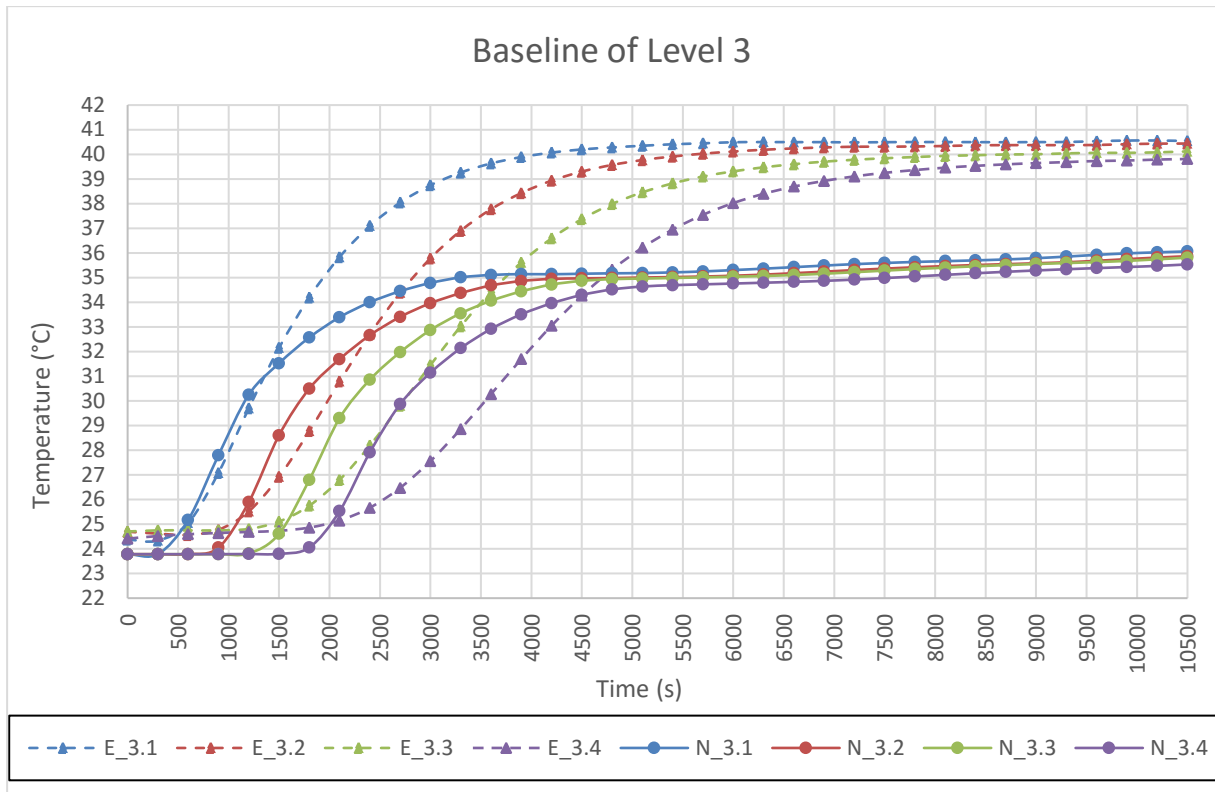


Figure 17.4 Graph of empirical vs numerical data of the baseline for Level 3

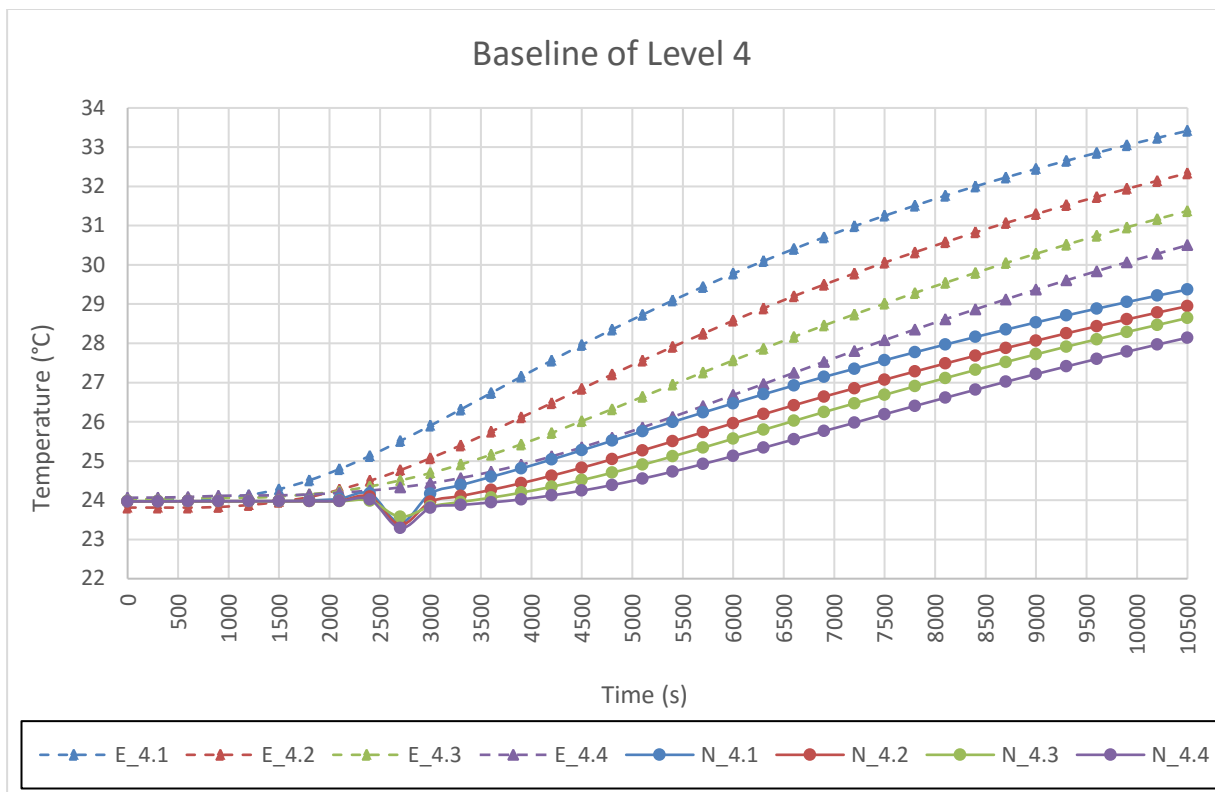


Figure 17.5 Graph of empirical vs numerical data of the baseline for Level 4

The sensitivity analysis was conducted to get the numerical data curves closer to the empirical data. The aim was not just to change the input values to generate a ‘best fit numerical curve’ that fits with the empirical curve, but also to use realistic data for the numerical model.

The porosity of the packed bed was changed from the initial value of 0.44 to 0.3, in order to increase the friction between the air and the rocks and to allow the temperature wave-front to move slower through the packed bed.

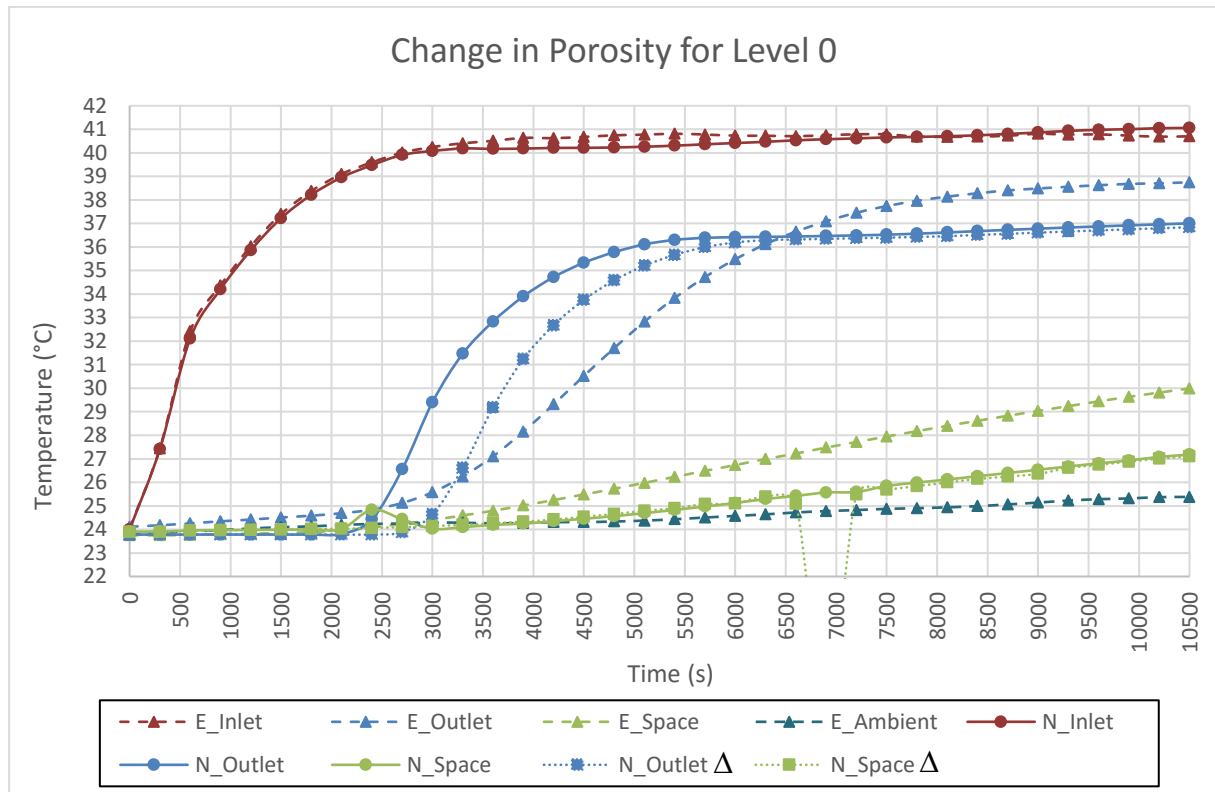


Figure 17.6 Graph of empirical vs numerical data of the changed porosity to 0.3 for Level 0

The results of Figure 17.6 show that the outlet curve of the numerical data moved slightly closer to the empirical outlet curve data. The space temperature was not affected by the change in porosity.

The temperature data in the packed bed (Level_1, Level_2 and Level_3) were affected in a similar manner; hence, only the data from Level_1 is shown in Figure 17.7.

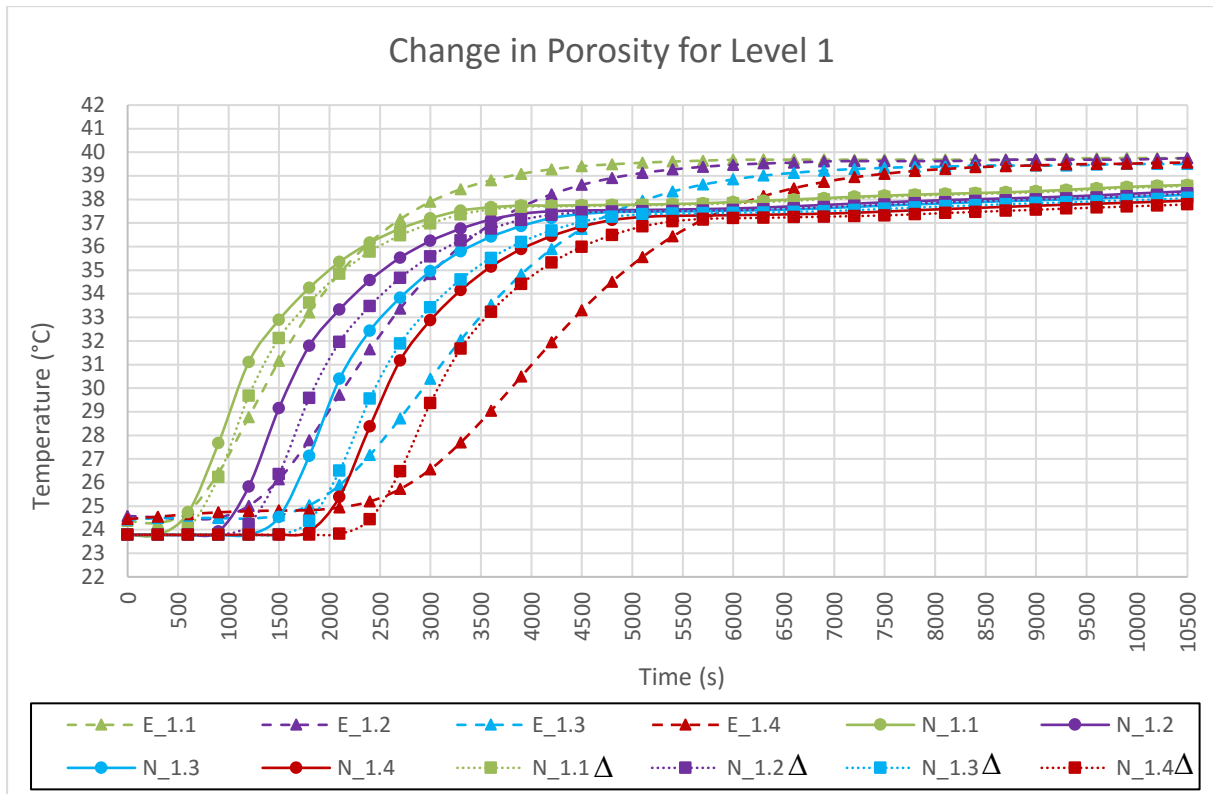


Figure 17.7 Graph of empirical vs numerical data of the changed porosity to 0.3 for Level 1

The trend of the temperature data of Level_1 is similar to that of Level_0, in that the adjusted porosity forces the numerical curves closer to the empirical data curves. The temperature data on the concrete surface did not change significantly, due to the change in porosity.

Although the change in porosity, from 0.44 to 0.3, had a 'positive' influence on the numerical curves of the outlet and packed bed temperature data, a change in the porosity was not done. An asymmetrical packed bed, with a porosity of 0.3 is not possible, because a minimum value of only 0.2595 is achieved with a FCC packing arrangement of monosized spherical particles.

The specific heat capacity of the rocks in the packed bed were changed from the empirical data value of $1097.321 \text{ J.kg}^{-1}.\text{K}^{-1}$ to $800 \text{ J.kg}^{-1}.\text{K}^{-1}$. A comparison of the outlet temperature curve and space temperature curve for the reduction in specific heat capacity is provided in Figure 17.8.

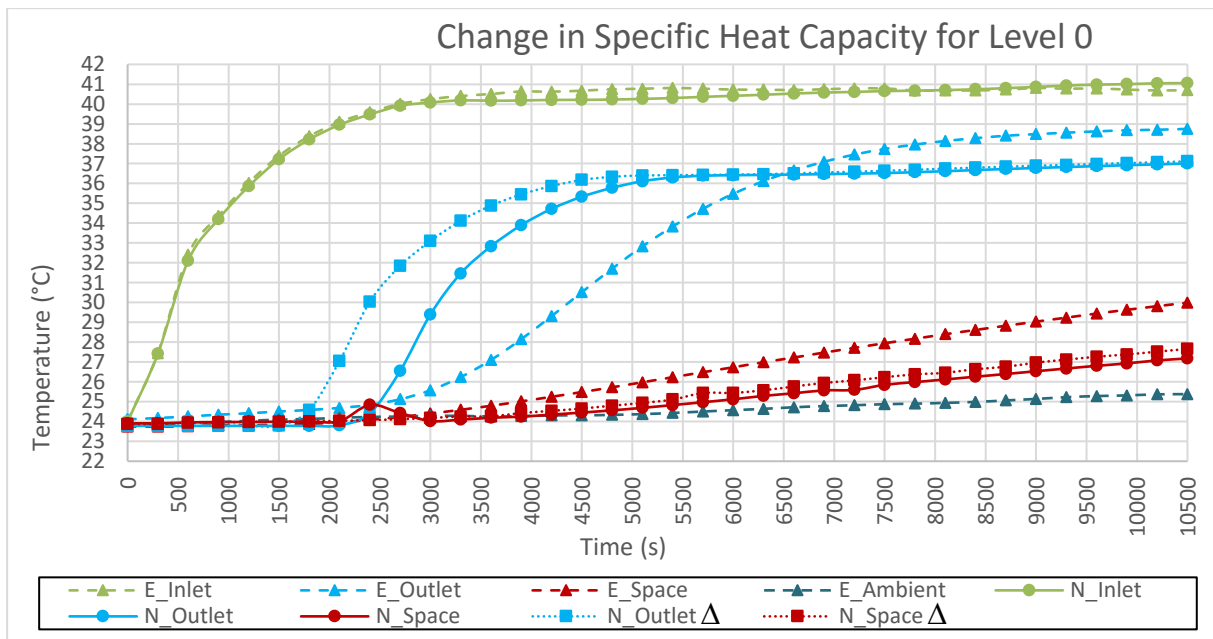


Figure 17.8 Graph of empirical vs numerical data of the changed specific heat capacity to $0.8 \text{ J.kg}^{-1}.\text{K}^{-1}$ for Level 0

The results indicate that the numerical outlet curve moved slightly to the left, moving further away from the empirical data curve. The space temperature data for the reduced specific heat capacity value, moved slightly closer to that of the empirical data. Similar results were obtained for the temperature data of the packed bed, by using Level_1 as an example, as shown in Figure 17.9.

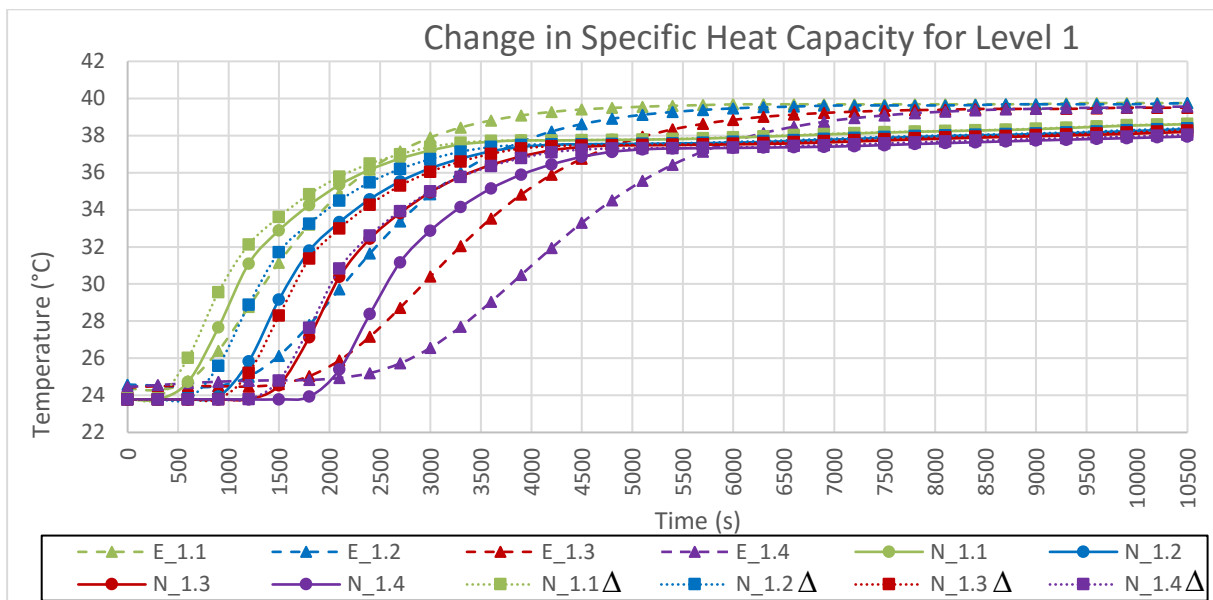


Figure 17.9 Graph of empirical vs numerical data of the changed specific heat capacity to $0.8 \text{ J.kg}^{-1}.\text{K}^{-1}$ for Level 1

The results show that all of the temperature data of the numerical results have moved further away from the empirical temperature data. The graphical representation in Figures 18.8 and 18.9 concludes that the reduction in the specific heat capacity does not have a positive effect on the data.

The resistance values of the materials used for construction were increased and decreased by 50%. The change in resistance values did not have any major effect on the temperature data of the outlet, the packed bed and the space probes. The sensitivity analysis was only conducted for 10500 seconds (approximately three hours); hence, more changes could have occurred when it was carried out for a complete eight-hour charging cycle and a 16-hour discharge cycle.

The thermal conductivity of the concrete slab was the final variable to be analysed for the sensitivity analysis. The original thermal conductivity value of $0.54 \text{ W.m}^{-1}.\text{K}^{-1}$, for concrete was provided by the STAR-CCM+[®] library. The value was changed to $1.4 \text{ W.m}^{-1}.\text{K}^{-1}$ for a concrete stone mix, as used by (Özkahraman *et al.*, 2004). The results are provided in Figure 17.10.

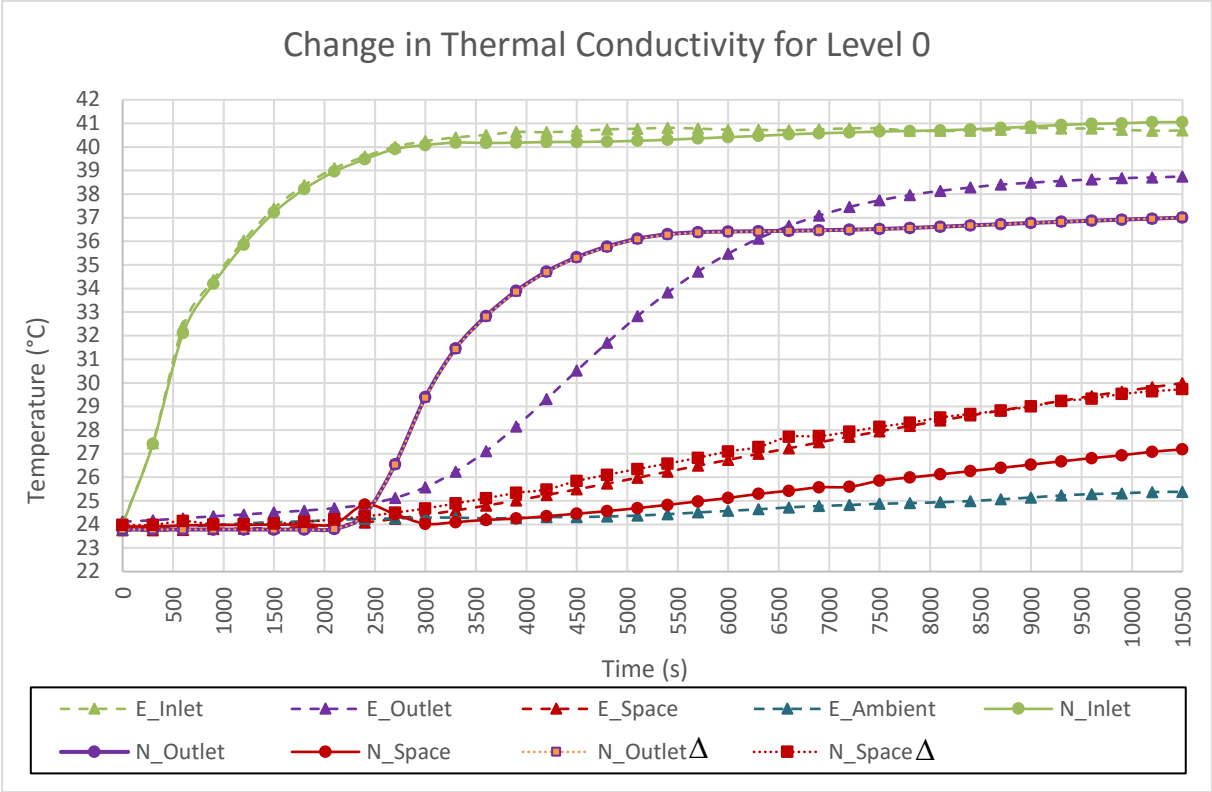


Figure 17.10 Graph of empirical vs numerical data of the changed thermal conductivity to $1.4 \text{ W.m}^{-1}.\text{K}^{-1}$ for Level 0

The results indicate that the outlet curve was not affected at all by the change in the thermal conductivity of the concrete slab; however, the space temperature of the numerical data increased dramatically and followed the empirical data curve very well. The temperature data

of the packed bed was not affected a lot, whereas the temperature data on the concrete surface (Level_4) also changed, as shown in Figure 17.11.

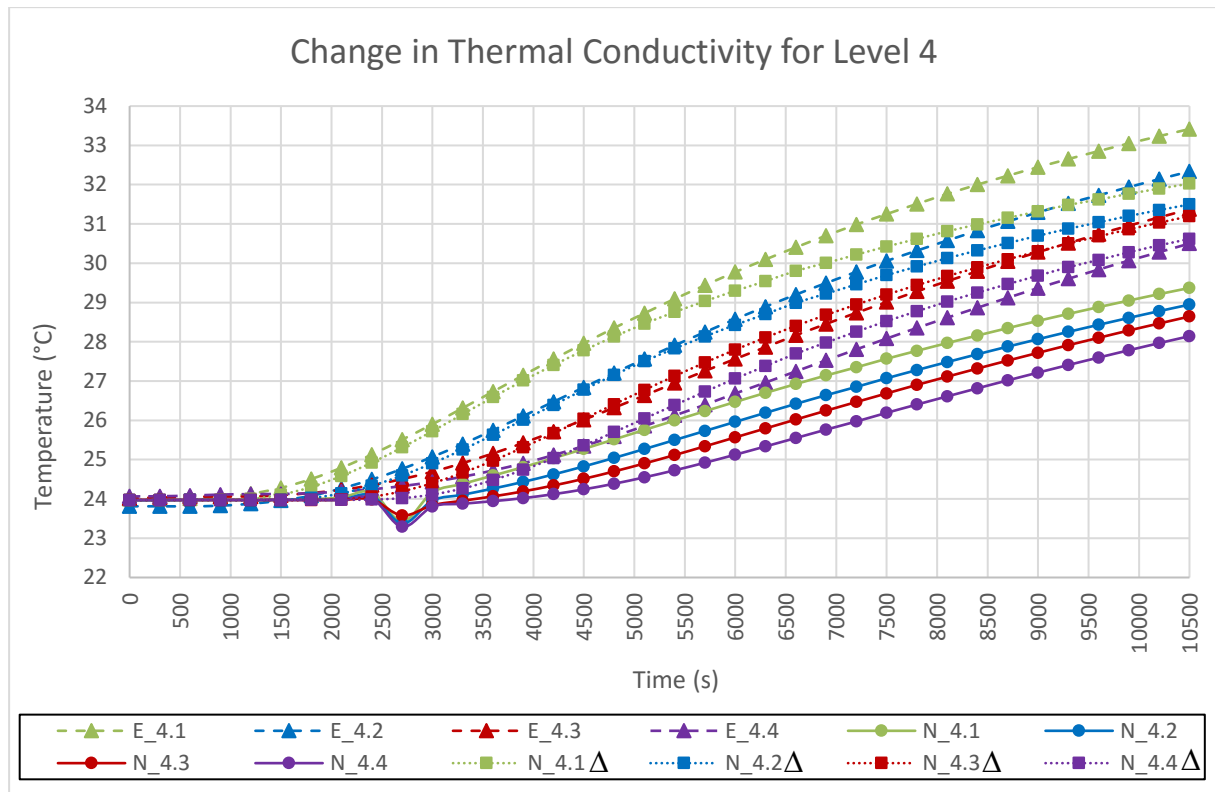


Figure 17.11 Graph of empirical vs numerical data of the changed thermal conductivity to $1.4 \text{ W.m}^{-1}.\text{K}^{-1}$ for Level 4

The data on the graph shows that, with an increase in the thermal conductivity, the temperature probe data of the numerical curve increased, to the point where the numerical data follow the empirical data a lot better.

The results of the sensitivity analysis indicated that, out of the four variables that were analysed, the thermal conductivity showed the greatest improvement in the numerical data curves, when compared with the empirical data. The proposed thermal conductivity value for implementation in the numerical design was selected, in order to improve the results for the numerical tests.

18. APPENDIX L: AVERAGE CHARGING TIME WITH A CHANGE IN TEMPERATURE AND MASS FLOW RATE

Table 18.1 Summary of the average reduction in charging time for a set temperature, with an increase in the mass flow rate

Inlet temperature (°C)	40				45			
Inlet mass flow rate (kg.h ⁻¹)	150	200	250	300	150	200	250	300
Time until charged* (s)	10200	9900	9300	7800	10800	10500	9600	9000
Δ time (s)	-300	-600	-1500		-300	-900	-600	
Average time (s)	-800				-600			
Inlet temperature (°C)	50				55			
Inlet mass flow rate (kg.h ⁻¹)	150	200	250	300	150	200	250	300
Time until charged* (s)	11400	10500	9600	9000	12000	11100	10500	9600
Δ Time (s)	-900	-900	-600		-900	-600	-900	
Average time (s)	-800				-800			
Total average time (s)	-750							
charged* - when the outlet temperature did not increase by more than 0.01°C in 300 s								

Table 18.2 Summary of the average reduction in the charging time for a set mass flow rate, with an increase in the inlet temperature

Inlet mass flow rate (kg.h ⁻¹)	150				200			
Inlet temperature (°C)	40	45	50	55	40	45	50	55
Time until charged* (s)	10200	10800	11400	12000	9900	10500	10500	11100
Δ time (s)	-600	-600	-600		-600	0	-600	
Average time (s)	-600				-400			
Inlet mass flow rate (kg.h ⁻¹)	250				300			
Inlet temperature (°C)	40	45	50	55	40	45	50	55
Time until charged* (s)	9300	9600	9600	10500	7800	9000	9000	9600
Δ time (s)	-300	0	-900		-1200	0	-600	
Average time (s)	-400				-600			
Total average time (s)	-500							
charged* - when the outlet temperature did not increase by more than 0.01°C in 300 s								

19. APPENDIX M: ENERGY BALANCE DATA

Table 19.1 Summary of the energy balance data of the charging phase for inlet temperatures of 40°C and 45°C at different mass flow rates

Test		40_150		40_200		40_250		40_300	
Time (s)	Region	%	kJ	%	kJ	%	kJ	%	kJ
0-28800	1. Input to bed	100.000	18305.285	100.000	23870.179	100.000	29628.640	100.000	30360.167
0-28800	2. Output from bed	57.607	10545.151	67.875	16201.961	72.874	21591.619	74.919	22745.553
0-28800	3. Theoretical energy stored in bed (1 - 2)	42.393	7760.134	32.125	7668.218	27.126	8037.021	25.081	7614.613
0-max*	4. Energy stored in the system (5 + 6 + 7)	18.963	3471.165	14.467	3410.223	11.701	3394.015	11.261	3138.494
0-28800	5. Energy stored in the bed	14.910	2729.271	11.434	2686.214	9.212	2656.358	8.990	2449.004
0-max*	6. Energy stored in the concrete	4.046	740.675	3.028	722.744	2.485	736.376	2.267	688.283
0-max*	7. Energy stored in the space	0.007	1.218	0.005	1.265	0.004	1.281	0.004	1.206
0-28800	8. Energy lost to the environment (3 - 4)	23.430	4288.969	17.658	4257.995	15.425	4643.006	13.820	4476.120
Test		45_150		45_200		45_250		45_300	
Time (s)	Region	%	kJ	%	kJ	%	kJ	%	kJ
0-28800	1. Input to bed	100.000	20556.197	100.000	24246.870	100.000	33673.434	100.000	37935.987
0-28800	2. Output from bed	56.609	11636.748	65.468	15873.900	72.044	24259.733	75.622	28687.791
0-28800	3. Theoretical energy stored in bed (1 - 2)	43.391	8919.448	34.532	8372.970	27.956	9413.701	24.378	9248.196
0-max*	4. Energy stored in the system (5 + 6 + 7)	17.210	3853.479	14.661	3827.394	10.690	4015.415	9.284	3644.305
0-28800	5. Energy stored in the bed	13.277	3044.936	11.256	3001.846	8.105	3144.968	7.194	2851.718
0-max*	6. Energy stored in the concrete	3.927	807.161	3.399	824.138	2.580	868.940	2.086	791.207
0-max*	7. Energy stored in the space	0.007	1.382	0.006	1.409	0.004	1.507	0.004	1.380
0-28800	8. Energy lost to the environment (3 - 4)	26.180	5065.969	19.871	4545.576	17.266	5398.286	15.095	5603.892
max* - the time at which the maximum amount of energy was achieved in a region [Max* = charging time (28800 s) + lag-time]									

Table 19.2 Summary of the energy balance data of the charging phase for inlet temperatures of 50°C and 55°C at different mass flow rates

Test		50_150		50_200		50_250		50_300	
Time (s)	Region	%	kJ	%	kJ	%	kJ	%	kJ
0-28800	1. Input to bed	100.000	25451.928	100.000	36174.636	100.000	43923.652	100.000	54248.033
0-28800	2. Output from bed	58.501	14889.740	67.432	24393.222	72.327	31768.770	75.101	40740.630
0-28800	3. Theoretical energy stored in bed (1 - 2)	41.499	10562.188	32.568	11781.415	27.673	12154.882	24.899	13507.403
0-max*	4. Energy stored in the system (5 + 6 + 7)	14.420	4446.962	10.489	4941.722	8.617	4875.148	7.032	5001.672
0-28800	5. Energy stored in the bed	10.723	3506.034	7.545	3876.603	6.214	3819.580	5.031	3916.162
0-max*	6. Energy stored in the concrete	3.691	939.344	2.939	1063.283	2.399	1053.738	1.998	1083.632
0-max*	7. Energy stored in the space	0.006	1.584	0.005	1.837	0.004	1.830	0.003	1.878
0-28800	8. Energy lost to the environment (3 - 4)	27.078	6115.226	22.079	6839.692	19.056	7279.734	17.867	8505.731
Test		55_150		55_200		55_250		55_300	
Time (s)	Region	%	kJ	%	kJ	%	kJ	%	kJ
0-28800	1. Input to bed	100.000	34740.176	100.000	45422.463	100.000	52194.497	100.000	72023.820
0-28800	2. Output from bed	58.625	20366.415	66.682	30288.732	72.067	37615.214	75.314	54244.282
0-28800	3. Theoretical energy stored in bed (1 - 2)	41.375	14373.761	33.318	15133.731	27.933	14579.282	24.686	17779.538
0-max*	4. Energy stored in the system (5 + 6 + 7)	11.431	5844.044	8.861	6086.163	7.586	5752.036	5.627	6228.458
0-28800	5. Energy stored in the bed	7.856	4602.278	6.009	4790.583	5.229	4521.898	3.789	4905.274
0-max*	6. Energy stored in the concrete	3.568	1239.673	2.847	1293.365	2.353	1228.028	1.834	1320.928
0-max*	7. Energy stored in the space	0.006	2.093	0.005	2.216	0.004	2.110	0.003	2.256
0-28800	8. Energy lost to the environment (3 - 4)	29.944	8529.717	24.457	9047.567	20.347	8827.246	19.059	11551.079
max* - the time at which the maximum amount of energy was achieved in a region [Max* = charging time (28800 s) + lag-time]									

Table 19.3 Summary of the energy balance data of the discharge phase for inlet temperatures of 40°C and 45°C at different mass flow rates

Test		40_150		40_200		40_250		40_300	
Time (s)	Description	%	kJ	%	kJ	%	kJ	%	kJ
28800	Amount of energy in the packed bed at 28800 s	100.000	2729.271	100.000	2686.214	100.000	2656.358	100.000	2449.004
86400	Amount of energy in the packed bed at 86400 s	71.118	1941.016	69.489	1866.628	71.169	1890.492	73.223	1793.239
28800	Amount of energy in the concrete slab at 28800 s	100.000	740.675	100.000	722.744	100.000	736.376	100.000	688.283
86400	Amount of energy in the concrete slab at 86400 s	64.927	480.896	61.790	446.585	64.188	472.665	66.011	454.340
28800	Amount of energy in the space region at 28800 s	100.000	1.218	100.000	1.265	100.000	1.281	100.000	1.206
86400	Amount of energy in the space region at 86400 s	61.986	0.755	60.827	0.770	61.927	0.793	62.054	0.748
Test		45_150		45_200		45_250		45_300	
Time (s)	Description	%	kJ	%	kJ	%	kJ	%	kJ
28800	Amount of energy in the packed bed at 28800 s	100.000	3044.936	100.000	3001.846	100.000	3144.968	100.000	2851.718
86400	Amount of energy in the packed bed at 86400 s	71.396	2173.965	73.161	2196.194	71.343	2243.713	70.720	2016.749
28800	Amount of energy in the concrete slab at 28800 s	100.000	807.161	100.000	824.138	100.000	868.940	100.000	791.207
86400	Amount of energy in the concrete slab at 86400 s	65.114	525.571	66.371	546.990	64.254	558.329	62.165	491.851
28800	Amount of energy in the space region at 28800 s	100.000	1.382	100.000	1.409	100.000	1.507	100.000	1.380
86400	Amount of energy in the space region at 86400 s	64.489	0.891	63.750	0.898	60.581	0.913	56.400	0.778

Table 19.4 Summary of the energy balance data of the discharge phase for inlet temperatures of 50°C and 55°C at different mass flow rates

Test		50_150		50_200		50_250		50_300	
Time (s)	Description	%	kJ	%	kJ	%	kJ	%	kJ
28800	Amount of energy in the packed bed at 28800 s	100.000	3506.034	100.000	3876.603	100.000	3819.580	100.000	3916.162
86400	Amount of energy in the packed bed at 86400 s	69.102	2422.756	69.916	2710.368	70.081	2676.783	69.290	2713.523
max*	Amount of energy in the concrete slab at max* s	100.000	939.344	100.000	1063.283	100.000	1053.738	100.000	1083.632
86400	Amount of energy in the concrete slab at 86400 s	64.767	608.381	64.956	690.662	64.572	680.416	63.462	687.689
max	Amount of energy in the space region at max* s	100.000	1.584	100.000	1.837	100.000	1.830	100.000	1.878
86400	Amount of energy in the space region at 86400 s	65.173	1.032	63.110	1.159	61.179	1.119	58.423	1.097
Test		55_150		55_200		55_250		55_300	
Time (s)	Description	%	kJ	%	kJ	%	kJ	%	kJ
28800	Amount of energy in the packed bed at 28800 s	100.000	4602.278	100.000	4790.583	100.000	4521.898	100.000	4905.274
86400	Amount of energy in the packed bed at 86400 s	68.619	3158.016	69.211	3315.634	68.212	3084.482	67.329	3302.667
max*	Amount of energy in the concrete slab at max* s	100.000	1239.673	100.000	1293.365	100.000	1228.028	100.000	1320.928
86400	Amount of energy in the concrete slab at 86400 s	65.841	816.207	65.477	846.850	62.373	765.954	62.571	826.520
max*	Amount of energy in the space region at max* s	100.000	2.093	100.000	2.216	100.000	2.110	100.000	2.256
86400	Amount of energy in the space region at 86400 s	66.748	1.397	62.436	1.383	56.369	1.190	57.466	1.297
max* - the time at which the maximum amount of energy was achieved in a region [Max* = charging time (28800 s) + lag-time]									